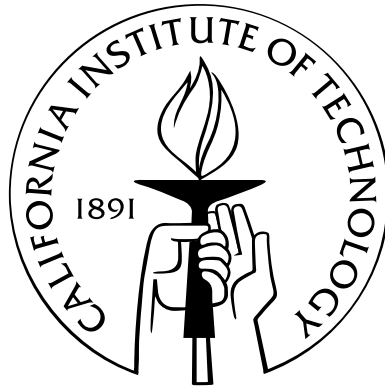


The gravity of the situation

Thesis by
Tristan L. Smith

In Partial Fulfillment of the Requirements
for the Degree of
Doctor of Philosophy



California Institute of Technology
Pasadena, California, USA

2008
(Defended May 20, 2008)

For my grandmother Miriam K. Smith.

“I know nothing except the fact of my ignorance”– Socrates

“No, ’tis not so deep as a well, nor so wide as a church-door; but ’tis enough, ’twill serve: ask for me to-morrow, and you shall find me a grave man”– Mercutio in Shakespeare’s *Romeo and Juliet*

Acknowledgements

Some of my earliest memories are of my grandmother, Mickey, and her impromptu scientific investigations. Whether it was going out to a lobster dinner—which inevitably lead to a dissection of ganglia and a discussion of chiton—or a rainy afternoon filled with the observation of tap water under a microscope looking for paramecia, stentor, and rotifer, my grandmother was always training me for a life of curiosity and hunger for knowledge. Although she tried her best to get a doctor (or *at least* a biologist) out of me she instead got a theoretical physicist (I just couldn't get used to the smell of agar). It is my grandmother to whom I have dedicated this thesis and it is her that I thank for my insatiable desire to learn and to think. Without her, I might have ended up an actor and would have learned more about cosmetology than cosmology!

It took a short stint in acting to point me in the direction of theoretical physics. I want to thank the nameless tutor I had when understudying in a Lohman Family Picnic who lent me a copy of Richard Feynman's *What Do You Care What Other People Think?* and let me read it instead of doing my schoolwork. Looking back on it, that is possibly the only time in my life when it was a good thing that I didn't do my schoolwork.

My family has been right next to me along this long and winding road. There were nights spent with me in the hospital, taxi rides to after-school auditions, long conversations through dark and cold winters when I was at the University of Chicago and putting up with longwinded explanations of my research which were incredibly met with more questions and interest on their part. Without my father and mother I would not have appreciated the creativity and art that is necessary when pursuing a life in science; without my brother I would not have had such a deep and inspiring friendship to hold me up and remind me what is worthwhile.

My earliest years were fraught with innumerable hospital stays and surgeries. Without Charlie, Carol and Jake Stolar my ability to extol the virtues of gravitational waves and to explore the consequences of alternative gravity theories might not have had time to develop (and consider what would have been lost to the world!). Any time that I have had the great fortune of experiencing something which has made me thankful to be alive (such as this thesis) I think of them.

Now, of course I couldn't have made it through grad school without the most amazing group of friends that I can imagine (and when I first accepted Caltech's offer of admission I tried to imagine

the types of friends I would have and definitely did *not* come close to imagining the ones I ended up with). From the Windy City to the City of Roses, Nate Bode and I have been through a lot together. From the realization that *if* Caltech accepted both of us all of the other prospective grad students would have to have perfect scores on their GREs to my first explorations of Southern California to the process of writing this thesis, Nate has been an amazing Friend (and I mean that with a capital ‘F’). He has also taught me, in his sometimes subtle, sometimes not so subtle ways, how to love life, to explore and to challenge myself in ways I could have never expected. Partae Onum. Nate’s parents, Faith and Jerry, and his wife Lucia, have been a second family to me. I always found it corny when some one would say something like that—their love and support and care has shown me what it means to have a second family. I thank Jenny Roizen for her love and support. Your love has allowed me the freedom to take more risks with the confidence that you would be there at the end. Her banana bread, although difficult to get, is well worth the wait. I look forward to many more slices in the years to come. Hernan Garcia has taken me to glaciers in Argentina, suffered with me through the qualifying exams and been the best roommate I could imagine (I never have to remember to pay the rent—because he always reminds me several times). Eric Peterson passed through the fires of Jackson as well as traveled throughout South America and Europe with me. Whether we were playing pirates at a live Clue party or we were enjoying our one lazy day in Paris, when Eric and I hang out you would never guess that we were both physics grad students (and that’s a good thing). Dan Grin (a.k.a. Hey Steve!), a fellow student in my research group, has been the first person I want to talk to when I want an intelligent and thorough critique of any research question. He has also been my National Parks exploring partner, and is definitely a Park Ranger. Ketan Vyas has shown me a lot of patience when it comes to my physics questions (he is a string theorist) and has always been there if I want to go out for dinner and spend like I was a postdoc. Jenn Stockdill has been a great friend and has an uncanny ability of calming me down—especially if it is on a dune in the middle of Death Valley on June 3rd (120° F!). Tristan Ursell is the one who organized that Death Valley trip and I thank him for helping to introduce me to the great outdoors as well as for sharing with me his insatiable curiosity, whether it be biophysics or some crazy restaurant in Baker, CA.

There are many other people I want to thank for their friendship throughout my years at Caltech: Lotty Ackerman, Dan Babich, Mike Boyle, Ben Collins, Steph Culler, Jen Dionne, Katy Elortegui, Dan Elortegui, Adrienne Erickcek, Kevin Hoff, Mike Kesden, Geoffrey Lovelace, George Matheou, Jen Mederos, Reynier Molenaar, Anusha Narayan, Pedro Ochoa, Rob Owen, Raviv Perahia, Jonathan Prtichard, Anthony Pullen, Iggy Sawicki, Kevin Setter, Kris Sigurdson, Sean Tullin, and Melanie Probisko Yen.

I want to thank Shirley Hampton and JoAnn Boyd for keeping TAPIR up and running and Chris Mach for keeping the computers and printers in check.

I thank my collaborators with whom I completed the work presented in this thesis: Robert Caldwell, Takeshi Chiba, Asantha Cooray, Adrienne Erickcek, Marc Kamionkowski, Hiranya Pieris, and Elena Pierpaoli.

Finally, I want to thank my advisor Marc Kamionkowski. It is because of his dedication to me as his student that I am able to present this thesis. Besides learning how to find and approach research problems I come away from this experience with the example of Marc's diverse interests and his desire to always learn new things. As I stated at the beginning of these acknowledgments, from a very young age I have wanted to be a scientist because to me it represented the life of curiosity and knowledge. Most youthful impressions become corroded with time as reality sets in. In this case, Marc's example and his mentoring has allowed for my youthful impression of a scientific life to emerge strengthened rather than diminished.

Abstract

In this thesis we examine several ways in which we can explore the early universe through gravitational waves and the fundamental nature of gravity through cosmology and observations of dynamics within the solar system. Both of these topics have taken center stage, as we are living at a unique time which promises to bring fundamental insights into the nature of gravity with the discovery of new binary pulsar systems, the building of increasingly precise solar system and tabletop experiments and the birth of gravitational-wave observatories— to name a few recent and upcoming advances.

We first discuss whether we may be able to directly detect gravitational waves from inflation using future space-based interferometers. We then describe how the direct detection of inflationary gravitational waves will allow us to probe the fundamental physics that operated at the earliest moments of the universe. Next, a new constraint to a general cosmological gravitational wave background is presented using the observations of the cosmic microwave background. Moving away from general relativity, we consider alternative theories of gravity. One reason to consider alternative theories of gravity is the observation that the expansion of the universe is currently accelerating. It is possible that this accelerated expansion is due to a modification of gravity. However, any theory that modifies gravity in order to produce accelerated expansion must also conform to the dynamics that we observe within the Solar System. We discuss how the observation of the deflection of light around the Sun places severe limitations on a particular modified gravity theory, known as $f(R)$ gravity. Our discussion of $f(R)$ gravity leads us to ask whether the parameterized post Newtonian parameter, γ_{PPN} , takes on a universal value. We identify measurements made of strong lensing around early type galaxies in the Sloan Lens ACS (SLACS) survey as a first step in performing this new test of gravity. Finally, we explore some consequences of Chern-Simons gravity. One of the unique aspects of Chern-Simons gravity is that it introduces parity violation into the gravitational sector. As a consequence, it predicts a different gravitomagnetic field around the rotating Earth than is predicted in general relativity. We show how recent measurements of this gravitomagnetic field made by observing the two LAsER GEODynamics Satellites (LAGEOS) and Gravity Probe B satellites constrain Chern-Simons gravity. Finally, we discuss how future observations of binary pulsar systems may allow for a more general exploration of the gravitomagnetic structure around rotating objects.

Contents

Acknowledgements	iv
Abstract	vii
1 Introduction and Summary	1
1.1 The uniqueness of gravity	1
1.2 Gravitational waves from inflation	5
1.3 Combining CMB/matter power spectrum and GWO observations	6
1.4 A new constraint to the cosmological gravitational-wave background	6
1.5 Solar system tests of $f(R)$ gravity	8
1.6 Constraints to Chern-Simons gravity	9
2 Detecting the stochastic gravitational wave background	11
2.1 Introduction	11
2.1.1 Inflationary dynamics and perturbations	12
2.1.1.1 Homogeneous evolution	12
2.1.1.2 Perturbations	13
2.1.1.3 Number of e -foldings	14
2.1.2 Constraints to inflationary observables	16
2.1.3 Gravitational-wave transfer function	17
2.2 Direct-detection thresholds	18
2.3 The connection between $n_s < 1$ and the IGWB amplitude	21
2.4 BBO/DECIGO amplitudes	22
2.4.1 Power-law inflation	23
2.4.2 Chaotic inflation	25
2.4.3 Hybrid inflation	29
2.4.4 Symmetry breaking inflation	31
2.4.5 PNGB inflation	33
2.4.6 Coleman-Weinberg inflation	34

2.5	The (running) power-law approximation	36
2.6	Broken scale invariant spectrum	38
2.7	Discussion	40
3	Deciphering inflation with gravitational waves: cosmic microwave background polarization vs. direct detection with laser interferometers	44
3.1	Introduction	44
3.2	Monte Carlo calculational method	45
3.3	A fundamental test of slow-roll inflation	49
3.4	Summary	52
4	A new cosmic microwave background constraint to primordial gravitational waves	54
4.1	Introduction	54
4.2	The high-frequency CGWB as a component of the radiative energy density	56
4.3	The effects of a relativistic species on the CMB and LSS	59
4.3.1	Homogeneous influence	59
4.3.1.1	Effects in the CMB	60
4.3.1.2	Effects on the matter powerspectrum	62
4.3.2	Inhomogeneous influence	64
4.4	Results	67
4.5	Conclusions	69
5	Observational tests of $f(R)$ gravity	72
5.1	Introduction	72
5.2	The particular example of $f(R) = -\mu^4/R$	73
5.3	Conditions on general $f(R)$ theories	78
5.3.1	Weak-field solution around a spherical star	78
5.3.2	Case studies	84
5.4	How to evade solar system tests in $f(R)$ -gravity	87
5.5	Testing for the universality of γ_{PPN}	90
5.5.1	Universality of γ_{PPN} from strong lensing	90
5.6	Conclusions	99
6	Solar system constraints to Chern-Simons gravity	101
6.1	Introduction	101
6.2	Chern-Simons gravity	102
6.3	The Chern-Simons gravitomagnetic equations	103
6.4	Gravitomagnetism due to a spinning sphere in Chern-Simons gravity	106

6.5	Gravitomagnetic perturbations to Keplerian orbits	108
6.5.1	Perturbed planetary equations	109
6.5.2	Application of the Gaussian perturbation equations to gravitomagnetism . .	111
6.5.3	Lorentz force	114
6.5.4	Application to the Lense-Thirring drag	116
6.5.5	Detecting gravitational parity violation through gravitomagnetism	119
6.5.6	Secular gravitomagnetic perturbations and the disturbing function	121
6.6	Orbital and gyroscopic precession in Chern-Simons gravity	122
6.6.1	Orbital precession	122
6.6.2	Gyroscopic precession	123
6.7	Conclusions	125
A	An expression for the high-frequency gravitational-wave transfer function	127
A.0.1	Transfer function during reheating	129
A.0.2	Transfer function during radiation domination	130
B	Setting the homogeneous initial condition for the CGWB	134
C	Review of scalar tensor equivalence	144
D	A string-inspired derivation of the Chern-Simons field equations	146
E	Calculation of the vector potential	149
F	An alternative method to solve the Chern-Simons gravitomagnetic field equations	152
F.0.3	Decomposition of a solenoidal vector field	153

List of Figures

1.1	Current and future constraints to the cosmological gravitational wave background . . .	7
2.1	Detecting the inflationary gravitational-wave background	20
2.2	Gravitational wave foregrounds	21
2.3	CMB/BBO amplitudes for Power-law inflation	24
2.4	CMB/BBO amplitudes for Chaotic inflation	26
2.5	CMB/BBO amplitudes for Hybrid inflation	28
2.6	CMB/BBO amplitudes for symmetry breaking inflation	31
2.7	CMB/BBO amplitudes for PNGB inflation	33
2.8	CMB/BBO amplitudes for Coleman-Weinberg inflation	35
2.9	Derivatives of the Coleman-Weinberg potential during inflation	35
2.10	Comparison between the slow-roll approximation and an exact solution	37
2.11	What we can conclude without a detection of inflationary gravitational waves	42
3.1	Sets of inflationary potentials satisfying constraints from both CMB/LSS observations and the direct detection of the inflationary gravitational wave background	47
3.2	Testing the single field consistency relation with the direct detection of the inflationary gravitational wave background	50
4.1	The ability to constrain extra relativistic energy density through various observations	61
4.2	The effects of extra relativistic energy density on the CMB temperature anisotropy and matter power spectrum	63
4.3	The degeneracy between Ω_M and N_{eff}	65
4.4	A comparison between the effect of homogeneous and adiabatic initial conditions on the CMB temperature anisotropies	66
4.5	Results of the constraints to CGWB coming from the CMB and LSS	68
4.6	Constraints to the CGWB from CMB and LSS observations	70
5.1	Evolution of the linearization condition in $f(R)$ gravity as a function of redshift	89
5.2	The angular diameter distance factor in the expression for the Einstein mass	93

5.3	Constraints to γ_{PPN} as a function of the slope of the total mass density α	94
5.4	γ_{PPN} as a function of the error in the line-of-sight velocity dispersion	96
5.5	The Lilliefors test applied to the mock data sets of γ_{PPN}	97
5.6	SLACS measurements of γ_{PPN} as a function of redshift and richness	98
6.1	Diagram of osculating orbital elements	112
6.2	The coordinate system associated with the orbiting test body	114
6.3	The oscillation of the eccentricity for an orbit perturbed by the Lense-Thirring gravitomagnetic field	118
6.4	The ratio $\dot{\Omega}_{\text{CS}}/\dot{\Omega}_{\text{GR}}$ for the LAGEOS satellites	123
6.5	The ratio $\dot{\Phi}_{\text{CS}}/\dot{\Phi}_{\text{GR}}$ for Gravity Probe B	124
A.1	The gravitational wave transfer function A_{gw} at a frequency of 0.1 Hz (corresponding to the frequency of BBO) as a function of the reheating temperature	132
B.1	The evolution of the various perturbation variables for CGWB homogeneous initial conditions	143

Chapter 1

Introduction and Summary

1.1 The uniqueness of gravity

Among the four basic forces, gravity plays a very special role. This statement has been made so many times that it may be considered cliché, but this does not belie its truth. As the ‘universal force’ it plays a fundamental role in the evolution of the universe, from the big bang to today. As the only known force that cannot be written within a consistent quantum theory its fundamental nature is expected to elucidate the complete ‘theory of everything’. As the weakest force it allows us to observe physics at energy scales approaching the Planck scale. Besides playing this unique role within nature, we are living at a unique time which promises to bring fundamental insights into the nature of gravity: incredibly precise measurements of the motion of bodies within the solar system have recently allowed us to test the behavior of gravity around the Sun and Earth to previously unimaginable accuracy; table-top experiments are being designed which test gravity on smaller and smaller length scales; laser interferometers are currently collecting data which will inevitably lift the veil from the gravitational-wave sky; the discovery of binary pulsars presents us with a laboratory in which to ask new questions of the strong-field behavior of gravity; measurements of the polarization of the cosmic microwave background (CMB) may soon give evidence of gravitational waves produced during the earliest moments of the universe; measurements indicating that the expansion of the universe is accelerating may actually be pointing us toward previously unknown aspects of gravity.

In the first part of this thesis we take the point of view that general relativity is correct and use the properties of gravitational waves in order to probe processes occurring during the earliest moments of the universe. Our ability to make quantitative statements about cosmology is directly linked to the requirement that the photons from the primeval fireball travel to us undergoing relatively few interactions. This in turn sets the earliest time from which we have direct information about the universe: 300,000 years after the big bang electrons combined with protons freeing the photons to travel to us nearly unimpeded. If we were able to directly observe neutrinos, the earliest directly observable epoch would be pushed back 13 orders of magnitude to around 1 s. Following Ref. [1],

we can estimate this time by noting that neutrino decoupling occurs when the interaction rate, Γ , drops below the Hubble parameter. The interaction rate between neutrinos and electrons is given by $\Gamma = n_e \langle \sigma v \rangle$ where n_e is the electron number density and $\langle \sigma v \rangle$ is the thermally averaged cross section. The interaction vertex involves a factor of G_F since the interaction proceeds through the weak force, which leads to $\sigma \propto G_F^2$. Dimensional analysis (in units where $c = \hbar = 1$) tells us that we have $\sigma \sim G_F^2 E^2$. Furthermore, since the electrons and neutrinos are relativistic when they decouple we have $v = 1$ and $n_e \sim T^3$ so that

$$\Gamma \sim G_F^2 T^5. \quad (1.1)$$

We also know that $H \sim T^2/m_{\text{Pl}}$, where m_{Pl} is the Planck mass, so that

$$\left(\frac{\Gamma}{H}\right)_\nu \sim \frac{G_F^2 T^3}{m_{\text{Pl}}} \sim \left(\frac{T}{1 \text{ MeV}}\right)^3, \quad (1.2)$$

which corresponds to a decoupling epoch of $t \sim 1/H(T = 1 \text{ MeV}) \sim m_{\text{Pl}}/(\text{MeV})^2 \sim 1 \text{ s}$. Performing the same analysis for gravitons we need only note that the interaction strength is dictated by $1/m_{\text{Pl}}$ as opposed to G_F so that $\sigma \sim G = 1/m_{\text{Pl}}^2$ and we have

$$\left(\frac{\Gamma}{H}\right)_{\text{grav}} \sim \left(\frac{T}{1 \text{ mPl}}\right)^3, \quad (1.3)$$

which corresponds to a decoupling epoch of $t \sim 1/m_{\text{Pl}} = 10^{-44} \text{ s}$. Therefore, in principle, by detecting gravitational waves we would be able to directly probe the dynamics of the universe up to a temperature of $m_{\text{Pl}} = 1.2 \times 10^{19} \text{ GeV}$ or a time of 10^{-44} s ! Such energies are far beyond what we may have access to in any sense of the ‘near future’—for comparison, the Large Hadron Collider at CERN will probe energies approaching 10 TeV, a full 15 orders of magnitude smaller.

One possible origin for a background of gravitational waves in the early universe is a period of early accelerated expansion known as inflation [2–4]. Inflation was first proposed to solve theoretical issues related to the initial conditions of the homogeneous and isotropic universe we see around us today. One of its generic predictions is the production of a scale-invariant spectrum of perturbations in the energy density of the universe [5–8]. This prediction has been confirmed by observations of the CMB and the clustering of galaxies. Another generic prediction is the production of a background of gravitational waves which has yet to be observed [9–15]. If observed, the amplitude of this background would tell us the energy scale at which inflation took place, an essential piece of information in our attempt to understand the fundamental physics which underlies inflation. The additional measurement of the slope of the spectrum of gravitational waves would allow for an even more fundamental test of inflation. The simplest model that leads to inflation proposes that the energy density of the universe was dominated by a single scalar field at early times. Since in this case a single degree of freedom would be responsible for producing both fluctuations in the density

and the gravitational wave background there exists a consistency relation between these two spectra. A confirmation of this consistency relation would be a ringing confirmation of the single scalar field model for inflation; if not confirmed it would force us to consider more complicated models.

Besides understanding what information we may learn by observing a gravitational-wave background from inflation it is also of use to consider how we may detect the influence of a generic gravitational-wave background. Many possible exotic processes may produce gravitational-wave backgrounds including networks of global cosmic strings, phase transitions in the early universe, cosmic turbulence and the cyclic universe [16–19]. There are many ways in which we may make observations which are sensitive to a generic background of gravitational waves. A detection would force us to consider how such a background was produced and what information we may glean from its discovery; a non-detection serves to constrain new theories.

The second half of this thesis is dedicated to exploring modifications of general relativity. Given that general relativity has passed every test we have put before it we must have good reasons to look for alternative theories. Recent interest in alternative theories of gravity peaked when it became clear that the universe is currently undergoing an epoch of accelerated expansion [20, 21]. Although this observation can be explained within the context of general relativity, this explanation must evoke the existence of a mysterious and exotic new material, i.e., ‘dark energy’ [22–27]. Unfortunately, this explanation has yet to lead to any fundamental insights into the true nature of this acceleration and as a result there have been many attempts to explain it through an alternative gravity theory [28–33]. However, it is not a simple task to build a theory of gravity that both agrees with the observed dynamics within the solar system as well as ‘naturally’ leads to a period of late time acceleration. Part of the difficulty is due to the fact that general relativity has many special properties (such as Birkhoff’s theorem [34]) which simplify many calculations and which are lost in alternative theories. We must then take care in computing the predictions in these theories and in understanding the consequences of those predictions. Articulating how to compute these predictions serves to develop the framework in which we may start to explore new tests of the basic nature of gravity, whatever that nature may be.

Another view on why it is important to look for alternative theories is related to the fact that we have access to a very limited set of tests of gravity. As Sir Arthur Eddington said in the preface to his famous book *The Mathematical Theory of Relativity* [35] (published only eight years after Einstein’s formulation of general relativity): “The present widespread interest in the theory [of general relativity] arose from the verification of certain ‘minute deviations from Newtonian laws.’ To those who are still hesitating and reluctant to leave the old faith, these deviations will remain the chief centre of interest...” General relativity has now been with us for 93 years and anyone who would still maintain the absolute validity of Newton’s laws would be considered a quack. However, the direct evidence of its validity is still predominantly attached to those “minute deviations from

Newtonian laws.” In other words, our only direct experience with gravity is through its effects in the Solar System and since the gravity of the Sun is so (relatively) weak we can only hope to measure small deviations from Newton’s predictions.

It is only recently, with the discovery of the Hulse-Taylor and other binary pulsars [36–39], that we have had access to more extreme gravitational laboratories. In the near future, with the fifth science run complete at the two Laser Interferometer Gravitational Wave Observatory (LIGO) sites [40], we may look forward to the direct observation of gravitational waves. Such observations will allow us to peer into dynamics displaying the strongest gravitational interactions that are accessible. However, since most of our experience with gravity has been in the weak-field regime we have yet to develop many of the tools and framework that will be needed to interpret the consequences of what we are and will soon be observing. In this sense, explorations into the gravitational unknown is very different than explorations into unknown parts of the electromagnetic spectrum. In the electromagnetic case it is easy to imagine how serendipitous discoveries can occur. In the gravitational case most observations are looking for effects which lie just above the noise or which may have other, non-gravitational, explanations.

For this reason it is necessary to explore the consequences of alternative gravity theories in order to properly understand the implications of the observations. Starting soon after Einstein’s first formulation of general relativity in 1915, people took an agnostic view of alternative theories of gravity: if a new term in the action isn’t forbidden by some fundamental symmetry or observation then add it and explore the consequences [35]. In this thesis we take the same point of view. Such studies make progress formulating tests of fundamental properties of gravity. For example, as pointed out by Stückelberg [41] soon after the verification of parity violation in the weak sector, there are no known reasons why parity violation should not also occur in the gravitational sector and therefore it is of interest to construct gravity theories that violate parity in order to understand the consequences. Such arguments are especially important when we consider what information we may extract from the observation of gravitational waves. Unlike other types of radiation, the inherent weakness of gravitational waves forces us to know, *a priori*, what form the gravitational-wave signal will take [42]. It is clear that with such an observing scheme serendipitous discoveries will be hard to come by and that we must compare the data to a suite of predicted signals in order to be confident that we understand how those observations test our understanding of gravity.

The rest of this chapter summarises the contents of this thesis which, in part, consists of the contents of seven previously published papers. In Chapter 2 we discuss how we may use current constraints to inflationary models from observations of the CMB and matter power spectrum to predict the inflationary gravitational-wave signal that may be observed directly with a gravitational-wave observatory. In Chapter 3 we articulate what insight into the fundamental physics of inflation we may gain by combining observations of the CMB and the direct observation of the inflationary

gravitational waves. In Chapter 4 we present a new constraint to the cosmological gravitational-wave background. In Chapter 5 we present work on using solar system tests in order to constrain an alternative theory of gravity which leads to a period of accelerated expansion, known as $f(R)$ gravity, and by doing so identify a new test of gravity. In Chapter 6 we present work on an alternative theory of gravity, known as Chern-Simons gravity, which violates parity, and show how tests of gravitomagnetism serve to constrain such theories.

1.2 Gravitational waves from inflation

The second chapter of this thesis discusses the production and (possible) observation of gravitational waves produced during inflation. There are two ways we may detect the inflationary gravitational-wave background (IGWB). First, it induces a curl component in the polarization signal of the CMB [43–47]. Many groups are currently conducting observations that are approaching interesting sensitivities to this component of the CMB polarization [48]. Second, we may be able to directly observe the IGWB with a future gravitational wave observatory (GWO) [1]. Many studies have explored under what circumstances the IGWB will be indirectly observed in the polarization signal of the CMB. In this chapter we emphasize the use of laser interferometers to directly observe these gravitational waves. Current observations of the CMB and matter power spectrum serve to place several constraints on models of inflation which can then be used to constrain the gravitational-wave background produced in these models. In particular recent results from the Wilkinson Microwave Anisotropy Probe (WMAP) team indicate that the slope of the primordial density fluctuations is different from scale invariant [49]. Many groups have claimed that such a finding indicates that the gravitational-wave signal from single scalar field inflationary models will produce an observable gravitational-wave background in the CMB [50, 51]. We explore the validity of these claims and extend the analysis to gravitational waves that may be observed at a GWO. In doing so we must be careful in how we extend our analysis between CMB/matter power spectrum observations and observations with a GWO since these observations span a length interval of about 16 orders of magnitude. In this chapter we solve for the inflationary dynamics directly, instead of appealing to approximations as is usually done in the literature. We find that if gravitational waves from inflation are observed in the CMB, it is likely for them to be seen at a GWO. We also discuss what information we may gain if the IGWB is too weak to be observed in the CMB.

1.3 Combining CMB/matter power spectrum and GW observations

In the third chapter we explore how we may combine observations of the CMB and the clustering of galaxies with GW observations to constrain the inflationary parameter space. In the first part of this chapter we use a Monte Carlo method to generate a large set of inflationary models that are consistent with current and future CMB/matter power spectrum observations. We then consider how GW observations, made at length scales 16 orders of magnitude smaller than CMB observations, further restrict the allowed set of models. Several different proposed GW designs are considered. In addition to placing further constraints on the inflationary model space, GW observations may allow us to test a unique consistency relation between the spectrum of density fluctuations and the spectrum of inflationary gravitational waves. The ability to test this consistency relation depends on our ability to measure the slope of the gravitational wave spectrum. Observations of the IGWB in the CMB are limited to a small range in frequencies due to contamination from weak lensing and are therefore poor at measuring the slope of the gravitational-wave spectrum. Direct observations with GWs may have access to a much larger range in frequencies and hence may make a more precise measurement of the slope. Combining such a measurement with measurements made in the CMB may allow for a significant measurement of the consistency relation which would present us with a truly fundamental test of the inflationary paradigm. We discuss how such a measurement of the consistency relation may be made and under what conditions it may be precise enough to discriminate between different theories.

1.4 A new constraint to the cosmological gravitational-wave background

In the fourth chapter we discuss a new constraint to the cosmological gravitational-wave background (CGWB). There are many ways in which we can place constraints to the CGWB, some of which are shown in Fig. 1.1. At the longest wavelengths (smallest frequencies) we have constraints coming from measurements of the CMB and the clustering of galaxies (labeled ‘WMAP’ and ‘CMB Pol’ in Fig. 1.1). As a result of error intrinsic to measurements of the CMB (known as cosmic variance), current observations are sensitive to CGWB amplitudes down to around a tenth of the amplitude of the density fluctuations. This will improve as CMB experiments become more sensitive to the curl component of the polarization signal. Constraints placed at intermediate frequencies monitor the path length between us and some source. As a gravitational wave passes it will cause this length to change in time. An example is the monitoring of timing residuals from pulsars (labeled ‘msec

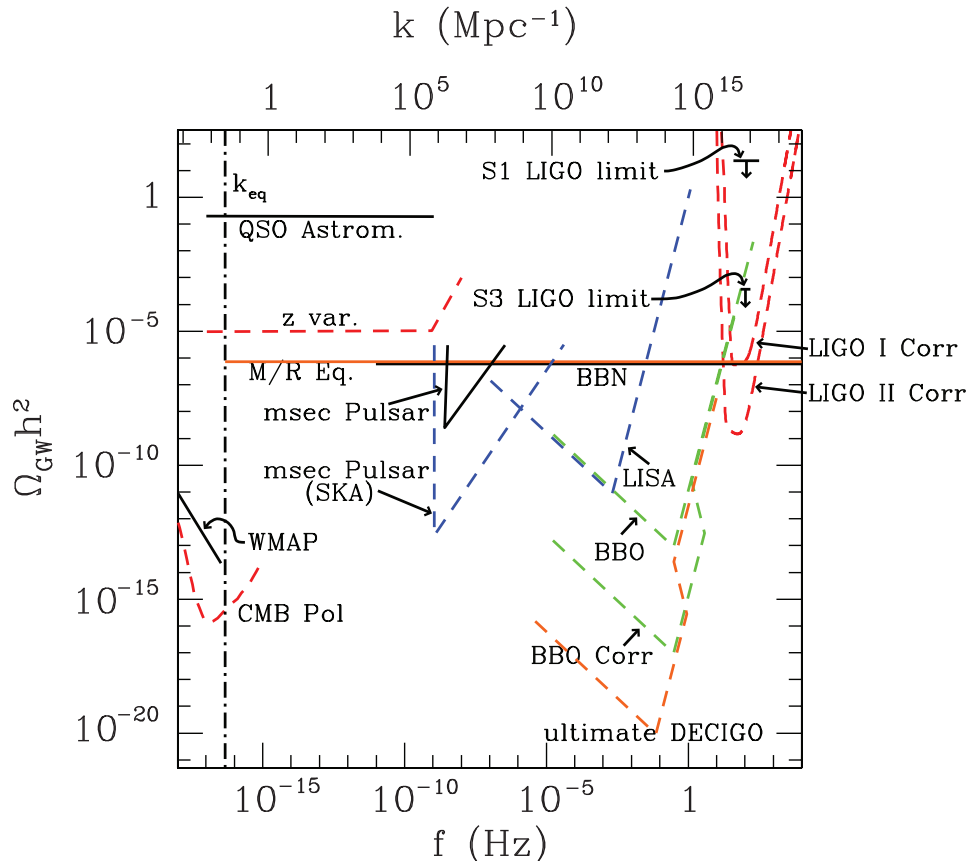


Figure 1.1: Current limits and projected sensitivities to a stochastic gravitational-wave background. The solid curves all indicate current upper limits, while the dashed curves indicate projected sensitivities. The LISA curve is from Ref. [52] and BBO correlated from Ref. [53]. The BBN constraint results from the limit to the number of relativistic degrees of freedom at big-bang nucleosynthesis (e.g., Ref. [54]); the ‘M/R’ constraint is from CMB/LSS constraints to matter-radiation equality [55]; the ‘z. var.’ curve is from Ref. [56]; and the quasar-astrometry limit from Refs. [57, 58]. LIGO sensitivities, taken from the *LIGO Scientific Collaboration White Paper on Detector Research and Development* [59] are given in terms of a correlated analysis between the Hanford, WA and Livingston, LA, sites. The run 1 LIGO limit (‘S1 LIGO’) is from Ref. [60] and the run 3 LIGO limit (‘S3 LIGO’) is from Ref. [61]. Also shown are millisecond-pulsar timing constraints (current [62, 63] and sensitivities projected for the Square-Kilometer Array [64]).

Pulsar’ in Fig. 1.1). Timing residuals from pulsars allow us to constrain the CGWB above frequencies $f \gtrsim 1/T_{\text{obs}}$, where T_{obs} is the total duration of the observation (this is due to the inability to observe a complete cycle for frequencies greater than this value) and below frequencies $f \lesssim 1/\text{day} = 10^{-5}$ Hz (since we must add the timing residuals over some time interval in order to have significant signal). The sensitivity of these constraints depends on the accuracy of the timing residuals. We can also monitor the location of quasars through both their redshift and their transverse location (labeled as ‘z var.’ and ‘QSO Astrom.’, respectively, in Fig. 1.1). Since these objects are at a distance of about 1 Gpc from us these constraints apply to frequencies between the Hubble horizon (10^{-17} Hz) and

the inverse of the length of time of the observations (10^{-9} Hz for a 10-year observation). At the highest frequencies the LIGO team has used its data in order to place constraints on the CGWB. In Fig. 1.1 we also show the projected sensitivities of various future GWOs. Finally, the widest constraint, in terms of a frequency range, comes from measurements of the primordial abundance of light elements, such as ^4He (labeled ‘BBN’ in Fig. 1.1) [1]. This constraint takes advantage of the fact that the short wavelength part of the CGWB behaves as a radiative fluid. The primordial abundance of the light elements was set through the competition between the Hubble expansion rate, which depends on the radiative content of the universe, and the rate of light element creation. Only that part of the CGWB whose wavelengths were within the Hubble horizon during Big Bang nucleosynthesis (BBN) will contribute to the radiative energy density. This constraint therefore only applies to frequencies greater than $\sim 10^{-11}$ Hz.

In this chapter we present a new constraint to the CGWB made in the same spirit as the BBN constraint. The CGWB that is within the horizon when the CMB was formed (corresponding to a frequency of 10^{-16} Hz) contributes to the total radiative energy density and hence affects our observations of the CMB and the clustering of galaxies. The constraint we obtain is competitive with the BBN constraint (see the line labeled ‘M/R Eq.’ in Fig. 1.1) but, in contrast to the BBN constraint, will both improve with future observations (i.e., the Planck satellite) and extends down to lower frequencies by 5 orders of magnitude. In this chapter we also discuss how different data sets affect the final constraint, as well as describe the unique subtleties encountered when viewing the short wavelength CGWB as a radiative fluid.

1.5 Solar system tests of $f(R)$ gravity

The alternative gravity theory, known as $f(R)$ gravity, is an attempt to explain the observed late time accelerated expansion of the universe through a modification of general relativity. The theory proposes to alter the Einstein-Hilbert action from R , where R is the Ricci scalar, to $R + f(R)$, where $f(R)$ is some function of the Ricci scalar. The simplest example to consider takes $f(R) \propto 1/R$ [32, 65]. We can heuristically understand how this modification leads to a late period of accelerated expansion: as the universe evolves it becomes increasingly dilute driving the cosmological Ricci scalar toward zero and causing the ‘correction’, $f(R) \propto 1/R$, to grow in comparison to R . Once this term becomes dominant the dynamics of the theory change and we find the universe evolves towards a period of accelerated expansion. It is possible to construct a function $f(R)$ which reproduces the observed expansion history but we must then check whether this theory conforms to our observations of gravity in other contexts. In particular, we present an analysis that calculates the behavior of this theory within the solar system. Before the appearance of this work the literature was filled with conflicting results: some claiming that the $1/R$ theory passed solar system tests, others claiming it

did not.

After establishing that the $1/R$ theory severely violates the measurement of the deflection of light around the Sun (parameterized by γ_{PPN} , which is measured to be equal to unity to one part in 10^4 but which can be $1/2$ in some $f(R)$ theories) we go on to generalize our results and present conditions which, if satisfied, imply an $f(R)$ theory violates solar system observations. Our findings indicate that non-linear effects may allow certain $f(R)$ theories to pass solar system tests (i.e., these theories predict $\gamma_{\text{PPN}} = 1$). The conditions which lead to these non-linear effects may depend both on the redshift as well as on the strength of the local gravitational field.

This leads to a proposal for a new test of gravity. In all previous studies the value of γ_{PPN} has been assumed to be universal but here we have a theory of gravity for which the value of γ_{PPN} depends on both the local environment and redshift. In this chapter we present a preliminary analysis to explore how we might test the universality of γ_{PPN} . We discuss how one may be able to use measurements of strong lensing to build a set of measurements of γ_{PPN} and what types of statistical tests we may use to explore whether these measurements imply a universal value. We then apply our analysis to a small data set of 15 strong lenses using observations from the Sloan Lens ACS (SLACS) survey [66], noting that this survey should increase the number of strong lenses to 100 in the near future.

1.6 Constraints to Chern-Simons gravity

Continuing to consider alternative theories of gravity, in the next chapter we explore some observable consequences of an alternative gravity theory known as Chern-Simons gravity [67, 68]. One of the main aspects of this theory is that it introduces parity violation into the gravitational sector. As such it has the notable property of leaving many of the best tested spacetimes unchanged [69, 70]. In particular, any spacetime with spherical symmetry is still a solution of this new theory. This includes the Schwarzschild and Friedmann-Robertson-Walker spacetimes, so that our standard solar system and cosmological tests of gravity are insensitive to Chern-Simons gravity. Instead we must look for spacetimes that break spherical symmetry. This leads us to consider the spacetime due to the rotation of the Earth. The rotation of the Earth produces gravitational effects akin to the magnetic field generated by a rotating sphere of charge and hence are called gravitomagnetism. These effects were fully worked out for the weak-field limit of general relativity by Lense and Thirring [71]. It turns out that in weak-field general relativity the field equations can take a form which is formally identical to Maxwell's equations of electromagnetism. Using this analogy we know that the gravitomagnetic field around the rotating earth will be dipolar and completely poloidal. However, Chern-Simons gravity alters the gravitational field equations and, because of its parity violation, produces both poloidal and toroidal gravitomagnetic fields. This modification of the spacetime around the Earth

is then used to constrain parameters in Chern-Simons gravity by using data collected from the two LAser GEOdynamics satellites (LAGEOS) satellites. We also explore what types of constraints we may expect from another satellite mission known as Gravity Probe B [72]. Finally, through our study of Chern-Simons gravity we discuss how future observations of binary pulsar systems may allow a more general exploration of the gravitomagnetic structure around rotating objects.

Chapter 2

Detecting the stochastic gravitational wave background¹

2.1 Introduction

Long a subject of theoretical speculation, inflation [2–4] has now, with the advent of precise cosmic microwave background (CMB) measurements [73–81], become an empirical science. The concordance of the measurements with the inflationary predictions of a flat Universe and a nearly scale invariant spectrum of primordial density perturbations [5–8] is at least suggestive and warrants further tests of inflation. Among the predictions of inflation yet to be tested is a stochastic gravitational-wave background with a nearly scale invariant spectrum [9–15]. Detection of the CMB polarization pattern induced by inflationary gravitational waves of wavelengths comparable to the horizon has become a goal of next-generation CMB experiments [43–47]. And now, direct detection of the inflationary gravitational wave background (IGWB) with future spaced-based gravitational-wave detectors at deci-Hertz frequencies has become the subject of serious study [82, 83].

Detection of a gravitational-wave background, at either CMB or direct-detection frequencies, would constitute a ‘smoking gun’ for inflation. Moreover, since the amplitude of the IGWB is determined by the energy scale of inflation at the time that the relevant distance scale exited the horizon during inflation, detection would provide important information about the new ultra-high-energy physics responsible for inflation [84, 85]. Since the frequencies probed by the CMB and by direct detection are separated by 16 orders of magnitude, the combination of both provides a large lever arm with which the shape of the inflaton potential can be constrained.

In this chapter, we survey a range of inflationary models to investigate the detectability of the IGWB with satellite experiments, like NASA’s Big Bang Observer (BBO) [82] and the Japanese

¹Most of the material presented in this chapter was first published in, *Direct detection of the inflationary gravitational wave background*, Tristan L. Smith, Marc Kamionkowski, and Asantha Cooray, Phys. Rev. **D73**, 023504 (2006) and *The inflationary gravitational-wave background and measurements of the scalar spectral index*, Tristan L. Smith, Marc Kamionkowski, and Asantha Cooray, astro-ph/0802.1530. Reproduced here with permission, copyright (2006) by the American Physical Society.

Deci-Hertz Interferometer Gravitational-Wave Observatory (DECIGO) [83], currently under study. We restrict our attention to slow-roll inflation models that are consistent with measurements from the CMB and large-scale structure. We show how measurements of the IGWB amplitude at both CMB and direct-detection scales can be used to constrain the inflationary parameter space.

Previous work [86–88] on direct detection of the IGWB has taken the gravitational-wave spectrum to be a pure power law, considered chaotic inflation [89, 90] or the IGWB due to a broken scale-invariant potential [91]. In this chapter, we consider a wider range of inflationary models (in the spirit of Refs. [92, 93]), and we solve the inflationary dynamics to go beyond the assumption of power-law power spectra. With this more accurate analysis, we find that for the forms of the inflaton potential considered here the direct detection of the IGWB can break degeneracies between distinct inflationary models that produce the same slow-roll parameters at CMB/large-scale-structure scales for broken scale invariant potentials.

Recent results from the WMAP team [94] indicate that the slope of the scalar perturbations, n_s , is different from scale invariant with a best fit value at $n_s \approx 0.95$ (for a zero tensor contribution). Although some groups have challenged the exact statistical significance of this result (see, e.g., Refs. [95, 96]) the conclusion that $n_s < 1$, if upheld by future observations, may have important implications for the IGWB. In particular, as argued in Refs. [50, 51], the confirmation of a spectral index less than one may indicate (with caveats that we explore below) that the effects of the IGWB on the CMB polarization pattern will be large enough to be detectable with future missions [48, 97]. In this chapter we discuss how the curvature of the inflaton potential determines, to a large extent, whether the indication that $n_s < 1$ implies a large IGWB amplitude. The same reasoning applies to the chances of directly observing the relic IGWB today with future space-based gravitational-wave observatories.

2.1.1 Inflationary dynamics and perturbations

2.1.1.1 Homogeneous evolution

Inflation occurs when the cosmological expansion accelerates; i.e., when $\ddot{a} > 0$, where $a(t)$ is the scale factor, and the overdot denotes a derivative with respect to time t . The evolution of the scale factor is determined by the Friedmann equation,

$$H^2 \equiv \left(\frac{\dot{a}}{a}\right)^2 = \frac{8\pi}{3m_{\text{Pl}}^2}\rho - \frac{K}{a^2}, \quad (2.1)$$

the continuity equation, $\dot{\rho} + 3H(\rho + P) = 0$, and an equation of state $P(\rho)$, where H is the Hubble parameter, ρ is the total energy density, P is the pressure, m_{Pl} is the Planck mass, and K is a constant related to the 3-space curvature. From Eq. (2.1) and the continuity equation follows the

‘acceleration’ equation,

$$\frac{\ddot{a}}{a} = -\frac{4\pi}{3m_{\text{Pl}}^2}(\rho + 3P). \quad (2.2)$$

For an equation of state of the form $P = w\rho$, where w is a constant, inflation occurs when $w < -1/3$.

Consider now a spatially homogeneous scalar field ϕ , the ‘inflaton’. It has an energy density and pressure,

$$\rho = \frac{1}{2}\dot{\phi}^2 + V(\phi), \quad (2.3)$$

$$P = \frac{1}{2}\dot{\phi}^2 - V(\phi), \quad (2.4)$$

from which it follows that inflation occurs if $V(\phi) > \dot{\phi}^2$.

The equation of motion for the inflaton is given by $\ddot{\phi} + 3H\dot{\phi} + V' = 0$, where the prime denotes differentiation with respect to ϕ . We assume that inflation has been proceeding for a long time before any observable scales have exited the horizon, and so for our purposes, the energy density is dominated by the inflaton during inflation, the curvature term, K/a^2 , is negligible as compared to the inflaton energy density, and the evolution of the inflaton has been attracted to the slow-roll regime (e.g., Ref. [98]). If so, the evolution of the inflaton and the scale factor are uniquely determined by $V(\phi)$. Within the slow-roll approximation, the evolution is described by the usual slow-roll parameters,

$$\epsilon \equiv \frac{m_{\text{Pl}}^2}{16\pi} \left(\frac{V'}{V} \right)^2, \quad (2.5)$$

$$\eta \equiv \frac{m_{\text{Pl}}^2}{8\pi} \frac{V''}{V}, \quad (2.6)$$

$$\xi \equiv \frac{m_{\text{Pl}}^4}{64\pi^2} \frac{V'V'''}{V^2}, \quad (2.7)$$

which are required to be small compared with unity for the slow-roll approximation to be valid. Toward the end of inflation, ϵ grows, and inflation ends when $\epsilon \simeq 1$. This statement can be made precise by the use of ‘Hubble slow-roll’ parameters [98].

2.1.1.2 Perturbations

To leading order in the slow-roll approximation, the amplitudes of the power spectra for density perturbations (scalar ‘s’ metric perturbations) and gravitational waves (tensor ‘t’ metric perturbations)

can be written (e.g., Refs. [99, 100])

$$P_s(k) \approx \frac{128\pi}{3m_{\text{Pl}}^6} \frac{V^3}{V'^2} \Big|_{k=\alpha H}, \quad (2.8)$$

$$P_t(k) \approx \frac{128}{3} \frac{V}{m_{\text{Pl}}^4} \Big|_{k=\alpha H}, \quad (2.9)$$

as a function of wavenumber k , where V and V' are evaluated when the relevant scale exits the horizon during inflation. The power spectra can be expanded in power laws,

$$P_s(k) \approx P_s(k_0) \left(\frac{k}{k_0} \right)^{1-n_s+(\alpha_s/2)\ln(k/k_0)}, \quad (2.10)$$

$$P_t(k) \approx P_t(k_0) \left(\frac{k}{k_0} \right)^{n_t+(\alpha_t/2)\ln(k/k_0)}, \quad (2.11)$$

where k_0 is a pivot wavenumber at which the spectral parameters (e.g., Ref. [101]),

$$n_s(k) \simeq 1 - 6\epsilon + 2\eta, \quad (2.12)$$

$$n_t(k) \simeq -2\epsilon, \quad (2.13)$$

$$\alpha_s(k) \simeq 16\epsilon\eta - 24\epsilon^2 - 2\xi, \quad (2.14)$$

$$\alpha_t(k) \simeq 4\epsilon\eta - 8\epsilon^2, \quad (2.15)$$

are to be evaluated. To a first approximation, the power spectra are power laws with power-law indices n_s and n_t , although these indices may ‘run’ slightly with k , with a running parameterized by α_s and α_t [102]. Finally, the tensor-to-scalar ratio is

$$r \equiv \frac{P_t(k)}{P_s(k)} = 16\epsilon. \quad (2.16)$$

In this chapter, we will generally evaluate P_s , n_s , and α_s at the distance scales of the CMB and large-scale structure (LSS), where they are measured or constrained. In the figures below, the tensor spectral index n_t will be evaluated at the distance scale relevant for direct detection of gravitational waves.

2.1.1.3 Number of e -foldings

The number of e -foldings of expansion between the time, determined by $k = a_k H_k$, when a comoving distance scale labeled by k exited the horizon during inflation, and the end of inflation is $N(k) \equiv \ln(a_{\text{end}}/a_k)$, where a_{end} is the scale factor at the end of inflation. A given scale exits the inflationary

horizon when $k = a_k H_k$, so we can form the ratio

$$\frac{k}{a_0 H_0} = \frac{a_k H_k}{a_0 H_0} = \frac{a_{\text{end}} H_k}{a_0 H_0} e^{-N(k)}. \quad (2.17)$$

After the initial period of inflation the universe must be populated with matter and be dominated by radiation by the formation of the light elements (~ 1 MeV). This period is referred to as reheating. We then suppose that during the reheating phase the dominant energy density scales as $\rho \propto a^{-p}$ (so that, for coherent oscillations of a scalar field with a potential of the form $V \sim \phi^n$ we have $p = 6n/(n+2)$ [103]) and we have the relationship, $a \propto \rho^{-1/p}$. With this and the conservation of entropy density we can write

$$e^{N(k)} = \left(\frac{k}{a_0 H_0} \right)^{-1} \left(\frac{g_*(T_0)}{g_*(T_{\text{rh}})} \right)^{1/3} \left(\frac{\rho_{\text{rh}}}{\rho_{\text{end}}} \right)^{1/p} \frac{H_k}{H_0}, \quad (2.18)$$

where T_{rh} is the temperature at the beginning of radiation domination, T_0 is the temperature of the CMB today, and $g_*(T)$ is the number of relativistic degrees of freedom at temperature T . Writing the energy density at reheat in terms of the reheat temperature we have $\rho_{\text{rh}} = \pi^2/30 T_{\text{rh}}^4 g_*(T_{\text{rh}})$. Finally, we can write the energy density at the end of inflation, $\rho_{\text{end}} = E_{\text{end}}^4$ and $H_k = \sqrt{8\pi/3} E_k^2/m_{\text{Pl}}$. With this we have (e.g., Ref. [104]),

$$N(k) = 60.5 + \frac{3.5}{p} - \ln \frac{k}{a_0 H_0} - \ln \frac{10^{16} \text{ GeV}}{E_k} + \ln \frac{E_k}{E_{\text{end}}} - \frac{4-p}{p} \ln \frac{E_{\text{end}}}{T_{\text{rh}}} + \frac{3-p}{3p} \ln g_{*100}(T_{\text{rh}}), \quad (2.19)$$

and we have $g_*(T_0) = 3.36$ for photons and three species of massless neutrinos; $g_{*100}(T_{\text{rh}})$ is the number of relativistic degrees of freedom in units of 100 at the beginning of radiation domination. In terms of the inflaton potential, the number of e -foldings between two field values, ϕ_i and ϕ_f , is

$$N(\phi_i, \phi_f) \approx \frac{8\pi}{m_{\text{Pl}}^2} \int_{\phi_f}^{\phi_i} \frac{V(\phi)}{V'(\phi)} d\phi, \quad (2.20)$$

where we have supposed the potential increases as the field increases so that the field rolls towards the origin. Furthermore, if the potential determines a field value at which inflation ends, we can combine this equation with Eq. (2.19) and ρ_{rh} to identify the field value when the current Hubble volume exited the inflationary horizon.

Fixing $p = 3$, and using 10^{16} GeV for all the densities in Eq. (2.19), we require 62 e -folds of inflation between the time the current horizon distance exited the horizon during inflation and the end of inflation. The strength of the IGWB is proportional to the inflaton-potential height [see Eq. (2.9)], and as we will see, detectability requires $E \gtrsim 10^{15}$ GeV. We will also see that E_{end} is never much smaller than E_k . Thus, the only ratio in Eq. (2.19) that might be large is the second to last. Conservatively, the reheat temperature must be $\gtrsim 1$ MeV to preserve the successes of big-bang

nucleosynthesis, implying a lower limit of $N(a_0 H_0) \gtrsim 47$. This lower limit is significant, as the ratio of gravitational-wave frequencies probed by the CMB/LSS (corresponding to $k \simeq 0.05 \text{ Mpc}^{-1}$) and direct detection is $\sim e^{35}$. Therefore, if inflation results in an IGWB in the ballpark of detectability by the CMB, then inflation will last long enough to ensure the production of gravitational waves on BBO/DECIGO scales (although it does not necessarily guarantee a detectable amplitude).

When we apply the above analysis to a specific class of inflationary models we assume that the form of the inflation potential is known throughout observable inflation. Removing this assumption we can alternatively view a specific class of modes as a good approximation for only that part of inflation between CMB and BBO/DECIGO scales. In this case the constraint to the total number of e -folds of inflation does not apply.

2.1.2 Constraints to inflationary observables

We would like to survey only those inflationary models that are consistent with current data. Measurements of the ‘inflationary observables’—i.e., the scalar and tensor power-spectrum amplitudes, spectral indices, and running—come from CMB measurements that probe scales from the current Hubble distance ($\sim 10^4 \text{ Mpc}$) to $\sim 10 \text{ Mpc}$ scales, galaxy surveys that constrain the matter power spectrum from 600 Mpc down to 20 Mpc , and from the Lyman- α forest, which probes down to $\sim 1 \text{ Mpc}$ [105, 106]. Constraints to the classical cosmological parameters (e.g., the Hubble parameter, the deceleration parameter, the baryon density, the matter density) from other measurements help limit the range of plausible values for the inflationary observables that come from CMB/LSS measurements.

The precise constraints to the inflationary observables depend in detail on the combination of observational data sets. In our discussions, we simply take as conservative ranges $P_s(k_0) = (2.45 \pm 0.23) \times 10^{-9}$ and $|\alpha_s| < 0.04$ at a pivot wavenumber $k_0 = 0.05 \text{ Mpc}^{-1}$ [107]. These ranges are in agreement with the constraints using the latest data (e.g., Ref. [108]).

In our numerical analysis we use the CMB constraints derived from considering the WMAP third-year data release (WMAP3, Ref. [94]) and those derived by considering a suite of CMB observations (including WMAP3) as well as measurements of the linear matter power spectrum coming from the Sloan Digital Sky Survey (SDSS) and the Lyman-alpha forest, measurements of the baryon acoustic peak from SDSS, and measurements of supernovae luminosity distances (WMAP3+, Ref. [109]). We note that the analysis in Ref. [94] fixes the pivot wavenumber at $k_0 = 0.002 \text{ Mpc}^{-1}$ whereas the analysis in Ref. [109] uses $k_0 = 0.05 \text{ Mpc}^{-1}$. As pointed out in Ref. [110], the overall constraints do not depend on the choice of k_0 , but the value of k_0 may change the shape of contours for marginalized constraints (such as contours in the $n_s - r$ plane). The CMB constraints used in this chapter fix the running of the scalar spectral index to zero and therefore, according to the analysis in Ref. [110], are only slightly affected by the choice of pivot wavenumber. The results from the

5-year WMAP data release change our results slightly. In their analysis [49] (as opposed to previous analyses) it was found that $n_s > 1$ is disfavored even when considering a non-zero tensor-to-scalar ratio. Furthermore, they find that $r \lesssim 0.2$ at 95% confidence level. Although our results make use of observational constraints our conclusions are made independent of those data sets and are applicable to both the most recent as well as future constraints.

2.1.3 Gravitational-wave transfer function

The gravitational-wave power spectrum $P_t(k)$ provides the variance $\langle |h_k|^2 \rangle$ of the gravitational-wave amplitude h_k as that mode enters the horizon. Once the wavelength is smaller than the horizon, the gravitational wave begins to oscillate, and its energy density $\rho_k \sim k^2 h_k^2$ redshifts $\propto a^{-4}$ like radiation. It follows that the gravitational-wave amplitude today is $h_k(t_0) = h_k(t_k)(a_k/a_0)$, where t_0 is the time today, t_k is the time of horizon entry, and $a_k = a(t_k)^2$. During radiation domination (RD), $H \propto a^{-2}$, so that $k \propto 1/a_k$, and during matter domination (MD), $H \propto a^{-3/2}$, so that $k \propto 1/a_k^{1/2}$. From these relations, we find that the value of h_k today scales with k as

$$h_k \propto k^{-1} \text{ (horizon entry during RD),} \quad (2.21)$$

$$h_k \propto k^{-2} \text{ (horizon entry during MD).} \quad (2.22)$$

Calculations (e.g., Refs. [111, 112]) of the transfer function intended for CMB predictions evolve the wave equation more carefully through matter-radiation equality, but the direct-detection frequencies are so high that the scalings we have used here are fairly precise. The sensitivities of BBO/DECIGO will peak near a frequency 0.1 Hz, or wavenumber $k = 6.47 \times 10^{13} \text{ Mpc}^{-1}$. Matter-radiation equality corresponds to $k_{\text{eq}} \approx 0.05 h^2 \text{ Mpc}^{-1}$. Therefore, the primordial gravitational waves observed by the planned gravitational-wave observatories entered the horizon *well* before matter/radiation equality. In fact, the modes that entered the horizon during big-bang nucleosynthesis (at $T \sim 1 \text{ MeV}$) have frequencies $\sim 10^{-11} \text{ Hz}$. Therefore, the gravitational waves probed by BBO/DECIGO are ~ 10 orders of magnitude smaller than those associated with big-bang nucleosynthesis (BBN) and must have entered the horizon at temperatures $T \sim 10^7 \text{ GeV}$ or, if $T_{\text{rh}} < 10^7 \text{ GeV}$, then the observed gravitational waves enter the horizon during reheating.

The transfer function during reheating can have different behavior than the transfer function during the standard expansion history. We may understand how the transfer function depends on k through the same argument above. Generalizing to an equation of state w we have

$$h_k \propto k^{1/(1-3/2[1+w])}. \quad (2.23)$$

²This can be shown more rigorously by solving the equation of motion for h during radiation domination and then comparing the oscillation amplitude at late times with the initial amplitude. We perform such an analysis in Appendix A.

The simplest reheating scenario involves coherent oscillations of the inflaton within a quadratic potential. This leads to $w = 0$ [103]. In the other extreme, the kinetic energy of the scalar field may dominate the universe leading to $w = 1$. It is important to note that for reheating temperatures below 10^7 GeV [corresponding to a total number of e -folds of inflation $N < 55$ for $p = 3$ ($w = 0$)] the transfer function depends on knowledge of the reheating epoch (see Appendix A).

We outline the derivation of the high-frequency transfer function for gravitational waves in Appendix A. If the wavenumber entered the horizon during radiation domination we then have

$$\Omega_{\text{gw}} h^2 = \frac{16}{9} \Omega_r h^2 \left(\frac{g_*(T_0)}{g_*(T_k)} \right)^{1/3} \frac{V}{m_{\text{Pl}}^4}, \quad (2.24)$$

where $\Omega_{\text{gw}} \equiv (1/\rho_c) d\rho_{\text{gw}}/d \ln k$, $\Omega_r \equiv \rho_r^0/\rho_c$,

$$\rho_r^0 = \frac{\pi^2}{30} T_0^4 g_*(T_0), \quad (2.25)$$

$$\rho_c = \frac{3H_0^2 m_{\text{pl}}^2}{8\pi}, \quad (2.26)$$

V is the inflaton potential, H_0 is the Hubble parameter today, $T_0 = 2.73$ K [113] is the photon temperature today, and $m_{\text{Pl}} = 1.2 \times 10^{19}$ GeV is the Planck mass. Photons plus three species of massless neutrinos [$g_*(T_0) = 3.36$] give

$$\Omega_{\text{gw}} h^2 = A_{\text{gw}} \frac{V}{m_{\text{Pl}}^4}, \quad (2.27)$$

where $A_{\text{gw}} = 2.39 \times 10^{-5} g_{100}^{-1/3}$ and $g_{100} \equiv g_*(T_k)/100$.

2.2 Direct-detection thresholds

Since the detection of a stochastic background of gravitational waves has to be separated from the effect of sources of noise intrinsic to the detector, the sensitivity to a stochastic background is different than the sensitivity to a nonstochastic source. The total stochastic signal in a given detector can be written as a sum of a stochastic signal plus a stochastic noise, $s(t) = h_n(t) + h(t)$. Taking the Fourier transform of the total signal and considering the spectral density of the noise and of the stochastic signal, we find that in order to have a signal-to-noise greater than unity,

$$\langle |h(f)|^2 \rangle^{1/2} \gtrsim \left(\frac{2f S_n(f)}{F} \right)^{1/2}, \quad (2.28)$$

where F is a filling factor that accounts for the fact that a primordial stochastic background will be isotropic on the sky, but the detector will only be sensitive to a fraction of the sky, while $S_n(f)$ is

the spectral density associated with the detector noise.

For omni-directional interferometers, such as the Laser Interferometer Space Antenna (LISA), $F = 2/5$. There is a great improvement in sensitivity when the signal from two independent detectors can be combined through a correlation analysis between the two detectors [1, 114–116]. Such a correlation increases the sensitivity to a stochastic background such that,

$$\langle |h(f)|^2 \rangle^{1/2} \gtrsim 1.12 \times 10^{-2} \left(\frac{2fS_n(f)}{F} \right)^{1/2} \left(\frac{\text{Hz}}{\Delta f} \right)^{1/4} \left(\frac{\text{yr}}{\Delta T} \right)^{1/4},$$

where Δf is the bandwidth over which the signals can be correlated and ΔT is the integration time. For a correlation analysis, the increase in sensitivity is under the assumption that the detector noises are independent between the two detectors, while the only correlation expected is due to stochastic signals such as inflation. For the single detector, the minimum observable strain is independent of the integration time, while for a correlation analysis, long-term observations are essential. While LISA will not allow an opportunity for such a correlation analysis, some mission concept studies for NASA's Big Bang Observer (BBO) and Japan's Deci-Hertz Interferometer Gravitational Wave Observatory (DECIGO) consider two (or more) systems such that the improvement related to the correlation analysis can be exploited. The design for LISA currently places the sensitivity at approximately $\Omega_{\text{gw}} h^2 \sim 10^{-11}$. Current designs for BBO place the sensitivity of a single detector at $\Omega_{\text{gw}} h^2 \sim 10^{-13}$ and the sensitivity of a correlated extension at $\Omega_{\text{gw}} h^2 \sim 10^{-17}$. Finally, the ultimate goal for DECIGO is a sensitivity to $\Omega_{\text{gw}} h^2 \sim 10^{-20}$ [83], corresponding to $V^{1/4} \sim 1.71 \times 10^{15}$ GeV ($r \sim 10^{-6}$ where we have taken $n_t = 0$ consistent with the consistency relation).

Besides a sensitivity to a stochastic background, one must also be concerned about sources of a stochastic background, other than inflation. Such sources have the potential to wash out any signal that would otherwise be observed from a primordial source, but the characterization of the amplitude and frequency dependence of these sources is still uncertain. Other sources of cosmological gravitational-wave backgrounds are white-dwarf/white-dwarf binaries [117], neutron-star/neutron-star binaries [118] and neutron-star/white-dwarf binaries [119].

Fig. 2.1 shows the sensitivities to a stochastic gravitational-wave background as a function of frequency f for a variety of gravitational-wave detectors. Also shown are various current limits (as solid curves) as well as a variety of projected direct and indirect sensitivities (dashed curves), and scale-invariant spectra parameterized by an energy scale $V^{1/4}$ of inflation (dotted curves). We also show limits from current CMB experiments as well as the sensitivities expected for future CMB-polarization experiments currently under study.

Fig 2.2 shows three putative foregrounds that may interfere with measurements of the IGWB in future gravitational-wave observatories. In particular, the background due to cosmological neutron star- neutron star binary systems overwhelms the expected amplitude of the IGWB for $r = 0.1$

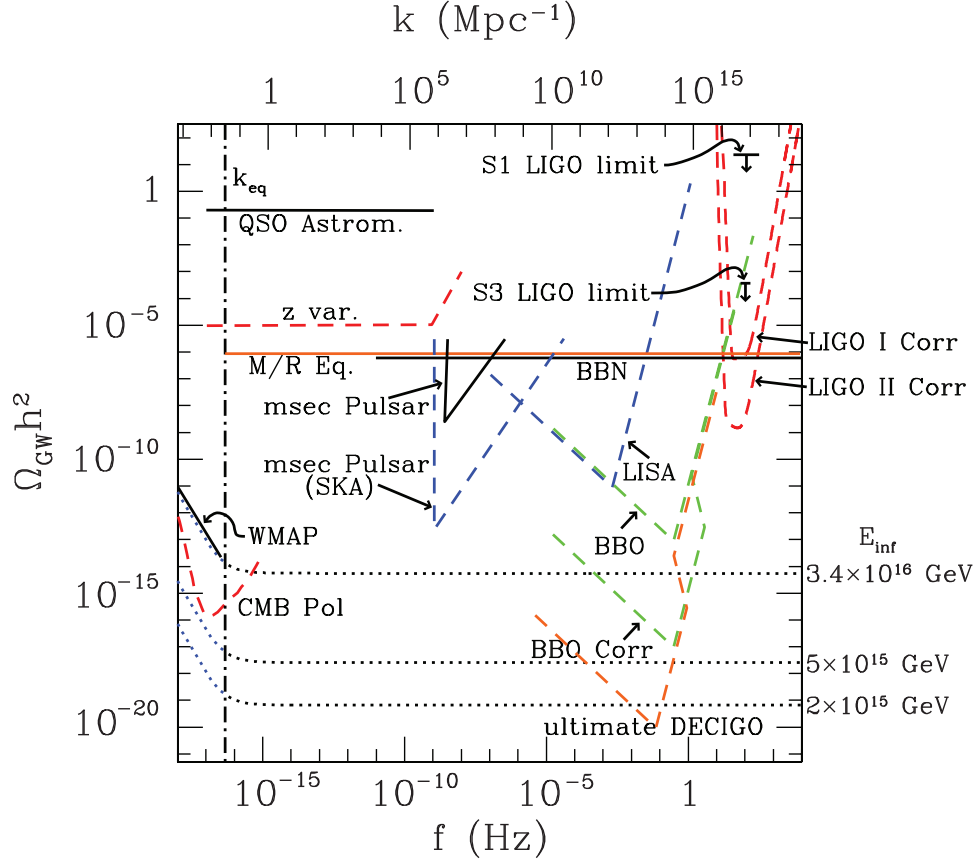


Figure 2.1: Current limits and projected sensitivities to a stochastic gravitational-wave background. The solid curves all indicate current upper limits, while the dashed curves indicate projected sensitivities. The LISA curve is from Ref. [52] and BBO correlated from Ref. [53]. The BBO sensitivity is estimated by increasing the BBO-correlated curve by 4 orders of magnitude [see Eq. (2.29)]. The BBN constraint results from the limit to the number of relativistic degrees of freedom at big-bang nucleosynthesis (e.g., Ref. [54]); the ‘M/R’ constraint is from CMB/LSS constraints to matter-radiation equality [55]; the ‘z. var.’ curve is from Ref. [56]; and the quasar-astrometry limit from Refs. [57, 58]. LIGO sensitivities, taken from the *LIGO Scientific Collaboration White Paper on Detector Research and Development* [59] are given in terms of a correlated analysis between the Hanford, WA and Livingston, LA sites [see Eq. (2.29)]. The run 1 LIGO limit (‘S1 LIGO’) is from Ref. [60] and the run 3 LIGO limit (‘S3 LIGO’) is from Ref. [61]. Also shown are millisecond-pulsar timing constraints (current [62, 63] and sensitivities projected for the Square-Kilometer Array [64]). Curves corresponding to scale-invariant (i.e., $n_t = 0$) gravitational-wave backgrounds are shown (dotted curves), labeled by the associated inflationary energy scales at CMB/LSS scales (but keep in mind that slow-roll inflation generically predicts $n_t < 0$, less power on small scales). The CMB/LSS currently constrains this value to be below 3.36×10^{16} GeV at CMB/LSS scales. Future CMB measurements may be able to reach energy scales near 10^{15} GeV [120–123].

($E_{\text{inf}} = 2 \times 10^{16}$ GeV). However, recent studies such as Ref. [124] show that with the current specifications for BBO’s design this foreground may be able to be significantly reduced so that the sensitivity is only slightly degraded.

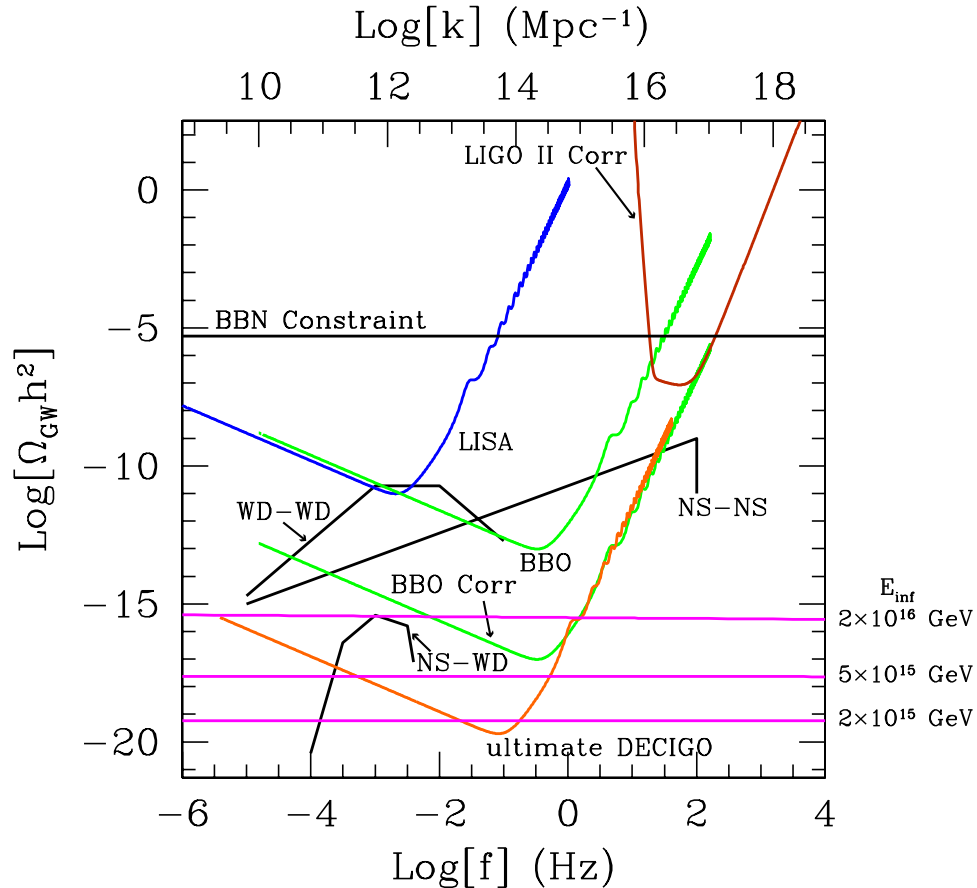


Figure 2.2: Here, as a companion to Fig. 2.1, we show the foreground sources of gravitational waves at frequencies related to the proposed BBO mission. We show foregrounds expected from white dwarf-white dwarf binaries [117], neutron star-neutron star binaries [118] and neutron star-white dwarf binaries [119]. We do not show the foreground from cosmological supernovae [53] since its presence is less certain than these other backgrounds (see Ref. [124]).

2.3 The connection between $n_s < 1$ and the IGWB amplitude

Many authors [50, 51] have noted that when $n_s \neq 1$ then the amplitude of the IGWB is, generically, significant. The argument for this conclusion is made by looking at the expression for n_s in terms of the slow-roll parameters ϵ and η ,

$$1 - n_s = 6\epsilon - 2\eta, \quad (2.29)$$

and the tensor-to-scalar ratio

$$r \equiv \frac{A_t}{A_s} = 16\epsilon. \quad (2.30)$$

In order to infer a value for r given the indication that $1 - n_s \approx 0.05^3$ one has to suppose some ‘natural’ relationship between ϵ and η . Many authors have supposed that $\epsilon \gtrsim \eta$ so that ‘at worst’ we have $\mathcal{O}(\epsilon) \approx \mathcal{O}(\eta)$. We can then conclude that $1 - n_s \approx 0.05$ implies that $r \approx \mathcal{O}(0.1)$. Such a value for the tensor-to-scalar ratio is easily accessible to future CMB experiments as well as to space-based gravitational-wave observatories. However, as we shall now show, there are caveats when making the above argument.

Taylor expanding the potential in terms of these slow-roll parameters evaluated at some value of the inflaton field, ϕ_* , we obtain [125]

$$V(\phi) \approx \frac{m_{\text{Pl}}^2 H_*^2}{8\pi} \left\{ (3 - \epsilon_*) + 12\sqrt{\pi\epsilon_*} \frac{\delta\phi}{m_{\text{Pl}}} + 2\pi[3\sqrt{\epsilon_*/\pi} + 6(\eta_* - \epsilon_*)] \left(\frac{\delta\phi}{m_{\text{Pl}}} \right)^2 \right\}, \quad (2.31)$$

where $\delta\phi \equiv \phi - \phi_*$. If we suppose that $\epsilon_* \ll \eta_*$ then we can see that the potential is well approximated by a quadratic function with the coefficient $(3/2)H_*^2 m_{\text{Pl}}^2 \eta_*$. Looking at Eq. (2.29) the fact that $1 - n_s > 0$ implies $\eta_* < 0$ in this case— i.e., the curvature of the potential must be negative.

For the case where $\eta < 0$ at some point, in order for inflation to lead to oscillations in ϕ resulting in the reheating of the universe, η must change sign so that the field evolves into a minimum of the potential. In Ref. [50] the fact that η must change sign was used to indicate fine tuning. However, as Ref. [50] points out, there are several scalar-field potentials that have this property as a result of particular symmetries (such as the Higgs potential) so that, in some sense, their ‘fine tuning’ is justified. As we shall see, it is exactly these potentials that allow for $n_s < 1$ and $r \ll 1 - n_s$.

2.4 BBO/DECIGO amplitudes

In this section, we calculate the gravitational-wave amplitude at BBO/DECIGO scales for several families of slow-roll inflation models consistent with CMB/LSS constraints.

Measurements of the scalar amplitude P_s and spectral index n_s at CMB/LSS scales, as well as upper limits to the tensor contribution r to the CMB and to the running α_s of the spectral index, constrain the inflaton potential and its derivatives at the field value ϕ_c that corresponds to the time at which CMB/LSS scales k_c exited the horizon. To be precise, we use $k_c = 0.05 \text{ Mpc}^{-1}$. In this work, we take as the nominal BBO/DECIGO frequency $f = 0.1 \text{ Hz}$, corresponding to $k = 6.47 \times 10^{13} \text{ Mpc}^{-1}$ (and we note that $\Omega_{\text{gw}}(k)h^2 \simeq \text{constant}$ for $n_t \simeq 0$, so our results will not depend too sensitively on the precise value of f we use). CMB/LSS and BBO/DECIGO scales are therefore separated by $\Delta N = \ln(6 \times 10^{13}/0.05) \simeq 35$ e -folds of inflation⁴. Eq. (2.20) can then be used to find the field value ϕ_g at the time that BBO/DECIGO scales exited the horizon.

³When making this argument we ignore the fact that current analyses indicating $n_s < 1$ fix $r = 0$. The full analysis presented in this chapter does not fix r .

⁴We note that the actual expression that relates two field values corresponding to known length-scales is not given

Table 2.1:

POTENTIALS CONSIDERED IN THIS CHAPTER	
Potential name	$V(\phi)$
Higgs:	$V_0(1 - [\phi/\mu]^2)^2$
Coleman-Weinberg:	$V_0 \left\{ \left(\frac{\phi}{\mu} \right)^4 \left(\log \left[\frac{\phi}{\mu} \right] - \frac{1}{4} \right) + \frac{1}{4} \right\}$
PNGB:	$V_0[1 - \cos(\phi/\mu)]$
Chaotic:	$V_0 \left(\frac{\phi}{m_{\text{Pl}}} \right)^p$
Power-law:	$V_0 e^{-p\phi/m_{\text{Pl}}}$
Hybrid:	$V_0 \left[1 + \left(\frac{\phi}{\mu} \right)^2 \right]$

2.4.1 Power-law inflation

In power-law inflation [10] the inflaton potential takes the form,

$$V(\phi) = V_0 e^{-p\phi/m_{\text{Pl}}}. \quad (2.32)$$

This form for the inflaton potential often appears in scalar-tensor models for inflation [126, 127]. Power-law inflation is so called because the scale factor is a power law $a(t) \propto t^{16\pi/p^2}$, and the Hubble parameter also evolves as a power of time t . The resulting scalar and tensor power spectra are then pure power laws, with no running of the spectral indices. The parameter $\epsilon = p^2/(16\pi)$ always, so that inflation must be ended artificially at some ϕ_{end} . Although the potential has only two free parameters (V_0 and p), there is an additional free parameter, namely, the value of ϕ_c , which we are free to choose in this particular family of models. This model has also $\eta = p^2/8\pi$, so $n_s = 1 - p^2/8\pi = 1 - 2\epsilon$, and for $n_s > 0.9$ we find a constraint $\epsilon < 0.05$. The constraint $r = 16\epsilon \lesssim 1$ is comparable or a bit weaker. Since n_s and r depend in this model only on the parameter p , these models occupy a curve in the n_s - r parameters space, which is indicated by the left two panels in Fig. 2.3. The constraint $\Delta N = 35$ to the number of e -folds between CMB/LSS and BBO/DECIGO scales tells us that

$$\Delta N = \frac{8\pi}{p} \frac{\phi_g - \phi_c}{m_{\text{Pl}}} \simeq 35, \quad (2.33)$$

by Eq. (2.20), which ignores, in part, the variation of H during inflation. Instead, the exact expression is given by,

$$\ln \left(\frac{k_1}{k_0} \right) = \sqrt{\frac{4\pi}{m_{\text{Pl}}^2}} \int_{\phi_1}^{\phi_0} \frac{1 - \epsilon}{\sqrt{\epsilon}} d\phi.$$

The error in our expression is expected to be small, since we are only considering the epoch of inflation far from its end, so that we can always take $\epsilon \ll 1$, in which case the above expression becomes approximately equivalent to Eq. (2.20).

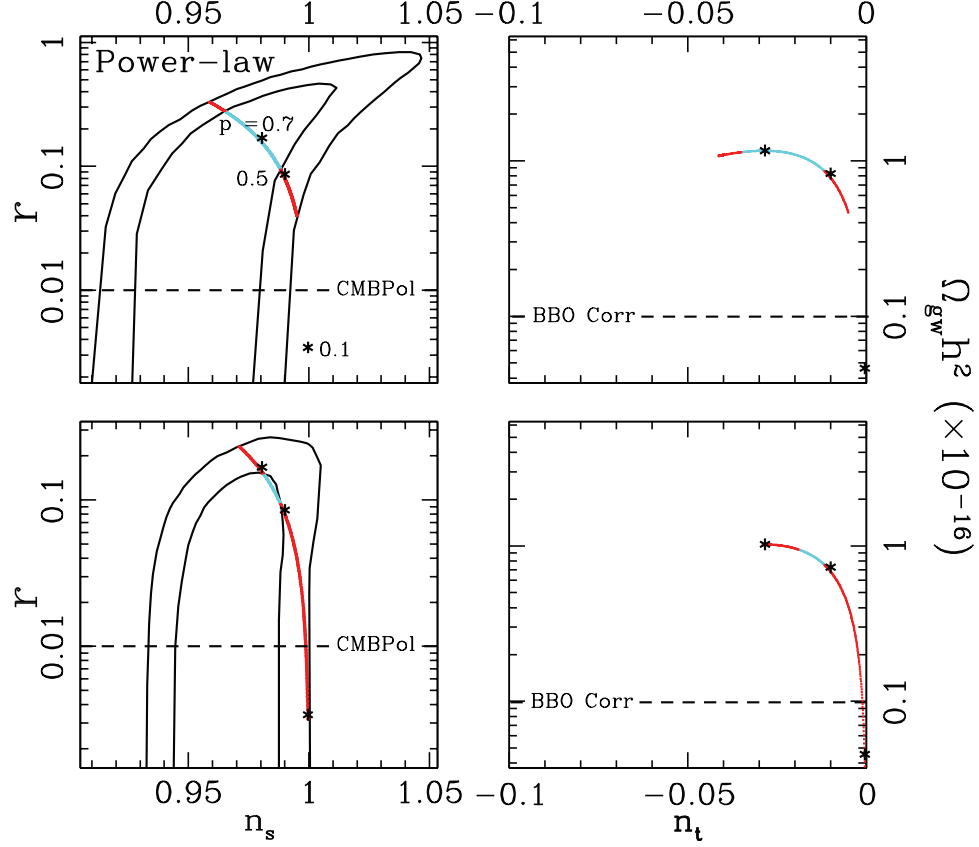


Figure 2.3: Results for power-law inflation. The left two panels show constraints (68% and 95% confidence levels) from CMB measurements, whereas the right two panels show the predicted amplitude and slope of the IGWB at 0.1 Hz. The upper panels correspond to WMAP3-only constraints, whereas the lower two panels correspond to WMAP3+ constraints. The dashed lines on the left-hand panels indicate $r = 0.01$ roughly the limit for CMBPol [128]. The panels on the right show the corresponding predictions for the IGWB given the CMB constraints. The dashed lines on the right-hand panels indicate the sensitivity of the second generation BBO interferometer known as ‘BBO correlated’ [129–131]. The stars indicate values for the power-law index, p . For a fixed scalar amplitude, P_s , this model occupies only a line in the $n_s - r$ plane because both ϵ and η are functions only of the index p and not of the field value.

from which it follows that

$$\frac{V(\phi_g)}{V(\phi_c)} = e^{-(p^2/8\pi)\Delta N} = e^{-(r/8)\Delta N}. \quad (2.34)$$

We thus find the gravitational-wave amplitude at DECIGO/BBO scales is

$$\begin{aligned} \Omega_{\text{gw}} h^2 &= A_{\text{gw}} V(\phi_g) = \frac{3}{128} r P_s A_{\text{gw}} e^{-(r/8)\Delta N} \\ &= 1.37 \times 10^{-15} r e^{-(r/(0.23))(\Delta N/35)} \times \left(\frac{P_s(k_c)}{2.45 \times 10^{-9}} \right) \left(\frac{A_{\text{gw}}}{2.39 \times 10^{-5}} \right). \end{aligned} \quad (2.35)$$

This expression is maximized for $r = 8/\Delta N \simeq 0.23$ at a value $\Omega_{\text{gw}}^{\text{max}} h^2 = 1.15 \times 10^{-16}$. Interestingly enough, the IGWB detectability through direct detection is maximized for relatively small ϵ , while

the detectability with the CMB is maximized at larger ϵ [89]. Given that CMB sensitivities are expected to get to $r \sim 0.01$ in the relatively near future with the CMB, and then to $r \sim 10^{-4}$ with a next-generation satellite experiment, it is unlikely that this model would produce a direct detection without producing a detectable CMB signal.

Fig. 2.3 shows the region of the $\Omega_{\text{gw}} h^2 - n_t$ parameter space (at BBO/DECIGO scales) that the $n_s - r$ parameter space shown in Fig. 2.3 maps to for power-law inflation. If power-law inflation is the correct model of inflation, then the IGWB is directly detectable with BBO for $r \gtrsim 10^{-3}$ and $r \gtrsim 10^{-6}$ with DECIGO.

2.4.2 Chaotic inflation

In chaotic inflation, the inflaton potential is,

$$V(\phi) = V_0 \left(\frac{\phi}{m_{\text{Pl}}} \right)^p. \quad (2.36)$$

This model was first proposed in Ref. [132]. Except for the choice of $p = 2$ (massive scalar field) and $p = 4$ this model may be thought of as a local approximation to a more complete theory. It is also a good approximation to both the PNGB potential and the Higgs potential in the appropriate limits. In this family of models, $\epsilon(\phi) = (p^2/16\pi)(m_{\text{Pl}}/\phi)^2$, and therefore inflation ends when $\phi = \phi_{\text{end}} \equiv pm_{\text{Pl}}/(4\sqrt{\pi})$. If there are N_c e -folds of inflation between CMB horizon exit and the end of inflation, then Eq. (2.20) gives us $\phi_c^2 = (m_{\text{Pl}}^2/16\pi)(4pN_c + p^2)$. We also have $\eta(\phi) = p(p-1)(m_{\text{Pl}}/\phi)^2/(8\pi)$ from which it follows that at CMB/LSS scales,

$$n_s = 1 - 2 \frac{p+2}{4N_c + p}. \quad (2.37)$$

Noting that $47 \lesssim N_c \lesssim 62$, the constraint $n_s > 0.9$ gives us a constraint $p \lesssim 4N_c/19 - 40/19$. The constraint on the tensor-to-scalar ratio, $r = 16\epsilon = 16p/(4N_c + p) \lesssim 1$, leads to a slightly less stringent limit, $p \lesssim 4N_c/15$. We note that the scalar running $\alpha_s = -2(1 - n_s)^2/(2 + p)$ is always within the current observational constraints since $|1 - n_s| \lesssim 0.1$. This family of models is thus parameterized by two parameters: $47 \lesssim N_c \lesssim 62$ and $p \lesssim 4N_c/19 - 40/19$. Note that each choice of (p, N_c) maps onto a point in the $n_s - r$ parameter space, so we could just as well choose n_s and r as our two independent parameters. If we choose to do so, then we assign N_c and p by $N_c = (1 - \epsilon)/(1 - n_s - 2\epsilon)$ and $p = 4\epsilon/(1 - n_s - 2\epsilon)$, where $\epsilon = r/16$.

For a fixed value of N_c , this family of models is represented by a curve in the $n_s - r$ parameter space; a spread in the range of values for N_c broadens this curve into a region in the $n_s - r$ parameter space, as indicated by left two panels in Fig. 2.4

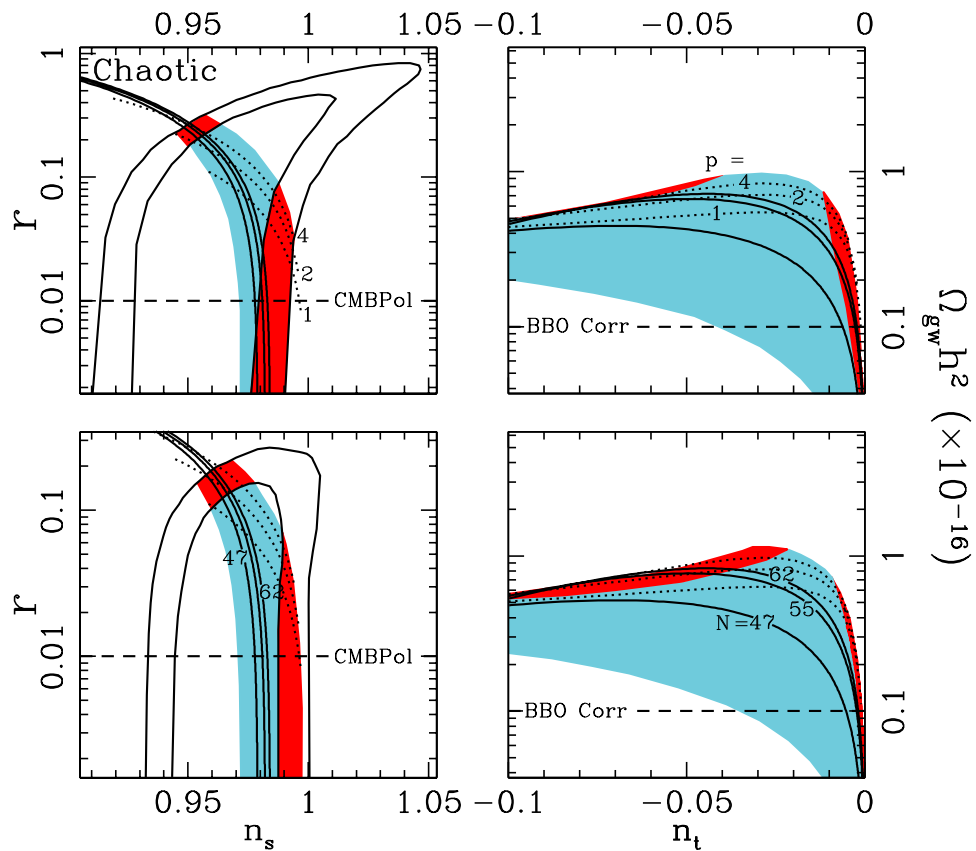


Figure 2.4: Same as Fig. 2.3 but for the chaotic potential. As commented in the text, only those models for which the index p is a positive even integer allow for a proper end to inflation. For other choices of p the form of the inflaton potential must change before inflation ends. As a result, we allow for the field value ϕ_{CMB} to be a free parameter, as discussed in the text. In order to indicate the predictions for those models in this class that reach a proper end of inflation (i.e., where p is a positive even integer), the solid black lines correspond to between 62 and 47 e -folds of inflation and the dotted lines indicate constant values for the index of the potential. As is commented in Ref. [94], a massive scalar field ($p = 2$) is a good fit to the data, whereas a quartic potential lies outside of the 2σ confidence region using just WMAP3 data. This disagreement is worsened when using the WMAP3+ constraints.

Once p and N_c are specified, the potential prefactor is fixed by

$$V_0 = \frac{3p^2 P_s(k_c)}{128 \pi} \left(\frac{16 \pi}{4pN_c + p^2} \right)^{(p+2)/2} m_{\text{Pl}}^4. \quad (2.38)$$

The gravitational-wave amplitude at direct-detection scales is then simply,

$$\Omega_{\text{gw}} h^2 = \frac{128}{3} A_{\text{gw}} \frac{V_0}{m_{\text{Pl}}^4} \left(\frac{\phi_g}{m_{\text{Pl}}} \right)^p, \quad (2.39)$$

where the field value ϕ_g at the time direct-detection scales undergo horizon crossing is given by

$$\phi_g^2 = \frac{m_{\text{Pl}}^2}{16\pi} (4pN_g + p^2), \quad (2.40)$$

and where $N_g = N_c - 35 \equiv N_c - \Delta N$ is the number of e -folds before the end of inflation that DECIGO/BBO scales exit the horizon. For chaotic inflation, the value of n_t at DECIGO/BBO scales will differ from (and generally be larger in amplitude, or more negative than) that at CMB/LSS scales. The value of n_t at DEICGO/BBO scales will differ from that at CMB/LSS scales; it will be given by $n_t(\phi_g) = -2\epsilon(\phi_g)$.

Since in order for inflation to end and for oscillations in the inflaton field to begin, p must be even, by considering models for with arbitrary p we are implicitly supposing that the form of the potential changes between the field values corresponding to CMB and gravitational-wave observatory observations and the end of inflation. In order to take this into account we allowed the field value corresponding to CMB observations, ϕ_c , to be a free parameter, only requiring that it be at least 35 e -folds before the field reached the value $\phi = p m_{\text{Pl}}/(4\sqrt{\pi})$ where $\epsilon = 1$. If we allowed for a value for ϕ_c to be lower then this, then the form of the potential must change between field values corresponding to CMB observations and the direct observation of the IGWB. Such a situation was explored in Ref. [133] in the form of a broken scale-invariant potential.

The right-hand panels in Fig. 2.4 show the region of the $\Omega_{\text{gw}} h^2 - n_t$ parameter space (at BBO/DECIGO scales) that the $n_s - r$ parameter space shown in the left-hand panels in Fig. 2.4 maps to for chaotic inflation. The breadth in $\Omega_{\text{gw}} h^2$ of the region is due to the spread in the $p - N_c$ parameter space for fixed $P_s(k_c) = 2.45 \times 10^{-9}$; there will be a slight additional vertical broadening beyond that shown due to the uncertainty in this parameter. If chaotic inflation is the correct model of inflation, then the IGWB is directly detectable with BBO for $r \gtrsim 10^{-3}$ and $r \gtrsim 10^{-6}$ with DECIGO.

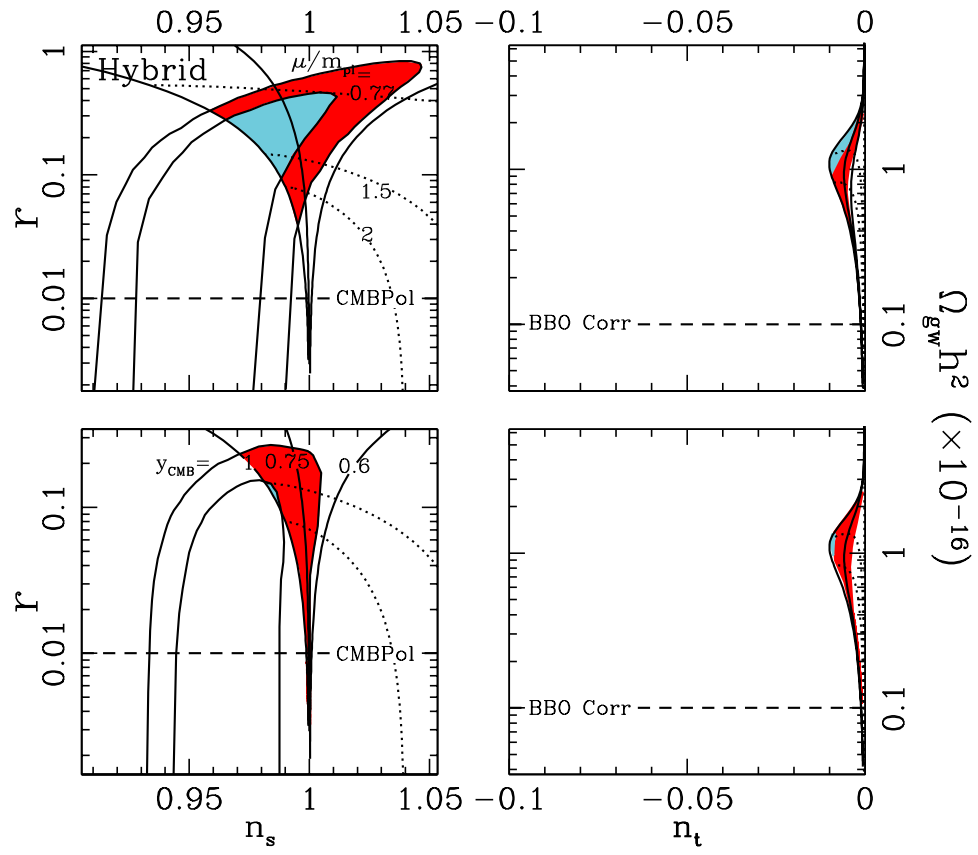


Figure 2.5: Results for hybrid inflation. See the caption for Fig. 2.3 for details.

2.4.3 Hybrid inflation

Hybrid inflation generally requires two scalar fields [134], but the phenomenology can be modeled by a single scalar field with the potential,

$$V(\phi) = V_0 \left[1 + \left(\frac{\phi}{\mu} \right)^2 \right], \quad (2.41)$$

and the selection of a value for ϕ_{end} (with the only requirement that $\phi_{\text{end}} > 0$). We note that this form for the potential is not to be taken to be generic within the class of hybrid inflation but only as a particular example. Other forms exist, such as those found in, e.g., Refs. [135–137]. Defining $y \equiv \phi/\mu$, we find that the slow-roll parameters are given by, $\epsilon(y) = (m_{\text{Pl}}/4\pi\mu^2)y^2[1+y^2]^{-2}$, and $\eta(y) = (m_{\text{Pl}}/4\pi\mu^2)[1+y^2]^{-1}$. In these models, ϵ is maximized at $y = 1$ with a value less than unity if $\mu > m_{\text{Pl}}/(4\sqrt{\pi})$. For smaller values of μ , inflation ends soon after $y = 1$ [138]⁵. The dynamics of these models resembles those of chaotic inflation, which we have already considered, and so we consider them no further. New inflationary dynamics arises for $\mu > m_{\text{Pl}}/(4\sqrt{\pi})$ and $y \leq 1$, and so we restrict our attention here to this regime.

The field value at which CMB/LSS scales undergo horizon crossing during inflation is,

$$y_c^2 = 2 \ln \left(\frac{y_c}{y_{\text{end}}} \right) - y_{\text{end}}^2 - \frac{N_c}{2\pi} \left(\frac{m_{\text{Pl}}}{\mu} \right)^2. \quad (2.42)$$

Since y_c is taken to be a free parameter, Eq. (2.42), along with $47 \lesssim N_c \lesssim 62$, determines the value of y_{end} . From the slow-roll parameters,

$$n_s = 1 + \frac{m_{\text{Pl}}^2}{2\pi\mu^2} \frac{1 - 2y_c^2}{(1 + y_c^2)^2}, \quad (2.43)$$

at CMB/LSS scales. The above expression for n_s is maximized at $y = 0$, and at this field value becomes $n_s = 1 + m_{\text{Pl}}^2/2\pi\mu^2$, which shows that we can have $n_s > 1$ in hybrid inflation. The pre-factor V_0 is then fixed by the constraint,

$$V_0 = \frac{3}{32\pi} \left(\frac{m_{\text{Pl}}}{\mu} \right)^2 P_s(k_c) \frac{y_c^2}{(1 + y_c^2)^3} m_{\text{Pl}}^4. \quad (2.44)$$

Once this normalization is fixed, these models are parameterized by μ and y_c , and n_s and r are fixed once these two parameters are specified. As in chaotic inflation, we may alternatively take as our two free parameters n_s and r , and then determine μ and y_c . In particular, these can be determined

⁵One can numerically determine that within a fraction of an e -folding $y \rightarrow 0$ and therefore must pass through y_{end} .

from

$$y_c = \left[\frac{r}{8(n_s - 1) + 2r} \right]^{1/2}, \quad (2.45)$$

$$\mu = 2 \left[\frac{2}{\pi} \frac{4(n_s - 1) + r}{[8(n_s - 1) + 3r]^2} \right]^{1/2} m_{\text{Pl}}. \quad (2.46)$$

The gravitational-wave amplitude at direct-detection scales is then simply given by,

$$\Omega_{\text{gw}} h^2 = \frac{128}{3} A_{\text{gw}} \frac{V_0}{m_{\text{Pl}}^4} (1 + y_g^2), \quad (2.47)$$

where the field value y_g at the time direct-detection scales undergo horizon crossing is given by

$$y_g^2 = 2 \ln \left(\frac{y_g}{y_{\text{end}}} \right) - y_{\text{end}}^2 - \frac{N_g}{2\pi} \left(\frac{m_{\text{Pl}}}{\mu} \right)^2, \quad (2.48)$$

and where again, $N_g = N_c - 35 \equiv N_c - \Delta N$ is the number of e -folds before the end of inflation and the time when DECIGO/BBO scales exit the horizon. The value of n_t at DECIGO/BBO scales will differ from that at CMB/LSS scales; it will be given by $n_t(y_g) = -2\epsilon(y_g)$. The running of the tensor spectral index,

$$\alpha_t(y) = \frac{1}{4\pi^2} \left(\frac{m_{\text{Pl}}}{\mu} \right)^4 \frac{y^2(1 - y^2)}{(1 + y^2)^4}, \quad (2.49)$$

can be positive in this class of models. Thus, for $y < 1$, $\alpha_t > 0$, and the running is positive, indicating that as y evolves, the tensor spectral index becomes less negative. As we have seen in the previous models, a non-negligible gravitational-wave amplitude at CMB/LSS scales leads to a “large” amplitude at direct-detection scales primarily due to a small, negative, tensor spectral index. We therefore expect this model to produce the largest gravitational-wave amplitude at direct-detection scales. We also note that the running of the scalar spectral index at CMB/LSS scales is

$$\alpha_s = \frac{m_{\text{Pl}}^4}{2\pi^2 \mu^4} \frac{y_c^2(y_c^2 - 2)}{(1 + y_c^2)^4}. \quad (2.50)$$

With the restriction that $y_c \leq 1$, α_s is maximized at $y = \sqrt{2 - \sqrt{3}}$. We note from this that if $\mu \geq 0.69 m_{\text{Pl}}$ the observational bound on α_s is satisfied for all $y_c \leq 1$. For μ not satisfying this restriction, there will be some range of y_c which are incompatible with observations. This restriction is taken into account in our numerical calculations.

The right-hand panels in Fig. 2.5 show the region of the $\Omega_{\text{gw}} h^2 - n_t$ parameter space (at BBO/DECIGO scales) that the $n_s - r$ parameter space shown in the left-hand panels of Fig. 2.5 maps to for symmetry-breaking inflation. The breadth in $\Omega_{\text{gw}} h^2$ of the region is due to the spread in the $\mu - N_c$ parameter space for *fixed* $P_s(k_c) = 2.45 \times 10^{-9}$. If hybrid inflation is the correct model of inflation, then the

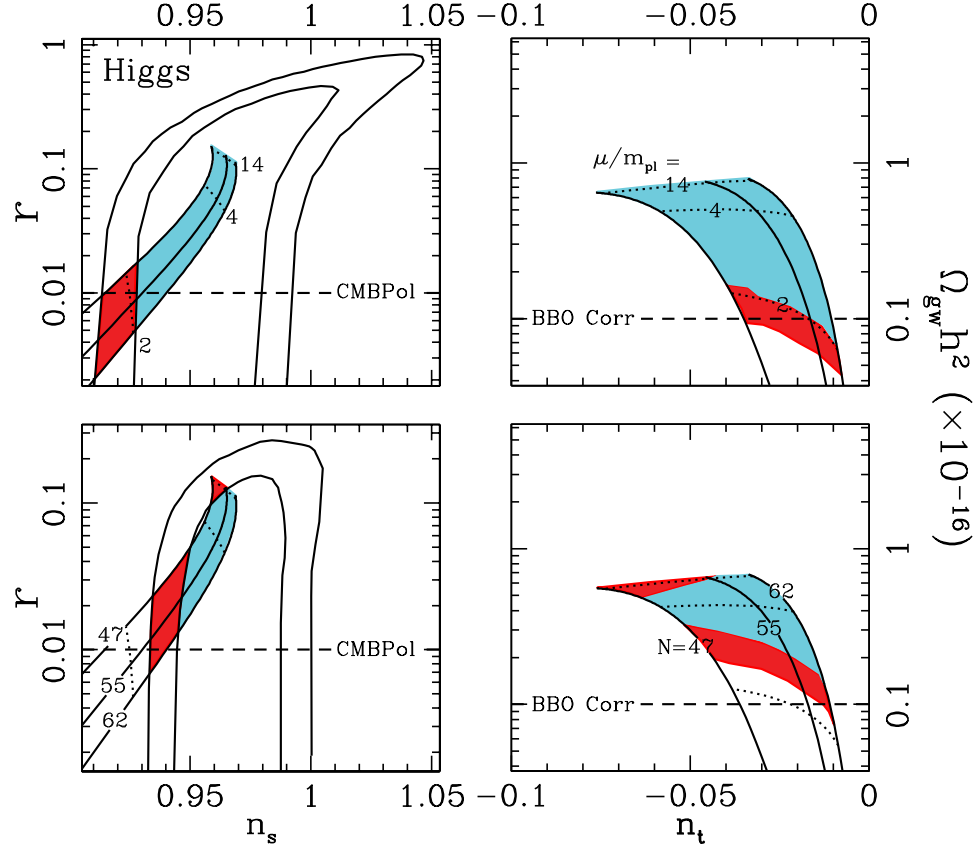


Figure 2.6: Results for the Higgs potential. See the caption for Fig. 2.3 for details.

IGWB may be detectable with BBO and DECIGO, but it is not guaranteed.

2.4.4 Symmetry breaking inflation

We now consider the Higgs potential,

$$V(\phi) = V_0 \left[1 - \left(\frac{\phi}{\mu} \right)^2 \right]^2, \quad (2.51)$$

parameterized by V_0 and a Higgs vacuum expectation value μ . Our treatment of this family of models will parallel that for chaotic inflation. In these models, ϕ starts near the origin and then rolls toward $\phi = \mu$. The slow-roll parameters are $\epsilon(\phi) = (m_{\text{Pl}}^2 \phi^2 / 4\pi \mu^4) [1 - (\phi/\mu)^2]^{-2}$, and $\eta(\phi) = (m_{\text{Pl}}^2 / 2\pi \mu^2) [3(\phi/\mu)^2 - 1] [1 - (\phi/\mu)^2]^{-2}$, from which we infer an end to inflation,

$$\phi_{\text{end}} = \left[\frac{m_{\text{Pl}}^2}{2\pi} \left(1 + 2\pi \frac{\mu^2}{m_{\text{Pl}}^2} - \sqrt{1 + 4\pi \frac{\mu^2}{m_{\text{Pl}}^2}} \right) \right]^{1/2}. \quad (2.52)$$

The field value at which CMB/LSS scales undergo horizon crossing during inflation is

$$\phi_c^2 = \frac{N_c m_{\text{Pl}}^2}{\pi} + \phi_{\text{end}}^2 - 2\mu^2 \ln(\phi_{\text{end}}/\phi_c). \quad (2.53)$$

At CMB/LSS scales,

$$n_s = 1 - \frac{1}{\pi} \left(\frac{m_{\text{Pl}}}{\mu} \right)^2 \frac{1 + 3y_c^2}{(1 - y_c^2)^2}, \quad (2.54)$$

where $y_c \equiv \phi_c/\mu$. Since n_s is a decreasing function of y , the constraint $n_s > 0.9$ requires $\mu \gtrsim 1.8 m_{\text{Pl}}$. The prefactor V_0 is then fixed by the constraint,

$$V_0 = \frac{3}{8\pi} P_s(k_c) (m_{\text{Pl}}/\mu)^2 \frac{y_c^2}{(1 - y_c^2)^4} m_{\text{Pl}}^4. \quad (2.55)$$

Once this normalization is fixed, these models are parameterized by μ and N_c , and n_s and r are fixed once these two parameters are specified. As in chaotic inflation, we may alternatively take as our two free parameters n_s and r , and then determine μ and N_c , although the inversion is not as tractable algebraically as in chaotic inflation.

The gravitational-wave amplitude at direct-detection scales is then simply,

$$\Omega_{\text{gw}} h^2 = \frac{128}{3} A_{\text{gw}} \frac{V_0}{m_{\text{Pl}}^4} (1 - y_g^2)^2, \quad (2.56)$$

where $y_g \equiv \phi_g/\mu$, and the field value ϕ_g at the time direct-detection scales undergo horizon crossing is given by

$$\phi_g^2 = \frac{N_g m_{\text{Pl}}^2}{\pi} + \phi_{\text{end}}^2 - 2\mu^2 \ln(\phi_{\text{end}}/\phi_g), \quad (2.57)$$

and where again, $N_g = N_c - 35 \equiv N_c - \Delta N$ is the number of e -folds before the end of inflation and the time when DECIGO/BBO scales exit the horizon. The value of n_t at DECIGO/BBO scales will differ from that at CMB/LSS scales; it will be given by $n_t(\phi_g) = -2\epsilon(\phi_g)$. We also note that the running of the scalar spectral index at CMB/LSS scales is

$$\alpha_s = -\frac{1}{\pi^2} \left(\frac{m_{\text{Pl}}}{\mu} \right)^4 y_c^2 \frac{5 + 3y_c^2}{(1 - y_c^2)^4}. \quad (2.58)$$

We check in our numerical results that all of the models we consider are consistent with the bound to this parameter, $|\alpha_s| < 0.04$. In particular we find that $|\alpha_s| \lesssim 10^{-3}$.

The right-hand panels of Fig. 2.6 show the region of the $\Omega_{\text{gw}} h^2 - n_t$ parameter space (at BBO/DECIGO scales) that the $n_s - r$ parameter space shown in the left-hand side of Fig. 2.6 maps to for symmetry-breaking inflation. The breadth in $\Omega_{\text{gw}} h^2$ of the region is due to the spread in the $\mu - N_c$ parameter space for *fixed* $P_s(k_c) = 2.45 \times 10^{-9}$. If symmetry-breaking inflation is the correct model of inflation, then the majority of the parameter space indicates that the IGWB will be detectable with BBO and DECIGO. Incidentally, we have also investigated potentials of the form $V(\phi) = V_0 [1 - (\phi/\mu)^p]^2$

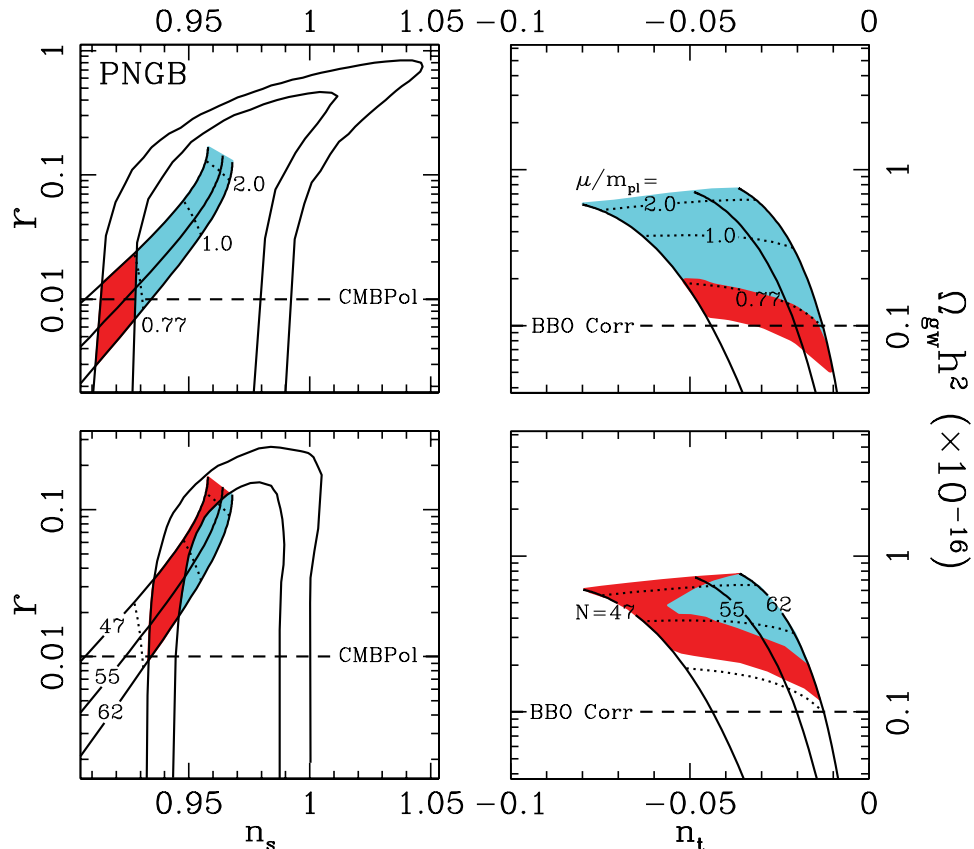


Figure 2.7: Results for the PGNB potential. See the caption for Fig. 2.3 for details.

with $p > 2$ [139]. In these models, the symmetry-breaking scale can be reduced below m_{Pl} , however the IGWB amplitude is then reduced below the level accessible to BBO/DECIGO for $\mu \lesssim 0.1 m_{\text{Pl}}$.

2.4.5 PGNB inflation

The pseudo Nambu-Goldstone boson (PNGB) potential [140–143] proposes that the inflaton may be associated with explicit symmetry breaking within an already spontaneously broken symmetry. Its form is given by

$$V(\phi) = V_0(1 - \cos[\phi/\mu]). \quad (2.59)$$

An example is the Peccei-Quinn axion which gains a small mass as the result of an explicit symmetry breaking through non-perturbative corrections. The strength of the interactions between the PGNBs and other fields are set by the the inverse of the energy scale at which the explicit symmetry is broken. Therefore, if the symmetry is broken at a high energy scale, it is natural for this field to have very weak interactions. The theoretical strength of this model is that its small mass and weak interactions are ‘natural’ and are not spoiled by higher order corrections.

Comparing the functional form for the PNGB and the Higgs potential it is clear that its dynamics will be closely related to those of the Higgs potential. Additionally, the dynamics cannot be derived in an analytic form. Therefore, we refer the reader to Sec. 2.4.4 for an approximate discussion of the dynamics of this model but solve the model numerically. We check in our numerical results that all of the models we consider are consistent with the bound $|\alpha_s| < 0.04$. The right-hand panels of Fig. 2.7 show the region of the $\Omega_{\text{gw}}h^2-n_t$ parameter space (at BBO/DECIGO scales) that the n_s-r parameter space shown in the left-hand side of Fig. 2.7 maps to for symmetry-breaking inflation. If PNGB inflation is the correct model of inflation, then, just as in the Higgs case, the most of the parameter space produces an IGWB that will be detectable with both BBO and DECIGO.

2.4.6 Coleman-Weinberg inflation

Coleman-Weinberg inflation [3, 8, 144–146] is inflation driven by a scalar field possessing a potential produced through loop corrections as first outlined in Ref. [147]. The potential takes the form

$$V(\phi) = V_0 \left\{ \left(\frac{\phi}{\mu} \right)^4 \left(\log \left[\frac{\phi}{\mu} \right] - \frac{1}{4} \right) + \frac{1}{4} \right\}. \quad (2.60)$$

If we couple a scalar field in an SU(5) field theory to gauge bosons we develop such a potential. However, the amplitude of that potential (of order g^4 where g is the gauge coupling) is too large in order to drive a period of inflation [144]. An alternative scenario is to couple an SU(5) singlet to the adjoint and fundamental Higgs fields [148]. Such a coupling also leads to a Coleman-Weinberg potential, but with a largely arbitrary normalization. Observationally, the unique aspect of this potential is that it is exceptionally flat near the origin. This property leads to a particularly ‘steep’ region in the n_s-r plane, with r decreasing rapidly around $n_s \sim 0.94$. This is particularly interesting given our desire to understand how a measurement of n_s impacts our predictions for r .

The flatness of this potential near the origin brings up an interesting question of ‘fine tuning’. In Ref. [50] it is argued that an inflaton potential should be considered to be fine tuned if it possesses a large number of zeros in its derivatives throughout the period of inflation. A convenient way of measuring this is given by considering either slow-roll parameter (ϵ or η) and its derivatives. If a potential has many zeroes in either ϵ or η during inflation it is considered to be fine tuned. We show the value of η for the Coleman-Weinberg potential in Fig. 2.9 and it is clear that η passes through many zeros during inflation. Therefore, according to the criteria of Ref. [50] the Coleman-Weinberg potential is fine tuned. However, it can also be argued that it is produced through natural couplings and therefore should be considered as such. As in the case of the PNGB potential, the dynamics of Coleman-Weinberg inflation are not analytical. We solved for the dynamics numerically and check that all models that we consider are consistent with the bound $|\alpha_s| < 0.04$. The right-hand panels of Fig. 2.8 show the region of the $\Omega_{\text{gw}}h^2-n_t$ parameter space (at BBO/DECIGO scales) that the n_s-r

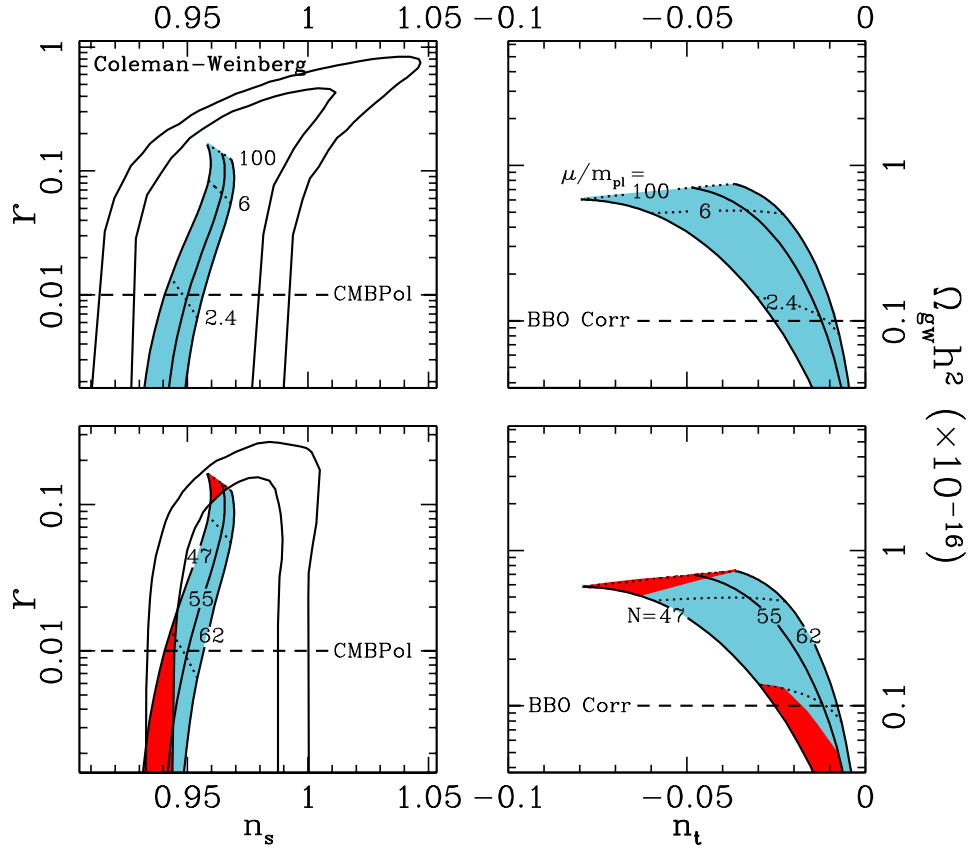


Figure 2.8: Results for the Coleman-Weinberg potential. See the caption for Fig. 2.3 for details.

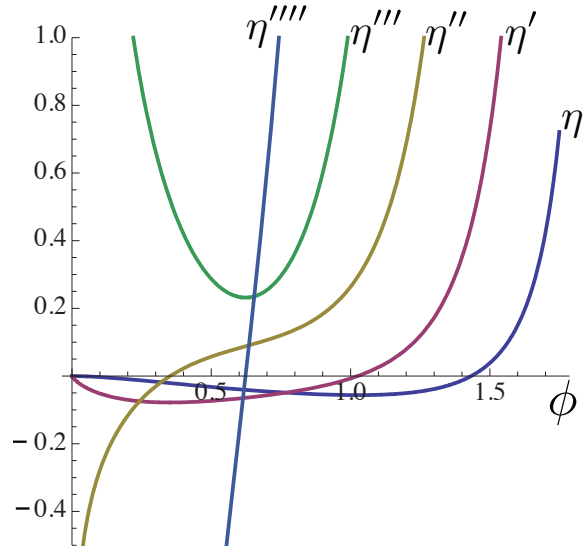


Figure 2.9: Here we show the slow-roll parameter η as a function of the inflaton field value ϕ for the Coleman-Weinberg potential. For this example we have chosen $\mu = 2$ in units of m_{pl} . Given the large number of zeros found in η and its derivatives throughout inflation, this potential is considered extremely fine tuned according to the criteria discussed in Ref. [50].

parameter space shown in the left-hand side of Fig. 2.8 maps to for symmetry-breaking inflation. If Coleman-Weinberg inflation is the correct model of inflation, then, just as in the Higgs case, the most of the parameter space produces an IGWB that will be detectable with both BBO and DECIGO.

2.5 The (running) power-law approximation

During inflation, the value ϕ of the scalar field can change very little as the scale factor $a(t)$ grows extremely rapidly. It is therefore a feature of inflation that a vast range of distance scales can correspond to a small change in ϕ . This motivates the power-law expansions (with a slight running of the spectral index) in Eqs. (2.10) and (2.11), which assume that the inflaton potential can be accurately approximated by its Taylor expansion (to second order) about a given inflaton value. These power-law expansions are particularly appropriate when studying the CMB and large-scale structure (e.g., Refs. [88, 107, 149]), which involve a spread in distance scales of maybe three orders of magnitude.

However, BBO/DECIGO frequencies are separated from those probed by the CMB/LSS by roughly sixteen orders of magnitude. The inflaton may thus traverse a significant distance, and so it is not obvious that the Taylor expansion approximation that underlies the power-law approximation (even with the running of the spectral index) will remain valid. For example, in Eqs. (2.12) and (2.13), the tensor and scalar tilt are written in terms of the first-order slow-roll parameters, while second- and higher-order corrections (e.g., Ref. [150]) may be important when extending the power spectrum over large physical scales. Similarly, one must also account for higher-order derivatives of the tilt, beyond the running considered with α_s and α_t . For the calculation performed here, higher-order corrections are not important as $\Omega_{\text{gw}}h^2$ was directly determined with model parameters describing the inflaton potential, rather than through the power spectrum. Assuming the Taylor approximation is valid, then measurements of P_s , n_s , and r at CMB/LSS scales fix the parameters $P_t(k_c)$, n_t , and α_t in Eq. (2.11), which can then be used to predict $P_t(k_q) \propto \Omega_{\text{gw}}h^2$, the IGWB amplitude at BBO/DECIGO scales. An approach based on the Taylor expansion was considered in Ref. [88] to estimate the GW amplitude at frequencies corresponding to direct detections. Fig. 2.10 plots the exact IGWB amplitude obtained from the calculation in the previous section vs. that obtained from the power-law approximation. For small IGWB amplitudes, $r = 16\epsilon \rightarrow 0$, and so the potentials are very close to flat and the power law tends to be a good approximation, and is indeed a good approximation for the classes of models we have considered. For power-law inflation, where the power spectra are precisely power laws, the two results are identical. For chaotic and symmetry-breaking inflation, ϵ becomes large when the IGWB amplitude becomes large, and ϵ evolves during inflation in such a way that the power-law approximation overestimates the true IGWB amplitude at direct-detection scales. The behavior of hybrid inflation is a bit more subtle. The running of

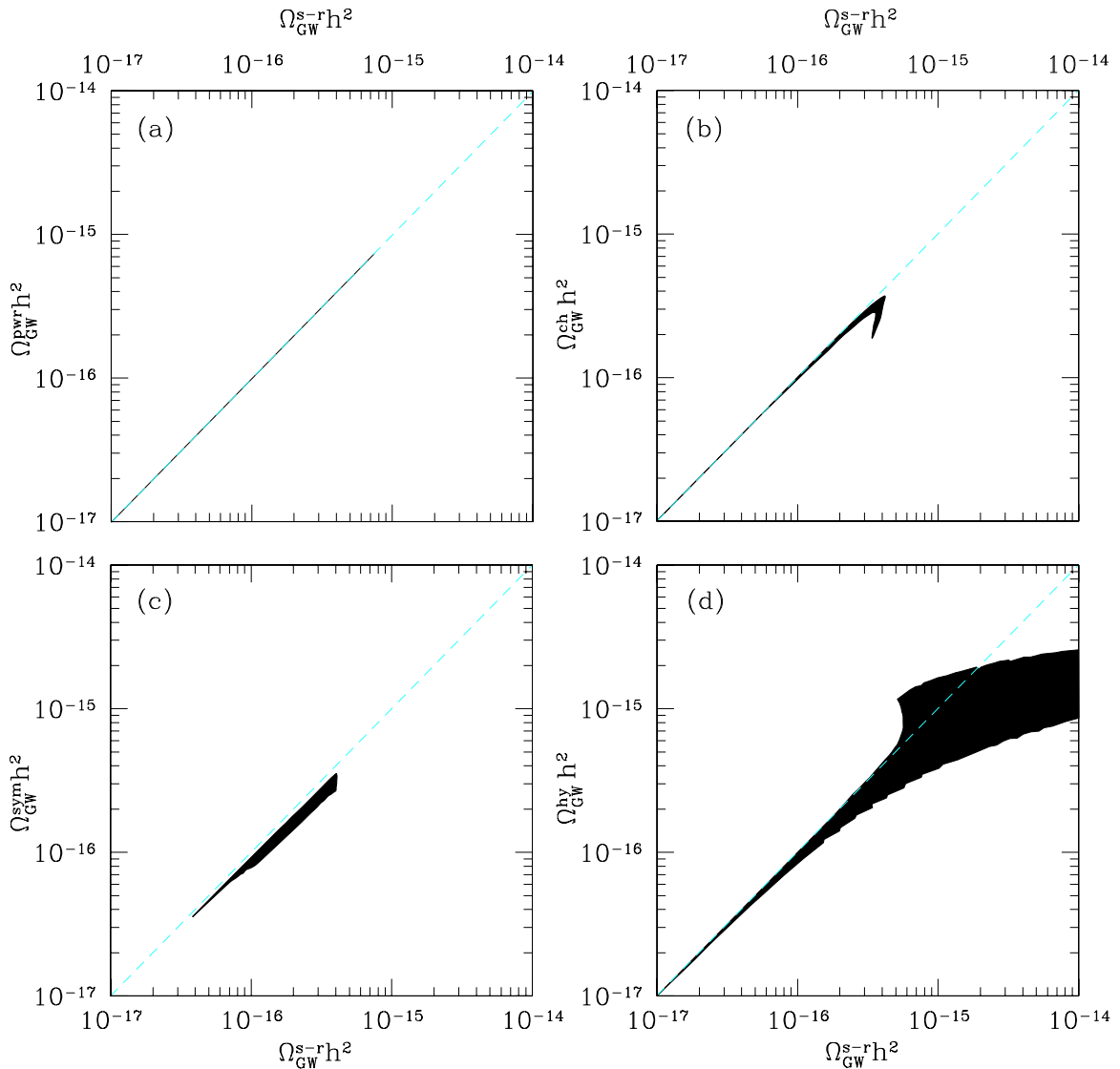


Figure 2.10: Here we plot the inflationary gravitational-wave background amplitude $\Omega_{\text{gw}} h^2$ obtained with the exact inflationary dynamics described in Section IV versus the amplitudes obtained with the power-law approximations (with slow-roll parameters fixed by CMB/LSS observations) given in Section IIb. The panels show results for (a) power-law, (b) chaotic, (c) symmetry-breaking, and (d) hybrid inflation. The regions are models taken from the allowed n_s-r parameter space and the blue dashed curves indicate equality.

the tensor spectral index is $\alpha_t = (r/8)(n_s - 1 + r/8)$ which, for $n_s > 1 - r/8$ can be positive. The (running) power-law would then suggest that n_t will become positive at some small distance scale, which cannot be [see Eq. (2.13)]. The power-law approximation can then overestimate the true IGWB amplitude at BBO/DECIGO scales. On the other hand, in hybrid inflation, unlike chaotic and symmetry-breaking inflation, ϵ can indeed decrease as inflation proceeds, and so the direct-detection amplitude may also be underestimated by the power-law approximation. Both behaviors are seen in Fig. 2.10.

It should also be kept in mind that the tensor spectral index n_t is most generally different at CMB scales than it is at direct-detection scales, and it is conceivably measurable at both. Determination of n_t at both distance scales could therefore distinguish between inflationary models. For example, in power-law inflation, n_t remains precisely constant, while it can change by roughly a factor of two for chaotic inflation for models with a directly detectable IGWB. Realistically, though, the tensor spectral indices are generically (although not in full generality) small, and so running of the tensor spectral index will be difficult to measure.

Finally, the classes of models we have considered are not at all exhaustive, and another inflaton potential could yield a direct-detection IGWB amplitude different from those we have considered here and different from what extrapolation from CMB/LSS would suggest from the power-law approximation. For example, in models with broken scale invariance [151, 152], the direct-detection amplitude could be considerably different.

2.6 Broken scale invariant spectrum

To demonstrate that direct observations of the IGWB can distinguish between different forms of the inflaton potential, we consider as a toy model the broken scale invariant (BSI) potential, which features a sharp change in the slope of the inflaton potential at some transition scale [91, 151, 152]. Such models have been invoked to explain, e.g., the paucity of dwarf galaxies observed around the Milky Way [153–155].

Consider a potential of the form,

$$V(\phi) = V_0 \times \begin{cases} (1 + A\phi), \phi \gtrsim 0 \\ (1 + cA\phi), \phi \lesssim 0, \end{cases} \quad (2.61)$$

where V_0 is the overall normalization, A is the slope of the potential at CMB/LSS scales and c parameterizes how the slope changes after the break at $\phi = 0$. We allow ϕ_c to be a free parameter, only requiring that it be before the break in the potential at $\phi = 0$. This freedom supposes that the field value at which inflation ends is not necessarily determined by the form of the potential in

Eq. (2.61). In order to choose ϕ_c , we place the break (i.e., $\phi = 0$) N_0 e -folds from ϕ_c . A natural choice for N_0 is 10, since we suppose that CMB/LSS scales constrain the inflaton potential from 10^4 Mpc to 1 Mpc. The normalization of the scalar power-spectrum then fixes the normalization V_0 of the potential through the expression,

$$V_0 = \frac{3P_s(k_c)}{128} \frac{A^2 m_{\text{Pl}}^2}{(1 + A\phi_c)^3} m_{\text{Pl}}^4. \quad (2.62)$$

We then integrate Eq. (2.20), assuming the transition at $\phi = 0$ has a negligible contribution, between ϕ_c and ϕ_g with $N = 35$ in order to find ϕ_g . We require that inflation not end before we reach ϕ_g . For $V(\phi)$ as in Eq. (2.61), we find that inflation ends soon after the field reaches a value, $\phi_* = m_{\text{Pl}}/(4\sqrt{\pi}) - (cA)^{-1}$. This then places a constraint on the combination cA ,

$$cA < \frac{4\sqrt{\pi}}{m_{\text{Pl}}\sqrt{1 + 4(N_g - N_0)}}. \quad (2.63)$$

At CMB/LSS scales we find that $\eta(\phi_c) = 0$, and

$$\epsilon(\phi_c) = \frac{A^2 m_{\text{Pl}}^2}{4A^2 m_{\text{Pl}}^2 N_0 + 16\pi}. \quad (2.64)$$

From the above expression and Eqs. (2.12) and (2.16), we can see explicitly that n_s and r only depend on our choice of N_0 and A . At BBO/DECIGO scales we find

$$\Omega_{\text{gw}} h^2 = 4A_{\text{gw}} P_s(k_c) A^2 m_{\text{Pl}}^2 \frac{\sqrt{A^2 c^2 m_{\text{Pl}}^2 (N_0 - N_g) + 4\pi}}{(A^2 m_{\text{Pl}}^2 N_0 + 4\pi)^{3/2}}, \quad (2.65)$$

where N_g is the number of e -foldings between ϕ_c and ϕ_g . In order for there to be N_g e -folds between ϕ_c and ϕ_g the slope of the potential cannot be too large, requiring

$$cA \leq \frac{2\sqrt{\pi}}{m_{\text{Pl}}\sqrt{N_g - N_0}}. \quad (2.66)$$

Comparing this to Eq. (2.63), we find that this constraint is *slightly* less restrictive. We can see that this amplitude depends not only on N_0 and A but also on c . Therefore, potentials that share approximately the same Taylor expansion at CMB/LSS scales, but different expansions at BBO/DECIGO scales, will produce overlapping observations in the (n_s, r) plane at CMB/LSS scales and different gravitational-wave amplitudes at BBO/DECIGO scales. With the constraint in Eq. (2.63), we find that as c increases towards its maximum value (for a fixed A), the amplitude of the IGWB changes by an order of magnitude. For example, for $n_s = 0.9$ and $r = 0.27$ we have $2.0 \times 10^{-17} \lesssim \Omega_{\text{gw}} h^2 \lesssim 2.0 \times 10^{-16}$; for $n_s = 0.99$ and $r = 3.16 \times 10^{-3}$ we have $4.3 \times 10^{-19} \lesssim \Omega_{\text{gw}} h^2 \lesssim 4.3 \times 10^{-18}$; and for $n_s = 1.0$ and $r = 3.18 \times 10^{-5}$ we have $4.3 \times 10^{-21} \lesssim \Omega_{\text{gw}} h^2 \lesssim 4.3 \times 10^{-20}$.

2.7 Discussion

In this chapter we have calculated the gravitational-wave amplitude at direct-detection scales for six classes of inflationary potentials with parameters consistent with current constraints from the CMB and LSS. The gravitational-wave amplitude $\Omega_{\text{gw}}h^2$ is proportional to the height $V(\phi_g)$ of the inflaton potential at the time that direct-detection comoving scales exit the horizon. Our current theoretical understanding does not fix $V(\phi_g)$; it is constrained to be $V^{1/4} \lesssim 3.4 \times 10^{16}$ GeV from the CMB, and it could conceivably be as low as $T \sim 1$ MeV without violating observational constraints. Moreover, detectability of the IGWB with BBO or DECIGO requires $V^{1/4} \gtrsim 10^{15}$ GeV, close to the upper allowed limit. It thus seems, a priori, that detectable models occupy a small region of parameter space.

That said, however, there are indeed constraints to inflationary models that come from the CMB and large-scale structure, notably constraints to the density-perturbation amplitude and spectral index. The results for the six classes of inflationary models indicate that when we go through the exercise of writing down simple functional forms for the inflationary potentials and imposing current constraints, there are large regions of parameter space that lead to directly detectable IGWB amplitudes. In particular, for the symmetry-breaking potential, which looks perhaps like the type of Higgs potentials we might associate with grand unification, current constraints lead to a directly detectable IGWB amplitude.

The promise of detectability traces back to the fact that $\Omega_{\text{GW}}h^2 \propto V \propto (V')^{4/3}$, the last proportionality tracing back to Eqs. (2.8) and (2.9) for fixed density-perturbation amplitude P_s . Thus, if the potential is extremely flat, $V' \rightarrow 0$, then the IGWB will be tiny. However, if the potential takes a form in which $V' \sim V/\phi$, which seems theoretically natural, then the required density-perturbation amplitude is achieved with $V \sim 10^{(15-16)}$ GeV, the range that produces an accessible IGWB amplitude.

There is of course still plenty of room for inflation to be correct and for the IGWB amplitude to be well below the BBO or DECIGO threshold. For example, in power-law inflation and chaotic inflation, the IGWB amplitude becomes small when $n_s \rightarrow 1$; i.e., when scale invariance is achieved which, in these models corresponds to small V' . On the other hand, a value $n_s \rightarrow 1$ does not, more generally, imply a small IGWB amplitude. For example, in hybrid inflation one can have $n_s = 1$ if $y_c^2 = 1/2$ [see Eq. (2.43)], and for $\mu \gtrsim 1.8 m_{\text{Pl}}$, the potential can reach values at CMB/LSS scales of $V \sim 3 \times 10^{16}$ GeV, which even after the decrease to BBO/DECIGO scales remains within reach of detection, as shown in the figures.

There may of course be alternatives to inflation, such as cyclic models [156] or the pre big-bang model [157–162], that have completely different IGWB spectra. Although the cyclic model predicts a blue tensor spectrum, which might improve detectability at small scales, BBN constrains the

amplitude of the gravitational-wave amplitude to be orders of magnitude below the BBO/DECIGO sensitivities [19].

Recent measurements of the scalar spectral index indicate that it may be less than unity. This fact has caused a great deal of excitement given that it is believed that having $n_s < 1$ implies a significant amplitude for the gravitational-wave background produced by inflation. In this chapter we have investigated this claim by analyzing predictions derived from six classes of models of inflation. We have also extended the analysis to include not only the amplitude of the IGWB accessible to observations of the polarization of the CMB but also the IGWB accessible to direct observation.

Our results can be divided into two different classes of inflationary potentials. These classes are characterized by the curvature of the potential evaluated at the field value corresponding to CMB observations. The curvature of the potential at a given field value is related to the sign of the slow-roll parameter η . Models that have $\eta < 0$ (the inflaton is ‘falling off of a cliff’) have decreasing r as n_s deviates further from unity. Models that have $\eta > 0$ (the inflaton is ‘rolling down a bowl’) have increasing r as n_s deviates further from unity. This classification is directly related to the classification scheme presented in Ref. [163] in which inflationary models are said to be ‘large field’, ‘small field’, or ‘hybrid’. In their classification scheme the sign of η as well as its relation to ϵ is used to divide inflationary models. However, in this chapter we have emphasized how just the *sign* of η indicates how various constraints to n_s affect the model’s prediction for the IGWB.

In attempting to set a lower limit to the expected IGWB accessible to direct observation these two different classes of models split up accordingly: with $\eta < 0$ an increase in the lower limit to the amplitude of the IGWB is obtained with an improvement in the lower limit to n_s ; with $\eta > 0$ an increase in the lower limit benefits from an improvement in the upper limit to n_s .

In terms of the possibility of observing the IGWB directly, quoted sensitivities for a second generation BBO mission for a year long integration sets the lower limit to a detectible IGWB at $\Omega_{\text{gw}}h^2 \gtrsim 10^{-17}$. As can be seen in the figures, current constraints to n_s for the six inflationary models considered here imply that a large region in parameter space for all six models will produce IGWB amplitudes within reach of BBO. However, except for Higgs and PNGB inflation, there are regions of parameter space for which the IGWB amplitude can be arbitrarily small. As the errors on n_s shrink on both sides then, depending on the central value for n_s , each of the six models analyzed here may eventually predict a *minimum* IGWB amplitude. In particular, the Planck satellite is expected to attain 0.5% in a determination of n_s at a fiducial value $n_s = 0.957$ [97]. This would then translate into a lower bound, $r \gtrsim 0.0046$, for Coleman-Weinberg inflation which translates into $\Omega_{\text{gw}}h^2 \gtrsim 10^{-17}$ for direct observation.

Barring a detection of the IGWB in the CMB our discussion shows that even an upper limit to r and a precise measurement of n_s tells us useful information on the curvature of the inflaton

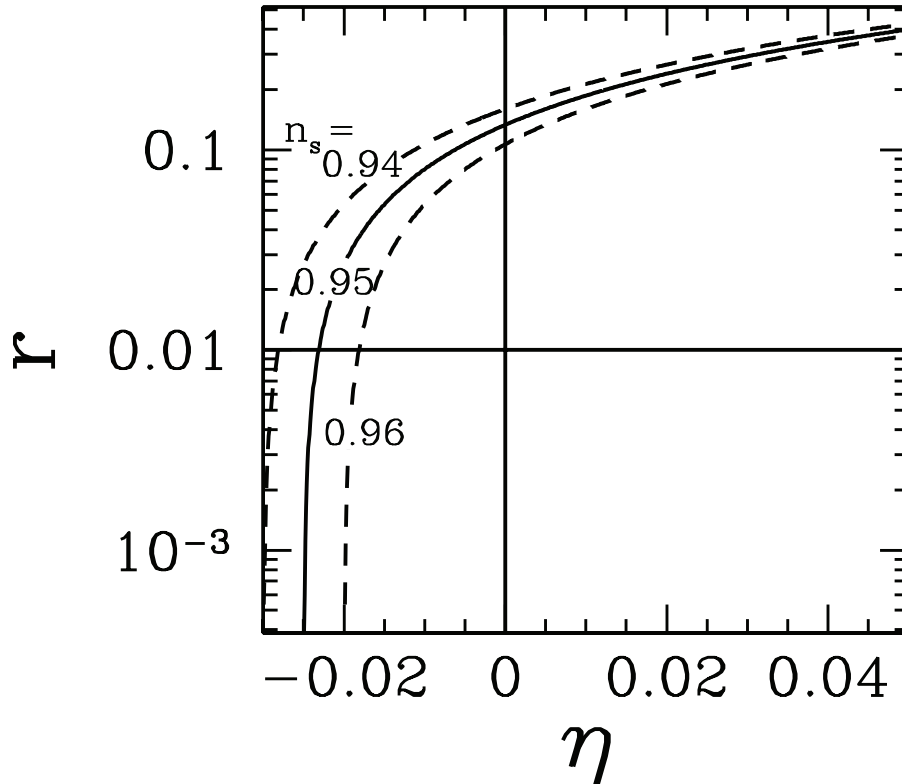


Figure 2.11: An upper limit to r along with a measurement of n_s will tell us information on the curvature of the inflaton potential. If we find that $r \lesssim 0.1$ and $0.94 \lesssim n_s \lesssim 0.96$ then we may conclude, within the context of single-field slow-roll inflation, that $\eta < 0$ which implies $V'' < 0$. Although qualitative, this conclusion would have far-reaching implications for inflationary model building.

potential. From the Eqs. (2.29) and (2.30) we can write

$$r = \frac{8}{3}(1 - n_s + 2\eta). \quad (2.67)$$

In Fig. 7 we show curves in the (η, r) plane for $0.94 \leq n_s \leq 0.96$. From that figure, we can see that for n_s in this range an upper limit of $r \lesssim 0.1$ implies that the potential has a *negative* curvature (this trend can also be seen in Fig. 9 in Ref. [125]). This qualitative conclusion would have important implications for inflationary model building.

Our conclusion is that direct detection of the IGWB is unlikely without detection with the CMB polarization. Still, direct detection could be extraordinarily valuable even if the IGWB is detected first in the CMB. Direct detection would provide yet another cross-check that the curl component in the CMB polarization is due to gravitational waves, as opposed to some other mechanism (e.g., vector modes, cosmic shear, or foregrounds). Since it occurs on such vastly different distance scales, direct detection can verify that it is a nearly scale invariant spectrum of gravitational waves, as predicted by inflation, as opposed to some other phenomenon that might only produce large-wavelength

gravitational waves. It would provide evidence for the continuation of inflation to distance scales well beyond those implied by the smoothness of the Universe suggested by the successes of BBN. The large lever arm provides an opportunity to discriminate between inflationary models that produce the same CMB/LSS observables. Even within the context of a given inflationary potential, the large lever arm associated with direct detection may allow a measurement of inflationary parameters that may be more precise than those accessible with the CMB/LSS alone. For example, an uncertainty of 10% in ϵ from the CMB/LSS translates to a $\sim (10^{15})^{0.2} \sim 1000$ uncertainty in the BBO/DECIGO amplitude. Thus, a detection *alone*, with no better than an order-unity amplitude uncertainty, corresponds to a measurement of ϵ to roughly 0.02, probably better than is accessible with the CMB/LSS alone. Finally, the deci-Hertz IGWB amplitude counts the number of relativistic degrees of freedom at temperatures a bit above the electroweak symmetry-breaking scale, and may thus be used to probe for new degrees of freedom associated with supersymmetry or some other new physics at the electroweak scale [164]. The direct search for inflationary gravitational waves may thus be warranted.

Acknowledgments

We thank W. Kinney, D. Baumann, and D. Grin for useful discussions. We thank E. S. Phinney and A. A. Starobinsky for pointing out the erroneous factor of 4 in our previous expression for the gravitational-wave transfer function. This work was supported at Caltech by DoE DE-FG03-92-ER40701, NASA NNG05GF69G, and the Gordon and Betty Moore Foundation, and at UC Irvine by NSF CAREER AST-0645427. TLS acknowledges the support of a NSF Graduate Fellowship.

Chapter 3

Deciphering inflation with gravitational waves: cosmic microwave background polarization vs. direct detection with laser interferometers¹

3.1 Introduction

Recent high precision measurements of the cosmic microwave background (CMB) anisotropy power spectrum [81, 94, 125, 149] have confirmed inflation [2–4] as the dominant paradigm to explain the origin of primordial fluctuations with a nearly scale invariant spectrum. In addition to density perturbations, inflationary models predict a stochastic background of gravitational waves [9, 10] with the amplitude of the gravitational wave background given by the height of the inflaton potential when relevant modes exit the horizon.

Inflationary gravitational waves with wavelengths comparable to the horizon size are now being sought via ground-based CMB polarization experiments [44, 46], and eventually with a dedicated satellite generally named CMBPol [128]. In addition to the CMB effort, concept studies are now underway to investigate the possibility of directly detecting the relic background with a laser interferometer in space (Big Bang Observer [82]; for the DECIGO proposal in Japan, see Ref. [83]). The direct-detection technique will be sensitive to modes with wavelengths roughly an arm length of the interferometer. Based on the expected foreground confusion and technological improvements, current concept studies aim for the frequency regime between 0.1 Hz to a few Hz. Since physical scales

¹The material presented in this chapter was first published in, *Deciphering inflation with gravitational waves: Cosmic microwave background polarization vs. direct detection with laser interferometers*, Tristan L. Smith, Hiranya V. Peiris, and Asantha Cooray, Phys. Rev. **D73**, 123503 (2006). Reproduced here with permission, copyright (2006) by the American Physical Society.

probed by the CMB and laser interferometers differ by ~ 17 orders of magnitude in wavelength, the large lever arm produced by combining the two techniques allows the inflaton potential to be pinned down better than any single method [87, 88, 133, 165].

Here, we consider two separate studies on inflation using the combined information from CMB and direct detection experiments. First, based on a Monte Carlo description of the inflationary dynamics, we study the relative abilities of the CMB and a direct detection method to probe the inflaton potential in detail by making no assumptions on the power-law behavior [88] or on a model shape for the potential [133]. We first consider inflationary models allowed by CMB data, making use of constraints on both the scalar and tensor spectrum, and address if laser interferometers can further improve the identification of potentials. For the CMB, we make use of the expected level of uncertainty with Planck², a possible detection with CMBPol, and the foreground-limit from CMBPol. For details on the potential detectability of the tensor amplitude with CMB polarization observations, we refer the reader to Ref. [166]. For the direct detection experiments, we make use of predictions related to BBO and DECIGO [130, 131]. Since our goal is to see how the simplest models of inflation can be constrained, our comparisons are for a general single-field potential in the slow-roll regime.

In the second part of the chapter, we drop all assumptions related to single-field slow-roll inflation and study how well the CMB and the direct detection experiments can be combined to constrain the single-field consistency relation between tensor spectral index and the ratio of tensor-to-scalar amplitudes for single-field inflationary models. Previous work on this possibility is found in Ref. [167] where the test was limited to simply the information on the tensor spectral index from CMB data alone. We show the extent to which a CMB-only analysis can be improved by adding direct-detection information as the latter allows a better determination of the tensor spectral index.

3.2 Monte Carlo calculational method

To calculate observable spectra, we make use of a Monte Carlo technique to formulate the inflationary dynamics through an infinite hierarchy of flow equations involving the generalized ‘Hubble Slow Roll’ (HSR) parameters [168–171]. We link the Hubble parameter directly to the field ϕ instead of time, $H \equiv H(\phi)$, under the assumption that ϕ is monotonic in time. The equation of motion for the background is

$$[H'(\phi)]^2 - \frac{12\pi}{m_{\text{Pl}}^2} H^2(\phi) = -\frac{32\pi^2}{m_{\text{Pl}}^4} V(\phi), \quad (3.1)$$

²[http://www.rssd.esa.int/SA/PLANCK/docs/Bluebook-ESA-SCI\(2005\)1.pdf](http://www.rssd.esa.int/SA/PLANCK/docs/Bluebook-ESA-SCI(2005)1.pdf)

where the inflaton field evolves as $\dot{\phi} = -m_{\text{Pl}}^2 H'(\phi)/4\pi$. Here, an overdot corresponds to the time derivative and a prime denotes the derivative with respect to ϕ . The advantage of this formulation is that one can study the generic behavior of slow-roll single-field inflation without assuming a particular shape for the potential, except for the assumption of a single field. In terms of the HSR parameters ${}^\ell\lambda_H$, the dynamics of inflation is described through:

$$\epsilon(\phi) \equiv \frac{m_{\text{Pl}}^2}{4\pi} \left[\frac{H'(\phi)}{H(\phi)} \right]^2; \quad (3.2)$$

$${}^\ell\lambda_H \equiv \left(\frac{m_{\text{Pl}}^2}{4\pi} \right)^\ell \frac{(H')^{\ell-1} d^{(\ell+1)}H}{H^\ell d\phi^{(\ell+1)}}; \quad \ell \geq 1. \quad (3.3)$$

Substituting Eq. (3.3) in Eq. (3.1) gives the inflaton potential

$$V(\phi) = \left(\frac{3m_{\text{Pl}}^2 H^2(\phi)}{8\pi} \right) \left[1 - \frac{1}{3}\epsilon(\phi) \right]. \quad (3.4)$$

The trajectories of the flow parameters are now governed by a set of coupled first-order differential equations. In practice, one has to truncate the infinite hierarchy at some finite order; in this chapter we retain terms up to 10th order. Truncating the hierarchy of flow parameters at the term ${}^M\lambda_H$ means that ${}^{M+1}\lambda_H = 0$ at all times as well. From Eq. 3.3, it also follows that $d^{(M+2)}H/d\phi^{(M+2)} = 0$ at all times. This simply describes a polynomial of order $M + 1$ in $H(\phi)$ [172] with

$$H(\phi) = H_0 \left[1 + A_1 \left(\frac{\phi}{m_{\text{Pl}}} \right) + \dots + A_{M+1} \left(\frac{\phi}{m_{\text{Pl}}} \right)^{M+1} \right]. \quad (3.5)$$

Further, from the definition of $\epsilon(\phi)$,

$$\epsilon(\phi) = \frac{m_{\text{Pl}}^2}{4\pi} \left[\frac{(A_1/m_{\text{Pl}}) + \dots + (M+1)(A_{M+1}/m_{\text{Pl}})(\phi/m_{\text{Pl}})^M}{1 + A_1(\phi/m_{\text{Pl}}) + \dots + A_{M+1}(\phi/m_{\text{Pl}})^{M+1}} \right]^2,$$

when the coefficients A_i , with $i > 1$, are written in terms of the initial values of the HSR parameters as

$$A_{\ell+1} = \frac{(4\pi)^\ell {}^\ell\lambda_{H,0}}{(\ell+1)! A_1^{\ell-1}}, \quad (3.6)$$

where $A_1 = \sqrt{4\pi\epsilon_0}$ specifies the direction the field is rolling. These slow-roll parameters require a prior assumption on the ranges of values taken. In the absence of any a priori theoretical knowledge, one can assume flat priors with the requirement that the potential satisfies the slow-roll condition; the latter is simply a statement about the smoothness of the potential. Since we are not attempting to make any statements about the measure of inflationary trajectories, but simply use the method as a Monte Carlo generator for potentials satisfying the slow roll conditions, such an assumption is

justified. This work does not depend on the density of potentials as a function of tensor-to-scalar ratio, which is determined by the measure on the initial conditions.

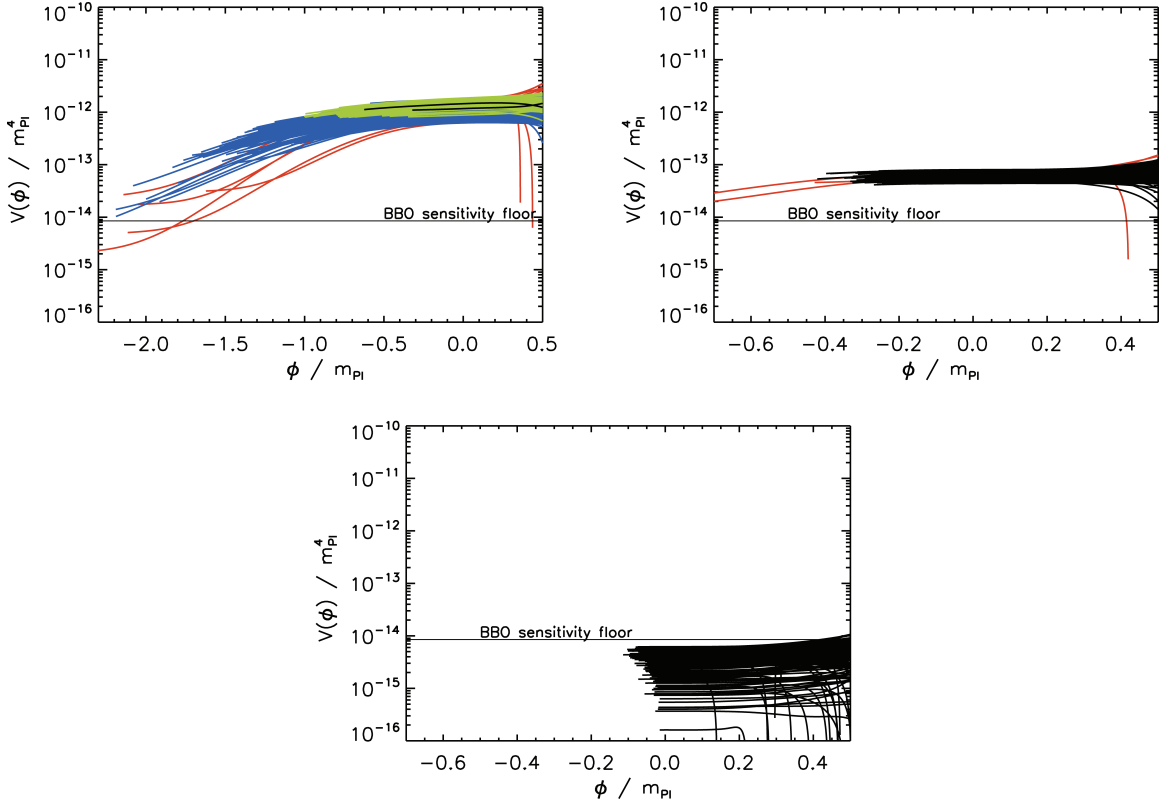


Figure 3.1: The set of potentials satisfying $0.9 < n_s < 1.0$ from the Monte Carlo flow simulations: *Upper Left*: constraints from Planck with $r = 0.02 \pm 0.01$, $dn_s/d \ln k = 0.0 \pm 0.01$, BBO-standard, BBO-grand (factor 10 more sensitive than BBO-standard) *Upper Right*: constraints from CMBPol with optimistic foregrounds [166]: $r = 0.001 \pm 0.0003$, $dn_s/d \ln k = 0.0 \pm 0.005$, BBO-standard, BBO-grand *Lower Center*: the sensitivity limit due to foregrounds for CMBPol with $r < 10^{-4}$ and DECIGO (factor 400 more sensitive than BBO-standard). *Color coding*: red and blue denote the CMB experiment without and with the $dn_s/d \ln k$ constraint, respectively. Green: BBO-standard. Black: BBO-grand (*Upper Left*, *Upper Right*) and DECIGO (*Lower Center*). The direct detection constraints are applied to the tensor amplitude and tilt at 1 Hz, following the procedure described in the text. If a particular color does not appear in a plot, it has been overwritten by the next tightest constraint, and the latter is therefore *not* helpful in constraining the potential. The meaning of the color coding is further clarified in the text. Here $\phi = 0$ corresponds to CMB scales while curves end at $\phi < 0$ corresponding to a frequency of 1 Hz probed by direct detection methods.

Without loss of generality, we can pick some fiducial physical scale that corresponds to ϕ_c , which we take to be at $k_{\text{CMB}} = 0.002 \text{ Mpc}^{-1}$. Then, with the above convention, $\phi > \phi_{\text{CMB}}$ corresponds to scales larger than k_{CMB} (i.e., going further back in time), and $\phi < \phi_{\text{CMB}}$ corresponds to smaller scales. The physical wavenumber is associated with a value of ϕ through

$$\frac{d\phi}{d \ln k} = -\frac{m_{\text{Pl}}}{2\sqrt{\pi}} \frac{\sqrt{\epsilon}}{1 - \epsilon}, \quad (3.7)$$

while the number of e-folds before the end of inflation, N , comes from $d\phi/dN = m_{\text{Pl}}\sqrt{\epsilon}/2\sqrt{\pi}$, with

the convention that N increases as one goes further back in time. Here, we require that each potential generated by the Monte Carlo flows provide at least $N = 55$ e-folds of inflation. For potentials where inflation ends through the breakdown of slow-roll, the CMB observables are calculated at 55 e-folds before the end of inflation; for potentials corresponding to the hybrid case, the CMB observables are arbitrarily calculated at the 600th e-fold, assuming inflation ends at 655 e-folds through an orthogonal mechanism.

The standard observables are given in terms of the flow parameters to second order in the slow roll [98, 99]:

$$n_s = 1 + 2\eta - 4\epsilon - 2(1 + C)\epsilon^2 - \frac{(3 - 5C)}{2}\epsilon\eta + \frac{(3 - C)}{2}\xi \quad (3.8)$$

$$r = 16\epsilon [1 + 2C(\epsilon - \eta)] \quad (3.9)$$

$$n_t = -2\epsilon - (3 + C)\epsilon^2 + (1 + C)\epsilon\eta, \quad (3.10)$$

where n_s , r , and n_t are the tilt of the scalar spectrum, tensor-to-scalar ratio, and the tilt of the tensor spectrum, respectively. Additionally, we consider the running of the scalar tilt with

$$\begin{aligned} \frac{dn_s}{d \ln k} = & -\frac{1}{1 - \epsilon} \left\{ 2 \frac{d\eta}{dN} - [4 + 4(1 + C)\epsilon] \frac{d\epsilon}{dN} \right. \\ & \left. - \frac{(3 - 5C)}{2} \left(\epsilon \frac{d\eta}{dN} + \eta \frac{d\epsilon}{dN} \right) + \frac{(3 - C)}{2} \frac{d\xi}{dN} \right\}, \end{aligned} \quad (3.11)$$

where $d\epsilon/dN = 2\epsilon(\eta - \epsilon)$, $d\eta/dN = -\epsilon\eta + \xi$, and $d\xi/dN = \xi(\eta - 2\epsilon) + {}^3\lambda_H$. Here and above, $C = 4(\ln 2 + \gamma) - 5$ and $\gamma = 0.5772$ is the Euler-Mascheroni Constant, $\eta = {}^1\lambda_H$, and $\xi = {}^2\lambda_H$.

For direct-detection experiments, we take a fiducial frequency of $f = 1$ Hz with $k_{\text{dir}} = 6.47 \times 10^{14}$ Mpc $^{-1}$ for observations. With $\ln(k_{\text{dir}}/k_{\text{CMB}}) = 40.3$ the large lever arm is expected to improve constraints on the inflationary model [133]. The direct detection observables are calculated from the potentials by finding the ϕ corresponding to $\ln(k_{\text{dir}}/k_{\text{CMB}}) = 40.3$. In these experiments, at 1 Hz, the signal-to-noise ratio for a detection of the gravitational wave background is $\text{SNR} = X(\Omega_{\text{gw}}/10^{-18})$, where X is ~ 0.25 , 2.5, and 100 for concept study designs involving a standard BBO, an optimistic version of BBO, and DECIGO. The last two possibilities improve sensitivities through multiple detector correlations. The uncertainty of the tensor spectral index at 1 Hz is taken to be $\sigma_{n_T} \sim 6/\text{SNR}$ [130, 131].

Fig. 3.1 shows a set of potentials from the Monte Carlo flow simulations that satisfy levels of tensor and scalar modes reachable by Planck, a CMBPol-style polarization satellite designed to probe primordial gravity waves [166], and the foreground limit of this satellite. We show all potentials with $0.9 < n_s < 1.0$, though in practice the CMB measurements will also yield strong constraints on this parameter. In Fig. 1 we also show the improvement in constraints on the potential using

information from direct detection experiments with uncertainties in the tensor amplitude and tilt calculated following results of the analysis in Ref. [130, 131].

In Fig. 1, the potentials generated by the Monte Carlo process are color-coded in the following way. First, all potentials with $0.9 < n_s < 1.0$ which are *not* ruled out by applying the constraints on r from the CMB experiment are shown in red. Then the potentials which are *not* ruled out by further applying the $dn_s/d\ln k$ constraint from the CMB experiment are over-plotted in blue. Next, the potentials which are *not* eliminated by adding the constraint from BBO-standard on the tensor amplitude and tilt to the CMB experiment are over-plotted in green. Finally, the potentials which are *not* eliminated by adding the constraints from either BBO-grand (left, centre) or DECIGO (right) to the CMB experiment are over-plotted in black. At each stage, the elimination of a larger fraction of potentials indicates the usefulness of the extra constraints. If a particular color does not appear in a given panel, it means that all potentials have been overwritten by the next tightest constraint, and therefore the next tightest constraint does not aid in constraining the potential. Therefore, while the combination of Planck and BBO-standard, and especially BBO-grand, leads to an improvement in constraints on the potential, these direct detection experiments do not compete at all with CMBPol either in the case of a detection at $r = 0.001$ or the limit of $r < 10^{-4}$ at CMB scales. A more sensitive experiment such as DECIGO probing $\Omega_{\text{gw}} h^2 > 10^{-20}$ competes well with CMBPol if $r \lesssim 0.01$ and is both desirable and useful to understand inflation.

3.3 A fundamental test of slow-roll inflation

To further understand the usefulness of a direct-detection experiment, we also study how well the inflationary single-field consistency condition can be tested [167], as any departure can capture important physics [173]. We define $\mathcal{R} \equiv -r/8n_t$ so that $\mathcal{R} = 1$ corresponds to the consistency relation. The uncertainty in determining \mathcal{R} (given $\mathcal{R} = 1$ as the fiducial value) can be written in terms of uncertainty in measurements of r and n_t assuming these are uncorrelated,

$$\sigma_{\mathcal{R}} = [\sigma_r^2 + 64\sigma_{n_t}^2]^{1/2} r^{-1}. \quad (3.12)$$

A 10% determination of \mathcal{R} with the expected value of unity requires measuring n_t with an uncertainty of $\sigma_{n_t} \sim 0.0125r$. Using tables of Ref. [166], CMBPol with a 10% foreground contamination and $r = 0.01$ gives $\mathcal{R} = 1.0 \pm 80$. The obstacle is the inability of CMB polarization observations to measure n_t precisely, since polarization anisotropies probe a limited range in the underlying tensor spectrum modes, and the range probed is also contaminated by cosmic shear [120, 121].

When combining with a direct-detection experiment, however, the situation improves significantly. We calculate the 1σ error expected in \mathcal{R} at CMB scales based on a determination of n_t from

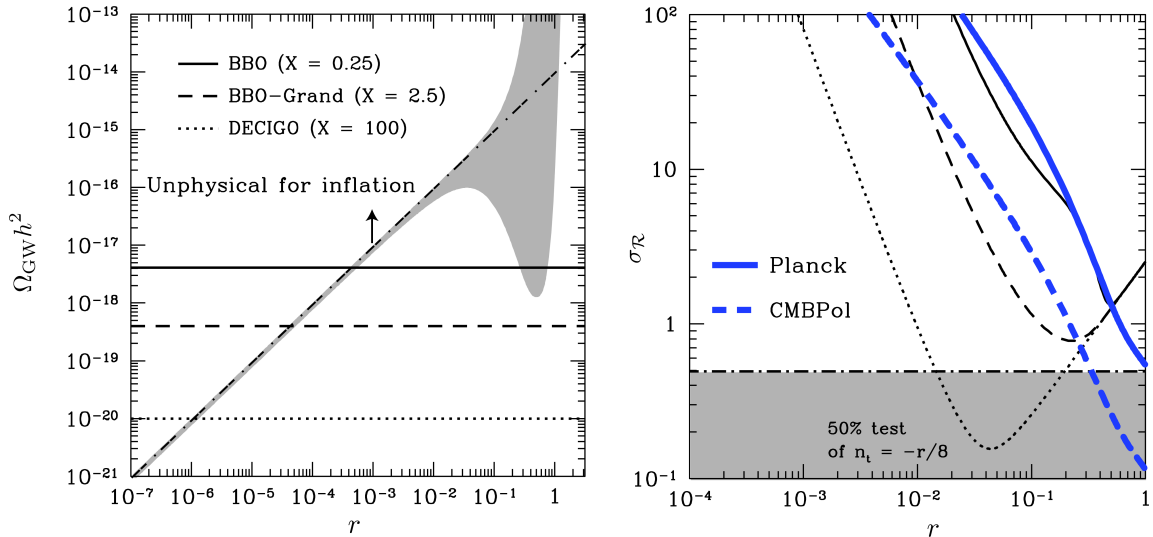


Figure 3.2: *Left*: The mapping between tensor-to-scalar ratio r at CMB scales and $\Omega_{\text{gw}}h^2$ at 1 Hz for a direct detection. The gray shaded region shows the uncertainty implied with $n_s = 0.95 \pm 0.1$ [107] by keeping terms up to second order (running of the tensor spectral index) in the slow-roll power-law expansion. We include the line ‘Unphysical for inflation’ to indicate the region above which $n_t > 0$. The three horizontal curves are the 2σ detection amplitudes for BBO-standard, BBO-grand, and DECIGO in solid, dashed, and dotted lines respectively. In these three experiments, at 1 Hz, the signal-to-noise ratio for detecting the gravitational wave background is $\text{SNR} = X(\Omega_{\text{gw}}/10^{-18})$, with values for X shown in the panel. *Right*: The 1σ uncertainty in the single-field consistency relation $\mathcal{R} \equiv -r/8n_t$. The thin lines follow laser interferometers in the right panel, showing the error expected by combining direct detection measurements of n_t with CMBPol measurements of the tensor-to-scalar ratio, r . The two thick lines indicate errors in \mathcal{R} when n_t is determined from CMB alone. The thick solid curve corresponds to the expected accuracy of ESA’s Planck satellite, the thick dashed curve corresponds to CMBPol. The shaded region indicates a 50% determination of the consistency relation ($\mathcal{R} = 1.0 \pm 0.5$). For direct-detection observations, sensitivity is degraded at large r because of an increase in the uncertainty of the importance of the running of the tensor spectral index from direct detection scales to CMB scales; at small r , the accuracy with which \mathcal{R} can be determined is dominated by the error in measuring n_t with CMB [167] and laser interferometers [130, 131], where the latter is $\sigma_{n_t} \propto 1/r$.

direct-detection scales and a determination of r by CMBPol. In Ref. [130, 131] it was shown that a laser interferometer (whose sensitivity peaks at ~ 1 Hz) would be able to determine the spectral tilt of a gravitational wave background, with an amplitude Ω_{gw} , to an accuracy of

$$\sigma_{n_t} = \frac{6 \times 10^{-18}}{X\Omega_{\text{gw}}h^2}, \quad (3.13)$$

where the various values of X corresponding BBO-standard, BBO-grand, and DECIGO are shown in Fig. 3.2 and h is the Hubble parameter today in units of $100 \text{ km s}^{-1} \text{ Mpc}^{-1}$.

While we take our fiducial model to be single-field slow-roll inflation (i.e., $\mathcal{R} = 1.0$), we make no assumptions about single-field slow-roll inflation when we relate $\Omega_{\text{gw}}h^2$ to the tensor-to-scalar ratio.

First we relate $\Omega_{\text{gw}}h^2$ to the primordial spectrum as in Ref. [133],

$$\Omega_{\text{gw}}(k)h^2 = A_{\text{gw}}P_t(k), \quad (3.14)$$

where $P_t(k)$ is the primordial power spectrum of inflationary gravitational waves, and $A_{\text{gw}} = 2.74 \times 10^{-6}$.³ The factor, A_{gw} , takes into account how the gravitational waves have evolved after re-entering the horizon. The primordial inflationary gravitational wave power spectrum can be approximated as a power law with a running spectral index,

$$P_t(k) \approx P_t(k_0) \left(\frac{k}{k_0} \right)^{n_t + \frac{1}{2}\alpha_t \ln(k/k_0)}. \quad (3.15)$$

Using the expressions in Eqs. (3.8–3.10) to first order in the slow-roll parameters along with the expression for the running of the tensor spectral index, α_t ,

$$\alpha_t(k) \simeq 4\epsilon\eta - 8\epsilon^2, \quad (3.16)$$

we are able to express n_t and α_t in terms of r and n_s ,

$$P_t(k) \approx rP_s(k_0) \left(\frac{k}{k_0} \right)^{-\frac{r}{8}[1 - ((n_s - 1) + \frac{r}{8}) \ln(k/k_0)]}, \quad (3.17)$$

where $P_s(k_0)$ is the amplitude of the scalar perturbations at some pivot wavenumber k_0 and all of the spectral quantities are also measured at this wavenumber. For this analysis we take $n_s = 0.95$ and $P_s(k_0) = 2.21 \times 10^{-9}$ at $k = 0.002 \text{ Mpc}^{-1}$ [81, 94, 125, 149].

Since we must connect a measurement of n_t at BBO scales to the n_t at CMB scales in order to determine \mathcal{R} , we must posit some scale-dependent relation between these two measurements. We emphasize that we *cannot* use the flow equation approach of the previous section here; those equations assume single-field inflation and therefore implicitly embody the consistency relation, whereas here we are attempting to *test* the single-field assumption. Instead, we assume that the gravitational wave spectrum is close to scale invariant with an unknown, but higher order, running so that $n_t^{\text{BBO}} \approx n_t^{\text{CMB}}$. Since the running of n_t is unlikely to be determined by either the CMB or direct detection we include an additional uncertainty due to the unknown running, $\sim (1/2) \ln(k_{\text{dir}}/k_{\text{CMB}})n_t^2$, as in Eq. (3.16). This leads to a decrease in the sensitivity of direct-detection measurements of \mathcal{R}

³The value of A_{gw} used in this chapter differs by a factor of four from the value used in the previous Chapter. As derived in Appendix A the value used in the previous Chapter is correct. However, this difference does not have a significant affect on the conclusions.

at ‘large’ values of r . In particular, the error on our determination of n_t is given by the expression,

$$\sigma_{n_t}(r) = \left\{ \left[\frac{6 \times 10^{-18}}{X A_{\text{gw}} P_t(k)} \right]^2 + \left[\frac{1}{2} \ln \left(\frac{k_{\text{dir}}}{k_{\text{CMB}}} \right) \left(\frac{r}{8} \right)^2 \right]^2 \right\}^{1/2}. \quad (3.18)$$

Our results are summarized in Fig. 3.2. The left panel shows the mapping between tensor-to-scalar ratio r at CMB scales and $\Omega_{\text{gw}} h^2$ at 1 Hz for a direct detection. After this work appeared in preprint, another study [174] was submitted, where a criticism was made of a region on this panel, describing it as unphysical. In fact this region is *only* unphysical if inflation is being assumed as the generating mechanism for tensor modes, and one cannot do that if one is attempting, as we are, to test that assumption in the first place. Therefore we continue to show this region, while indicating that it is unphysical under the assumption of inflation. As shown in the right panel, BBO improves relative to CMBPol alone by a factor of \sim a few in the uncertainty of \mathcal{R} if $r \sim 0.1$. This is unlikely to be useful given that current observations already limit r to be below 0.3. A determination of \mathcal{R} as 1.0 ± 0.5 is achievable when $10^{-1} \gtrsim r \gtrsim 10^{-2}$ with DECIGO, while if $r \sim 10^{-4}$, it is unlikely that even DECIGO would provide a determination of \mathcal{R} to a reasonable accuracy. In general, either version of BBO is unlikely to be competitive with CMBPol, and the sensitivity level of DECIGO must be considered as the experimental target goal to pursue a direct detection at ~ 1 Hz. Further limits on r from the CMB will tighten this conclusion and could only lead to a further increase in required sensitivity unless a detection is made with the CMB at $r > 0.01$. Our conclusions are independent of the choice of a fiducial frequency between 0.1 Hz and few Hz, but could be subjected to the highly uncertain impact of foregrounds at direct detection frequencies [130, 131]. Additional physics between the CMB and 1 Hz scales [175] only strengthen our conclusions on the required sensitivity for a laser interferometer as these exotic models generally lower the tensor amplitude further.

3.4 Summary

To summarize, we have considered the relative strengths of CMB polarization observations and direct-detection laser interferometers in constraining the inflaton potential. For single-field slow-roll inflation models, without relying on any particular shape for the potential, we find that direct detection experiments with sensitivities around BBO can improve constraints on inflationary models relative to Planck. However, when combined with CMBPol, these direct detection sensitivities are unlikely to be competitive. While we have not considered exotic models, and a case can certainly be made for a low-sensitivity direct-detection experiment based on non-standard descriptions for inflation including models of bubble nucleation [16, 17, 176, 177] and pre-Big Bang descriptions [178], it is also important to understand first how these experiments test the simplest forms of

inflation.

In this context, we also discuss a determination of the single-field slow-roll consistency relation, which is a way to establish an underlying model within the inflationary paradigm to probe physics at the earliest times of the Universe. In general, we find an experiment like DECIGO, with sensitivity level of $\Omega_{\text{gw}}h^2 > 10^{-20}$ to be the preferred option; however, it is unlikely that the consistency relation will be determined to the accuracy needed to see loop corrections [173], unless the tensor-to-scalar ratio is greater than 0.05 and loop corrections are at the level of 10% or more.

Acknowledgments

After completing this work, we became aware of the preprint [174] on the same topic using an approach similar to ours; we thank George Efstathiou for useful discussions on their calculation. We thank Richard Easther and Naoki Seto for useful discussions. TLS acknowledges support from the NSF. HVP is supported by NASA through Hubble Fellowship grant #HF-01177.01-A awarded by the Space Telescope Science Institute. AC is supported by the DOE at UC Irvine.

Chapter 4

A new cosmic microwave background constraint to primordial gravitational waves¹

4.1 Introduction

There are many conjectured sources of a primordial cosmological gravitational-wave background (CGWB), including inflation, pre-big bang theories, phase transitions, and the ekpyrotic model [1]. Such backgrounds are among the targets of the Laser Interferometric Gravitational-Wave Observatory (LIGO), and they will be sought with future observatories, such as NASA’s Laser Interferometer Space Antenna (LISA), the Big Bang Observer (BBO), and Japan’s Deci-Hertz Interferometer Gravitational-Wave Observatory (DECIGO).

The CGWB amplitude is constrained at the lowest observable frequencies, $\sim 10^{-17} - 10^{-16}$ Hz (corresponding to wavelengths comparable to the cosmological horizon today), by large-angle fluctuations in the cosmic microwave background (CMB) temperature [10–13]. Prospects for probing lower CGWB amplitudes at these frequencies come from future measurements of the polarization of the CMB [44, 46]. Apart from a window around $10^{-9} - 10^{-8}$ Hz, where the CGWB is constrained by pulsar timing [62, 63], the strongest constraint to the CGWB amplitude for frequencies greater than $\sim 10^{-10}$ Hz comes from big-bang nucleosynthesis (BBN) [54]. The lower limit to the frequency range is determined by the comoving horizon size at the time of BBN. Primordial gravitational waves of shorter wavelengths, or larger frequencies, contribute to the radiation density at the time of BBN, thereby increasing the expansion rate and thus the light-element abundances. Measurements of light-element abundances limit the number of additional relativistic species at BBN to the equivalent of 1.4 neutrino degrees of freedom [179], which translates to a limit to a current CGWB energy density $\Omega_{\text{gw}} h^2 \lesssim 7.8 \times 10^{-6}$.

¹The material presented in this chapter, except for Sections 4.4 and 4.5, is previously unpublished work by the author.

The frequency range $\sim 10^{-16} - 10^{-10}$ Hz remains largely unconstrained. An upper limit $\Omega_{\text{gw}} h^2 \lesssim 0.1$ can be placed in this frequency range from QSO astrometry [57, 58]. It has been proposed that future measurements of anisotropy in the global rate of change of observed redshifts might someday get down to $\Omega_{\text{gw}} h^2 \sim 10^{-5}$ [56].

Here we note that recent measurements of the angular power spectrum of the cosmic microwave background (CMB) that constrain the nonrelativistic-matter density $\Omega_m h^2$ to roughly 10% [73–81] are, to a first approximation, constraints to the radiation energy density at the time of CMB decoupling; the constraint corresponds to a limit of a few extra neutrino degrees of freedom. From this, we infer that the CMB provides a limit to $\Omega_{\text{gw}} h^2$ that may be competitive with that from BBN, but extends to the lower frequencies, $\sim 10^{-15}$ Hz, corresponding to wavelengths comparable to the comoving horizon at CMB decoupling². This limit therefore improves upon previous constraints over the frequency interval $10^{-15} - 10^{-10}$ Hz by four orders of magnitude.

More precisely, the CGWB behaves as a free-streaming gas of massless particles, just like massless neutrinos, and therefore affects the growth of density perturbations in ways in addition to their effect on the expansion rate at decoupling. If the CGWB energy-density perturbations are adiabatic (i.e., have the same density distribution as other relativistic species), then the effects of the CGWB on the CMB/LSS are indistinguishable from those due to massless neutrinos. In this case, CMB/LSS constraints to the number of massless neutrino species [180] translates directly to a constraint to the CGWB energy density. If, however, the primordial perturbations to the CGWB energy-density perturbations are non-adiabatic, as might be expected if they are produced by inflation, pre-big-bang models, ekpyrotic, or phase transitions and/or cosmic turbulence (see, e.g., Refs. [16–19, 176, 181]), then the CMB/LSS effects of the CGWB may differ from those of adiabatic massless neutrinos.

In this chapter, we carry out a detailed analysis of current constraints to the CGWB amplitude that come from current measurements of the CMB power spectrum and matter power spectrum. Our calculations of the CMB and matter power spectra include the effects of the CGWB on the expansion rate and on the growth of perturbations, for both adiabatic and non-adiabatic initial conditions for the CGWB. We include current constraints from the CMB, galaxy surveys, and the Lyman- α forest. We then forecast how these constraints may be improved with future CMB measurements.

²This estimate was provided in Fig. 2 of Ref. [133].

4.2 The high-frequency CGWB as a component of the radiative energy density

We suppose that the zeroth-order (background) metric is given by the Friedmann-Robertson-Walker (FRW) solution to Einstein's equations,

$$ds^2 = a(\tau)^2 \left(-d\tau^2 + \frac{dr^2}{1 - Kr^2} + r^2 d\Omega^2 \right), \quad (4.1)$$

where the conformal time, τ , is related to the cosmic time by $d\tau \equiv dt/a(t)$; length units are used such that the constant K can take on the values 0, +1, or -1; and $d\Omega$ is a differential solid angle. In terms of conformal time, the Hubble parameter is written in terms of the scale factor as $H = (1/a(\tau)^2)\dot{a}$, where the dot refers to a derivative with respect to conformal time. We let ρ_c denote the critical energy density for which the geometry is flat (i.e., $K = 0$). We then define $\Omega \equiv \rho/\rho_c$ and the evolution of the scale factor is determined by the equation,

$$\frac{K}{H^2 a(\tau)^2} = \Omega - 1. \quad (4.2)$$

From this equation, we are able to see that the normalization of the scale factor today, a_0 , is determined by K and the total energy density today through $a_0 = \sqrt{|K/(\Omega_0 - 1)|}H_0^{-1}$; when $K = 0$ ($\Omega_0 = 1$) we take $a_0 = 1$, where the subscript '0' indicates that the quantity is evaluated today. We now suppose that the metric can be written in the following form:

$$g_{\mu\nu} = g_{\mu\nu}^{(0)} + h_{\mu\nu}, \quad (4.3)$$

where the background metric, $g_{\mu\nu}^{(0)}$, is defined by Eq. (4.1) and $h_{\mu\nu}$ is some small rapidly varying perturbation. We then proceed as in Refs [182–184] to write the Einstein equation as,

$$G_{\mu\nu} \approx G_{\mu\nu}^{(0)} + G_{\mu\nu}^{(1)} + G_{\mu\nu}^{(2)} \approx 8\pi(T_{\mu\nu}^{(0)} + T_{\mu\nu}^{(1)}), \quad (4.4)$$

where we have taken geometrized units, $G = c = 1$, $T_{\mu\nu}^{(0)}$ is the spatially averaged stress-energy tensor (i.e., it contains $\bar{\rho}$ and \bar{P}), and $T_{\mu\nu}^{(1)}$ contains fluctuations in the cosmic fluid. Now we use a two-length scale approximation, denoting the typical length scale for the background metric (taken, typically, as the radius of curvature) by \mathcal{R} and the typical wavelength of the perturbation by λ . We then find that the zeroth order piece (the Einstein tensor evaluated using the background metric) is of order $1/\mathcal{R}^2$, the first-order piece is of order h/λ^2 and the second-order piece is of order h^2/λ^2 , where h denotes the typical amplitude of the perturbations. If we take an appropriate average over a region of space-time that is large compared to λ but a region small compared to the radius of

curvature of the background metric then the terms which are linear in the perturbation will vanish, leaving the relationship,

$$G_{\mu\nu}^{(0)} \approx 8\pi T_{\mu\nu}^{(0)} - \langle G_{\mu\nu}^{(2)} \rangle. \quad (4.5)$$

Considering that $G_{\mu\nu}^{(0)} \sim 1/\mathcal{R}^2$ and that $\langle G_{\mu\nu}^{(2)} \rangle \sim h^2/\lambda^2$, we find that $h \lesssim \lambda/\mathcal{R}$. Therefore, looking at the decomposition in Eq. (4.4), we see that in order for it to be satisfied, $G_{\mu\nu}^{(1)}$ must be determined by the first-order stress-energy tensor, $T_{\mu\nu}^{(1)}$ (the other terms are both smaller by an extra factor of h). Therefore the equation of motion for the perturbation is given by,

$$G_{\mu\nu}^{(1)} \approx 8\pi T_{\mu\nu}^{(1)}. \quad (4.6)$$

From the above expressions [Eqs. (4.5) and (4.6)], we conclude that perturbations to the metric follow a linear equation of motion, sourced by fluctuations in the otherwise homogeneous and isotropic stress-energy tensor (e.g., Ref. [185]) but contribute, though a quadratic average, to the evolution of the background metric. This non-linear average can be thought of as an effective stress-energy tensor due to the perturbations,

$$T_{\mu\nu}^{\text{eff}} \equiv -\langle G_{\mu\nu}^{(2)} \rangle. \quad (4.7)$$

In particular, it can be shown that it obeys the usual conservation equation, $\nabla_\mu T_\nu^{\text{eff} \mu} = 0$, to within a fractional error of order $(\lambda/\mathcal{R})(T_{\mu\nu}^{\text{eff}}/\mathcal{R})$ [186]. A detailed analysis of the above equations shows that the accuracy of the evolution equation, Eq. (4.6), is independent of the length-scale of the perturbation (it is of order h^2) whereas the effective stress-energy tensor is only useful to a fractional error of order h and λ/\mathcal{R} . Therefore, as is found in the literature (e.g., [187]), the evolution equation is used to evolve the perturbations past the Hubble horizon, however we must be aware of the applicability of the effective stress-energy tensor when considering perturbations on length-scales comparable to the Hubble horizon. The Ricci scalar for a metric of the form given in Eq. (4.1) is given by,

$$R = -6 \left(\frac{1}{a} \frac{d^2 a}{dt^2} + H^2 + \frac{K}{a(\tau)^2} \right) \sim \frac{1}{\mathcal{R}^2}. \quad (4.8)$$

Einstein's equations applied to the background metric shows that the first and second terms are of the same order, we find that the typical radius of curvature for the background metric is given by $\mathcal{R} \sim \min\{H^{-1}, a(\tau)|K|^{-1/2}\}$.

We will now specialize to consider only tensor perturbations to the metric, i.e., gravitational-waves. However, we note that Eq. (4.5) dictates that scalar, vector, and tensor perturbations induce an effective stress-energy tensor which sources the expansion. With the definition,

$$\bar{h}_{\alpha\beta} \equiv h_{\alpha\beta} - \frac{1}{2} h g_{\alpha\beta}^{(0)}, \quad (4.9)$$

and a gauge choice such that $\bar{h}_{\mu|\alpha}^{\alpha}$ and $\bar{h} = 0$, the effective stress-energy tensor for gravitational-waves takes the form,

$$T_{\mu\nu}^{\text{gw}} = \frac{1}{32\pi} \left\langle \bar{h}_{\alpha\beta|\mu} \bar{h}^{\alpha\beta}_{|\nu} \right\rangle, \quad (4.10)$$

where the subscript bar indicates covariant differentiation with respect to the background metric. For perturbations well within the horizon and fluctuating much faster than the typical time-scale of the background evolution (i.e., H^{-1}), we can consider the gravitational-waves as though they were propagating on a flat, Minkowski, background. On a flat background the equation of motion for $\bar{h}_{\mu\nu}$ becomes [34],

$$\partial^\alpha \partial_\alpha \bar{h}_{\mu\nu} = 0. \quad (4.11)$$

General solutions to this equation can be built from plan-wave solutions, so we consider an unpolarized plane-wave solution traveling up the positive z -axis which yields,

$$T_{\text{tt}}^{\text{gw}} = T_{\text{zz}}^{\text{gw}} = -T_{\text{tz}}^{\text{gw}} = \frac{\omega^2 h_c^2}{16\pi}, \quad (4.12)$$

where h_c is the strain amplitude. In order to be consistent with our assumption of an FRW background we require the CGWB to be isotropic and homogeneous, which implies that there must also be waves of the same frequency traveling along the other two axes in both the positive and negative directions. With this, we find that the total effective stress-energy tensor is given by

$$T_{\mu\nu}^{\text{gw}} = \text{diag}(6\mathcal{A}, 2\mathcal{A}, 2\mathcal{A}, 2\mathcal{A}), \quad (4.13)$$

where $\mathcal{A} \equiv (\omega^2 h_c^2)/(16\pi)$. Therefore, $\rho_{\text{gw}} = (3\omega^2 h_c^2)/(8\pi)$, $P_{\text{gw}} = (\omega^2 h_c^2)/(8\pi)$. Given that the stress-energy tensor is locally conserved, it follows that the stress-energy tensor associated with an isotropic homogeneous background of weak gravitational-waves has the form of a perfect fluid with an equation of state, $P_{\text{gw}} = (1/3)\rho_{\text{gw}}$, as we would expect for true radiation, so that $\rho_{\text{gw}} \propto a^{-4}$. We note that the equation of state of a fluid is a gauge-invariant quantity.

From this point on we take the point of view that the short wavelength component of a stochastic background of gravitational waves acts as a fluid of non-interacting massless particles. Furthermore, we do not deal with the subtlety of considering how the gravitational-wave energy density sourcing the expansion changes as the universe expands and more modes fall within the Hubble horizon. Instead, we suppose that either the CGWB we are constraining is always contained within the horizon on the length scales probed in order to establish the constraint, or we only consider that part of the CGWB which is contained within the horizon on the length scales probed in order to establish the constraint (usually the CGWB extends to very small scales, in which case ignoring the dynamical effects of the long-wavelength part of its spectrum should be justified). Therefore, since CMB measurements extend down to a length-scale of ~ 1 Mpc, when using CMB measurements to

constrain the energy density in the CGWB we only consider that part of the CGWB spectrum that has frequencies greater than 10^{-15} Hz. The same criteria is applied when using the BBN constraint: since the BBN horizon has an associated frequency of 10^{-12} Hz, only that part of the spectrum of the CGWB with frequencies greater than this are constrained. We have left such details to future work.

Since we are considering the short-wavelength CGWB as a fluid of non-interacting massless particles there is a natural association between the CGWB and massless neutrinos, which, in the standard scenario, decouple from the cosmic fluid at a temperature $T \sim 1$ MeV. The evolution of the distribution function for massless neutrinos has been worked out in detail before [185]. However, an important difference exists between constraints placed on the number of neutrinos from CMB and LSS studies and those placed on a CGWB: in all such studies considering the constraints on N_ν from the CMB and LSS the initial conditions for the perturbations in the neutrino fluid were assumed to be adiabatic. In general, however, the initial behavior of the gravitational-wave fluid will not follow that of the conventional species, such as photons and neutrinos. This statement is true even for the case of single-field inflation where it is usually assumed all fluids obtain adiabatic perturbations.

4.3 The effects of a relativistic species on the CMB and LSS

In this section we will outline the predominant ways in which extra relativistic energy density affects predictions for the CMB and clustering of large scale structure.

4.3.1 Homogeneous influence

The presence of extra relativistic energy density which contributes to the homogeneous evolution of the Universe will affect observations in several ways. We write the total relativistic energy density as

$$\Omega_{\text{rad}} h^2 = \Omega_\gamma h^2 [1 + 0.2271(3.04 + N_{\text{eff}})], \quad (4.14)$$

where $\Omega_\gamma h^2 = 2.469 \times 10^{-5}$ for $T_{\text{CMB}} = 2.725\text{K}$ [113]. When we have $N_{\text{eff}} = 0$ we regain the standard cosmology with 3.04 neutrino species (see Refs. [188–192] for a discussion of the various effects that lead to the ‘0.04’ correction). Physically, it is clear that the presence of both radiation and matter defines a value of the scale factor (and corresponding length scale) that should be imprinted in measurements of the perturbations. The scale factor when $\Omega_{\text{M}} = \Omega_{\text{rad}}$ is denoted by $a_{\text{eq}} = \Omega_{\text{rad}}/\Omega_{\text{M}}$. Associated with this, we have a length scale given by the value of the Hubble parameter evaluated at a_{eq} ,

$$H(a_{\text{eq}}) = \sqrt{2} H_0 \sqrt{\frac{\Omega_{\text{M}}}{a_{\text{eq}}^3}}. \quad (4.15)$$

We divide our discussion into effects seen in the CMB and effects seen in the clustering of matter.

4.3.1.1 Effects in the CMB

This new scale will be imprinted in the height of the first acoustic peak in the temperature anisotropies. Besides the initial anisotropy of the photon fluid at the surface of last scattering and perturbations due to its motion, the height of the first peak is in large part determined by the evolution of the Newtonian potentials as the photons propagate to us. As a photon approaches a deeper potential, it is blueshifted, and as it emerges from that potential it is redshifted. If the potential is static during this time, the photon's overall frequency is unchanged. However, if the potential is evolving, then the photon can gain or lose energy (if the potential decays then the photon will undergo an overall blueshift; if the potential strengthens then the photon undergoes an overall redshift). This effect is referred to as the integrated Sachs-Wolfe (ISW) effect; in particular, the ISW effect which contributes to the first peak in the temperature powerspectrum is called the early ISW. During matter domination the potentials do not evolve, therefore if photon decoupling occurred within a totally matter dominated universe, then there would be no ISW effect on these scales. On the other hand, the potentials (in conformal Newtonian gauge) decay during radiation domination. Photon decoupling depends weakly on cosmology since, for the most part, it is determined by atomic physics [193], so for the purposes of this discussion we take it to occur at $z_{\text{dec}} = 1089$. Therefore, as the time elapsed between matter-radiation equality and photon decoupling decreases, the strength of the early ISW grows. Recasting this in terms of N_{eff} , as N_{eff} increases the height of the first peak increases.

The presence of extra relativistic energy density also shifts the location of the peaks in the CMB. Limber's approximation³ allows us to relate a given multipole to a physical size through the relation $\ell \approx k\chi(z_{\text{dec}})$, where $\chi(z_{\text{dec}})$ is the conformal distance to the surface of last scattering. The physical size observed in the acoustic oscillations in the CMB is set by the sound horizon at decoupling. This, in turn, is approximately proportional to the conformal time at decoupling. Therefore, the location of the peaks are proportional to

$$\ell \propto \frac{\chi(z_{\text{dec}})}{\tau(z_{\text{dec}})}. \quad (4.16)$$

Fixing the geometry to flat, we then have

$$\ell \propto \frac{\sqrt{1 + a_{\text{eq}}} - \sqrt{a_{\text{dec}} + a_{\text{eq}}}}{\sqrt{a_{\text{eq}}} - \sqrt{a_{\text{dec}} + a_{\text{eq}}}}. \quad (4.17)$$

³The peak structure in the CMB is formed by the Sachs-Wolfe contribution whose time evolution can be approximated as a Dirac delta function at the surface of last scattering. Limber's approximation uses the fact that the transfer function $P(k)\Delta_{\text{SW}}^2(k)$ varies much slower than the spherical Bessel function which allows us to write $C_\ell \sim \int k^2 dk P(k)\Delta_{\text{SW}}^2(k)[j_\ell(k\chi_{\text{dec}})]^2 \propto \int k^2 dk P(k)\Delta_{\text{SW}}^2(k)\delta(\ell + 1/2 - k\chi_{\text{dec}})$, where χ_{dec} is the conformal distance to decoupling. The Dirac delta function then enforces the equality $k = (\ell + 1/2)/\chi_{\text{dec}} \approx \ell/\chi_{\text{dec}}$, where the second equality follows from the limit $\ell \gg 1$.

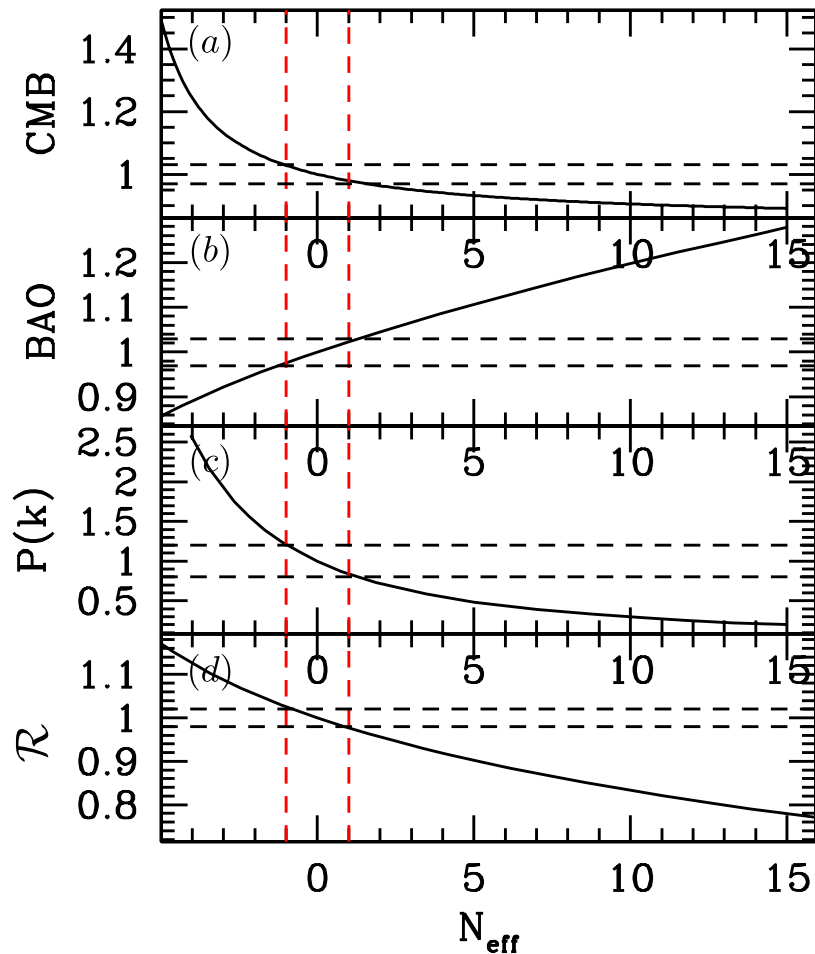


Figure 4.1: Panel (a) shows the suppression of power in the small scale CMB temperature anisotropies as a function of N_{eff} fixing all other cosmological parameters. We can see that the suppression increases with increasing N_{eff} . Panel (b) shows the ratio $r_s(z_d, N_{\text{eff}})$ as is measured by the BAO. As N_{eff} is increased while holding $\Omega_M h^2$ fixed the sound horizon is increased. Panel (c) shows the suppression of power in the matter powerspectrum for large wavenumbers. We can see that, just as in the CMB case, as N_{eff} is increased the suppression becomes more pronounced. The lowest panel (d) shows the ratio of the location of the peaks in the CMB temperature anisotropy powerspectrum for the standard cosmology to a cosmology with extra relativistic degrees of freedom. As N_{eff} is increased the peaks shift to *higher* values since $\mathcal{R} \equiv \ell_{N_{\text{eff}}=0}/\ell$. The red vertical dashed line indicates a constraint to within $N_{\text{eff}} = 1$ for each of these measurements. For the location of the peaks in the CMB this corresponds to a determination of the location to within a few percent; for the suppression of small scale power in the matter powerspectrum this corresponds to a fractional error of about ten percent; for a measurement of the BAO this corresponds to a fractional error of a few percent; for a measurement of the relative power in the small and large scale CMB to a fractional error of a few percent. Current measurements can reach these accuracies. However, in this figure we are ignoring any degeneracies that exist between N_{eff} and other cosmological parameters.

We then define a ratio as in Ref. [194] $\mathcal{R} \equiv \ell_{N_{\text{eff}}=0}/\ell$. We show this ratio for a flat geometry in Fig. 4.1. From that figure it is clear that if the location of the peaks can be determined to an accuracy of less than $\sim 10\%$ then, with $\Omega_M h^2$ fixed, we could constrain N_{eff} to within a few.

4.3.1.2 Effects on the matter powerspectrum

At large scales the matter powerspectrum rises as k and at small scales it falls off as k^{-3} . The break between these two behaviors occur at k_{eq} , the wavenumber at the time of matter-radiation equality,

$$k_{\text{eq}} = a_{\text{eq}} H_{\text{eq}} = \sqrt{2} H_0 \left(\frac{\Omega_M}{\Omega_{\text{rad}}} \right)^{1/2}. \quad (4.18)$$

In addition to this, writing the matter powerspectrum in terms of a transfer function, $P(k) \propto k^{n_s} T^2(k)$, the transfer function on scales $k \gg k_{\text{eq}}$ is given by [195]

$$T(k) \approx \frac{12k_{\text{eq}}^2}{k^2} \ln \left(\frac{k}{8k_{\text{eq}}} \right), \quad (4.19)$$

while it is normalized to unity on large scales. Therefore, the power at a given wave number $k \gg k_{\text{eq}}$ relative to the large scale power is suppressed as k_{eq} decreases. We show this behavior in Fig. 4.2.

The acoustic oscillations found in the CMB are also present in the matter powerspectrum. These oscillations are called baryon acoustic oscillations (BAO). Just as the location of the peaks in the CMB is set, in part, by considering the sound horizon, r_s , of the photon-baryon fluid at decoupling, the peaks in the BAO are set by the sound horizon in the photon-baryon fluid when the baryons fully decouple from the photons. This redshift is not necessarily coincident with decoupling. Denoting this redshift (known as the drag redshift since it is at this redshift that Compton drag is insufficient to couple the baryons to the photons) by z_d and taking the best fit cosmology to the WMAP 3rd year maximum likelihood we have $z_d = 1017$ according to the fitting formula presented in Ref. [193]. BAO observations average over a sphere giving a measurement of the ratio $r_s(z_d)/D_V(z)$ where the distance $D_V(z)$ is given by [196]

$$D_V(z) = \left[(1+z)^2 D_A(z)^2 \frac{cz}{H(z)} \right]^{1/3}, \quad (4.20)$$

and $D_A(z)$ is the angular diameter distance to redshift z . The results from Ref. [197] indicate that this ratio can be measured to an accuracy of about 3% at $z = 0.2$ and $z = 0.35$ using galaxy clustering data from both the Sloan Digital Sky Survey (SDSS) and the Two Degree Field Galaxy Redshift Survey (2dFGRS) [197]. If we fix the cosmological parameters that determine the low redshift evolution [i.e., fix $D_V(z)$] then we can see that these measurements allow us to constrain N_{eff} . We show this in Fig. 4.1.

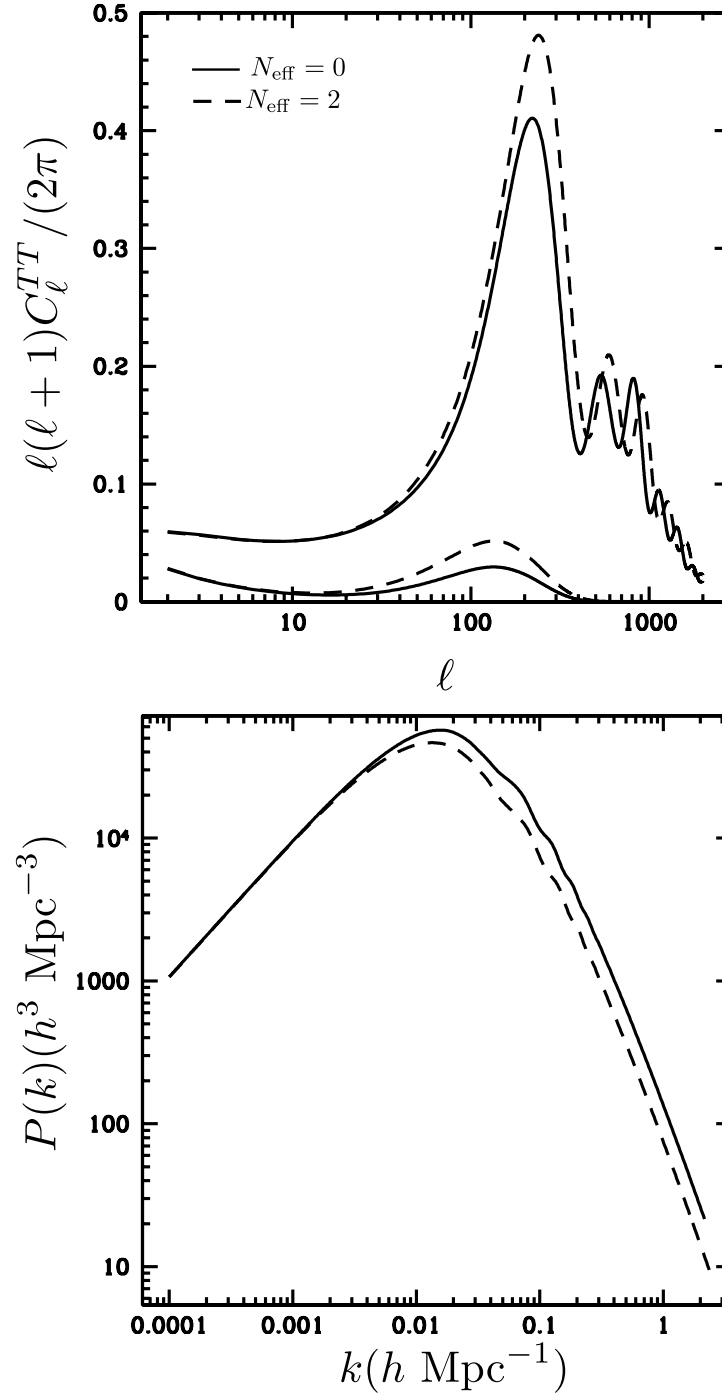


Figure 4.2: The temperature anisotropy (upper panel) and the matter powerspectrum (lower panel) for the standard cosmology (solid line) and for a cosmology with extra relativistic degrees of freedom (dashed). The lower curves in the upper panel also show the ISW effect for the two cosmologies. Note that, as discussed in the text, the additional relativistic energy density causes the early ISW to become enhanced.

4.3.2 Inhomogeneous influence

The perturbative effects of adding additional non-interacting relativistic degrees of freedom is to change the amplitude of the anisotropic stress and free streaming as well as possibly introduce non-adiabatic initial conditions.

The presence of anisotropic stress alters the relationship between the two Newtonian potentials (in conformal Newtonian gauge). Since a massless species propagate at the speed of light they stream out of any initial perturbations. This further dampens the size of the potentials during radiation domination, so that the small scale CMB anisotropy powerspectrum is damped relative to the Sachs-Wolfe plateau as [198]

$$\frac{C_\ell^{\text{SW}}}{C_{\ell \gg 100}} \approx \frac{1}{25 \left(1 + \frac{4f}{15}\right)^2}, \quad (4.21)$$

where the fraction $f \equiv (\rho_{\text{rad}} - \rho_\gamma)/\rho_{\text{rad}} = [0.2271(3.04 + N_{\text{eff}})]/[1 + 0.2271(3.04 + N_{\text{eff}})]$. Finally, the acoustic horizon for a decoupled radiative fluid is greater than that of the photon-baryon fluid. This induces a small *additive* phase shift $\Delta\ell \approx -4$ for $N_{\text{eff}} = 1$ [199]. However, this phase-shift is subdominant to the multiplicative shift caused by the change in the sound horizon and the distance to the surface of last scattering.

From the preceding discussion it is clear that extra radiative energy density is degenerate with Ω_M . In particular, the homogeneous effects depend on either a_{eq} or k_{eq} , which in turn depend on some combination of N_{eff} and Ω_M . This degeneracy is shown in Fig. 4.3. Since z_{eq} and k_{eq} depend on Ω_M and k_{eq} differently, measurements of both quantities can be used to break the degeneracy to a certain extent. Measurements of the luminosity distance from type Ia supernovae also help to break this degeneracy since they give an independent constraint to Ω_M and Ω_Λ . Finally, since the presence of extra relativistic energy density suppresses the temperature powerspectrum at large ℓ (or large k) we have a degeneracy between N_{eff} and n_s , the scalar spectral index. As N_{eff} is increased, an increase in n_s will offset the loss of power on small scales.

Finally, the introduction of a new species might introduce non-adiabatic initial conditions. In particular this will occur when a species is created during inflation but has only gravitational interactions with the rest of the species that fill the universe so that it cannot come into thermodynamic equilibrium. Axions and the CGWB are two examples of such species.

There are many different initial conditions that are accessible to the CGWB. In this chapter we explore how the constraints depend on the choice of initial condition by considering two different examples. In the first case, we choose the usual adiabatic initial conditions. In this case, the CGWB is indistinguishable from a massless neutrino species. In the second case we choose to set the density contrast ($\delta\rho_{\text{gw}}/\bar{\rho}_{\text{gw}}$) to zero in the conformal Newtonian gauge (a choice of coordinates such that the spatial hypersurfaces are shear free [200]). We call this second choice ‘homogeneous’ initial

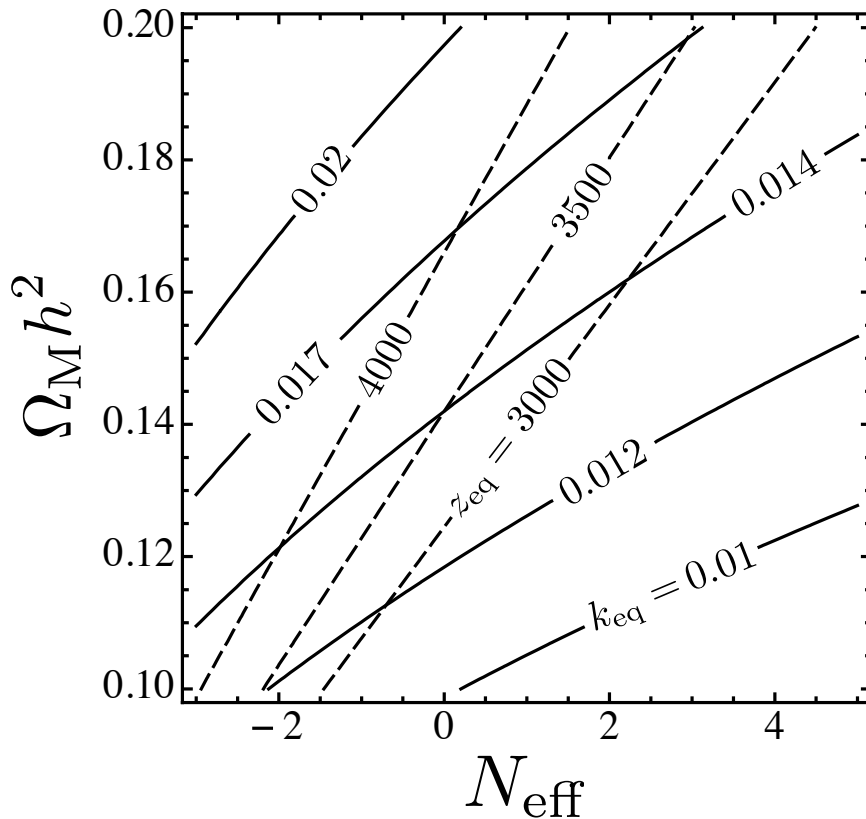


Figure 4.3: This figure shows the degeneracy between $\Omega_M h^2$ and N_{eff} through measurements of both the redshift at matter-radiation equality (z_{eq}) and the wavenumber at matter-radiation equality (k_{eq}). The solid lines correspond to constant k_{eq} in units of $h \text{ Mpc}^{-1}$; the dashed lines correspond to constant z_{eq} .

conditions. We discuss how we set the initial conditions in Appendix B, here we only discuss how the homogeneous initial conditions affect the theoretical predictions.

The choice of initial conditions has little effect on the matter powerspectrum. Therefore, we concentrate on the CMB and in particular the temperature anisotropies since these are the measured with the highest signal to noise. We find that the homogeneous initial conditions cause a rise in power at large scales. This behavior breaks the degeneracy between N_{eff} , $\Omega_M h^2$, and n_S for the CGWB and produces a tighter constraint on the CGWB than adiabatic initial conditions. In order to explore why these new initial conditions have this effect, we have divided the calculation of the temperature powerspectrum into three parts. These three parts are easiest to identify if one calculates the powerspectrum using the line-of-sight technique first introduced in Ref. [201]. Without

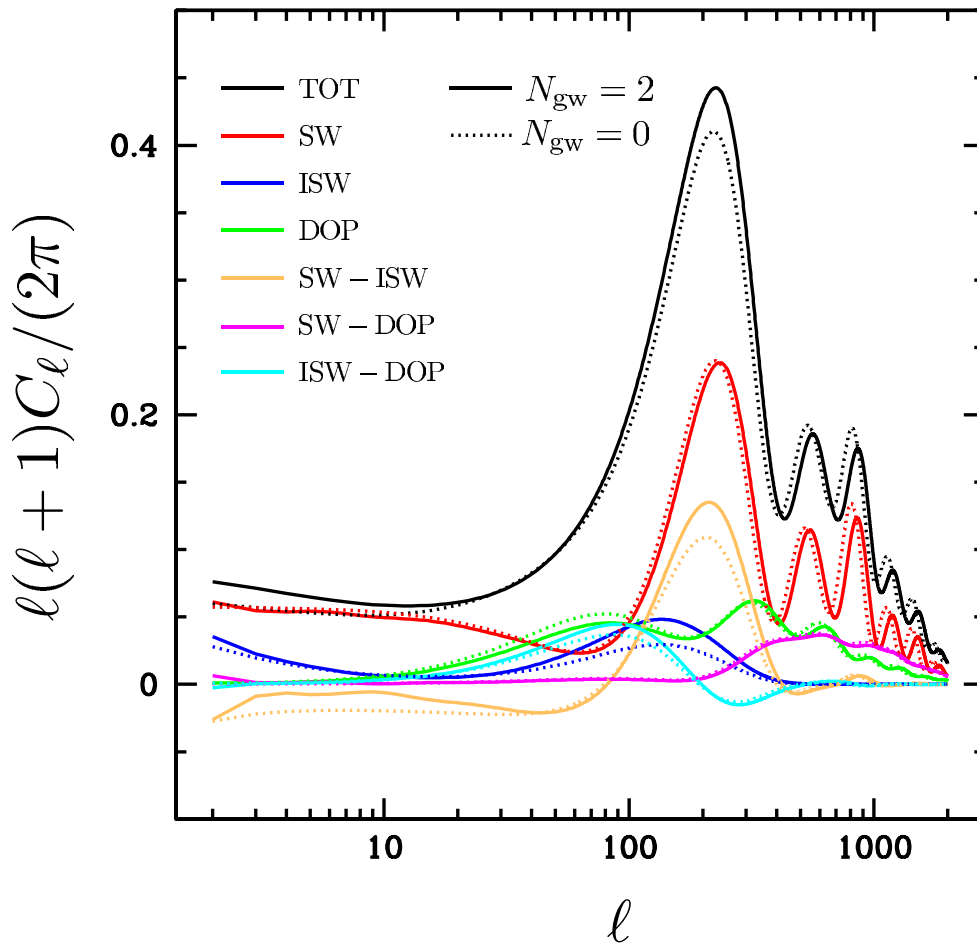


Figure 4.4: Here we present a decomposition of the temperature anisotropies. The dotted curves correspond to the case with zero gravitational waves and three neutrinos with adiabatic initial conditions, the solid curves correspond to 3 standard neutrinos plus 2 effective gravitational waves with homogeneous initial conditions. We have decomposed the temperature anisotropies as discussed in the text into various terms. Most importantly we can see that the main difference between these two cases comes from the ISW-doppler cross correlation: the homogeneous initial conditions for the ISW-doppler cross correlation are *less negative* than the adiabatic case.

going into the details, we can schematically write the full power spectrum as

$$C_\ell^{TT} = \int k^2 dk P_\Psi(k) [\Delta_\ell^{\text{SW}}(k) + \Delta_\ell^{\text{ISW}}(k) + \Delta_\ell^{\text{DOP}}(k)]^2, \quad (4.22)$$

where $\Delta_\ell^{\text{SW}}(k)$ is the transfer function for the Sachs-Wolfe effect, $\Delta_\ell^{\text{ISW}}(k)$ is the transfer function for the integrated Sachs-Wolfe effect, and $\Delta_\ell^{\text{DOP}}(k)$ is the transfer function for the doppler motion of the photons in the photon-baryon fluid. In this decomposition, the full powerspectrum is then composed of six terms. We show the results of this calculation in Fig. 4.4. From this figure we can see that the homogeneous initial conditions causes a *decrease* in the cross correlation between the

Sachs-Wolfe and integrated Sachs-Wolfe effects, effectively boosting the large scale power.

4.4 Results⁴

We first consider the case when the CGWB has adiabatic initial conditions. In this case, the effects of the CGWB on the expansion history and structure formation are identical to those of massless neutrinos. The analysis proceeds just as in Ref. [180]. We have updated this analysis to include new small-scale CMB results, as well as constraints from the Lyman- α forest. The CMB results we use are from WMAP, ACBAR, CBI, VSA, and BOOMERanG, and we use the measurement of the galaxy power spectrum from the 2dF Galaxy Redshift Survey and the Sloan Digital Sky Survey (SDSS), and the Lyman- α forest [202–212]. We implement the Lyman- α constraints following the method discussed in Ref. [213], with minor modifications that were suggested by the authors. To translate the constraint to the number of extra neutrino degrees of freedom to a CGWB energy density, we use the relation $\Omega_{\text{gw}}h^2 = 5.6 \times 10^{-6}$, the density contributed by a single massless-neutrino species.

Results for adiabatic initial conditions are shown in Fig. 4.5. A limit at 95% CL of $\Omega_{\text{gw}}h^2 \lesssim 3.9 \times 10^{-5}$ is obtained from a combination of current CMB data, galaxy power spectrum, and the Lyman- α forest, and under the assumption that the number of neutrino degrees of freedom is $N_\nu = 3.04$ and that neutrino masses are free to vary. Due to a slight discrepancy between the matter power spectrum from the best-fit CMB model and that measured in galaxy surveys and Lyman- α forest measurements, the addition of galaxy surveys and the Lyman- α forest weakens the bound by roughly a factor of two. A small CGWB component improves slightly the CMB+galaxy+Ly α agreement (see the solid curve in Fig. 4.5), although the difference between $N_{\text{gw}} = 0$ and $N_{\text{gw}} = 2$ is statistically insignificant. Although not shown, we find that the exclusion of the Lyman- α forest weakens the CMB+galaxy+Ly α bound only slightly. If neutrino masses are assumed to be undetermined, then the CMB+galaxy+Ly α bound is shifted by approximately two neutrinos (see the dot-dash curve in Fig. 4.5), which indicates that there is a degeneracy between the neutrino mass and the CGWB. This same trend has been observed in Ref. [214]. Note that the bound is improved by roughly a factor of 4 if we include only current CMB data.

If the CGWB is initially homogeneous, then the initial conditions for the CGWB perturbations differ from those for massless neutrinos. This will affect the growth of perturbations, especially at large scales, and the degeneracy between the CGWB and massless neutrinos is thus broken, as shown in Fig. 4.4. The bound to the CGWB then turns out to be stronger than in the adiabatic case. Fig. 4.5 shows results for the likelihood for $\Omega_{\text{gw}}h^2$ for different combinations of current data sets as well as forecasts for the likelihoods expected when future CMB experiments are included. If the CGWB

⁴The results presented in this section and Section 4.5 were first published in, *A new cosmic microwave background constraint to primordial gravitational waves*, Tristan L. Smith, Elena Pierpaoli, and Marc Kamionkowski, Phys. Rev. Lett. **97**, 021301 (2006). Reproduced here with permission, copyright (2006) by the American Physical Society.

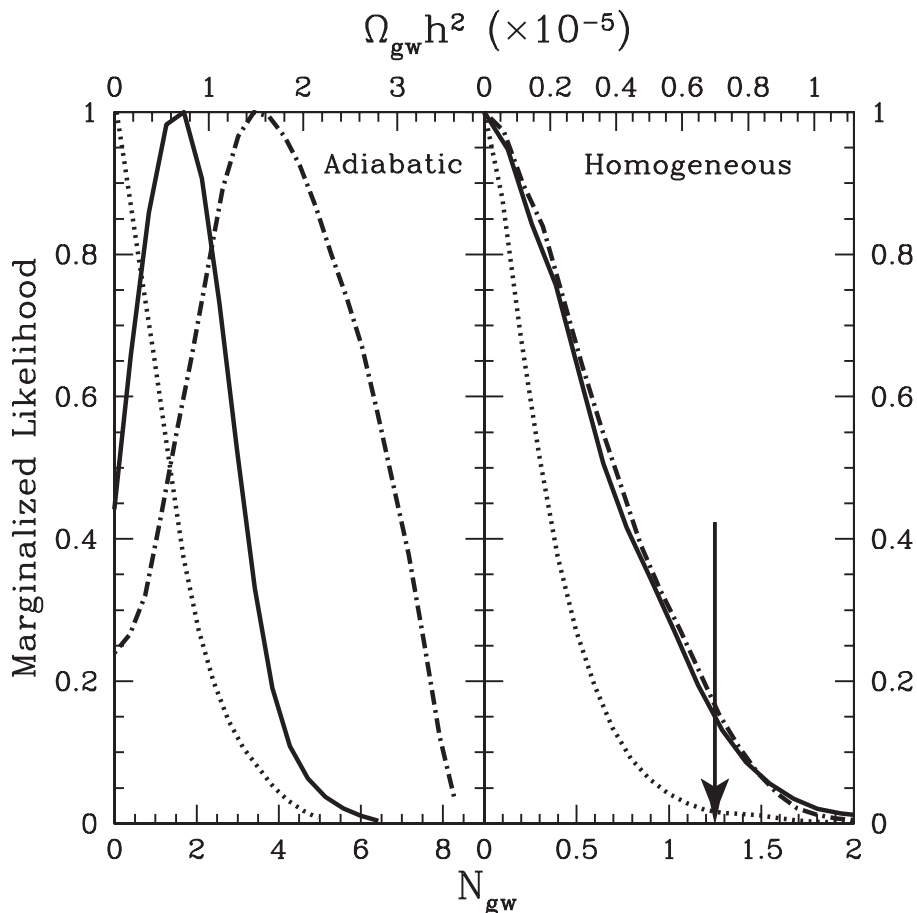


Figure 4.5: *Adiabatic*: The marginalized (unnormalized) likelihoods for the CGWB energy density if perturbations to the CGWB density are adiabatic. The dotted curve is the result obtained using only CMB data. The thick solid curve includes galaxies as well as the Lyman- α forest. In all of the aforementioned curves, the marginalization is over the nonrelativistic-matter density $\Omega_m h^2$, baryon density $\Omega_b h^2$, scalar spectral index n_s , power-spectrum amplitude A_s , the optical depth τ to the surface of last scatter, and the angle θ subtended by the first acoustic peak (marginalization over θ essentially stands in for marginalization over the Hubble constant). We hold the geometry fixed to flat, the number of neutrinos to $N_\nu = 3.04$, and the neutrino masses fixed to zero. Finally, the dot-dash curve (to the right) shows current constraints from the CMB+galaxies+Ly α if we allow for and marginalize over nonzero neutrino masses as well. The number of equivalent neutrino degrees of freedom (N_{gw}) is shown on the bottom axis. *Homogeneous*: same as the left panel, except for homogeneous initial conditions for the CGWB. The arrow indicates the 95% CL upper limit $\Omega_{\text{gw}} h^2 \leq 6.9 \times 10^{-6}$ that we adopt as our central result. This is obtained from the analysis that includes current CMB+galaxy+Ly α +free m_ν .

is produced by some mechanism that leaves its primordial density uncorrelated with the curvature perturbation—e.g., inflation or perhaps some post-inflation phase-transition mechanism—then this is the result that should be applicable. We adopt as our 95% CL upper bound, $\Omega_{\text{gw}} h^2 \lesssim 6.9 \times 10^{-6}$, for homogeneous CGWB initial conditions from the combination of data from current CMB experiments, galaxy surveys, and the Lyman- α forest and under the assumption that the number of neutrino

Table 4.1:

CMB EXPERIMENTAL SPECIFICATIONS FOR FISHER MATRIX

Experiment	θ_{beam}	$(w_T)^{-1/2}$	$(w_P)^{-1/2}$	f_{sky}	$\Omega_{\text{gw}}h^2$
Planck:	7.1	42.2	80.5	0.8	1.4×10^{-6}
	5.0	64.8	132.3	–	–
CMBPol:	4.0	1.0	1.4	0.8	5×10^{-7}

NOTES—The beam width, θ_{beam} , (FWHM) is given in arcminutes. Weights, $(w_{T,P})^{-1/2}$, are in arcminutes μK . The sky fraction is given by f_{sky} . The sensitivities to $\Omega_{\text{gw}}h^2$ are 95% CL for homogeneous initial conditions.

degrees of freedom is $N_\nu = 3.04$ and that neutrino masses are free to vary. Note, again, that the bound would be roughly twice as strong if we were to restrict ourselves only to CMB data. And again, although not shown, we find that the exclusion of the Lyman- α forest weakens the CMB+galaxy+Ly α bound only slightly.

4.5 Conclusions

Our central results are summarized in Fig. 4.6, which shows $\Omega_{\text{gw}}h^2$ vs. gravitational-wave frequency. Our new constraints are competitive with the BBN constraint over the frequency range where both constraints apply. The precise value of the BBN constraint depends on the precise constraint to the maximum number of neutrino degrees of freedom allowed by BBN. Some authors [215] claim a limit $(N_\nu - 3.04) \lesssim 0.2$ (at 95% CL), but more recent and conservative estimates (that include new ${}^4\text{He}$ measurements and the CMB value for the baryon density) [179], which we choose to adopt, place the limit at $(N_\nu - 3.04) \lesssim 1.4$, comparable to the CMB/LSS bound we have derived. However, our new results apply four decades lower in frequency, and provide the strongest constraint to the CGWB amplitude over the frequency range $10^{-15} - 10^{-10}$ Hz.

To forecast the sensitivity of future CMB experiments to the CGWB, we have carried out a Fisher analysis that shows that when Planck and CMBPol fly, the sensitivity should be increased by a factor of roughly 10, while the BBN constraint may continue to be limited by the same astrophysical systematic uncertainties. See Table 1 for the experimental specifications used in our Fisher analysis. In our Fisher analysis we included the improved CMB observations as well as the current galaxy and Lyman- α constraints and allowed m_ν to vary with $N_\nu = 3.04$.

We have not determined precisely the lower end of the frequency range for which our bound applies. In order for the constraint to apply, the gravitational-wave wavelength must be within the horizon at roughly the time of, or slightly before, recombination. Otherwise the waves do not propagate as massless modes. Analytic and numerical integrations of the mode equations for gravitational waves in an expanding Universe (e.g., Fig. 2 in Ref. [112]), indicate that the mode

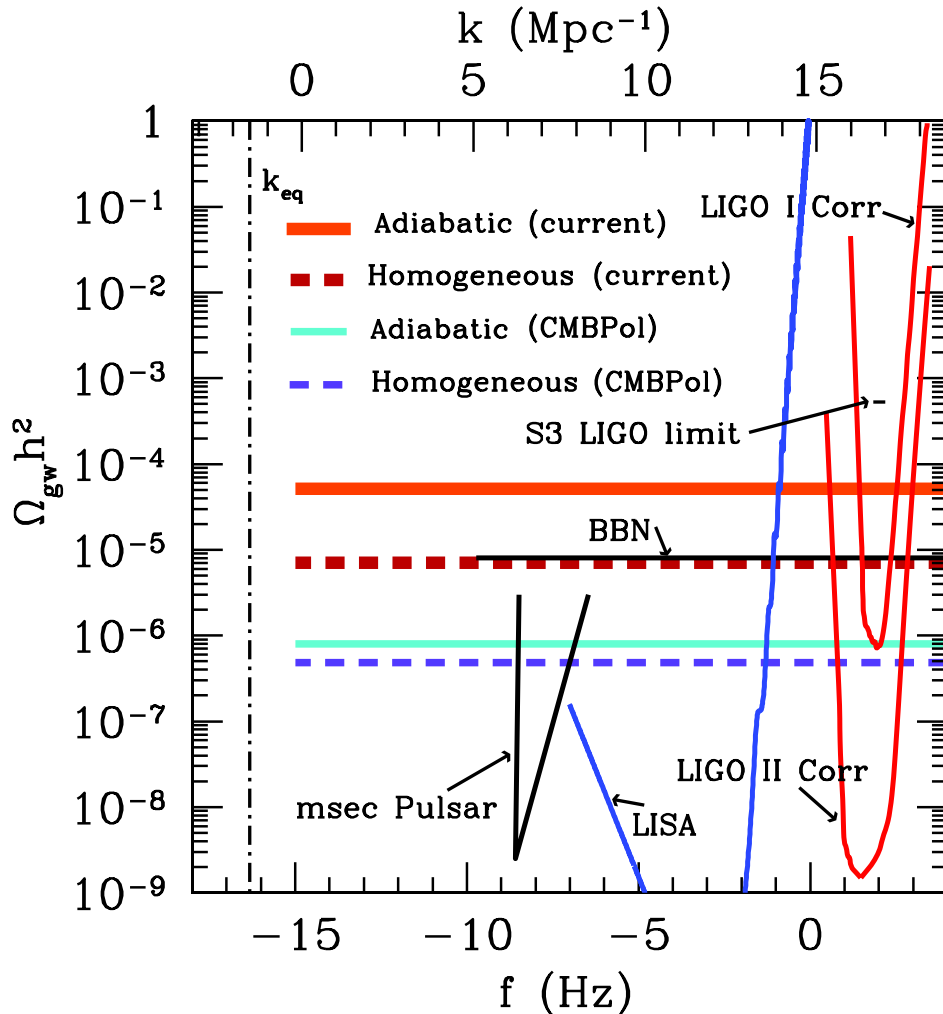


Figure 4.6: The gravitational-wave density $\Omega_{\text{gw}} h^2$ vs. frequency. The BBN constraint corresponds to a limit of 1.4 extra neutrino degrees of freedom. We also show our constraints, from current CMB, galaxy, and Lyman- α data, for a CGWB with adiabatic primordial perturbations (‘Adiabatic (current)’ and for homogeneous initial conditions (‘Homogeneous (current)’), as well as our forecasts for the sensitivities if current CMB data are replaced by data from CMBPol. Also shown are the reaches of LIGO and LISA. BBO (not shown) should go deeper, but primarily at frequencies ~ 1 Hz. Large-angle CMB fluctuations (also not shown) constrain $\Omega_{\text{gw}} h^2 \lesssim 10^{-14}$, but only at frequencies $\lesssim 10^{-16}$ Hz. The LIGO S3 upper limit is from Ref. [61] and the msec pulsar curve is from Refs. [62, 63].

is oscillating when $k\tau \simeq 10$, where k is the wavenumber and τ the conformal time evaluated at decoupling. This translates to a frequency $\nu \simeq 5 \times 10^{-17}$ Hz. More realistically, the gravitational wave will need to oscillate for a while before recombination in order to have the effects we have considered here. We therefore tentatively estimate 10^{-15} Hz as the lowest frequency for which our bound applies, although the precise value may differ slightly. We leave a more precise calculation for future work.

There is also a slight correction if our bound is applied to a scale-invariant spectrum. In this case, the number of gravitational-wave modes propagating as massless modes changes with time, as more modes enter the horizon. As a result, the energy density does not scale with scale factor a simply as a^{-4} . This, however, produces only a logarithmic correction, which is within the theoretical error of the treatment we have presented here.

We point out that the limit is probably not relevant for scale-invariant spectra, such as those produced by inflation. Those are already constrained to be roughly eight orders of magnitude lower in amplitude, at slightly lower frequencies $\sim 10^{-17}$ Hz, from large-angle fluctuations in the CMB. However, phase transitions or other exotic mechanisms that produce a CGWB at frequencies $\gtrsim 10^{-15}$ Hz will now face this new constraint.

Acknowledgments

TLS was supported by an NSF Graduate Fellowship. EP is an ADVANCE fellow (NSF grant AST-0340648), also supported by NASA grant NAG5-11489. This work was supported in part by DoE DE-FG03-92-ER40701 and NASA NNG05GF69G. This work was supported in part by the NSF through the TeraGrid resources provided by NCSA and SDSC under TeraGrid grant AST050005T.

Chapter 5

Observational tests of $f(R)$ gravity¹

5.1 Introduction

The discovery of an accelerated cosmic expansion [20, 21] has led to a flurry of theoretical activity. One class of solutions to the cosmic-acceleration puzzle consists of modifications to the general-relativistic theory of gravity. One particular proposal is the addition of a $1/R$ term to the Einstein-Hilbert action [32, 65]. Such a term gives rise to a vacuum solution with constant curvature, the de Sitter spacetime, rather than the Minkowski vacuum of the usual Einstein-Hilbert action.

Shortly after this proposal, Chiba [216] argued that this theory is inconsistent with solar system tests of gravity. In particular, he showed that the theory is equivalent to a scalar-tensor theory that is known to make solar system predictions that conflict with measurements.

Since then, however, there have been a number of papers arguing or implying that Chiba's analysis is flawed [217–221]. The crux of the counter-argument is that $1/R$ theories admit as a static spherically symmetric solution the usual vacuum Schwarzschild-de Sitter spacetime. Apart from a cosmological constant that is too small by many orders of magnitude to affect anything observable in the solar system, these solutions are just the usual Schwarzschild solution. Consequently, they argue, there is no effective difference between the solar system spacetime in these models and that in ordinary general relativity.

Here we point out that these arguments are incorrect, and that Chiba was right. The crucial point is that although the Schwarzschild-de Sitter spacetime is indeed a spherically symmetric vacuum solution to the $1/R$ equations of motion, it is not the *unique* spherically symmetric vacuum solution in this theory. The correct solution is determined by matching onto the solution in the interior of the star. When this is done correctly, it is found that the Schwarzschild-de Sitter spacetime does *not* describe the spacetime around the Sun, and that Chiba's result stands. This misunderstanding has

¹The material presented Sections 5.1-5.3 in this chapter were first published in, *Solar system tests do rule out $1/R$ gravity*, Adrienne L. Erickcek, Tristan L. Smith, and Marc Kamionkowski, Phys. Rev. **D74**, 121501 (2006) and *Solar system constraints to general $f(R)$ gravity*, Takeshi Chiba, Tristan L. Smith, and Adrienne L. Erickcek, Phys. Rev. **D75**, 124014 (2007). Reproduced here with permission, copyright (2006 and 2007) by the American Physical Society.

now propagated through a number of papers. There are moreover a number of other papers that cite these incorrect papers in a way that suggests that they may be onto something. We thought it worthwhile to correct the error before it propagates any further.

Before describing the correct spherically-symmetric spacetime for $1/R$ gravity, we consider a very simple and analogous problem that illustrates what is going on. Suppose we wanted to know the electric field around a spherically-symmetric charge distribution $\rho(r)$ confined to radii $r < R$. For radii $r > R$, the Poisson equation $\nabla^2\phi = 4\pi\rho$ relating the electric potential ϕ to the charge-density distribution ρ reduces to $\nabla^2\phi = 0$. A spherically symmetric solution to this equation, one might argue, is $\phi = 0$, implying no electric field. This is clearly incorrect.

What went wrong? Although $\phi = 0$ is indeed a spherically symmetric solution to $\nabla^2\phi = 0$, it is not the *unique* solution. Another solution is $\phi = c/r$, for $r > R$. The constant c in this equation is furthermore fixed in this case to be $c = Q$, where $Q = \int \rho \, d^3x$ is the total charge, by integrating the right- and left-hand sides of the Poisson equation $\nabla^2\phi = 4\pi\rho$ over the entire volume.

In brief, something similar happens in $1/R$ gravity. The differential equations for the metric components $g_{tt}(r)$ and $g_{rr}(r)$ are supplemented by a differential equation for the curvature R , as we will see below. The three differential equations have the Schwarzschild-de Sitter spacetime as a solution, but these vacuum solutions do not match onto the solutions in the presence of a source (i.e., the Sun). There is an additional vacuum solution that correctly matches onto the solution in the presence of the source.

In this chapter we first consider the example of a particular form for $f(R) = -\mu^4/R$. In doing so, the salient features of the solar system predictions of this theory can be clearly understood. In the next section of this chapter we generalize these results and show under what conditions a theory with an unspecified form for $f(R)$ will violate solar system tests. Finally, we briefly discuss how a mechanism particular to $f(R)$ theories may allow the theory to evade solar system tests and how this mechanism allows us to identify a new test of gravity theories.

5.2 The particular example of $f(R) = -\mu^4/R$

The gravitational action of $1/R$ gravity is given by,

$$S = \frac{1}{16\pi G} \int d^4x \sqrt{-g} \left(R - \frac{\mu^4}{R} \right) + \int d^4x \sqrt{-g} \mathcal{L}_M, \quad (5.1)$$

and may be varied with respect to the metric $g_{\mu\nu}$ to obtain the field equation [32]

$$8\pi GT_{\mu\nu} = \left(1 + \frac{\mu^4}{R^2} \right) R_{\mu\nu} - \frac{1}{2} \left(1 - \frac{\mu^4}{R^2} \right) R g_{\mu\nu} + \mu^4 (g_{\mu\nu} \nabla_\alpha \nabla^\alpha - \nabla_\mu \nabla_\nu) R^{-2}. \quad (5.2)$$

We begin by using the trace of the field equation to determine the Ricci scalar R . Contracting Eq. (5.2) with the inverse metric yields

$$\square \frac{\mu^4}{R^2} - \frac{R}{3} + \frac{\mu^4}{R} = \frac{8\pi GT}{3}, \quad (5.3)$$

where $T \equiv g^{\mu\nu} T_{\mu\nu}$.

The constant-curvature vacuum solution is obtained by setting $T = 0$ and $\nabla_\mu R = 0$. It is $R^2 = 3\mu^4$, corresponding to the de Sitter spacetime with Hubble parameter $H^2 = \mu^2/(4\sqrt{3})$, equivalent to the general-relativistic vacuum solution with a cosmological constant $\Lambda = 3H^2 = \sqrt{3}\mu^2/4$. The metric for this spacetime can be written as a static spherically symmetric spacetime:

$$ds^2 = -(1 - H^2 r^2) dt^2 + (1 - H^2 r^2)^{-1} dr^2 + r^2 d\Omega^2. \quad (5.4)$$

To match the observed acceleration of the universe, the effective cosmological constant must be set to $\Lambda \sim \mu^2 \sim H^2 \sim 10^{-56} \text{ cm}^{-2}$.

We now consider the spacetime in the solar system in this theory. First of all, the distances ($\sim 10^{13} \text{ cm}$) in the solar system are tiny compared with the distance $\mu^{-1} \sim 10^{28} \text{ cm}$, so $\mu r \ll 1$ everywhere in the solar system. Moreover, the densities and velocities in the solar system are sufficiently small that we can treat the spacetime as a small perturbation to the de Sitter spacetime. The spacetime should also be spherically symmetric and static. The most general static spherically symmetric perturbation to the vacuum de Sitter spacetime given by Eq. (5.4) can be written

$$ds^2 = -[1 + a(r) - H^2 r^2] dt^2 + [1 + b(r) - H^2 r^2]^{-1} dr^2 + r^2 d\Omega^2, \quad (5.5)$$

where the metric-perturbation variables $a(r), b(r) \ll 1$. In the following, we work to linear order in a and b , and also recall that $\mu r \ll 1$. However, a, b are *not* necessarily small compared with μr .

We now return to the trace of the field equation, given by Eq. (5.30), and solve it for the Ricci scalar $R(r)$ in the presence of the Sun. We write the trace equation in terms of a new function,

$$c(r) \equiv -\frac{1}{3} + \frac{\mu^4}{R^2(r)}, \quad (5.6)$$

and demand that $c(r) \rightarrow 0$ as $r \rightarrow \infty$ so that R approaches its background value of $\sqrt{3}\mu^2$ far from the source of the perturbation. Therefore, $c(r)$ parameterizes the departure of R from the vacuum solution, and we anticipate that $c(r)$ will be the same order in the perturbation amplitude as the metric perturbations $a(r)$ and $b(r)$. In terms of $c(r)$, Eq. (5.30) becomes an *exact* equation,

$$\square c(r) + \frac{\mu^2 c}{\sqrt{c + \frac{1}{3}}} = \frac{8\pi G}{3} T. \quad (5.7)$$

In the Newtonian limit appropriate for the solar system, the pressure p is negligible compared to the energy density ρ , and so $T = -\rho$. Neglecting terms that are higher order in $a(r)$, $b(r)$, and $\mu^2 r^2$, we are able to rewrite Eq. (5.7) as

$$\nabla^2 c + \sqrt{3}\mu^2 c = -\frac{8\pi G}{3}\rho, \quad (5.8)$$

where ∇^2 is the flat-space Laplacian operator. Note that in writing this equation, which is linear in $c(r)$, we have also neglected higher-order terms in $c(r)$. Below, we will check that the solutions we obtain have $c(r) \ll 1$ everywhere, consistent with our assumptions. The Green's function for Eq. (5.8) is $-\cos(3^{1/4}\mu r)/(4\pi r)$. Convolving this with the density gives us the solution to Eq. (5.8). However, we are restricting our attention to the region where $\mu r \ll 1$, so the Green's function reduces to that for the Laplacian operator. Therefore the equation we need to solve is $\nabla^2 c = -(8\pi G\rho)/3$. Integrating the right-hand side over a spherical volume of radius r gives us $-8\pi Gm(r)/3$, where $m(r)$ is the mass enclosed by a radius r . Using Gauss's law to integrate the left-hand side gives us $4\pi r^2 c'(r)$, where the prime denotes differentiation with respect to r . Thus, the equation for $c(r)$ becomes

$$\frac{dc}{dr} = -\frac{2Gm(r)}{3r^2} [1 + \mathcal{O}(\mu r)]. \quad (5.9)$$

Integrating Eq. (5.9) and using the boundary condition that $c \rightarrow 0$ as $r \rightarrow \infty$ gives us the solution $c(r) = (2/3)(GM/r)[1 + \mathcal{O}(\mu r)]$ for $r > R_\odot$. Note also that integration of the equation for $c'(r)$ to radii $r < R_\odot$ inside the star implies that the scalar curvature R remains of order μ^2 , even inside the star. We thus see that $c \ll 1$, so we were justified in using the linearized equation for $c(r)$.

This solution for $c(r)$ implies that

$$R = \sqrt{3}\mu^2 \left(1 - \frac{GM}{r} \right), \quad r > R_\odot. \quad (5.10)$$

We have thus shown that R is not constant outside the star and have already arrived at a result at odds with the constant-curvature Schwarzschild-de Sitter solution. Notice that had we (*incorrectly*) used $\rho = 0$ in Eq. (5.8), then the equations would have admitted the solution $c(r) = 0$; i.e., the constant-curvature solution. However, *this would be incorrect, because even though $\rho = 0$ at $r > R_\odot$, the solution to the differential equation at $r > R_\odot$ depends on the mass distribution $\rho(r)$ at $r < R_\odot$* . In other words, although the Schwarzschild-de Sitter solution is a static spherically symmetric solution to the vacuum Einstein equations, *it is not the solution that correctly matches onto the solution inside the star*. Note further that the solution for R both inside and outside the star is (to linear order in c),

$$R = \sqrt{3}\mu^2 \left[1 - \frac{3}{2}c(r) \right]. \quad (5.11)$$

Clearly, $1/R$ gravity produces a spacetime inside the star that is *very* different from general relativity. This result shows that in this theory one should not assume that $R = 8\pi G\rho$; this has led to some

confusion [222–224].

To proceed to the solutions for $a(r)$ and $b(r)$, we rearrange the field equation for $1/R$ gravity [Eq. (5.2)] to obtain equations,

$$R_{\mu\nu} = \left(1 + \frac{\mu^4}{R^2}\right)^{-1} \left[8\pi GT_{\mu\nu} + \frac{1}{2} \left(1 - \frac{\mu^4}{R^2}\right) R g_{\mu\nu} - \mu^4 (g_{\mu\nu} \nabla_\alpha \nabla^\alpha - \nabla_\mu \nabla_\nu) R^{-2}\right], \quad (5.12)$$

for the Ricci tensor in terms of the Ricci scalar. When the expression for R obtained from the trace equation is inserted into the right-hand side, we obtain equations for the nonzero components of the Ricci tensor,

$$R_t^t = 3H^2 - 6\pi G\rho - \frac{3}{4}\nabla^2 c, \quad (5.13)$$

$$R_r^r = 3H^2 - \frac{3c'(r)}{2r}, \quad (5.14)$$

$$R_\theta^\theta = R_\phi^\phi = 3H^2 - \frac{3}{4} \left(\frac{c'(r)}{r} + c''(r) \right), \quad (5.15)$$

where we have neglected terms of order $\mu^2 c$, $G\rho c$, and c^2 in all three expressions.

For the perturbed metric given by Eq. (5.5), the tt component of the Ricci tensor is (to linear order in small quantities) $R_t^t = 3H^2 - (1/2)\nabla^2 a(r)$. Applying $\nabla^2 c = -(8\pi G\rho)/3$ to Eq. (5.13) leaves us with an equation for $a(r)$,

$$\frac{1}{2}\nabla^2 a = 4\pi G\rho, \quad (5.16)$$

plus terms that are higher order in GM/r and μr . The solution to this equation parallels that for $c(r)$; it is

$$\frac{da}{dr} = 2G \frac{m(r)}{r^2} \quad (5.17)$$

both inside and outside the star. Outside the star, this expression may be integrated, subject to the boundary condition $a(r) \rightarrow 0$ as $r \rightarrow \infty$, to obtain the metric perturbation,

$$a(r) = -\frac{2GM}{r}, \quad r > R_\odot, \quad (5.18)$$

exterior to the star. Note that this recovers the Newtonian limit for the motion of nonrelativistic bodies in the solar system, as it should.

The rr component of the Ricci tensor is (to linear order in small quantities) $R_r^r = 3H^2 - (b'/r) - (a''/2)$. Given our solution for $a'(r)$ and $c'(r) = -(2/3)Gm(r)/r^2$, Eq. (5.14) becomes a simple

differential equation for $b(r)$,

$$\begin{aligned}\frac{db}{dr} &= \frac{Gm(r)}{r^2} - \frac{Gm'(r)}{r} \\ &= \frac{d}{dr} \left[\frac{-Gm(r)}{r} \right].\end{aligned}\tag{5.19}$$

Integrating this equation subject to the boundary condition $b(r) \rightarrow 0$ as $r \rightarrow \infty$ gives an expression for $b(r)$ that is applicable both inside and outside the star:

$$b(r) = -\frac{Gm(r)}{r}.\tag{5.20}$$

This expression for $b(r)$ and Eq. (5.17) for $a'(r)$ also satisfy Eq. (5.15) for the angular components of the Ricci tensor. The Ricci scalar [Eq. (5.10)] is recovered from the Ricci tensor components if terms higher order in $\mathcal{O}(\mu r^2 GM/r)$ are included in our expressions for $a(r)$ and $b(r)$.

The linearized metric outside the star thus becomes

$$ds^2 = -\left(1 - \frac{2GM}{r} - H^2 r^2\right) dt^2 + \left(1 + \frac{GM}{r} + H^2 r^2\right) dr^2 + r^2 d\Omega^2.\tag{5.21}$$

Noting that in the solar system, $Hr \ll 1$ and that the PPN parameter γ is defined by the metric,

$$ds^2 = -\left(1 - \frac{2GM}{r}\right) dt^2 + \left(1 + \frac{2\gamma GM}{r}\right) dr^2 + r^2 d\Omega^2,\tag{5.22}$$

we find that $\gamma = 1/2$ for $1/R$ gravity, in agreement with Chiba's claims [216, 225], and prior calculations; e.g., Refs. [226, 227]. We note that recent measurements give $\gamma = 1 + (2.1 \pm 2.3) \times 10^{-5}$ [228, 229].

Other authors have noted that Birkhoff's theorem—that the unique static spherically symmetric vacuum spacetime in general relativity is the Schwarzschild spacetime—is lost in $1/R$ gravity, and that there may be several spherically-symmetric vacuum spacetimes. Although this is true, what we have shown here is that the solar system spacetime is determined uniquely by matching the exterior vacuum solution to the interior solution. When this is done correctly, it is found that the theory predicts a PPN parameter $\gamma = 1/2$ in gross violation of the measurements, which require γ to be extremely close to unity.

A few final comments: It is important to note that the structure of $1/R$ gravity (for example, the way matter sources the metric) is completely different than the structure of general relativity, even in the limit $\mu \rightarrow 0$. In particular, the theory does not reduce to general relativity in the $\mu \rightarrow 0$ limit, and this can lead to confusion. This is due to the fact that the introduction of additional terms in the Einstein-Hilbert action brings to life a scalar degree of freedom that lies dormant in general relativity. We also note that Chiba's mapping of $f(R)$ theories to scalar-tensor theories is perfectly

valid; it amounts to no more than a variable change, from R to $\phi \equiv 1 + \mu^4/R^2$. The trace equation, Eq. (5.30), is then equivalent to the scalar-field equation of motion in the scalar-tensor theory. Also, the fact that general relativity is not recovered in the $\mu \rightarrow 0$ limit becomes particularly apparent in the scalar-tensor theory, as we will discuss elsewhere. Although we have restricted our analysis, for clarity, to $1/R$ theory, similar results can also be derived for other $f(R)$ theories. For example, the correct matching of the exterior and interior solutions can be used to distinguish between the spherically symmetric vacuum spacetimes for $R^{1+\delta}$ gravity discussed in Ref. [230].

5.3 Conditions on general $f(R)$ theories

In this section, we generalize the analysis of Ref. [231] to a broad class of $f(R)$ gravities, namely those theories that admit a Taylor expansion of $f(R)$ around the background value of the Ricci scalar. We work in the metric formalism, where the field equations are obtained by varying the action with respect to the metric and treating the Ricci scalar as a function of the metric. The Palatini formalism, which treats the Ricci scalar as a function of the connection and varies the action with respect to the connection and the metric independently, yields different field equations for $f(R)$ gravity and has been studied extensively elsewhere (e.g., Refs. [232–236]).

This section is organized as follows: In Section 5.3.1, we solve the linearized field equations around a spherical mass and find that the solution in the solar system is in agreement with the solution obtained using the equivalent scalar-tensor theory. When $f(R)$ satisfies a condition that is analogous to the scalar field being light in the equivalent scalar-tensor theory, the resulting spacetime is incompatible with solar system tests of general relativity. In Section 5.3.2, we consider how our analysis applies to several $f(R)$ gravity theories, including general relativity. This particular example illustrates the connection between $f(R)$ gravity and general relativity and clarifies the requirements for a general relativistic limit of an $f(R)$ theory. We summarize our conclusions in Section 5.6.

5.3.1 Weak-field solution around a spherical star

We consider gravitational theories with actions of the form

$$S = \frac{1}{2\kappa} \int d^4x \sqrt{-g} f(R) + S_m, \quad (5.23)$$

where $f(R)$ is a function of the Ricci scalar R and S_m is the matter action. The field equation obtained by varying the action with respect to the metric is

$$f_R R_{\mu\nu} - \frac{1}{2} f g_{\mu\nu} - \nabla_\mu \nabla_\nu f_R + \square f_R g_{\mu\nu} = \kappa T_{\mu\nu}, \quad (5.24)$$

where $f_R \equiv df/dR$. In previous studies, predictions of solar system dynamics in these theories were analyzed by appealing to an equivalence with scalar-tensor theories [216]. We review this equivalence in Appendix 1. Since the equivalent scalar-tensor theory is incompatible with solar system observations if the scalar field propagates on solar system scales, Ref. [216] concluded that the corresponding $f(R)$ theories are ruled out. We now show that this conclusion can be made *without* appealing to the equivalence between $f(R)$ and scalar-tensor gravity. Instead, we work directly with the linearized field equations about a spherical mass distribution. Our treatment clarifies and amends a similar analysis presented in Ref. [237], and we extend it to cases where the background value of the Ricci scalar equals zero.

We now find the metric that describes the spacetime around a spherical body in $f(R)$ gravity in the weak-field regime. To do this, we must choose a background spacetime around which to linearize the field equations. The only physically relevant choice is an isotropic and homogeneous background spacetime that solves Eq. (5.24) for some spatially uniform cosmological stress-energy tensor $T_{\mu\nu}^{\text{cos}}$. The evolution of the time-dependent and spatially homogeneous background scalar curvature $R_0(t)$ is determined by the trace of Eq. (5.24),

$$f_{R0}(t)R_0(t) - 2f_0(t) + 3\Box f_{R0}(t) = \kappa T^{\text{cos}}(t), \quad (5.25)$$

where $f_{R0} \equiv df/dR|_{R=R_0}$, $f_0 \equiv f(R_0)$ and $T^{\text{cos}} \equiv g^{\mu\nu}T_{\mu\nu}^{\text{cos}}$.

In order to investigate perturbations away from this background, we express the Ricci scalar as the sum of two components:

$$R(r, t) \equiv R_0(t) + R_1(r), \quad (5.26)$$

where $R_0(t)$ is the spatially homogenous background curvature that solves Eq. (5.25) and $R_1(r)$ is a time-independent perturbation to this background curvature. We assume that all derivatives of $f(R)$ are well defined at the present-day value of R_0 so that we may use a Taylor expansion of $f(R)$ around $R = R_0$ to evaluate $f(R_0 + R_1)$ and $f_R(R_0 + R_1)$. We will terminate the expansion by neglecting terms nonlinear in R_1 . Provided that the higher-order terms of the Taylor series do not cancel in some contrived way, neglecting the higher-order terms is only justified if the sum of the zeroth-order and linear terms is greater than all other terms in the Taylor expansion. Specifically, we require that

$$f_0 + f_{R0}R_1 \gg \frac{1}{n!}f^{(n)}(R_0)R_1^n, \quad (5.27)$$

$$f_{R0} + f_{RR0}R_1 \gg \frac{1}{n!}f^{(n+1)}(R_0)R_1^n, \text{ for all } n > 1, \quad (5.28)$$

where $f_{RR0} \equiv d^2f/dR^2|_{R=R_0}$ and $f^{(n)}(R_0) \equiv d^n f/dR^n|_{R=R_0}$.

Now we consider the trace of Eq. (5.24) with both a cosmological matter source described by

T^{cos} and a finite, time-independent, spherically symmetric matter source, described by T^{s} :

$$f_R R - 2f + 3\Box f_R = \kappa(T^{\text{cos}} + T^{\text{s}}). \quad (5.29)$$

Using first-order Taylor expansions to evaluate f_R and f and neglecting $\mathcal{O}(R_1^2)$ terms, we obtain a linearized version of Eq. (5.29):

$$3f_{RR0}\Box R_1(r) - \left[f_{R0}(t) - f_{RR0}(t)R_0(t) - 3\Box f_{RR0}(t) \right] R_1 = \kappa T^{\text{s}}. \quad (5.30)$$

To obtain this equation, we used the fact that $R_0(t)$ solves Eq. (5.25) to eliminate terms that are independent of R_1 . By dropping $\mathcal{O}(f_{RR0}R_1^2)$ terms from Eq. (5.30) while keeping the $f_{RR0}R_0R_1$ term, we have implicitly assumed that $R_1 \ll R_0$ if R_0 is nonzero. We will check that this condition is satisfied after the discussion following Eq. (F.21). If R_0 is zero, then the $\mathcal{O}(f_{RR0}R_1^2)$ is guaranteed to be smaller than the nonzero terms in Eq. (5.30) by virtue of Eq. (5.27). Note that if $f_{RR0} = 0$, as in general relativity, this equation becomes simply $f_{R0}R_1 = -\kappa T^{\text{s}}$. If in addition f_{R0} is nonzero then R_1 must vanish outside the star and hence the Schwarzschild-de Sitter solution becomes the solution to the field equation outside the source. However, if $f_{RR0} \neq 0$, this is no longer necessarily the case.

Finally, we take our background metric to be a flat Friedmann-Robertson-Walker (FRW) metric. We then consider a spherically symmetric perturbation to this background so that the linearized perturbed metric takes the form

$$ds^2 = -[1 + 2\Psi(r)]dt^2 + a(t)^2\{[1 + 2\Phi(r)]dr^2 + r^2d\Omega^2\}, \quad (5.31)$$

where the present value of $a(t)$ is one. When solving the field equations, we will keep only terms linear in the perturbations Ψ and Φ .

We will now solve Eq. (5.30) for a nonzero f_{RR0} . Since we confine our analysis to a static perturbation $R_1(r)$, \Box becomes the flat-space Laplacian operator ∇^2 . Restricting our analysis to a source with mass density $\rho(r)$ and negligible pressure, we may rewrite Eq. (5.30) as

$$\nabla^2 R_1 - m^2 R_1 = -\frac{\kappa\rho}{3f_{RR0}}, \quad (5.32)$$

where we have defined a mass parameter

$$m^2 \equiv \frac{1}{3} \left(\frac{f_{R0}}{f_{RR0}} - R_0 - 3\frac{\Box f_{RR0}}{f_{RR0}} \right). \quad (5.33)$$

Due to the evolution of $R_0(t)$, this mass parameter varies in time. However, the time-scale of variation in the cosmological background spacetime is comparable to the current Hubble time. Since this time-

scale is much longer than the time-scale of solar system dynamics, we may neglect the time variation of the background spacetime when considering the behavior of bodies within the solar system [227]. Therefore, for the purposes of this calculation, we take m to be time-independent.

The Green's function $G(r)$ for this differential equation depends on the sign of m^2 :

$$G(r) = \begin{cases} -\cos(mr)/(4\pi r) & m^2 < 0, \\ -\exp(-mr)/(4\pi r) & m^2 > 0, \end{cases} \quad (5.34)$$

where $m \equiv \sqrt{|m^2|}$. If $mr \ll 1$, then both Green's functions are approximately $-1/(4\pi r)$, which is the Green's function for Laplace's equation. In this case, the term proportional to m^2 in Eq. (E.5) may be neglected and the solution outside the star is given by

$$R_1 = \frac{\kappa}{12\pi f_{RR0}} \frac{M}{r}, \quad (5.35)$$

where M is the total mass of the source. We note that when applied to $1/R$ gravity with a static de Sitter background, this result agrees with the result presented in Ref. [231].

We emphasize that in order for this solution for R_1 to be valid, we must have $mr \ll 1$. Only when this condition is satisfied is the trace of the field equation well-approximated by Laplace's equation. This restriction was not mentioned in Ref. [237]. The physical interpretation of this constraint is clear when one considers the equivalent scalar-tensor theory. When one switches to a frame where the scalar degree of freedom is canonical, the effective mass of the scalar field evaluated in the Jordan frame is [216]

$$m_\varphi^2 = \frac{f_{R0}}{3} \left(\frac{1}{f_{RR0}} + \frac{R_0}{f_{R0}} - \frac{4f_0}{(f_{R0})^2} - \frac{2\kappa T^{\text{cos}}}{(f_{R0})^2} \right). \quad (5.36)$$

Since R_0 is the solution to Eq. (5.25), this expression may be simplified to

$$m_\varphi^2 = \frac{1}{3} \left(\frac{f_{R0}}{f_{RR0}} - R_0 - 6 \frac{\square f_{R0}}{f_{R0}} \right). \quad (5.37)$$

It is clear that both m_φ and m [defined by Eq. (5.33)] are of the same order. Therefore, the condition that $mr \ll 1$ is equivalent to demanding that the scalar field be light ($m_\varphi r \ll 1$). See Appendix A for more details.

In summary, Eq. (5.35) is a solution to the trace of the field equation within the solar system only if *the scalar degree of freedom propagates on solar system scales*. In terms of $f(R)$, the necessary condition is

$$|m^2| r^2 \equiv \left| \frac{1}{3} \left(\frac{f_{R0}}{f_{RR0}} - R_0 - 3 \frac{\square f_{RR0}}{f_{RR0}} \right) \right| r^2 \ll 1. \quad (5.38)$$

The triangle inequality tells us that the mass constraint given by Eq. (5.38) implies that

$$\left| \frac{f_{R0}}{f_{RR0}} \right| r^2 - \left| R_0 - 3 \frac{\square f_{RR0}}{f_{RR0}} \right| r^2 \ll 1. \quad (5.39)$$

Finally, since $\square f_{RR0}/f_{RR0} \sim H^2$, where $H \equiv \dot{a}/a$ is the current Hubble parameter, and we know that $R_0 r^2 \sim H^2 r \ll 1$ by cosmological constraints, the mass constraint implies that

$$\left| \frac{f_{R0}}{f_{RR0}} \right| r^2 \ll 1. \quad (5.40)$$

We will now use the expression for R_1 given by Eq. (5.35) to solve the field equations for the metric perturbations Ψ and Φ . As we did for the trace of the field equation, we simplify the field equations by replacing $f(R)$ and $f_R(R)$ with first-order Taylor expansions around the background value R_0 to obtain field equations that are linear in R_1 . Using Eq. (5.25) to simplify this expression, we obtain

$$f_{R0}(R_\nu^\mu - [R_0]_\nu^\mu) + f_{RR0}R_1R_\nu^\mu - \frac{1}{2}f_{R0}R_1\delta_\nu^\mu - f_{RR0}\nabla^\mu\nabla_\nu R_1 + \delta_\nu^\mu f_{RR0}\square R_1 = \kappa T_{\nu}^{\mu}, \quad (5.41)$$

where $[R_0]_\nu^\mu$ is the unperturbed FRW Ricci tensor and δ_ν^μ is the Kronecker delta. We neglected time derivatives of the background metric when deriving this equation. As previously noted, the time-scale of variations in R_0 is much longer than that of solar system dynamics, making the terms involving time derivatives of R_0 irrelevant to gravitational effects within the solar system.

We simplify Eq. (5.41) further by dropping several negligible terms. We continue to ignore terms that depend on the variation of the background spacetime by dropping terms that involve products of Φ , Ψ , and $f_{RR0}R_1$ with H and dH/dt . Since we are working in the weak-field regime, we neglect all terms that are nonlinear functions of the metric perturbations Φ and Ψ . Keeping only terms that are linear in Φ and Ψ allows us to replace the \square with the flat-space Laplacian operator ∇^2 since the perturbation is assumed to be static. Finally, we know from Eq. (5.35) that $f_{RR0}R_1 \sim \kappa M/r$, and we expect Ψ and Φ to be proportional to $\kappa M/r$ as well. Therefore, $f_{RR0}R_1\Psi$ and $f_{RR0}R_1\Phi$ are second-order quantities, and we may neglect them. With these simplifications, the $tt, rr, \theta\theta$ components of Eq. (5.41) are respectively

$$f_{R0}\nabla^2\Psi + \frac{1}{2}f_{R0}R_1 - f_{RR0}\nabla^2R_1 = \kappa\rho, \quad (5.42)$$

$$f_{R0}\left(-\Psi'' + \frac{2}{r}\Phi'\right) - \frac{1}{2}f_{R0}R_1 + \frac{2}{r}f_{RR0}R_1' = 0, \quad (5.43)$$

$$f_{R0}\left(\frac{1}{r}\Phi' - \frac{1}{r}\Psi' + \frac{2}{r^2}\Phi\right) - \frac{1}{2}f_{R0}R_1 + \frac{1}{r}f_{RR0}R_1' + f_{RR0}R_1'' = 0, \quad (5.44)$$

where the prime denotes differentiation with respect to r . The $\phi\phi$ component of Eq. (5.41) is

identical to the $\theta\theta$ component given by Eq. (5.44).

Recalling that R_1 solves Eq. (E.5) with $m^2 = 0$ so that $\nabla^2 R_1$ is proportional to the density ρ , Eq. (5.42) may be rewritten

$$f_{R0} \nabla^2 \Psi = \frac{2}{3} \kappa \rho - \frac{1}{2} f_{R0} R_1. \quad (5.45)$$

We express Ψ as the sum of two functions: $\Psi = \Psi_0 + \Psi_1$, where

$$f_{R0} \nabla^2 \Psi_0 = \frac{2}{3} \kappa \rho, \quad (5.46)$$

$$f_{R0} \nabla^2 \Psi_1 = -\frac{1}{2} f_{R0} R_1. \quad (5.47)$$

Provided that $f_{R0} \neq 0$, Eq. (5.46) may be integrated via Gauss's Law to give

$$\Psi_0'(r) = \frac{\kappa}{6\pi f_{R0}} \frac{m(r)}{r^2}, \quad (5.48)$$

where $m(r)$ is the mass enclosed in a sphere of radius r . If we assume that Ψ_0 vanishes as $r \rightarrow \infty$, we may integrate Eq. (5.48) to obtain

$$\Psi_0 = -\frac{\kappa}{6\pi f_{R0}} \frac{M}{r}, \quad (5.49)$$

outside the star. Solving Eq. (5.47) outside the star using Eq. (5.35) for R_1 yields

$$|\Psi_1| = \frac{1}{48\pi f_{RR0}} \kappa M r \ll \frac{1}{f_{R0}} \frac{\kappa M}{r}, \quad (5.50)$$

where the inequality follows from Eq. (5.40). Since $\Psi_0 \sim \kappa M / (f_{R0} r)$ outside the star we have shown that $|\Psi_1| \ll |\Psi_0|$. Therefore, we may neglect Ψ_1 and conclude that $\Psi = \Psi_0$ as given by Eq. (5.49). This expression for Ψ is used to define Newton's constant: $G \equiv \kappa / (6\pi f_{R0})$. For $1/R$ gravity with a static vacuum de Sitter background, $f_{R0} = 4/3$, so κ takes its standard value of $8\pi G$ and Eq. (5.49) matches the corresponding result in Ref. [231].

We now turn our attention to Eq. (5.43), which we will solve for Φ . First, we note that Eq. (5.35) implies that $R_1' = -R_1/r$. Therefore, the ratio of the second two terms in Eq. (5.43) is

$$\left| \frac{(1/2) f_{R0} R_1}{2 f_{RR0} R_1' / r} \right| \sim \left| \frac{f_{R0}}{f_{RR0}} \right| r^2 \ll 1, \quad (5.51)$$

where the inequality follows from Eq. (5.40). Consequently, the $f_{R0} R_1$ term is negligible, and we drop it from the equation. Differentiating Eq. (5.48) to find Ψ'' , and using Gauss's Law to obtain R_1' from Eq. (E.5) (with $m^2 = 0$), we may then rewrite Eq. (5.43) as

$$\Phi'(r) = \frac{\kappa}{12\pi f_{R0}} \frac{d}{dr} \left(\frac{m(r)}{r} \right). \quad (5.52)$$

Assuming that Φ vanishes as $r \rightarrow \infty$, this equation may be integrated to obtain

$$\Phi = \frac{\kappa}{12\pi f_{R0}} \frac{M}{r}, \quad (5.53)$$

outside the star. It is easy to verify that Eqs. (5.49) and (F.21) also satisfy the third field equation, Eq. (5.44).

We may now check our assumption that $R_1 \ll R_0$ for nonzero R_0 . From the expression for R_1 given by Eq. (5.35) and our definition that $\kappa \equiv 6\pi f_{R0}G$, we see that

$$\frac{R_1}{R_0} \lesssim \frac{1}{R_0} \left(\frac{GM}{R_s} \right) \frac{f_{R0}}{f_{RR0}}, \quad (5.54)$$

where R_s is the radius of the star. It is easy to check that this expression holds inside the star as well by integrating Eq. (E.5) into the interior of the star. Therefore, our assumption that $R_1 \ll R_0$ places an additional condition on the ratio f_{R0}/f_{RR0} :

$$\left| \frac{f_{R0}}{f_{RR0}} \right| \ll R_0 \left(\frac{R_s}{GM} \right) \text{ for } R_0 \neq 0. \quad (5.55)$$

If $f_{R0}/f_{RR0} \sim R_0$, as is the case for many $f(R)$ theories with nonzero R_0 , then this condition is always satisfied.

Thus we have shown explicitly that $\Psi = -2\Phi = -GM/r$ for all $f(R)$ theories with nonzero f_{RR0} that satisfy the conditions given by Eqs. (5.27), (5.28), (5.38), and (5.55). Transforming the metric given by Eq. (5.31) to isotropic coordinates, taking $a = 1$ today, and keeping only terms that are linear in GM/r gives

$$ds^2 = - \left(1 - \frac{2GM}{r} \right) dt^2 + \left(1 + \frac{GM}{r} \right) [dr^2 + r^2 d\Omega^2]. \quad (5.56)$$

It is clear that this spacetime is equivalent to a Parameterized Post-Newtonian spacetime with PPN parameter $\gamma = 1/2$. This result is in gross violation of observations; solar system tests require that $\gamma = 1 + (2.1 \pm 2.3) \times 10^{-5}$ [228, 229]. We also note that this result is in precise agreement with the results obtained using the equivalent scalar-tensor theory [216] (see also [225]).

5.3.2 Case studies

First, we show how we regain the results of general relativity if we take $f_{RR0} = 0$ and assume that our linearized Taylor expansion is a valid approximation. We note that general relativity [$f(R) = R$] satisfies both of these conditions.

Taking $f_{RR0} = 0$, Eq. (5.30) yields

$$f_{R0}R_1 = \kappa\rho. \quad (5.57)$$

When $f_{RR0} = 0$, the $f_{R0}R_1$ terms in the field equations [Eqs. (5.43–5.44)] are no longer negligible compared to the terms proportional to f_{RR0} since these terms vanish. The field equations then become

$$f_{R0}\nabla^2\Psi + \frac{1}{2}f_{R0}R_1 = \kappa\rho, \quad (5.58)$$

$$f_{R0}\left(-\Psi'' + \frac{2}{r}\Phi'\right) - \frac{1}{2}f_{R0}R_1 = 0, \quad (5.59)$$

$$f_{R0}\left(\frac{1}{r}\Phi' - \frac{1}{r}\Psi' + \frac{2}{r^2}\Phi\right) - \frac{1}{2}f_{R0}R_1 = 0. \quad (5.60)$$

Using Eq. (5.57), Eq. (5.58) becomes

$$f_{R0}\nabla^2\Psi = \frac{\kappa}{2}\rho, \quad (5.61)$$

and the solution outside the star is

$$\Psi = -\frac{\kappa}{8\pi f_{R0}}\frac{M}{r}. \quad (5.62)$$

From Eq. (5.59) and Eq. (5.60), we have

$$\frac{f_{R0}}{r^2}(r\Phi)' = \frac{\kappa}{2}\rho, \quad (5.63)$$

and the solution outside the star is

$$\Phi = \frac{\kappa}{8\pi f_{R0}}\frac{M}{r} = -\Psi. \quad (5.64)$$

Since $\Psi = -\Phi = -GM/r$, transforming to isotropic coordinates reveals that $\gamma = 1$ as expected.

With this result it is easy to see why the $\mu \rightarrow 0$ limit in $1/R^n$ ($n > 0$) gravity *does not* recover general relativity. In $1/R^n$ gravity [32], we have

$$f(R) = R - \frac{\mu^{2+2n}}{R^n}, \quad n > 0. \quad (5.65)$$

The static solution to Eq. (5.25) with $T^{\text{cos}} = 0$ is $R_0 = (n+2)^{1/(n+1)}\mu^2$, and $f_{RR0} \propto \mu^{-2}$. Therefore, f_{RR0} *diverges rather than vanishes* in the limit that $\mu \rightarrow 0$, and general relativity is *not* regained. The mass parameter for this theory has the dependence $m^2 \propto \mu^2$ and hence it vanishes in the limit that $\mu \rightarrow 0$. Furthermore, a Taylor series of Eq. (5.65) around R_0 is well behaved, and cosmological constraints tell us that $\mu \sim H$, so that $m^2 r^2 \ll 1$ in the solar system. We conclude that the analysis of general $f(R)$ gravity given in Section 5.3.1 applies and $\gamma = 1/2$ for these theories in a static background.

We note however that the static solution to Eq. (5.25) may not describe the current cosmological background in $1/R^n$ gravity. This solution is unstable, and without fine-tuning of the initial

conditions, this spacetime will evolve toward a spacetime with $R_0 \ll \mu^2$ [32]. In that case, we note that

$$\frac{(m!)^{-1} f^{(m)}(R_0) R_1^m}{f_0 + f_{R_0} R_1} \lesssim \left(\frac{GM}{r} \right)^m \ll 1, \quad (5.66)$$

$$\frac{(m!)^{-1} f^{(m+1)}(R_0) R_1^m}{f_{R_0} + f_{R R_0} R_1} \lesssim \left(\frac{GM}{r} \right)^m \ll 1, \quad (5.67)$$

so that Eqs. (5.27) and (5.28) are still satisfied. Furthermore, $m^2 \propto R_0$, so, as in the static-background case, the mass is of order the Hubble parameter today. Therefore, the $\gamma = 1/2$ result holds even during the late-time evolution of $1/R^n$ gravity.

Next we consider Starobinsky gravity [238] which has

$$f(R) = R + \frac{R^2}{\alpha^2}. \quad (5.68)$$

The static solution to Eq. (5.25) with $T^{\text{cos}} = 0$ is $R_0 = 0$ for this theory. Since $f(R)$ is a second-order polynomial, the first-order Taylor expansion of $f_R(R_0 + R_1)$ is exact. The $\mathcal{O}(R_1^2)$ term in the Taylor expansion of $f(R_0 + R_1)$ is suppressed compared to the linear term by a factor of GM/r and is therefore negligible. The mass parameter for this theory is proportional to α^2 , so Eq. (5.35) is a solution for R_1 if $\alpha^2 r^2 \ll 1$. Therefore, $\gamma = 1/2$ in this theory if $\alpha^2 r^2 \ll 1$ inside the solar system. If the mass parameter α is made large (i.e., if $\alpha \simeq 10^{12}$ GeV as proposed in Ref. [238]), then this condition is not satisfied and we cannot use the analysis in Section 5.3.1 to calculate γ for this theory.

Next we consider an example of a theory that uses two mass parameters: a hybrid between Starobinsky gravity and $1/R$ gravity. In particular, consider the function

$$f(R) = R + \frac{1}{\alpha^2} R^2 - \frac{\mu^4}{R}. \quad (5.69)$$

We then find that, as in the usual $1/R$ case, we have $R_0 = \sqrt{3}\mu^2$ (for a static background in vacuum). However,

$$m^2 = 3\mu^2 \left(\frac{\alpha^2}{9\mu^2 - \sqrt{3}\alpha^2} \right). \quad (5.70)$$

We can make this quantity as large as we want by letting the denominator tend towards zero, which gives the condition $\alpha \rightarrow 3^{3/4}\mu$. Thus, in this model we can violate the conditions listed in Section 5.3.1 by fine-tuning the parameters.

Finally, we consider power-law gravitational actions [230]:

$$f(R) = \left(\frac{R}{\alpha} \right)^{1+\delta}. \quad (5.71)$$

Assuming that $\delta \neq 1$, the static vacuum solution to Eq. (5.25) is $R_0 = 0$. If δ is not an integer, there will be some derivative that is not defined at $R = 0$, which causes the Taylor expansion to fail around that point. In particular, if it is supposed that $\delta \ll 1$, then at least the second derivative will be undefined so that the Taylor expansion will fail. For $\delta = 1$ the static vacuum background value R_0 is undetermined. However, if we choose $R_0 \neq 0$ then all of the conditions listed in Section 5.3.1 are satisfied and we conclude that $\gamma = 1/2$ in agreement with Ref. [239]. If δ is an integer greater than one, then the Taylor expansion around $f(R_0 = 0)$ is well-defined, but we cannot drop the terms that are nonlinear in R_1 since the linearized function vanishes. Therefore, this analysis is incapable of determining whether $f(R) = R^{1+\delta}$ gravity with $\delta \neq 1$ conflicts with solar system tests.

5.4 How to evade solar system tests in $f(R)$ -gravity²

The results of our previous discussion rely on the ability to linearize the equations so that $R_1/R_0 \ll 1$. This condition [given in Eq. (5.55)] can be rewritten in terms of the Newtonian potential of the source as

$$\left| \frac{R_0 f_{RR0}}{f_{R0}} \right| \gg \Psi_N, \quad (5.72)$$

where $R_0 \neq 0$. Let us explore what may happen when this condition is not met.

Going back to the trace of the field equation we have

$$\square f_R + \frac{dV}{df_R} = 0, \quad (5.73)$$

with

$$\frac{dV}{df_R} \equiv \frac{1}{3} [\kappa T + 2f - f_R R]. \quad (5.74)$$

We have rewritten the trace of the field equation in a suggestive form, identifying f_R as a new scalar degree of freedom. The extremum of this potential can be found by solving $dV/df_R = 0$ which gives

$$\kappa T = f_R R - 2f \quad (5.75)$$

We can see that in the limit that $f(R) \approx R$ and $f_R \approx 1$ (i.e., the GR limit) we regain the algebraic relationship between T and R at the extremum of this effective potential. The stability of this extremum is determined by the sign of the second derivative of the potential,

$$\frac{d^2V}{df_R^2} = \frac{1}{f_{RR}} [f_R - f_{RR} R]. \quad (5.76)$$

For the rest of our discussion we shall assume we are within a region of spacetime where $T \neq 0$.

²This section and Section 5.5 consists of previously unpublished work by the author.

Furthermore, we shall assume that $\kappa T \gg \{f(R_0), R_0 f_{R_0}, \dots\}$. Therefore, within the region, the effective potential is well approximated by

$$V \approx \frac{1}{3} \kappa T f_R. \quad (5.77)$$

Now, *if* the system is able to reach this extremum in some region of spacetime then Eq. (5.75) indicates the Ricci scalar is locally determined by the trace of the stress energy tensor in that region of spacetime. If we suppose that $f_R \approx 1$ and $f \ll \kappa T$ then from Eq. 5.75 we can see that we approximately regain the GR algebraic relationship between R and T . For the rest of this discussion we will assume that the extremum is a minimum [i.e., that the right-hand side of Eq. (5.76) is negative].

The question of whether a given system is able to reach this extremum can be understood by a simple argument [240]. We must compare the energy cost of fixing the field f_R at a high point in its effective potential against the gain in maintaining a nearly homogeneous field. The potential energy cost is simply given by $V \sim \kappa T(1 - f_R)$ whereas the gradient gain is $E \sim (1 - f_R)^2/R_s^2$. If the cost outweighs the gain then we have

$$(1 - f_R) \lesssim \kappa T R_s^2 \sim f_R \Psi_N. \quad (5.78)$$

This condition is the opposite of Eq. (5.72) if we have $1 - f_R \sim R f_{RR}$, which will typically be the case (it holds for $1/R$ theories). Therefore, when the assumption of linearity breaks down (i.e., $R_1/R_0 \gg 1$) the solution to the trace of the field equation forces the f_R towards the minimum in the potential and we regain an algebraic relationship between R and T . We expect the point at which this transition occurs is set by the location when $R_1(r)/R_0 \sim 1$.

We can see that the ability to reach the minimum in the effective potential then depends on the combination

$$\frac{f_{R0}}{R_0 f_{RR0}} \Psi_N. \quad (5.79)$$

When this quantity is small then linearization is accurate throughout the object; when it is unity or larger then linearization breaks down at some point and the field reaches the minimum of the effective potential. This quantity depends both on the local strength of the Newtonian potential as well as on the value of the background curvature and derivatives of $f(R)$. For example, in the case of the Sun we have $\Psi_N \approx 10^{-6}$. If we take the background curvature to be cosmological, $R_0 \sim H^2 = H_0^2 [\Omega_M(1+z)^3 + 1 - \Omega_M]$ and consider $f(R) = R + \mu^4/R$ with $\mu = \alpha H_0$ then the ratio in Eq. (5.79) evolves with redshift as

$$\frac{f_{R0}}{R_0 f_{RR0}} = \frac{\{1 + z[3 + z\Omega_M(3+z)]\}^2 - \alpha^4}{2\alpha^4}. \quad (5.80)$$

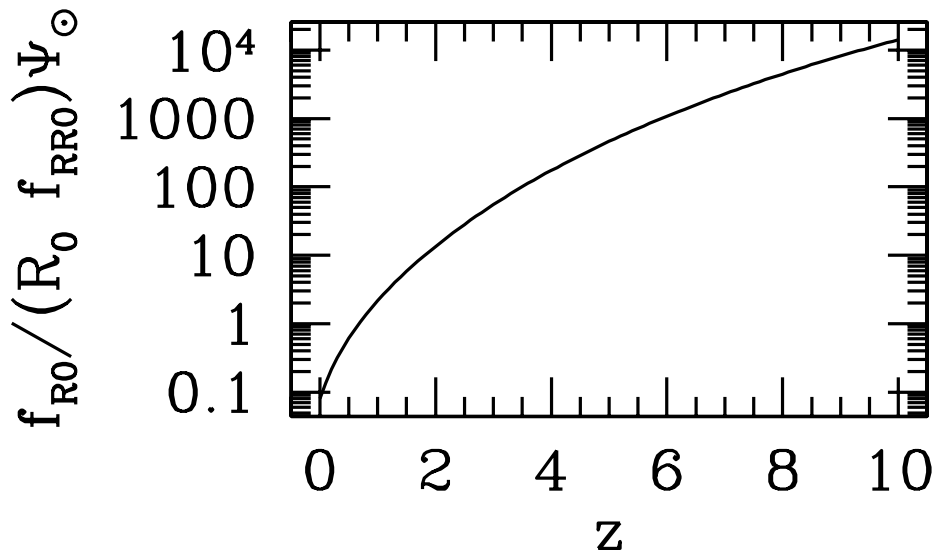


Figure 5.1: Here we show the evolution of the ratio given in Eq. (5.79) for the sun ($\Psi_{\odot} = 10^{-6}$). We have set $f(R) = R + u^4/R$ and $\Omega_M = 0.3$ and $\alpha = 0.05$. We can see that as we approach today ($z = 0$) the solution transitions from nonlinear to linear. Although this particular choice of $f(R)$ model is ruled out [241] the example shows how the solution can evolve from nonlinear to linear as a function of time.

We show a figure of this ratio in Fig. 5.1 for $\Omega_M = 0.3$ and $\alpha = 0.05$. We can see that the solution transitions from nonlinear to linear as we approach $z = 0$. Although this particular choice of $f(R)$ is ruled out due to the fact that it does not lead to an period of late acceleration [241], the time dependence of the linearity of the trace equation is instructive. We can also see that the linearity will be impacted by the environment around the object. For example, since the Sun resides within the galactic halo it may be inappropriate to consider the solution where the background curvature is taken to be cosmological. If instead our model is made slightly more complicated, we can ask whether the transition from a cosmological curvature to a galactic curvature forces the trace equation *in the galactic halo* to its minimum. It turns out that $\Psi_{\text{gal}} \sim 10^{-5}$ so that requiring the ratio to be larger than unity forces us to require

$$\frac{f_{R0}}{R_0 f_{RR0}} \gtrsim \Psi_{\text{gal}}^{-1}. \quad (5.81)$$

Using the same model as before this implies that

$$1 - f_R = \alpha^4 \lesssim \frac{\Psi_{\text{gal}}}{2 + \Psi_{\text{gal}}}, \quad (5.82)$$

and with $\Psi_{\text{gal}} \approx 10^{-5}$ this gives $1 - f_R \lesssim 5 \times 10^{-6}$. This compares very well with the limits placed on $1 - f_R$ in Ref. [240]. Then, when analyzing the linearity of the trace equation around the Sun the background curvature is given by $R_0 = \kappa \rho_{\text{gal}}$. Since $\rho_{\text{gal}} \approx 10^5 \rho_{\text{crit}} = 3 \times 10^5 H_0^2 / \kappa$ we have

$R_0 \approx 3 \times 10^5 H_0^2$ and $\alpha \approx 0.05$ so that in the solar system

$$\left(\frac{f_{R0}}{R_0 f_{RR0}} \Psi_N \right)_{\odot} \approx 7 \times 10^9 \gg 1, \quad (5.83)$$

and gravity around the Sun is well approximated by GR.

5.5 Testing for the universality of γ_{PPN}

The preceding discussion inspires a new test of gravity: a test of the universality of γ_{PPN} . In $f(R)$ -gravity we have just seen that $\gamma_{\text{PPN}} = 1/2$ when we are able to linearize the trace of the field equation. When nonlinear effects are important, GR is restored and we would measure $\gamma_{\text{PPN}} = 1$. Furthermore, we saw how the measurement of γ_{PPN} in $f(R)$ gravity depends on redshift as well as on environment (through the choice of the appropriate value for the background curvature R_0). Therefore, it is interesting to test gravity by measuring γ_{PPN} around various objects at various redshifts and to test whether we obtain a universal value. Data sets which would allow a test of the universality of γ_{PPN} are currently being assembled.

There are two obvious ways of constructing such a data set. First, we can combine measurements of the velocity dispersion of stars in massive galaxies, in order to get a measure of their dynamical masses, with measurements of strong lensing around these galaxies. A comparison of these two measurements, along with a model of the mass distribution in the lens galaxy, yields a measurement of γ_{PPN} . We have limited knowledge of the distribution of mass within these lenses so we must also consider degeneracies between various parameters (such as the slope of the density profile). As discussed below, we expect a one sigma error on γ_{PPN} of ~ 0.3 . Another way of building this data set is to use measurements of strong lens timing delays along with an external determination of H_0 (such as from the Hubble Key Project [242]). However, given the large uncertainties and systematic errors inherent to measurements of timing delays, we only concentrate on the latter method.

5.5.1 Universality of γ_{PPN} from strong lensing

The original idea of measuring γ_{PPN} from strong lenses was first discussed in Ref. [243]. It was first applied to real data in Ref. [244]. We can understand how we may measure γ_{PPN} from the data using the following simplified model. We suppose that the density distribution is well approximated by a singular isothermal sphere,

$$\rho = \frac{\sigma^2}{2\pi G r^2}, \quad (5.84)$$

where σ is the velocity dispersion. We imagine placing this galaxy within an FRW universe so that the scalar line element reads

$$ds^2 = a^2 \{ -(1 - 2\Phi)d\tau^2 + (1 + 2\Psi)dx^i dx^j \gamma_{ij} \}, \quad (5.85)$$

and we write $\Phi = \gamma_{\text{PPN}}\Psi$. The angular size of the Einstein ring for this lens is

$$\Theta_E = (1 + \gamma_{\text{PPN}})2\pi \frac{\sigma^2 D_{LS}}{c^2 D_S}, \quad (5.86)$$

where D_X is the angular diameter distance between the lens and the source ($X = LS$) and between us and the source ($X = S$). We assume that we have measured the spectrum of the lens, so that we have a measurement of the redshift z as well as of σ from the broadening of the spectral features [245]. Finally, we fix a fiducial cosmology although the choice of cosmological parameters do not have a big impact. We are then able to constrain γ_{PPN} . In practice, the problem is more complicated since we do not have such a simple model for the lens structure.

We can generalize this model in the following way due to Ref. [246]. First, we assume that the total mass density of the galaxy can be decomposed into a spherically symmetric part, $\nu_M(r)$, and a small departure from spherical symmetry. We then assume that the spherically symmetric part is dominant in determining the dynamics of the system. We suppose that the stars are a trace component of the total mass and have a power law distribution

$$\nu_s(r) = \nu_{s,0} r^{-\delta}. \quad (5.87)$$

The total mass density follows

$$\nu_M(r) = \nu_{M,0} r^{-\alpha}. \quad (5.88)$$

Finally, we allow for a non-zero anisotropy in the stellar velocity ellipsoid which is constant with radius,

$$\beta = 1 - \frac{\langle \sigma_\theta^2 \rangle}{\langle \sigma_r^2 \rangle}. \quad (5.89)$$

We then obtain the functional form for the radial velocity dispersion from the spherically symmetric Jeans equation [247] for the stellar component sourced by the total mass density. Using the fact that the line of sight velocity dispersion is related to the radial velocity dispersion through $\langle \sigma_{||}^2 \rangle = [z - \sqrt{1 - \beta}\rho]^2 / (z^2 + \rho^2) \langle \sigma_r^2 \rangle$ where $\rho \equiv \sqrt{x^2 + y^2}$ we have an expression for the luminosity weighted line of sight velocity dispersion within a circular aperture of projected radius R_A [which we denote by $\langle \sigma_{||}^2 \rangle(< R_A)$],

$$\langle \sigma_{||}^2 \rangle(< R_A) = \frac{1}{\pi} \left(\frac{GM_E}{R_E} \right) f(\alpha, \delta, \beta) \left(\frac{R_A}{R_E} \right)^{2-\alpha}, \quad (5.90)$$

where

$$f(\alpha, \delta, \beta) = 2\sqrt{\pi} \left(\frac{\delta - 3}{(\xi - 3)(\xi - 2\beta)} \right) \left\{ \frac{\Gamma[(\xi - 1)/2]}{\Gamma[\xi/2]} - \beta \frac{\Gamma[(\xi + 1)/2]}{\Gamma[(\xi + 2)/2]} \right\} \left\{ \frac{\Gamma[\delta/2]\Gamma[\alpha/2]}{\Gamma[(\delta - 1)/2]\Gamma[(\alpha - 1)/2]} \right\}, \quad (5.91)$$

and

$$\frac{M_E}{R_E^{3-\alpha}} = -\pi^{3/2} \nu_{M,0} \frac{\Gamma[(\alpha - 1)/2]}{\Gamma[\alpha/2]}. \quad (5.92)$$

Measurements of the mass M_E and the radius which encloses this mass, R_E , are made through lensing. Even though we are strictly interested in measuring the spherically symmetric part of the total mass density, the ellipticity of the lens must be taken into account when fitting the lensed images. Therefore, we model the lens as a singular isothermal ellipsoid (SIE) [248] and then expand the result in the ellipticity only keeping the lowest (spherically symmetric) terms. We note that lensing due to a spherically symmetric mass distribution is sensitive to both the total mass enclosed within a radius as well as the slope of the mass enclosed. The dependence on the total mass enclosed is independent of the specific density model used to analyze the data; it is the dependence on the slope that introduces a dependence on the specific model. However, as noted in Ref. [249], this model dependence results in a systematic error which is less than a few percent.

The SIE lens model yields a projected mass density (appropriately centered and rotated)

$$\Sigma(\vec{\xi}) = \frac{\sqrt{q_{\text{SIE}}}\sigma_{\text{SIE}}^2}{2G\sqrt{\xi_1^2 + q_{\text{SIE}}^2\xi_2^2}}, \quad (5.93)$$

where $q_{\text{SIE}} = (b/a)$ is the axial ratio of constant elliptical surface density contours. For $q_{\text{SIE}} \approx 1$ we may expand the above projected mass density to find the spherically symmetric part,

$$\Sigma_0(\xi) = \frac{\sigma_{\text{SIE}}^2}{2G\xi}. \quad (5.94)$$

Associated with Σ_0 is an Einstein radius

$$R_E = 4\pi \frac{\sigma_{\text{SIE}}^2}{c^2} \frac{D_L D_{LS}}{D_S}, \quad (5.95)$$

Integrating the projected mass density inside of R_E this model yields

$$M_E = 4\pi^2 \frac{\sigma_{\text{SIE}}^4}{c^2 G} \frac{D_L D_{LS}}{D_S}. \quad (5.96)$$

In order to introduce γ_{PPN} we note that the deflection angle is given in terms of the projected mass as

$$\vec{\alpha} = \frac{4G}{c^2} \frac{1 + \gamma_{\text{PPN}}}{2} \int \Sigma(\vec{\xi}') \frac{\vec{\xi} - \vec{\xi}'}{|\vec{\xi} - \vec{\xi}'|^2} d^2\xi'. \quad (5.97)$$

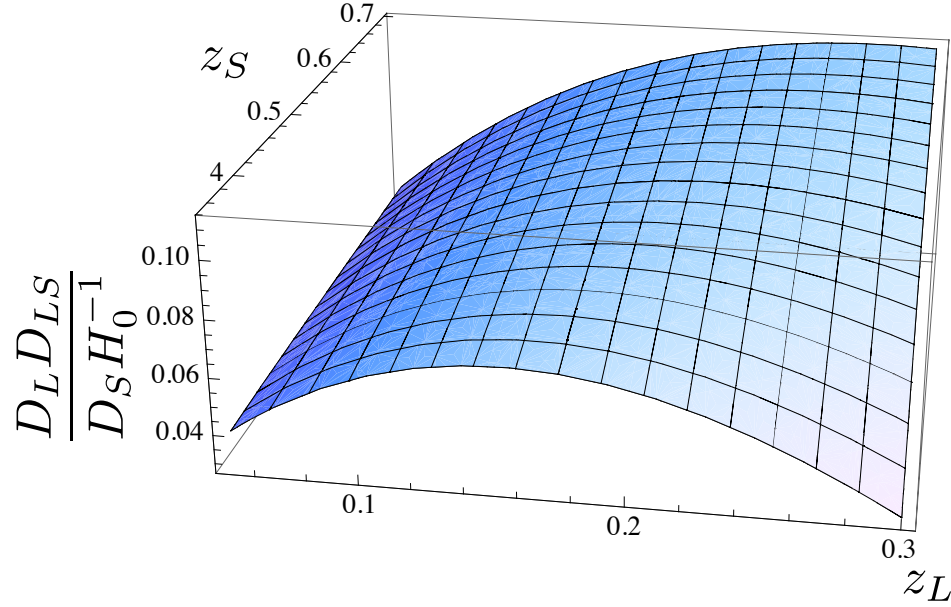


Figure 5.2: Here we show ratio $(D_L D_{LS}) / (D_S H_0^{-1})$ as a function of the redshift of the lens z_L and the redshift of the source z_S . We have fixed the cosmology to $\Omega_M = 0.3$ and $\Omega_\Lambda = 1 - \Omega_M$. We can see that this factor can range from ~ 0.1 (for the largest z_L and the largest difference with z_S) to ~ 0.01 (for the smallest z_L and the largest difference with z_S).

Therefore we need only make the substitution $\sigma_{\text{SIE}}^2 \rightarrow [(1 + \gamma_{\text{PPN}})/2]\sigma_{\text{SIE}}^2$. With this we can write our measured ‘lens’ mass and radius in terms of the dynamical mass and radius,

$$M_E^{\text{lens}} = \left(\frac{1 + \gamma_{\text{PPN}}}{2} \right)^2 M_E^{\text{dyn}}, \quad (5.98)$$

$$R_E^{\text{lens}} = \left(\frac{1 + \gamma_{\text{PPN}}}{2} \right) R_E^{\text{dyn}}, \quad (5.99)$$

In order to get a sense of the lens galaxy masses that we are working with, we write the mass enclosed can be expressed in terms of σ_{SIE}

$$M_E^{\text{dyn}} = 3 \times 10^{10} M_\odot h^{-1} \left(\frac{\sigma_{\text{SIE}}}{100 \text{ km/s}} \right)^4 \left(\frac{1 + \gamma_{\text{PPN}}}{2} \right)^{-2} \frac{D_L D_{LS}}{D_S H_0^{-1}}. \quad (5.100)$$

In Fig. 5.2 we show the ratio $D_L D_{LS} / (D_S H_0^{-1})$ for a range of lens and source redshifts.

We can now express the predicted luminosity averaged line-of-sight velocity dispersion in terms

of the observables,

$$\langle \sigma_{\parallel}^2 \rangle (< R_A) = \frac{1}{\pi} \left(\frac{GM_E^{\text{dyn}}}{R_E^{\text{dyn}}} \right) f(\alpha, \delta, \beta) \left(\frac{R_A}{R_E^{\text{dyn}}} \right)^{2-\alpha}, \quad (5.101)$$

$$= \left(\frac{2}{1 + \gamma_{\text{PPN}}} \right) \sigma_{\text{SIE}}^2 f(\alpha, \delta, \beta) \left(\frac{1 + \gamma_{\text{PPN}}}{2} \right)^{\alpha-2} \left(\frac{\theta_A c^2 D_S}{\sigma_{\text{SIE}}^2 D_{LS}} \right)^{2-\alpha}, \quad (5.102)$$

where we have rewritten $R_A = \theta_A D_L$ and θ_A is the angular aperture (in radians) of the spectrograph which measures the line of sight velocity dispersion. For the Sloan Digital Sky Survey (SDSS) it is approximately 1.188 arcseconds. In practice we are able to determine σ_{SIE}^2 , z_L , z_S , δ , and $\langle \sigma_{\parallel}^2 \rangle$ from observations. Given that the lens galaxies are well represented by a de Vaucouleurs profile (where the projected luminosity profile is given by $I(R) \propto \exp[-7.67(R/R_e)^{1/4}]$) and the fact that the SLACS observations probe around $0.5R_e$ we have that $\delta \approx 2.6$. We are then left with three free parameters, γ_{PPN} , α , and β . Let us investigate correlations between these parameters.

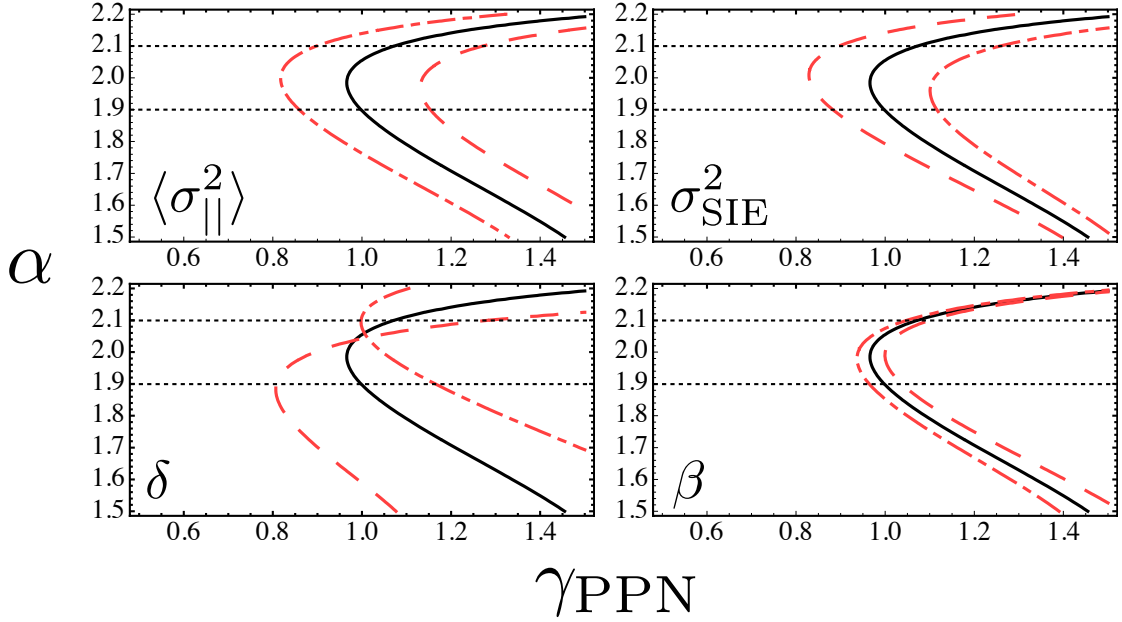


Figure 5.3: Here we show the constraints in the α - γ_{PPN} plane while varying $\langle \sigma_{\parallel}^2 \rangle^{1/2}$, σ_{SIE} , β , and δ . The solid black line corresponds to the fiducial model where we have chosen $\gamma_{\text{PPN}} = 1$ at $\alpha = 2$. The red long-dashed (dashed-dot) line corresponds to plus (minus) the fiducial value of the parameter indicated in the upper left of each panel. For $\langle \sigma_{\parallel}^2 \rangle^{1/2}$ we took ± 10 km/s, the typical error in this parameter from SDSS observations; for σ_{SIE} we took ± 10 km/s to explore the effects of any systematic error in a determination of this parameter; for β we took ± 0.1 ; for δ we took ± 0.1 .

We shall consider a fiducial lens with $z_L = 0.1$ and $z_S = 0.6$ with $\langle \sigma_{\parallel}^2 \rangle^{1/2} = 247$ km/s, $\sigma_{\text{SIE}} = 280$ km/s, $\beta = 0$ and $\delta = 2.6$. These choices ensure that at $\alpha = 2$ we have $\gamma_{\text{PPN}} = 1$. Fig. 5.3 shows the results of varying $\langle \sigma_{\parallel}^2 \rangle^{1/2}$, σ_{SIE} , β , and δ in the α - γ_{PPN} plane.

First, it is clear that we must place a prior on the value of α in order to measure γ_{PPN} . For

concreteness we show dotted lines corresponding to $\alpha = 2 \pm 0.1$, however a physically motivated choice could use intrinsic scatter in α as observed in low redshift systems [244]. In using this low redshift data we must assume that the intrinsic scatter and central value do not evolve significantly with redshift. From Fig. 5.3 we can see that a $\sim 3\%$ error on the line-of-sight velocity dispersion leads to a $\sim 20\%$ error in γ_{PPN} . If we systematically overestimated (underestimated) σ_{SIE} then we obtain a systematically lower (higher) value for γ_{PPN} . Shifting the power-law index for the luminous material affects the determination of γ_{PPN} by increasing (decreasing) γ_{PPN} for higher (lower) values of δ . Finally, varying the velocity anisotropy (β) has little effect.

Our main goal in this study is to look at the statistics of a collection of measurements of γ_{PPN} . Our discussion of $f(R)$ gravity as well as Ref. [250] indicates that within the context of scalar-tensor theories of gravity we can expect $1/2 \leq \gamma_{\text{PPN}} \leq 1$. Supposing that we have a collection of N measurements of γ_{PPN} with best fit values distributed between $1/2 + C \leq \gamma_{\text{PPN}} \leq 1 + C$ (where C takes into account any systematic error) we want to understand when we would be able to distinguish between a universal value for γ_{PPN} and a non-universal value.

The simplest assumption for the distribution of values is for any given measurement to have either $\bar{\gamma}_{\text{PPN}} = 1/2 + C$ or $\bar{\gamma}_{\text{PPN}} = 1 + C$ (where the bar denotes the mean value). We can then consider our N measurements as coming from two different distributions each with a different mean value for γ_{PPN} and different variance. Looking at Eq. (5.102) we can see that a fixed error in $\langle \sigma_{\parallel}^2 \rangle^{1/2}$ we have the error on σ_{PPN} scales as $(1 + \gamma_{\text{PPN}})^{3/2}$ (with $\alpha = 2$). Therefore, a smaller best fit value of γ_{PPN} gives a smaller error on γ_{PPN} for the same error in $\langle \sigma_{\parallel}^2 \rangle^{1/2}$. We show this error (for a fiducial $\alpha = 2$) in Fig. 5.4 as a function of the error in $\langle \sigma_{\parallel}^2 \rangle^{1/2}$. Current measurements have an error in $\langle \sigma_{\parallel}^2 \rangle^{1/2}$ of $\sim 3\%$ (which, for the lenses we are considering, corresponds to ~ 10 km/s). However, we can see that if we were able to reduce this by a factor of two we would improve our determination of γ_{PPN} by the same factor.

In order to understand when we might expect to be able to make a statistically significant statement concerning the universality of γ_{PPN} we consider several mock data sets which consist of values for γ_{PPN} pulled from two distributions. One is a normal distribution with a mean γ_{PPN} at 1 and a variance of either 0.3 (corresponding to an error of 10 km/s [3.5%] for $\langle \sigma_{\parallel}^2 \rangle^{1/2}$), 0.2 (corresponding to an error of 7 km/s [2.5%] for $\langle \sigma_{\parallel}^2 \rangle^{1/2}$), or 0.15 (corresponding to an error of 5 km/s [1.7%] for $\langle \sigma_{\parallel}^2 \rangle^{1/2}$). The other population is also a normal distribution with a mean at γ_{PPN} at 1/2 and a variance of either 0.2, 0.15, or 0.1, respectively. We consider mock data sets with 20, 50, and 100 measurements. Finally, for each mock data set we consider three distributions for the value of γ_{PPN} : 50–50, 30–70, and 10–90. For each data set we perform a standard Lilliefors test [251, 252] in order to compare our full distribution of values for γ_{PPN} against the null hypothesis that the values come from a single normal distribution. The Lilliefors test is related to the more common Kolmogorov-Smirnov test except it does not require *a priori* information on the mean and

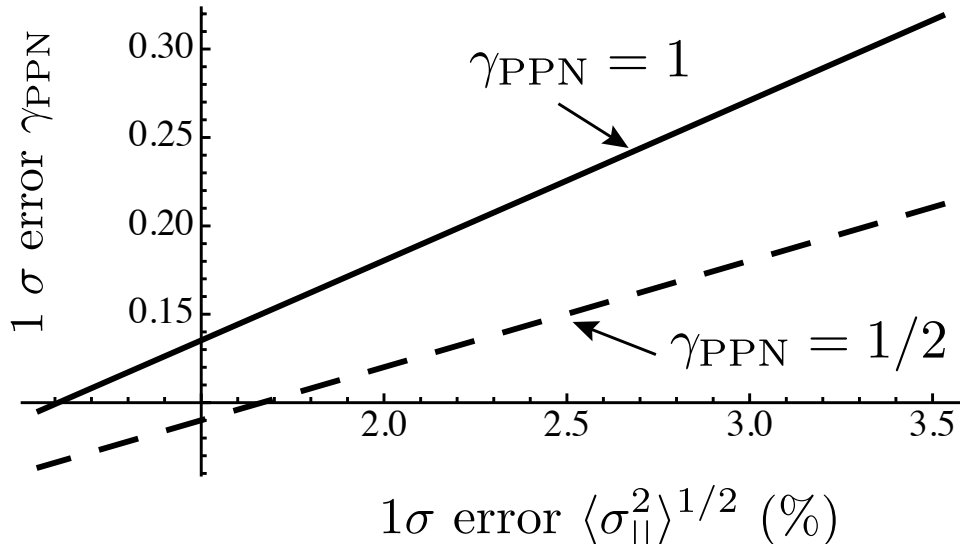


Figure 5.4: Here we show the error in γ_{PPN} as a function of the error in the line-of-sight velocity dispersion of the lens galaxy. We have assumed that the dominant statistical error will come from the line-of-sight velocity dispersion of the lens galaxy.

variance of the null hypothesis normal distribution. For each case we produce 500 realizations. We show the results in Fig. 5.5. In that figure we can see many trends that we would expect. As the accuracy of the measurement of γ_{PPN} improves and/or the total number of measurements in the set increases the ability to reject the hypothesis of a single Gaussian distribution for the total data set improves.

For surveys with a percent error in $\langle \sigma_{||}^2 \rangle^{1/2}$ of $\sim 3.5\%$ we find that if the distribution of values of γ_{PPN} is any different then 50-50 then we cannot reject the null hypothesis. This is because an accuracy of 3.5% in $\langle \sigma_{||}^2 \rangle^{1/2}$ corresponds to an error on γ_{PPN} of 0.3 , which, for a separation in the mean of the distributions of 0.5 is well within the 1σ of both distributions. Therefore, if we wish to test the universality of γ_{PPN} for distributions different from 50-50 we must obtain an accuracy better than ~ 0.3 .

Besides looking at the distribution of measurements of γ_{PPN} we also want to look for correlations between the values of γ_{PPN} and other measurements associated with those values. One obvious choice is to look for a correlation with redshift, since, as we saw before, the value of γ_{PPN} may evolve with redshift for the example of $f(R)$ gravity. Furthermore, we may want to look for correlations between γ_{PPN} and the environment around the lens. As mentioned previously, Ref. [244] has already compiled a collection of 15 measurements of γ_{PPN} . Their analysis used strong lenses measured in the Strong Lens ACS survey (SLACS) as described in their paper. In their analysis they assumed that the value of γ_{PPN} is universal and averaged their measurements to obtain an mean value of $\gamma_{\text{PPN}} = 0.98 \pm 0.07$ at 68% confidence. For the rest of this section we will take another look at their measurements in light of testing the universality of γ_{PPN} .

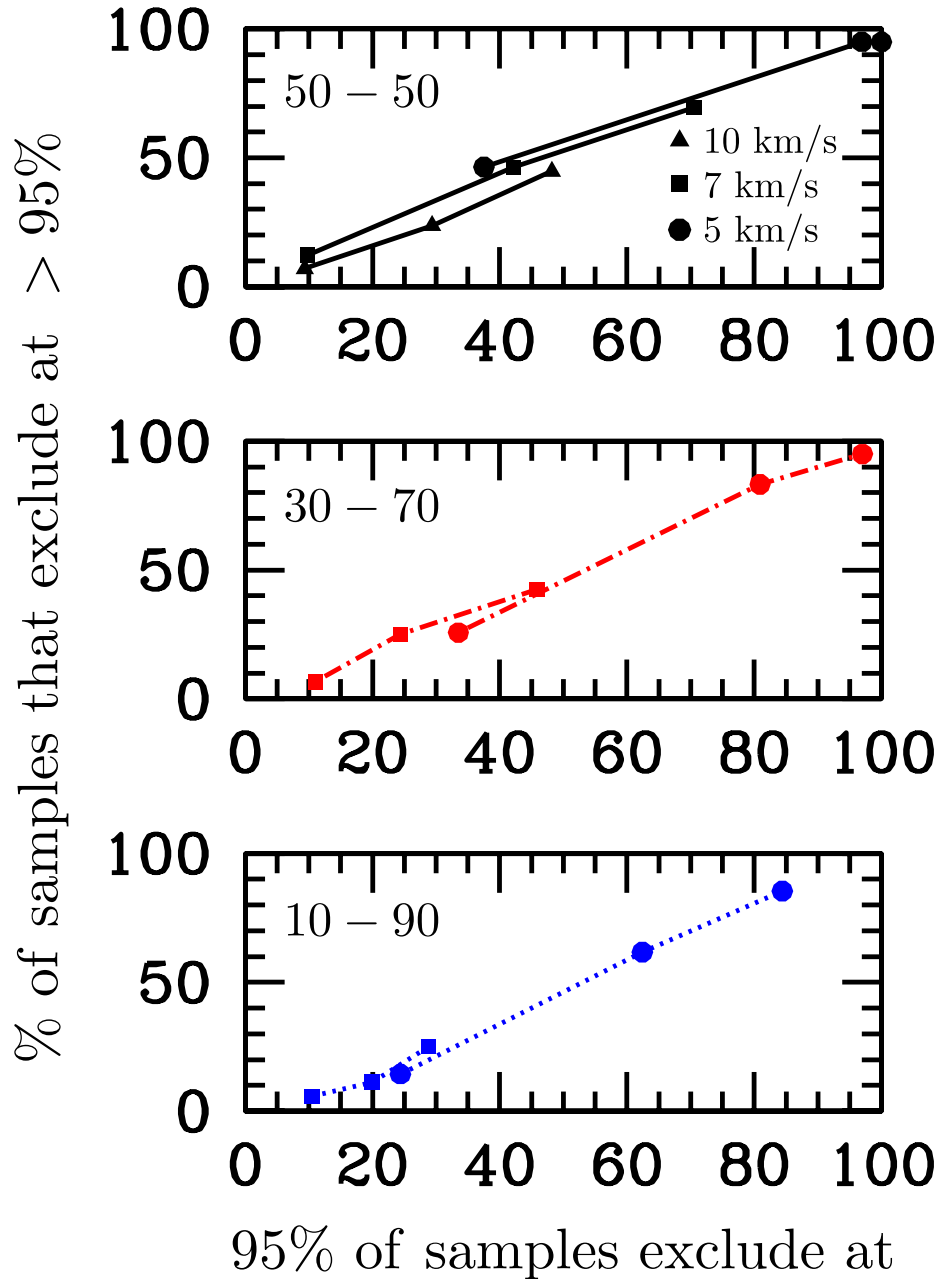


Figure 5.5: Here we show the results of the Lilliefors test on our mock data sets. Each panel shows a different distribution of values of γ_{PPN} (i.e., 30–70 means that 30% of the measurements come from the $\bar{\gamma}_{\text{PPN}} = 1/2$ distribution and 70% from $\bar{\gamma}_{\text{PPN}} = 1$). The three different point shapes correspond to different assumptions on the accuracy with which the velocity dispersion is measured in the lens galaxies. The lowest point on each curve corresponds to a data set with $N_{\text{tot}} = 20$, the second point corresponds to $N_{\text{tot}} = 50$ and the highest point to $N_{\text{tot}} = 100$. The x -axis gives the significance at which the null (normal) hypothesis is excluded for 95% of the trials and the y -axis gives the percent of samples which exclude the null hypothesis at 95%.

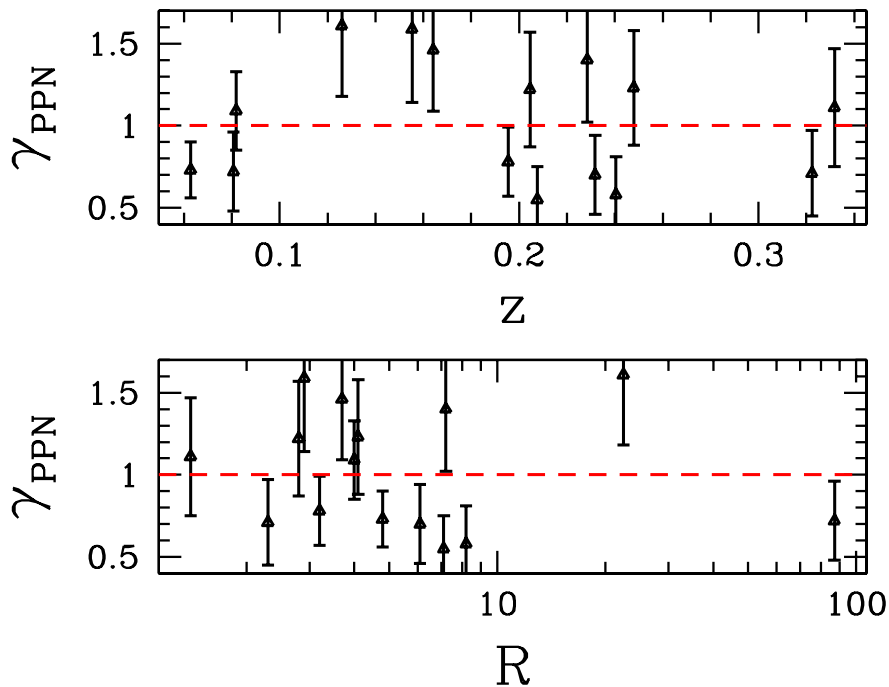


Figure 5.6: Here we show measurements of γ_{PPN} from the 15 SLACS objects as analyzed in Ref. [244]. We show these results as a function of the redshift of the lens as well as a function of the richness of the environment around the lens [253]. Because of the small number of measurements we do not attempt to search for any correlations. However, the SLACS survey reports that it will increase the number of lenses to ~ 100 in the near future [254]. With such an increase a search for statistically significant correlations may be possible.

In order to investigate a possible correlation between γ_{PPN} and the environment of the SLACS objects we use the results of Ref. [253] which presented estimates for the richness of the environments surrounding each of the 15 SLACS objects. Although the lens galaxies are necessarily massive and hence preferentially occur in over dense regions, the SLACS objects are chosen to be ‘isolated’ in the sense that those systems with two similar galaxies within ~ 4 Einstein radii from each other are excluded from the sample [255].

We present the results in Fig. 5.6. The upper panel gives the value of γ_{PPN} as a function of redshift. The lower panel shows γ_{PPN} as a function of the richness of the environment around the given lens. Finally, we performed a Lilliefors test on this data and found that the null hypothesis of a single normal distribution had a probability of 5.3%. Said another way, this rejects the null hypothesis at nearly 2σ . Splitting the data set into two subsets with higher and lower values of γ_{PPN} and performing the same test we find that the lower (higher) subset has a 11% (53%) probability of coming from a single normal distribution according to the Lilliefors statistic. We then fit a normal distribution to these subsets and found that the lower (higher) subset has a mean $\bar{\gamma}_{\text{PPN}} = 0.72$ ($\bar{\gamma}_{\text{PPN}} = 1.33$) and a variance $\sigma_{\gamma_{\text{PPN}}} = 0.14$ ($\sigma_{\gamma_{\text{PPN}}} = 0.2$). Producing 1000 mock data sets with

these parameters we find that $\sim 20\%$ of the trials exclude the null hypothesis at 95%. We note that the width of the distribution for each subset is much smaller than the errors attributed to each measurement (~ 0.2 for $\bar{\gamma}_{\text{PPN}} = 0.72$ and ~ 0.3 for $\bar{\gamma}_{\text{PPN}} = 1.33$) and attribute this to the paucity of the data. We must keep in mind that the number of measurements in this data set are too small (15) to perform any statistically significant tests. This is especially true if we want to look for any significant correlations between these parameters. Instead, the above analysis is meant to be an example of the types of statistical tools we can use in order to test for the universality of γ_{PPN} . We note that the SLACS survey will increase the number of measured lens systems to roughly 100 in the near future which will greatly increase the statistics and should enable such an analysis [254].

5.6 Conclusions

By analyzing the field equations around a spherically symmetric mass, we have shown that, in agreement with the analysis in Ref. [216], the PPN parameter γ of general $f(R)$ gravity is $\gamma = 1/2$ given the following conditions:

- I. The Taylor expansions of $f(R)$ and df/dR about the current background value $R = R_0$, where R_0 solves Eq. (5.25), are well defined and dominated by terms that are linear in deviations away from $R = R_0$. If R_0 is non-zero, then the deviations from R_0 are small compared to R_0 . This condition may be re-expressed as Eq. (5.55) and is closely related to the third condition stated below.
- II. The second derivative of $f(R)$ with respect to R is nonzero when evaluated at the background value of $R = R_0$.
- III. The mass parameter given by Eq. (5.33) respects the condition $mr \ll 1$ within the solar system.

For theories with one extra mass parameter and non zero R_0 , as in $1/R$ gravity, it is reasonable to assume that $f_{R0}/f_{RR0} \sim R_0$. In that case, the latter part of the first condition is always true and the third condition is satisfied provided that $R_0 r^2 \ll 1$ within the solar system. However, for theories with multiple mass parameters, such as the Starobinsky- $1/R$ hybrid presented in this chapter, it is possible that this condition can be violated.

The second and third conditions listed above correspond to synonymous conditions in the scalar-tensor treatment: $f(R)$ and scalar-tensor gravity are equivalent only if the second derivative of $f(R)$ is nonzero, and $\gamma = 1/2$ only if the scalar field is light enough to propagate through the solar system. Therefore, we have also verified that, contrary to the claim of some authors [217–221], calculating the solar system predictions of $f(R)$ gravity using the equivalent scalar-tensor theory is a valid

technique.

We have described a new test of gravity which attempts to establish whether the measurement of the parameterized post Newtonian parameter, γ_{PPN} , has a universal value. Our experience with $f(R)$ gravity gives us an example of an alternative gravity theory for which the value of γ_{PPN} depends both on the local environment as well as on redshift. We explored whether we can use recent measurements of γ_{PPN} around 15 strong lenses in the SLACS survey in order to test its universality. Future results from this survey promise to increase the number of measurements to ~ 100 greatly improving our ability to determine whether γ_{PPN} is a universal parameter.

Acknowledgments

ALE and TLS acknowledge useful conversations with several participants of session 86 of the Les Houches summer school. ALE acknowledges the support of an NSF Graduate Fellowship. MK and TLS are supported in part by DoE DE-FG03-92-ER40701, NASA NNG05GF69G, and the Gordon and Betty Moore Foundation.

During the final preparations of this work we learned of recent work along similar lines [256]. TLS and ALE thank Marc Kamionkowski for useful suggestions and conversations. TC was supported in part by a Grant-in-Aid for Scientific Research (No.17204018) from the Japan Society for the Promotion of Science and in part by Nihon University. TLS is supported in part by DoE DE-FG03-92-ER40701, NASA NNG05GF69G, and the Gordon and Betty Moore Foundation. ALE acknowledges the support of an NSF Graduate Fellowship.

Chapter 6

Solar system constraints to Chern-Simons gravity¹

6.1 Introduction

The study of modifications of the theory of general relativity has been of interest ever since Einstein first formulated general relativity in 1915. Particularly interesting are modifications that introduce terms to the Einstein-Hilbert action that are second order in the curvature, as such modifications represent high-energy corrections to the Einstein-Hilbert action that might arise in quantum gravity. Chern-Simons gravity is an example of such a second-order modification of the Einstein-Hilbert action.

Chern-Simons modifications to gravity were first considered in 2+1 dimensions [257]. Refs. [69, 70] investigated the structure of these theories in 3+1 dimensions and showed how they could arise as a low-energy consequence of string theory. Ref. [67] considered some early-universe implications of such theories. Refs. [258, 259] investigated how Chern-Simons terms might participate in leptogenesis. Ref. [68] renewed the investigation of Chern-Simons gravity, working out the linearized equations of the theory and their implications for gravitational waves. Most recently, Refs. [260, 261] solved the linearized Chern-Simons field equations around a collection of spinning point masses. In much of the work on Chern-Simons gravity, the Chern-Simons term is coupled to a scalar field (as detailed below), and this scalar field is assumed to be spatially homogeneous but time varying. This assumption can be motivated by arguments analogous to those that have been made suggesting that the quintessence field should be coupled to the Chern-Simons term of electromagnetism [262].

Chern-Simons gravity has thus far eluded constraints from solar system tests of weak-field gravity because it is indistinguishable from general relativity for all spacetimes that possess a maximally

¹The material presented in this chapter, except for Section 6.5, was first published in, *The effects of Chern-Simons gravity on bodies orbiting the Earth*, Tristan L. Smith, Adrienne L. Erickcek, Robert R. Caldwell, and Marc Kamionkowski, Phys. Rev. **D77**, 024015 (2008). Reproduced here with permission, copyright (2008) by the American Physical Society.

symmetric two-dimensional subspace and for all conformally flat spacetimes [69]. Therefore, the Schwarzschild spacetime as well as the Robertson-Walker spacetime are also solutions of the Chern-Simons gravitational field equations. Distinguishing Chern-Simons gravity from general relativity requires considerations of spacetimes that are not spherically symmetric, such as the spacetime around a spinning body. To this end, Refs. [260, 261] investigated the Chern-Simons modifications to the motion of bodies around a spinning point mass and found that the motion was indistinguishable from that in general relativity.

In this chapter we take further steps to link Chern-Simons gravity to current and forthcoming experimental tests of weak-field gravity. We assume, as in other recent work, that the scalar field coupled to the Chern-Simons term is time varying but spatially homogeneous. We then determine the spacetime around an extended spinning mass and find that it differs from the spacetime around a spinning point mass. We determine the orbits of test particles and the precession of gyroscopes moving in this spacetime and find that the Chern-Simons modification does lead to observable deviations from the predictions of general relativity. These deviations allow us to evaluate constraints to the Chern-Simons parameter space from current satellite experiments, as well as those regions to be probed with forthcoming experiments.

6.2 Chern-Simons gravity

We consider the theory defined by the action

$$S = \int d^4x \sqrt{-g} \left[-\frac{1}{2\kappa^2} R + \frac{\ell}{12} \theta \mathbf{R} \tilde{\mathbf{R}} - \frac{1}{2} (\partial\theta)^2 - V(\theta) + \mathcal{L}_{\text{mat}} \right], \quad (6.1)$$

where \mathcal{L}_{mat} is the Lagrangian density for matter, $g \equiv \det g_{\mu\nu}$ is the determinant of the metric $g_{\mu\nu}$, R is the Ricci scalar (with the convention $R^\lambda{}_{\mu\nu\kappa} \equiv \Gamma^\lambda_{\mu\nu,\kappa} + \dots$ for the Riemann tensor), and $\mathbf{R} \tilde{\mathbf{R}}$ is a contraction of the Riemann tensor and its dual:

$$\mathbf{R} \tilde{\mathbf{R}} \equiv R^\beta{}_\alpha{}^{\gamma\delta} \tilde{R}^\alpha{}_{\beta\gamma\delta}, \quad (6.2)$$

where the dual of the Riemann tensor is defined by

$$\tilde{R}^\mu{}_{\nu\alpha\beta} \equiv \frac{1}{2} \epsilon_{\sigma\tau\alpha\beta} R^\mu{}_{\nu}{}^{\sigma\tau}, \quad (6.3)$$

where $\epsilon_{\sigma\tau\alpha\beta}$ is the Levi-Civita tensor, including a factor of $\sqrt{-g}$. Finally, ℓ is a new length scale, a parameter of the theory, and $\kappa^2 \equiv 8\pi G$, where G is Newton's constant. Throughout this chapter we take Greek indices to range from 0 to 3. Appendix A shows how such an action may arise in string theory. This action is different from the action considered in Ref. [68] in that here θ is a

dynamical scalar field with a canonical kinetic term, so the ℓ parameter is required to make the action dimensionless.

The equation of motion for θ is given by

$$\square\theta = \frac{dV}{d\theta} - \frac{1}{12}\ell\mathbf{R}\tilde{\mathbf{R}}. \quad (6.4)$$

The gravitational field equations take the form

$$G_{\mu\nu} - \frac{2}{3}\ell\kappa^2 C_{\mu\nu} = -\kappa^2 T_{\mu\nu}, \quad (6.5)$$

where $G_{\mu\nu}$ is the Einstein tensor, $T_{\mu\nu}$ is the stress-energy tensor for the scalar field and the matter Lagrangian, and we refer to $C_{\mu\nu}$ as the Cotton-York tensor²,

$$C^{\mu\nu} = \frac{1}{2} \left[(\partial_\sigma\theta) \left(\epsilon^{\sigma\mu\alpha\beta} \nabla_\alpha R_\beta^\nu + \epsilon^{\sigma\nu\alpha\beta} \nabla_\alpha R_\beta^\mu \right) \nabla_\tau (\partial_\sigma\theta) \left(\tilde{R}^{\tau\mu\sigma\nu} + \tilde{R}^{\tau\nu\sigma\mu} \right) \right]. \quad (6.6)$$

Appendix D provides an alternative expression for the Cotton-York tensor.

Ref. [68] notes that if θ is a non-dynamical field (a Lagrange multiplier), the theory cannot accommodate a spacetime with a nonzero $\mathbf{R}\tilde{\mathbf{R}}$ because the Cotton-York tensor would have a non-zero divergence. However, if θ is a dynamical field, then the theory can indeed accommodate spacetimes with nonzero $\mathbf{R}\tilde{\mathbf{R}}$ since we have

$$-\frac{2}{3}\ell\kappa^2 \nabla^\mu C_{\mu\nu} = \frac{\ell\kappa^2}{12} (\partial_\nu\theta) \mathbf{R}\tilde{\mathbf{R}} = -\kappa^2 \nabla^\mu T_{\mu\nu}^\theta, \quad (6.7)$$

where $T_{\mu\nu}^\theta$ is the stress-energy tensor for θ . We see that whereas the scalar-field stress-energy and the Cotton-York tensors are separately conserved when $\mathbf{R}\tilde{\mathbf{R}} = 0$, the divergence of the scalar field stress-energy tensor is precisely balanced by the divergence of the Cotton-York tensor for non-zero $\mathbf{R}\tilde{\mathbf{R}}$ due to the novel coupling between the scalar field and gravity.

6.3 The Chern-Simons gravitomagnetic equations

We begin with a perturbation to the flat metric [using signature $(-+++)$],

$$g_{\mu\nu} = \eta_{\mu\nu} + h_{\mu\nu}, \quad (6.8)$$

and compute the linearized Einstein and Cotton-York tensors,

$$G_{\mu\nu}^{\text{linear}} = \frac{1}{2}(\square h_{\mu\nu} + \partial_\mu \partial_\nu h - \partial_\mu \partial_\alpha h_\nu^\alpha - \partial_\nu \partial_\alpha h_\mu^\alpha - \eta_{\mu\nu}[\square h - \partial_\alpha \partial_\beta h^{\alpha\beta}]), \quad (6.9)$$

$$\begin{aligned} C_{\mu\nu}^{\text{linear}} &= \frac{1}{8} \partial^\alpha \partial_\beta \theta [\eta_{\nu\gamma} \epsilon^{\gamma\beta\sigma\tau} (h_{\mu\sigma, \alpha\tau} - h_{\alpha\sigma, \mu\tau} - h_{\mu\tau, \alpha\sigma} + h_{\alpha\tau, \mu\sigma}) + \eta_{\mu\gamma} \epsilon^{\gamma\beta\sigma\tau} (h_{\nu\sigma, \alpha\tau} - h_{\alpha\sigma, \nu\tau} - h_{\nu\tau, \alpha\sigma} + h_{\alpha\tau, \nu\sigma})] \\ &+ \frac{1}{4} \partial_\beta \theta \epsilon^{\alpha\beta\sigma\tau} [\eta_{\alpha\mu} \partial_\tau (\square h_{\nu\sigma} - \partial_\nu \partial^\lambda h_{\lambda\sigma}) + \eta_{\alpha\nu} \partial_\tau (\square h_{\mu\sigma} - \partial_\mu \partial^\lambda h_{\lambda\sigma})], \end{aligned} \quad (6.10)$$

where \square is the flat-space d'Alembertian and the comma denotes partial differentiation. Since we will require below only the gravitomagnetic fields, we will be primarily interested in the time-space components of the linearized field equations.

In this chapter, we suppose that the scalar field depends only on cosmic time, $\theta = \theta(t)$, the assumption being that θ is either a quintessence field or some other field that somehow echoes the arrow of time associated with the cosmic expansion. This choice implies that the field equations are not Lorentz invariant in the solar system since $\partial_\sigma \theta$ points in the cosmic time direction and couples to local gravity through the Cotton-York tensor [Eq. (6.6)]. We note that a nonzero $\mathbf{R}\tilde{\mathbf{R}}$ will source spatial variations in θ through Eq. (6.4). By restricting θ to be spatially homogenous, we are effectively treating θ as a nondynamical field, and we leave a full dynamical treatment to future work. Finally, we neglect corrections due to the motion of the Earth with respect to the rest frame of the cosmic microwave background.

We work with the trace-reversed metric perturbation,

$$\bar{h}_{\mu\nu} \equiv h_{\mu\nu} - \frac{1}{2} \eta_{\mu\nu} h, \quad (6.11)$$

and impose the Lorenz-gauge condition, $\partial^\mu \bar{h}_{\mu\nu} = 0$, to obtain the linearized time-space field equations,

$$G_{0i}^{\text{linear}} - \frac{2}{3} \ell \kappa^2 C_{0i}^{\text{linear}} = -\kappa^2 T_{0i}, \quad (6.12)$$

with

$$G_{0i}^{\text{linear}} = \frac{1}{2} \square \bar{h}_{0i}, \quad (6.13)$$

$$C_{0i}^{\text{linear}} = \frac{\dot{\theta}}{4} \epsilon^0{}_{ijk} \partial^j \square \bar{h}^k{}_0, \quad (6.14)$$

where the dot denotes differentiation with respect to time and Latin indices are purely spatial and range from 1 to 3. The stress-energy tensor for $\theta(t)$ is diagonal, so it does not contribute to the time-space field equations.

²We note that this definition differs from the usual expression for the four-dimensional Cotton-York tensor (see Ref. [68]).

Let t^α be a unit vector in the coordinate time direction, and then define the 4-vector potential of this linearized theory,

$$A_\mu \equiv -\frac{1}{4}\bar{h}_{\mu\nu}t^\nu = -\frac{1}{4}\bar{h}_{\mu 0}. \quad (6.15)$$

We consider a source with mass density ρ , mass current \vec{J} and negligible pressure, so we can express the matter stress-energy tensor as

$$T_{\mu\nu} = 2t_{(\mu}J_{\nu)} - \rho t_\mu t_\nu, \quad (6.16)$$

where $J_\mu \equiv -T_{\mu\nu}t^\nu = (-\rho, \vec{J})$. In general relativity, the time-space components of the linearized field equations take the form

$$\partial^\mu \partial_\mu A_i = -4\pi G J_i, \quad (6.17)$$

which is (nearly) identical to Maxwell's equations for the vector potential in Lorenz gauge ($\partial_\mu A^\mu = 0$). Given our definition of A^μ , the Lorenz-gauge condition for A_μ is implied by our earlier gauge choice for $\bar{h}_{\mu\nu}$.

The classically 'physical' fields (i.e., those that enter into the geodesic equation) \vec{E} and \vec{B} are given by

$$E^i = \partial_i A_0 - \partial_0 A_i, \quad (6.18)$$

$$B^i = \epsilon^{0ijk} \partial_j A_k, \quad (6.19)$$

where we have defined $\epsilon^{0ijk} = 1$. Two of the Maxwell equations,

$$\vec{\nabla} \cdot \vec{B} = 0, \quad (6.20)$$

$$\vec{\nabla} \times \vec{E} = -\frac{\partial \vec{B}}{\partial t}, \quad (6.21)$$

are a direct consequence of the way in which the \vec{E} and \vec{B} fields are defined in terms of the vector potential, and so these two equations will be the same in Chern-Simons gravity. Gauss' law, which follows from the time-time component of the field equation, is now

$$\vec{\nabla} \cdot \vec{E} = 4\pi G(\rho + \rho_\theta) \quad (6.22)$$

where ρ_θ is the energy density of the scalar field $\theta(t)$ and is uniform throughout the solar system. Since ρ_θ cannot be larger than the mean cosmological energy density, it must be negligible compared to the density of the source ρ , and we do not consider it further. The only significant modification

will be to Ampère's law, which, for Chern-Simons gravity, is now given by

$$\vec{\nabla} \times \vec{B} - \frac{\partial \vec{E}}{\partial t} - \frac{1}{m_{\text{cs}}} \square \vec{B} = 4\pi G \vec{J}, \quad (6.23)$$

where we have defined $m_{\text{cs}} \equiv -3/(\ell\kappa^2\dot{\theta})$.

Given the metric perturbation represented by the gravitomagnetic potential and neglecting the time variation of the metric, slowly moving particles travel on geodesics such that a 'Lorentz force law' of the form,

$$\vec{a} = -\vec{E} - 4\vec{v} \times \vec{B}, \quad (6.24)$$

is obtained. Therefore, as in electrodynamics, only the physical fields, and not the potentials, have physical relevance.

We furthermore note that $\mathbf{R}\tilde{\mathbf{R}}$ can be expressed in terms of gravito-electric and gravitomagnetic fields as

$$\mathbf{R}\tilde{\mathbf{R}} = -16(\partial_i E_j)(\partial_k B_l)(\eta^{ik}\eta^{jl} + \eta^{il}\eta^{jk}). \quad (6.25)$$

Unlike the case with Maxwell fields [263], it is not sufficient for the fields to have a non-vanishing $\vec{E} \cdot \vec{B}$ in order to have a non-trivial coupling between gravity and the scalar field. The best example of a gravitational source which produces a non-vanishing $\mathbf{R}\tilde{\mathbf{R}}$ is a spinning, spherical body.

6.4 Gravitomagnetism due to a spinning sphere in Chern-Simons gravity

We are now in a position to calculate the gravitomagnetic field in Chern-Simons gravity for a spinning body. Appendix B provides details of the calculation.

We consider a homogeneous rotating sphere, and so the mass current is

$$\vec{J} = \rho [\vec{\omega} \times \vec{r}] \Theta(R - r), \quad (6.26)$$

where R is the radius of the rotating body, ρ is its density, $\vec{\omega}$ is its angular velocity, r is the distance from the origin, and Θ is the Heaviside step function. As detailed in Appendix B, the field equation, Eq. (6.23), is rewritten as an equation for \vec{A} and is solved by imposing the condition that the metric be continuous everywhere and that the gravitomagnetic field be finite and well behaved at the origin; the resulting vector potential is given in Appendix B. We note that in deriving this solution we have assumed that the time derivative of m_{cs} is negligible. The gravitomagnetic field is then obtained by

taking the curl of \vec{A} and may be written as $\vec{B} = \vec{B}_{\text{GR}} + \vec{B}_{\text{CS}}$, where

$$\vec{B}_{\text{GR}} = \frac{4\pi G\rho R^2}{15} \times \begin{cases} \left(5 - 3\frac{r^2}{R^2}\right) \vec{\omega} + 3\frac{r^2}{R^2} \hat{r} \times (\hat{r} \times \vec{\omega}), & r \leq R, \\ \frac{R^3}{r^3} [2\vec{\omega} + 3\hat{r} \times (\hat{r} \times \vec{\omega})], & r \geq R, \end{cases} \quad (6.27)$$

is the gravitomagnetic field inside and outside a spinning sphere in general relativity, and

$$\begin{aligned} \vec{B}_{\text{CS}} = & 4\pi G\rho R^2 \{D_1(r) \vec{\omega} + D_2(r) \hat{r} \times \vec{\omega} \\ & + D_3(r) \hat{r} \times (\hat{r} \times \vec{\omega})\}, \end{aligned} \quad (6.28)$$

is the new contribution in Chern-Simons gravity. Inside the sphere ($r \leq R$),

$$\begin{aligned} D_1(r) &= \frac{2}{(m_{\text{CS}}R)^2} + \frac{2R}{r} y_2(m_{\text{CS}}R) j_1(m_{\text{CS}}r), \\ D_2(r) &= \frac{m_{\text{CS}}r}{(m_{\text{CS}}R)^2} + m_{\text{CS}}R y_2(m_{\text{CS}}R) j_1(m_{\text{CS}}r), \\ D_3(r) &= m_{\text{CS}}R y_2(m_{\text{CS}}R) j_2(m_{\text{CS}}r), \end{aligned} \quad (6.29)$$

and outside the sphere ($r \geq R$)

$$\begin{aligned} D_1(r) &= \frac{2R}{r} j_2(m_{\text{CS}}R) y_1(m_{\text{CS}}r), \\ D_2(r) &= m_{\text{CS}}R j_2(m_{\text{CS}}R) y_1(m_{\text{CS}}r), \\ D_3(r) &= m_{\text{CS}}R j_2(m_{\text{CS}}R) y_2(m_{\text{CS}}r), \end{aligned} \quad (6.30)$$

where $j_\ell(x)$ and $y_\ell(x)$ are spherical Bessel functions of the first and second kind. We see that the Chern-Simons terms alter the components of the gravitomagnetic field along the rotation axis $\vec{\omega}$ and $\hat{r} \times (\hat{r} \times \vec{\omega})$, and they also introduce a new component perpendicular to the plane defined by $\vec{\omega}$ and \vec{r} . In other words, while in general relativity a toroidal mass current implies a poloidal gravitomagnetic field, the parity violation introduced in Chern-Simons gravity introduces a toroidal component to the gravitomagnetic field. Something similar occurs in Chern-Simons electromagnetism [263], although the detailed fields differ since the $\square\vec{B}$ term in Eq. (6.23) is simply \vec{B} in the electromagnetic theory.

The Chern-Simons addition to Ampère's law, Eq. (6.23), changes that equation from a first-order differential equation for \vec{B} to a second-order differential equation. As a result, the Chern-Simons modification to the gravitomagnetic field cannot, in general, be obtained by perturbing around the general-relativistic result, as the solution in Eq. (6.28) shows. In Chern-Simons gravity, the gravitomagnetic field oscillates with distance outside the source, and the amplitude of the oscillating field is not necessarily smaller than the general-relativistic gravitomagnetic field. Still, we expect from Eq. (6.23) that as $m_{\text{CS}} \rightarrow \infty$, the general-relativistic solution should be recovered. This occurs

since the oscillatory terms vanish as $m_{cs} \rightarrow \infty$, and so the effects on geodesics of these new terms will vanish.

If we take $\vec{\omega}$ to lie in the \hat{z} direction, then the Chern-Simons gravitomagnetic field has a nonzero azimuthal component B_ϕ . Since $B_\phi \neq 0$, one cannot find a coordinate transformation that causes both A_r and A_θ to vanish. This is at odds with claims (see, e.g., Ref. [264]) that a metric for stationary axisymmetric spacetimes in Chern-Simons gravity can always be found with $h_{t\theta} = h_{tr} = 0$. In general relativity, one can always find a coordinate system for which $A_r = A_\theta = 0$ for a stationary axisymmetric spacetime sourced by rotating perfect fluid. However, the proof of this statement assumes time-reversal invariance of the fundamental equations. This invariance implies that the metric components possess the same symmetries as the source, namely invariance under a transformation that takes $t \rightarrow -t$ and $\phi \rightarrow -\phi$. In that case, A_r and A_θ must be zero to keep the line element invariant under the same transformation. In Chern-Simons gravity, time-reversal invariance is explicitly broken by the rolling of the scalar field, $\dot{\theta} \neq 0$, and it is straightforward to verify that our solution for \vec{A} , given in Appendix B, implies that A_r and A_θ are both odd under time reversal. Consequently, the line element has the same symmetry as the source even though A_r and A_θ are nonzero.

Inspection of our solution for the vector potential given in Appendix B shows that it differs from the solution for a point-like mass-current dipole (i.e., a gravitomagnetic dipole) obtained by Alexander and Yunes (AY) [260, 261]. When applied to a single spinning source, the metric given by Refs. [260, 261] corresponds to a vector potential

$$\vec{A}_{\text{AY}} = \vec{A}_{\text{GR}} - \frac{4\pi G\rho R^3}{m_{cs}R} \left[\frac{2R^3}{15r^3} \vec{\omega} + \frac{R^3}{5r^3} \hat{r} \times (\hat{r} \times \vec{\omega}) \right]. \quad (6.31)$$

This vector potential is an exact solution to Eq. (6.23) outside of a spinning sphere, and we can see that every term in \vec{A}_{AY} also appears in our solution for \vec{A} . The additional oscillatory terms in our solution constitute a homogeneous solution to Eq. (6.23), but without these terms, \vec{A} would not be continuous across the surface of the sphere. Furthermore, only these oscillating terms contribute to \vec{B}_{CS} because $\vec{\nabla} \times \vec{A}_{\text{AY}} = \vec{\nabla} \times \vec{A}_{\text{GR}}$. The inclusion of oscillatory terms results in a Chern-Simons gravitomagnetic field that differs from general relativity, so we may use observations of the motion of test bodies in the Earth's gravitomagnetic field to constrain Chern-Simons gravity.

6.5 Gravitomagnetic perturbations to Keplerian orbits³

Since orbital dynamics is one of the oldest branches of modern theoretical physics [265] it comes as no surprise that the tools we need to analyze gravitomagnetic perturbations to Keplerian orbits

³This section consists of previously unpublished work by the author.

are already well developed. A solution for the perturbed motion, due to Lagrange, is expressed in terms of what are known as Lagrange's planetary equations [266]. These equations describe the time evolution of the usual Keplerian orbital elements, such as semi-major axis and eccentricity, due to the perturbation. However, we cannot use these equations as they are typically written since they explicitly assume that the perturbing force is derivable from a scalar potential. Gravitomagnetic forces follow a force law analogous to the Lorentz force in electromagnetism and hence cannot be derived from a scalar potential. Therefore we use a generalization of Lagrange's planetary equations, known as the Gaussian perturbation equations, which can easily accommodate nonconservative forces.

We note that previous work has observed that gravitomagnetic effects can be described in terms of the time variation of the Keplerian orbital elements. The original papers by Lense and Thirring [71] apply the Gaussian perturbation equations only to the gravitomagnetic field of a rotating spherical mass in GR, whereas the expressions presented here generalize the result to any gravitomagnetic field. More recently, Ref. [267] applied Lagrange's planetary equations to gravitomagnetism but, as we discuss later in this chapter, their expressions only apply to time-averaged perturbations. Here, by applying the Gaussian perturbation equations we present a system of equations that describe the full time evolution of the Keplerian orbital elements in the presence of a general gravitomagnetic force. In this section we work with units where $G = c = 1$.

6.5.1 Perturbed planetary equations

The derivation of the perturbed planetary equations can be found in most textbooks on celestial mechanics. In the following discussion we follow the treatment presented in Ref. [266].

We consider a binary system which moves under a Keplerian force and perturbative force, $\delta\vec{F}_{1,2}$

$$\ddot{\vec{x}}_1 + G \frac{m_2(\vec{x}_1 - \vec{x}_2)}{|\vec{x}_1 - \vec{x}_2|^3} = \frac{\delta\vec{F}_1}{m_1}, \quad (6.32)$$

$$\ddot{\vec{x}}_2 + G \frac{m_1(\vec{x}_2 - \vec{x}_1)}{|\vec{x}_1 - \vec{x}_2|^3} = \frac{\delta\vec{F}_2}{m_2}, \quad (6.33)$$

where $m_{1,2}$ is the mass of body 1 and 2 respectively, $\vec{x}_{1,2}$ is the position vector of body 1 and 2, respectively, the dot refers to a total time derivative, and G is Newton's gravitational constant. As is usually done for the 2 body problem, we consider the equivalent problem of the motion of body 1 with respect to body two and write $\vec{r} \equiv \vec{x}_1 - \vec{x}_2$, combining Eqs. (6.32) and (6.33),

$$\ddot{\vec{r}} + \frac{\mu}{r^3} \vec{r} = \delta\vec{f}, \quad (6.34)$$

where $\mu \equiv G(m_1 + m_2)$ and we have defined the perturbing function $\delta\vec{f} \equiv \delta\vec{F}_1/m_1 - \delta\vec{F}_2/m_2$. The unperturbed motion (with $\delta\vec{f} = 0$) is exactly soluble and therefore the location of the particle in

phase space is described by six constants of the motion which we shall denote by c_j ,

$$x_i = x_i(c_1, \dots, c_6, t), \quad (6.35)$$

$$\dot{x}_i = v_i = v_i(c_1, \dots, c_6, t). \quad (6.36)$$

As we shall see, these six constants are usually taken to coincide with the Keplerian orbital parameters which include the semi-major axis and the eccentricity.

Once the perturbation is ‘turned on’ the motion of the particle will not be described by these constants. Instead, we choose to describe the perturbed motion by viewing the c_j s as functions of time. This can be thought of as an inversion of Eqs. (6.35) and (6.36) given $x_i(t)$ and $v_i(t)$. Therefore, in order to follow the perturbed motion we need to seek out six differential equations that dictate the time evolution of the six functions $c_j(t)$.

The total time derivative of the position vector is now written

$$\frac{dx_i}{dt} = \frac{\partial x_i}{\partial t} + \sum_j \frac{\partial x_i}{\partial c_j} \frac{dc_j}{dt}. \quad (6.37)$$

Without loss of generality we demand that even in the perturbed motion both the coordinates and the velocity at time t are given in terms of the instantaneous value of the orbital elements $c_j(t)$. The $c_j(t)$ defined in this way are known as osculating orbital elements. This means that we have the identity,

$$\frac{\partial x_i}{\partial t} = \frac{dx_i}{dt} \quad (6.38)$$

at all times. With this Eq. (6.37) implies that

$$\sum_j \frac{\partial x_i}{\partial c_j} \frac{dc_j}{dt} = 0. \quad (6.39)$$

With this the force law can now be written

$$\frac{\partial^2 x_i}{\partial t^2} + \frac{\mu x_i}{r^3} + \sum_j \frac{\partial v_i}{\partial c_j} \frac{dc_j}{dt} = \delta f_i. \quad (6.40)$$

Since the x_i are the coordinates for a particle moving in a Keplerian orbit with the instantaneous orbital elements $c_j(t)$, we have

$$\frac{\partial^2 x_i}{\partial t^2} + \frac{\mu x_i}{r^3} = 0 \quad (6.41)$$

and we obtain

$$\sum_j \frac{\partial v_i}{\partial c_j} \frac{dc_j}{dt} = \delta f_i. \quad (6.42)$$

Eqs. (6.39) and (6.42) are the six desired equations that dictate the time evolution of the $c_j(t)$.

A derivation of Lagrange’s planetary equations then assumes that the perturbing force can be written as the gradient of a scalar, $\delta\vec{f} = \vec{\nabla}\mathcal{R}$, where \mathcal{R} is known as the disturbing function. One is then able to invert Eq. (6.42) to obtain evolution equations for the orbital elements in terms of $\partial\mathcal{R}/\partial c_j$. It is at this point that Ref. [267] identifies a disturbing function associated with magnetic-like forces. In particular, Ref. [267] writes $\mathcal{R} = \vec{A} \cdot \vec{v}$, where \vec{A} is the vector potential and \vec{v} is the velocity of the test body. From this they conclude $dc_j/dt \sim \partial(\vec{A} \cdot \vec{v})/\partial c_j$. We can see this expression is not gauge invariant by noting that if we take $\vec{A} \rightarrow \vec{A} + \vec{\nabla}\lambda$, where λ is some scalar function, then the equations of motion for the orbital elements gain an additive correction of the form $\partial(\vec{v} \cdot \vec{\nabla}\lambda)/\partial c_j$. This shows that unless we restrict ourselves to time-averaged effects these equations lack gauge invariance and hence lead to unphysical results.⁴

The formulation of Lagrange’s planetary equations in Ref. [267] is incomplete because magnetic-like forces are not conservative and hence cannot be written in terms of the divergence of a scalar function \mathcal{R} . Instead, to obtain the general form of the equations we invert Eq. (6.42) to obtain

$$\frac{dc_j}{dt} = \frac{\partial c_j}{\partial \vec{v}} \cdot \delta\vec{f}. \quad (6.43)$$

Since these equations refer only to the gravitomagnetic force they are manifestly gauge invariant. These perturbation equations, also known as the Gaussian perturbation equations [268], allow us to calculate the evolution of the orbital elements in the presence of a gravitomagnetic force.

6.5.2 Application of the Gaussian perturbation equations to gravitomagnetism

The application of these generalized equations to gravitomagnetism requires an expression for the gravitomagnetic force. Most texts that discuss GR have a discussion of gravitomagnetic forces (see, e.g., Ref. [34]). The gravitational four-vector potential is given in terms of the time-space metric coefficients $A_\mu = -(1/4)g_{0\mu}$. In GR the field equations linearized about a flat Minkowski spacetime (an approximation applicable for weak gravity) in Lorenz gauge ($\nabla^\mu A_\mu = 0$) assume a form that is analogous to Maxwell’s electromagnetic field equations. Alternative theories of gravity will, in general, have modified linearized field equations (see, e.g., Ref. [269]). Therefore, for a specific gravity theory and a specific source one can calculate the resulting gravitomagnetic field from the linearized field equations. For the following discussion we shall restrict ourselves to the Lorenz gauge, $\nabla^\mu A_\mu = 0$, where Greek indices denote spacetime indices that run from 0 – 3 and Latin

⁴To demonstrate this, consider the following example. Take the vector potential associated with a gravitomagnetic field to be \vec{A} and take the spacetime to be stationary (independent of the time coordinate). As we discuss in Sec. 6.3 the vector potential must be in Lorenz gauge so that $\vec{\nabla} \cdot \vec{A} = 0$. Gauge freedom is then restricted to scalar functions λ such that $\nabla^2\lambda = 0$. An example of such a gauge transformation is given by $\lambda = (K/r^2)\cos(\theta)$, where K is an arbitrary constant. For the case of Lense-Thirring drag one can show, using the formulae of Ref. [267], that this gauge transformation alters the equations of motion for the orbital parameters $c_j(t)$ leading to observable effects and hence violates gauge invariance.

indices are purely spatial and run from 1 – 3. We denote a vector in three-space by a vector arrow such as \vec{A} .

For the discussion here we need only note that under the approximation of slow motion and weak gravity the geodesic equation yields a force law

$$\vec{a} = -\vec{E} - 4\vec{v} \times \vec{B}, \quad (6.44)$$

where $\vec{E} = -\vec{\nabla}\Phi + \partial\vec{A}/\partial t$, Φ is the usual Newtonian gravitational potential, \vec{v} is the velocity of the test body, and $\vec{B} = \vec{\nabla} \times \vec{A}$ is the gravitomagnetic field in terms of the three-vector potential \vec{A} . With this gravitomagnetic field, we write the perturbative force per unit mass as

$$\delta\vec{f} = -4\vec{v} \times \vec{B}. \quad (6.45)$$

In order to solve for the perturbed motion, we must also specify the six orbital elements of the unperturbed motion. Following Ref. [266] we choose the semi-major axis (a), the eccentricity (e), the inclination (i), the argument of pericenter (ω), the longitude of the ascending node (Ω), and the time the test body passes pericenter (τ).

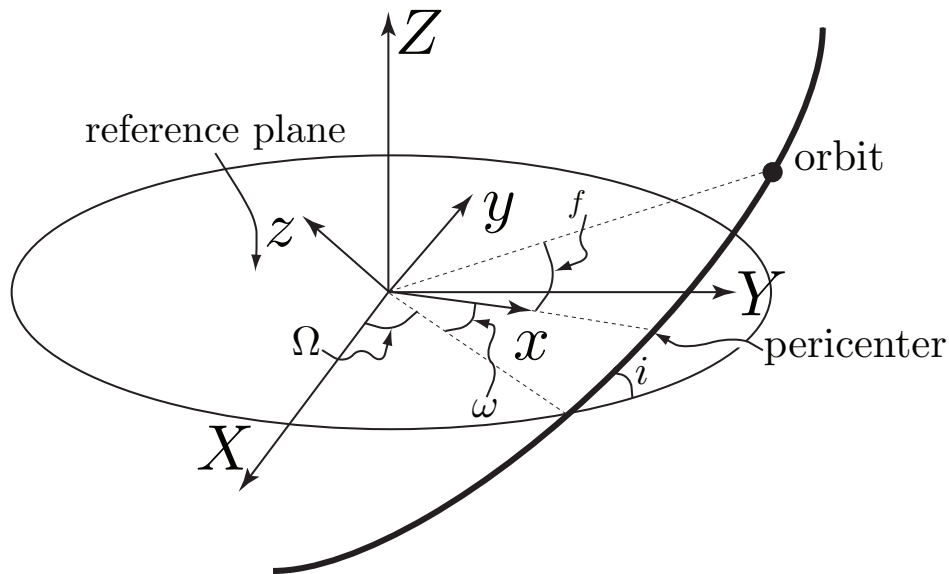


Figure 6.1: Here we show a diagram explaining the meaning of the various angular orbital elements discussed in the text. For the example of the Lense-Thirring drag the reference plane, (X, Y) , is taken to coincide with the earth's equator. Adapted from Ref. [270].

We will now explain the meaning of these orbital elements. We refer the reader to Fig. 6.1 for the geometrical meaning of these constants. The semi-major axis and eccentricity describe the shape of the unperturbed ellipse. The inclination angle, i , gives the angle between the plane of the orbit of

the test body and the reference plane (X, Y) . The argument of pericenter ω lies within the orbital plane and describes the angle between the intersection between the orbital plane and the reference plane and the line that extends between the origin and the location of pericenter (closest approach) of the test body. The longitude of the ascending node, Ω , describes the angle between the X-axis and the intersection between the orbital plane (x, y) and the reference plane (X, Y) . Finally, we must introduce the mean anomaly M defined by

$$M \equiv n(t - \tau), \quad (6.46)$$

where $n^2 a^3 = \mu$ is the mean motion and τ is the time at which the test body passes pericenter.

The location of the test body in space can be written, in terms of the reference coordinate system (X, Y, Z) , as

$$\begin{pmatrix} X \\ Y \\ Z \end{pmatrix} = r \begin{pmatrix} \cos(\Omega) \cos(u) - \sin(\Omega) \sin(u) \cos(i) \\ \sin(\Omega) \cos(u) + \cos(\Omega) \sin(u) \cos(i) \\ \sin(u) \sin(i) \end{pmatrix}, \quad (6.47)$$

where r , for an elliptical orbit ($e < 1$) is given by

$$r = \frac{a(1 - e^2)}{1 + e \cos(f)}, \quad (6.48)$$

f , defined in Fig. 1, is called the true anomaly, and $u \equiv \omega + f$. In order to express the position of the test body in terms of time, t , we must write f , the true anomaly, in terms of M , the mean anomaly. Unfortunately this relationship cannot be written in a simple form. Instead, one takes advantage of the fact that most orbits of interest have small eccentricities. Expanding in small eccentricity, one can derive a relationship between f and M . See Ref. [266] for details. To linear order in eccentricity we have

$$\sin(f) \simeq \sin(M) + e \sin(2M), \quad (6.49)$$

$$\cos(f) \simeq \cos(M) + e[\cos(2M) - 1] \quad (6.50)$$

We are now in a position to write down the Gaussian perturbation equations in a useful form.

First we note that when writing the Gaussian perturbation equations we need to decide on a coordinate system that is attached to the test mass in its orbit. Since the gravitomagnetic forces act perpendicular to the velocity, it makes most sense to use the direction of the velocity of the orbiting body as one of our axes. Setting up the rest of the coordinate system, we will choose an axis perpendicular to the velocity but within the orbital plane and then an axis parallel to the orbital

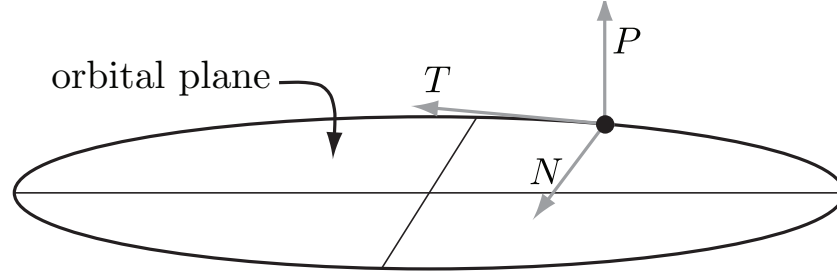


Figure 6.2: Here we show the coordinate system associated with the orbiting test body in which we write our perturbation equations.

angular momentum.

The tangential component of the force is obtained from

$$\hat{T} = \frac{\vec{v}}{|\vec{v}|}. \quad (6.51)$$

We can express the other two unit vectors in terms of the instantaneous Keplerian motion of the test particle,

$$\hat{N} = \frac{\vec{h} \times \vec{v}}{|\vec{h} \times \vec{v}|} = \frac{\vec{h} \times \vec{v}}{\mu[e^2 + 2p/r - 1]^{1/2}}, \quad (6.52)$$

$$\hat{P} = \frac{\vec{h}}{|h|} = \frac{\vec{r} \times \vec{v}}{\sqrt{\mu p}}, \quad (6.53)$$

where $\vec{h} \equiv \vec{r} \times \vec{v}$ is the orbital angular momentum vector and p is the semi-latus rectum which, for $e < 1$, is given by $p = a(1 - e^2)$.

6.5.3 Lorentz force

The components of the Lorentz force perturbing function is given by

$$\delta f_T = 0, \quad (6.54)$$

$$\delta f_N = -\Delta_L \vec{B} \cdot \hat{h}, \quad (6.55)$$

$$\delta f_P = \Delta_L \vec{B} \cdot \left(\frac{\vec{r} + \vec{e}}{|\vec{r} + \vec{e}|} \right) \quad (6.56)$$

where we have defined

$$\Delta_L \equiv 4an \sqrt{\frac{1 + e^2 + 2e \cos(f)}{1 - e^2}}, \quad (6.57)$$

and \vec{e} is known as the eccentricity vector and is given by

$$\vec{e} = \frac{1}{\mu} \left(\vec{v} \times \vec{h} - \mu \frac{\vec{r}}{r} \right). \quad (6.58)$$

The eccentricity vector points towards the pericenter of the orbit and has magnitude e . In the unperturbed motion \hat{h} is constant,

$$\hat{h} = \begin{pmatrix} 0 \\ -\sin(i) \\ \cos(i) \end{pmatrix}, \quad (6.59)$$

and we have

$$\frac{\vec{r} + \vec{e}}{|\vec{r} + \vec{e}|} = [1 + e^2 + 2e \cos(f)]^{-1/2} \times \begin{pmatrix} e \cos(\omega) + \cos(u) \\ \cos(i)[e \sin(\omega) + \sin(u)] \\ \sin(i)[e \sin(\omega) + \sin(u)] \end{pmatrix}. \quad (6.60)$$

With these expressions we can now write down the perturbation equations in terms of the gravitomagnetic field [268]

$$\frac{da}{dt} = 0, \quad (6.61)$$

$$\frac{de}{dt} = -\frac{1}{v} \frac{r}{a} \sin(f) \delta f_{\hat{N}}, \quad (6.62)$$

$$\frac{d\tau}{dt} = \frac{\sqrt{1-e^2} r}{nev} \frac{r}{a} \cos(f) \delta f_{\hat{N}}, \quad (6.63)$$

$$\frac{di}{dt} = \frac{r \cos(f + \omega)}{na^2 \sqrt{1-e^2}} \delta f_{\hat{P}}, \quad (6.64)$$

$$\frac{d\Omega}{dt} = \frac{r \sin(f + \omega)}{na^2 \sqrt{1-e^2} \sin(i)} \delta f_{\hat{P}}, \quad (6.65)$$

$$\frac{d\omega}{dt} = \frac{1}{ev} \left(\frac{r}{p} \cos(f) + e \left[1 + \frac{r}{p} \right] \right) \delta f_{\hat{N}} - \cos(i) \dot{\Omega}. \quad (6.66)$$

Note that since a determines the energy of the system and since magnetic forces do no work it makes sense that $da/dt = 0$. We emphasize that these equations are exact and do not depend on the magnitude of the perturbing force per unit mass, δf .

We can immediately see how such a set of equations yields quick intuition for the effect a given gravitomagnetic field has on the orbit of a test body. First, note that the radial position of the test body is determined by a , e , and τ . Therefore, the radial position can be perturbed only by the component of the magnetic field perpendicular to the plane of the orbit. Additionally, for orbits with small eccentricities the component $\delta f_{\hat{P}}$ picks out, to zeroth order, the radial component of the magnetic field. In turn, it is the radial component of the magnetic field that produces variation in the inclination i and longitude of the ascending node Ω .

6.5.4 Application to the Lense-Thirring drag

In this section we shall use the perturbation equations to derive the perturbations to an orbiting test body due to the gravitomagnetic field of a spherical homogeneous rotating source. The gravitomagnetic field due to a spherical homogeneous rotating source is given by [34],

$$\vec{B} = -\frac{1}{2} \frac{\vec{J} - 3(\vec{J} \cdot \hat{r})\hat{r}}{r^3}, \quad (6.67)$$

where

$$\vec{J} = \frac{2}{5} M_p R^2 \vec{\Omega} \quad (6.68)$$

is the angular momentum, M_p is the mass of the rotating object, R is its radius, and $\vec{\Omega}$ is its angular velocity. We choose $\vec{\Omega}$ to coincide with the \hat{Z} axis (see Fig. 6.1). Using the expression for the radial position of the test body given in Eq. (6.47) we can easily derive an expression for the velocity in terms of the instantaneous orbital elements given that

$$\dot{r} = n \frac{a}{\sqrt{1-e^2}} e \sin(f), \quad (6.69)$$

$$\dot{f} = n \frac{a^2 \sqrt{1-e^2}}{r^2}. \quad (6.70)$$

Using our expressions for the right-hand side of the perturbation equations we then find

$$\frac{de}{dt} = \frac{2J \cos(i)}{a^3(1-e^2)^2} \sin(f) \Delta_0(f), \quad (6.71)$$

$$\frac{d\tau}{dt} = -\frac{2J \cos(i)}{a^3 e (1-e^2)^{3/2} n} \cos(f) \Delta_0(f), \quad (6.72)$$

$$\frac{di}{dt} = \frac{J}{[a(1-e^2)]^3} \cos(\omega + f) \Delta_0(f) \Delta_1(f), \quad (6.73)$$

$$\frac{d\Omega}{dt} = \frac{J}{[a(1-e^2)]^3} \sin(\omega + f) \Delta_0(f) \Delta_1(f), \quad (6.74)$$

$$\frac{d\omega}{dt} = -\frac{J}{2e[a(1-e^2)]^3} \Delta_0(f) \Delta_2(f), \quad (6.75)$$

where

$$\Delta_0(f) \equiv [1 + e \cos(f)]^2, \quad (6.76)$$

$$\Delta_1(f) \equiv e \sin(\omega) + 4 \sin(\omega + f) + 3e \sin(\omega + 2f), \quad (6.77)$$

$$\Delta_2(f) \equiv 4 \cos(f) + e \{4 + 4 \cos[2(\omega + f)] + e[\cos(2\omega + f) + 3 \cos(2\omega + 3f)]\}. \quad (6.78)$$

In order to demonstrate how we may use these equations to determine the perturbed orbital motion we consider perturbations to the radial position of the test body with zero eccentricity.

Writing $e = \delta e(f)$ and $r = r_0 + \delta r$ we have

$$\delta r \simeq -a \cos(f) \delta e(f). \quad (6.79)$$

We can then approximate the evolution of $\delta e(f)$ by evaluating the right-hand side of Eq. (6.71) on the unperturbed orbit. We stress that this is the first time that we have made any approximations. We obtain

$$\delta e(f) = -2\tilde{J}[1 - \cos(f)] \cos(i) \quad (6.80)$$

where $\tilde{J} \equiv J/(a^3 n \sqrt{1 - e^2})$, the ratio of the orbital angular momentum to the rotational angular momentum and we have set the perturbations to zero at $f = 0$. We can then conclude that the radial position of the perturbed motion relative to the unperturbed motion will oscillate as,

$$\frac{\delta r(f)}{a} = 2\tilde{J} \cos(f) [1 - \cos(f)] \cos(i). \quad (6.81)$$

This does not imply that the radial motion of the test particle oscillates. The actual motion of the test particle is an ellipse which is shifted to coincide with the unperturbed ellipse at $f = 0$ (following our choice of initial conditions for δe) but which has an increased semi-major axis and an oscillating eccentricity. One can show this by matching the solution for the perturbed radial motion to an ellipse that is shifted to coincide with the unperturbed orbit at $f = 0$. The semi-major axis of the new orbit in the limit of small eccentricity is given by

$$a = a_0 \left[1 + 2 \frac{J \hat{h} \cdot \hat{z}}{a_0^3 n_0} \cos(i) \right]. \quad (6.82)$$

The eccentricity oscillates as

$$e(f, J) = A_0 [J/(a_0^3 n_0)] + A_1 [J/(a_0^3 n_0)] \cos(f), \quad (6.83)$$

with $\lim_{J \rightarrow 0} e(f, J) = e_0$. For small $J/(a_0^3 n_0)$ the amplitude of the oscillation is much smaller than the offset (it is second order in the perturbation) so that the orbit is nearly elliptical. This makes sense since the gravitomagnetic force per unit mass in the \hat{N} direction is given by

$$(\delta f_N)_{\text{LT}} = -\frac{2Jn \cos(i) \hat{h} \cdot \hat{z}}{a^2} [1 + 4e \cos(f)]. \quad (6.84)$$

To understand what this implies for the motion of the test particle we consider an instantaneous mass loss or gain by the central body ($\delta\mu$) so that the test particle experiences a perturbative force

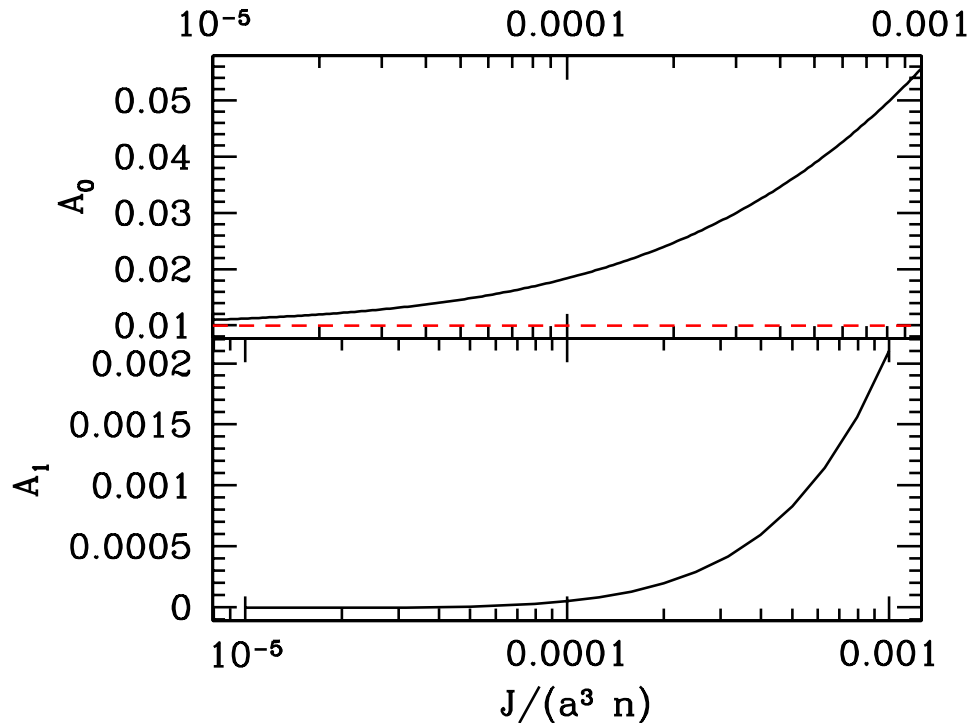


Figure 6.3: The oscillation of the eccentricity of the orbit of a test particle that is perturbed by the Lense-Thirring gravitomagnetic field given in Eq. (6.83) as a function of the rotational angular momentum. We have set the inclination to zero and $e_0 = 0.01$. We can see that the offset term, A_0 , in the upper panel approaches the initial eccentricity as $J \rightarrow 0$. The amplitude of the oscillations in the eccentricity, shown in the lower panel, decrease rapidly with $J \rightarrow 0$. At $J/(a^3 n) = 10^{-3}$ the amplitude of the oscillations is only 4% of the mean eccentricity. These oscillations occur at second order for the Lense-Thirring field.

per unit mass in the \hat{N} direction is given by

$$(\delta f_N)_{\text{Newton}} = \frac{\delta\mu}{a^2} [1 + 2e \cos(f)], \quad (6.85)$$

where we have assumed $e \ll 1$. If the mass loss/ gain were instantaneous and spherically symmetric we know that the angular momentum remains unchanged whereas the specific energy of the test particle instantaneously changes to $\delta\tilde{E} = -\delta\mu/r$. From this we can determine that the semi-major axis and the eccentricity change to

$$\frac{\delta a}{a_0} = -\frac{\delta\mu}{\mu_0}, \quad (6.86)$$

$$\delta e = -\frac{\delta\mu}{\mu_0}, \quad (6.87)$$

where we have assumed that the mass loss occurs when the particle had a true anomaly f_0 . We can now see that the Lense-Thirring gravitomagnetic field is approximately equivalent to an decrease in the gravitational field for a co-rotating orbit and a decrease for a counter-rotating orbit with a

magnitude

$$\delta\mu = -2Jn \cos(i)\hat{h} \cdot \hat{z}. \quad (6.88)$$

Therefore once the Lense-Thirring perturbation is ‘turned on’ the orbit will adjust to a semi-major axis and an eccentricity

$$a \approx a_0 \left[1 + \frac{2J \cos(i)\hat{h} \cdot \hat{z}}{a_0^3 n_0} \right], \quad (6.89)$$

$$e \approx e_0 + \frac{2J \cos(i)\hat{h} \cdot \hat{z}}{a_0^3 n_0}. \quad (6.90)$$

Since the perturbations have such small amplitudes (the size of \tilde{J} for a satellite around the Earth is $\sim 10^{-12}$!) the largest effect will occur for non-oscillatory (secular) perturbations, since these build up in time. In order to derive approximate expressions for the secular perturbations we will take the right-hand side of the evolution equations to be evaluated on a fixed Keplerian orbit. Taking the average over one period will separate out the secular part of the perturbation. Letting X denote the right-hand side of any of the perturbation equations we compute

$$\langle X \rangle = \frac{1}{T} \int_0^T X(f) dt = \frac{(1-e^2)^{3/2}}{2\pi} \int_0^{2\pi} \frac{X(f)}{[1+e \cos(f)]^2} df. \quad (6.91)$$

With this, we find that the only two orbital elements which have secular perturbations are Ω and ω ,

$$\left(\frac{d\Omega}{dt} \right)_S = \frac{2J}{a^3(1-e^2)^{3/2}}, \quad (6.92)$$

$$\left(\frac{d\omega}{dt} \right)_S = -\frac{6J}{a^3(1-e^2)^{3/2}}, \quad (6.93)$$

where the subscript ‘S’ indicates this is just the secular part of the perturbation. These results agree precisely with the original Lense-Thirring calculation [71]. It is straightforward to generalize this calculation to any gravitomagnetic field and, in particular, the field generated by a rotating homogeneous sphere in Chern-Simons gravity [see Eq. (6.28)].

6.5.5 Detecting gravitational parity violation through gravitomagnetism

As commented before, the presence of a gravitomagnetic field in the direction of a given mass current is an indication of the break down of parity conservation in the gravitational sector. In order to explore how such a gravitomagnetic field will affect our observations, we have considered a gravitomagnetic field of the form

$$\vec{B}_{\mathcal{P}} = \alpha \frac{J}{r^3} \hat{\phi}, \quad (6.94)$$

where we have supposed that the mass current flows in the direction $\hat{\phi}$. We repeat the analysis we performed above for the Lense-Thirring result.

Oscillations of the radial position of the test body for the case of $\vec{B}_{\mathcal{P}}$ are both qualitatively and quantitatively different than in the Lense-Thirring case. We can understand this through a simple physical argument. As the test body orbits both its velocity vector and the gravitomagnetic field maintain their relative orientation. Therefore, the gravitomagnetic force ($\propto \vec{v} \times \vec{B}$) is *always* pointing in the same direction leading to a situation where the test particle experiences an enhanced attraction towards the central body for half of its orbit and a slight repulsion for the other half. For the Lense-Thirring case the gravitomagnetic field points in the same direction for the entire orbit, so as the velocity vector rotates the direction of the gravitomagnetic force is either always attractive or repulsive.

The normal force for a parity violating gravitomagnetic field, which determines the radial motion of the test particle is given by

$$(\delta f_N)_{\mathcal{P}} = -\frac{4n\alpha J \cos(f + \omega) \sin(i) \hat{h} \cdot \hat{z}}{\sqrt{1 - \sin^2(i) \sin^2(f + \omega)}} [1 + 4e \cos(f)]. \quad (6.95)$$

As we did in the Lense-Thirring case we compare this perturbative force to the Newtonian perturbation to find an equivalent change in the mass of the gravitating body,

$$\delta\mu = -\frac{2n\alpha J \cos(f + \omega) \sin(i) \hat{h} \cdot \hat{z}}{\sqrt{1 - \sin^2(i) \sin^2(f + \omega)}}. \quad (6.96)$$

We can now see the qualitative difference between the Lense-Thirring and parity violating cases. Here the instantaneous mass is changing in time— for half of the orbit the perturbation ‘subtracts’ mass and for the other half it ‘adds’ mass. This is exactly what we expected given our reasoning that the parity violating field produces a force which is always pointing in the same direction. Furthermore, referring to the instantaneous eccentricity and semi-major axis in Eq. (6.87) we can see that they will also oscillate in time with a frequency of once per orbit. This oscillation is fundamentally different than the oscillation for the Lense-Thirring case since the oscillation of the eccentricity in that case is second order in $J/(a^3 n)$ whereas in the parity violating case it comes in at first order as well as occurs for the semi-major axis.

The parity violating field also leads to secular perturbations for all of the orbital elements except a . The expressions for these secular perturbations cannot be written in an analytical form, however, we can evaluate them for particular orbits.

We wish to use measurements of the orbits of satellites and planets in the Solar System in order to constrain the value of α . We do not attempt to reanalyze the data here, but quote results that can be easily compared to previous analyses. Therefore, we only compute the secular evolution of the

Table 6.1:

	a	e	i	Ω	ω	$n\tau$	$a^3/(\alpha J)\langle\dot{\Omega}\rangle$	$a^3/(\alpha J)\langle\dot{\omega}\rangle$
LAGEOS 1	12,265	0.0051	109.86	314	–	–	0.0046	–
LAGEOS 2	12,163	0.0136	52.68	48	–	–	0.0203	–
Mercury	5.8×10^7	0.2056	3.38	48.331	29.124	174.796	-6.9	6.299

NOTES.— The semi-major axis is given in km and all angular parameters are given in degrees. We do not quote numbers for the argument of pericenter and the time of pericenter passage for the LAGEOS satellites because their orbits are so close to circular that these parameters are poorly determined from the orbital data [272]. Orbital data for the LAGEOS satellites from http://ilrs.gsfc.nasa.gov/satellite_missions/list_of_satellites/lag2_general.html. Orbital data for Mercury was obtained from NASA’s HORIZONS web interface <http://ssd.jpl.nasa.gov/horizons.cgi>.

longitude of the ascending node (Ω), measured to be equal to its general relativistic value to 10% by the LAGEOS satellites [271], and the secular evolution of the argument of pericenter (ω) measured to a few tenths of an arcsecond per century for Mercury. See Table 6.1 for the orbital parameters and the corresponding secular evolution. We note that more in depth analysis might find other test bodies which place more restrictive constraints on α . The LAGEOS measurement of $\langle\dot{\Omega}\rangle$ gives $\alpha < 2 - 10$ where the range takes into account that the analysis of Ref. [271] combined the orbital data from both satellites. Using the rotational parameters of the Sun gives $J_{\odot}/a^3 = 0.0027''/\text{century}$ so that we find that the measurement of the perihelion advance of Mercury gives $\alpha < 37$.

6.5.6 Secular gravitomagnetic perturbations and the disturbing function

Finally, we show how the formulation discussed in Ref. [267] leads to correct results only when restricted to computing secular perturbations. We start with a Lagrangian formulation of the electromagnetic equations of motion. The Lagrangian can be written as

$$\mathcal{L} = \frac{1}{2}\dot{\vec{v}} \cdot \dot{\vec{v}} - \Phi + \vec{A} \cdot \vec{v}, \quad (6.97)$$

where we identify Φ with the Newtonian potential and \vec{A} is the gravitomagnetic vector potential. We can then write the perturbative force as

$$\delta\vec{F} = \vec{\nabla} \left[\vec{A} \cdot \vec{v} \right] - \frac{d\vec{A}}{dt}. \quad (6.98)$$

Taking the time average of the perturbative force it is clear that since \vec{A} depends only on the position of the test body we have

$$\langle\delta\vec{F}\rangle = \vec{\nabla}\langle\vec{A} \cdot \vec{v}\rangle. \quad (6.99)$$

Therefore we see that Lagrange's planetary equations with the disturbing function $\mathcal{R} = \vec{A} \cdot \vec{v}$ are only applicable when considering secular perturbations. See Ref. [273] for a further discussion.

6.6 Orbital and gyroscopic precession in Chern-Simons gravity

6.6.1 Orbital precession

In order to investigate how the Chern-Simons gravitomagnetic field will affect the motion of test particles around the Earth, we will use what are known as the Gaussian perturbation equations [266, 267]. Details of how these equations are applied to gravitomagnetic forces are discussed in the previous section. We will concentrate on analyzing the secular (non-periodic) time variation of the longitude of the ascending node⁵, Ω , but note that other Keplerian elements will also vary due to the terms introduced by Chern-Simons gravity. The time variation of Ω has been well studied since, in general relativity, it is connected with the Lense-Thirring drag [71],

$$\dot{\Omega}_{\text{GR}} = \frac{2GL}{a^3(1-e^2)^{3/2}}, \quad (6.100)$$

where L is the magnitude of the angular momentum of the central body, a is the semi-major axis of the orbit of the test body, and e is the orbit's eccentricity. Finally, in order to evaluate the secular perturbations, we approximate the orbit of the test body as circular (i.e., $e = 0$, a good approximation for current measurements), and we average the perturbing force over one orbital period to obtain

$$\frac{\dot{\Omega}_{\text{CS}}}{\dot{\Omega}_{\text{GR}}} = 15 \frac{a^2}{R^2} j_2(m_{\text{CS}} R) y_1(m_{\text{CS}} a), \quad (6.101)$$

where $\dot{\Omega}_{\text{CS}}$ is the precession due to \vec{B}_{CS} . The total precession is $\dot{\Omega}_{\text{GR}} + \dot{\Omega}_{\text{CS}}$. We note that $\dot{\Omega}_{\text{CS}}$ is an even function of m_{CS} .

Recent measurements of laser ranging data to the LAGEOS I and LAGEOS II satellites have measured $\dot{\Omega}$ to within 10% of its value in general relativity [271]. Requiring that the Chern-Simons contribution does not exceed 10% of the general relativity result, we find that we can place a lower limit to the Chern-Simons mass, $|m_{\text{CS}}| \gtrsim 0.001 \text{ km}^{-1}$, as shown in Fig. 6.4.

The Laser Relativity Satellite (LARES) mission [274] proposes to deploy a new laser ranging satellite and is predicted to measure $\dot{\Omega}$ to within 1% of its value in general relativity. With this improvement the bound on m_{CS} is increased by a factor of roughly five.

⁵The longitude of the ascending node is defined to be the angle between a stationary reference line and the line connecting the origin of the coordinate system and the point where the orbiting body intersects the XY reference plane as it is moving upwards (see Ref. [270]).

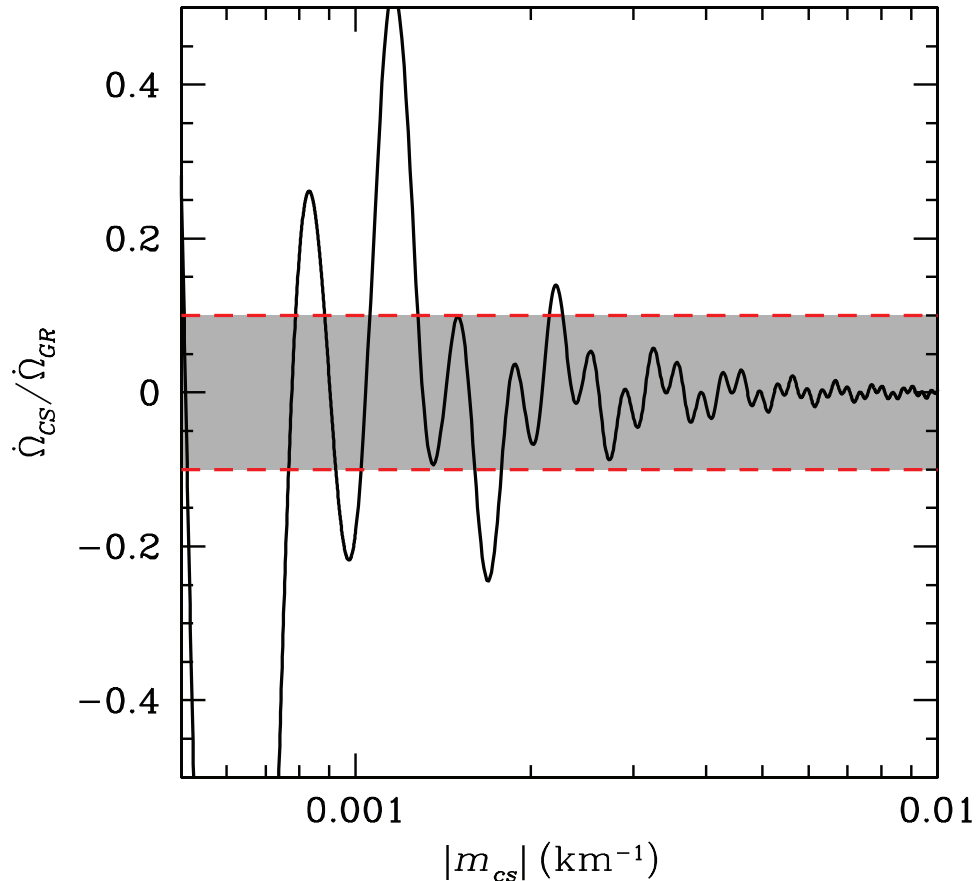


Figure 6.4: The ratio $\dot{\Omega}_{CS}/\dot{\Omega}_{GR}$ for the LAGEOS satellites orbiting with a semi-major axis of $a \approx 12,000$ km. A 10% verification of general relativity [271] (the shaded region) leads to a lower limit on the Chern-Simons mass of $|m_{cs}| \gtrsim 0.001 \text{ km}^{-1}$. A 1% verification of the Lense-Thirring drag will improve this bound on m_{cs} by a factor of roughly five.

6.6.2 Gyroscopic precession

The Earth's gravitomagnetic field will also cause a precession of gyroscopes moving in the spacetime. A gyroscope will undergo precession due to two torques. One is known as the geodetic precession and is independent of the Earth's gravitomagnetic field. The other torque is due to a coupling to the gravitomagnetic field and results in a rate of change of the spin of a gyroscope given by [275–277]

$$\dot{\vec{S}} = 2\vec{B} \times \vec{S}, \quad (6.102)$$

where \vec{S} is the angular momentum of the gyroscope.

NASA's Gravity Probe B (GPB) mission is currently attempting to measure this gyroscopic precession [72]. GPB consists of a satellite, in a polar orbit at an altitude of about 640 km, that contains four drag-free gyroscopes and a telescope. The gyroscopes are initially oriented such that their spins are aligned parallel to the optical axis of the telescope, which is pointing within the plane

of the orbit. The telescope points towards a guide star, allowing a measurement of the precession of the direction of the spins of the gyroscopes. Geodetic precession results in an annual precession in the North-South direction of about 6600 milliarcseconds (mas) whereas the general relativistic gravitomagnetic field causes an annual East-West precession of around 42 mas [72].

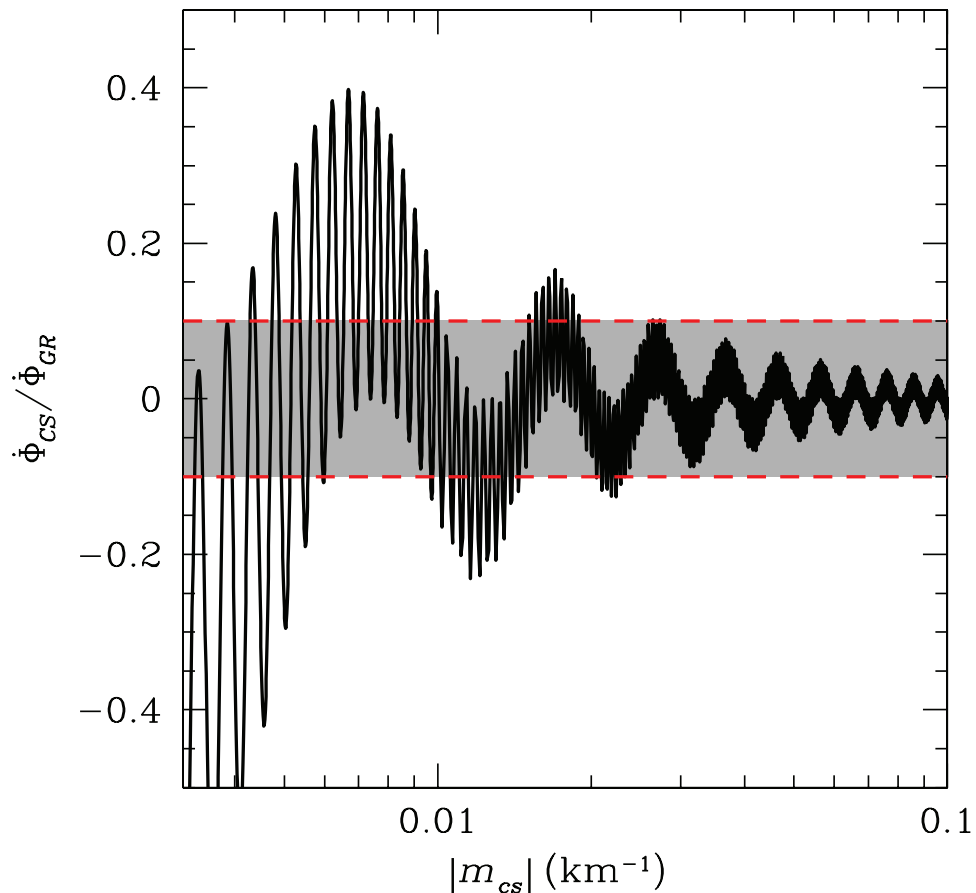


Figure 6.5: The ratio $\dot{\Phi}_{CS}/\dot{\Phi}_{GR}$ for Gravity Probe B in a polar orbit at an altitude of approximately 640 km. A 10% verification of general relativity (the shaded region) leads to a lower limit on the Chern-Simons mass of $|m_{cs}| \gtrsim 0.01 \text{ km}^{-1}$, an order of magnitude improvement over the LAGEOS result.

With the Chern-Simons expression for the gravitomagnetic field, given in Eq. (6.28), it is straightforward to calculate the resulting gyroscopic precession for a polar orbit (applicable to GPB). Relative to the general relativity result, we find

$$\frac{\dot{\Phi}_{CS}}{\dot{\Phi}_{GR}} = 15 \frac{a^2}{R^2} j_2(m_{cs}R) [y_1(m_{cs}a) + m_{cs}a y_0(m_{cs}a)], \quad (6.103)$$

where $\dot{\Phi} \equiv |\dot{\vec{S}}|/|\vec{S}| = \dot{\Phi}_{GR} + \dot{\Phi}_{CS}$ is the rate at which the angle of axis Φ changes in time due to the gravitomagnetic field. We note that $\dot{\Phi}_{CS}$ is an even function of m_{cs} .

It was initially projected that GPB would achieve a percent-level measurement of the gravitomag-

netic contribution to $\dot{\Phi}_{\text{GR}}$. However, since its launch in 2004, it has encountered several unexpected complications that will degrade the precision of the tests of gravity [278], although the extent of the degradation has yet to be reported. In Fig. 6.5, we plot Eq. (6.103) for a GPB detection of the gravitomagnetic precession to within 10% of its value in general relativity.

We have idealized the Earth to be a sphere of constant density throughout this work, when in reality, it is an oblate spheroid with layers that have different mean densities. However, we expect that the non-spherical corrections would affect both the general relativity and Chern-Simons calculations similarly and, to the accuracy we require, are negligible when we consider the ratio between general relativity and Chern-Simons results. Furthermore, it is easy to generalize our results to spheres with layered density profiles because \vec{B} depends linearly on ρ . We replaced our model of a homogeneous Earth with a model of the core and mantle and we found that the amplitudes of the oscillations in $\dot{\Omega}_{\text{CS}}$ and $\dot{\Phi}_{\text{CS}}$ were not affected. We conclude that our constraints on m_{cs} are not sensitive to the details of the density profile of the Earth.

Theories of gravity, including general relativity (GR), predict gravitational forces that act on test particles in the same way that a magnetic field acts on a moving charge. This phenomenon, called gravitomagnetism, is one of the most intriguing predictions of metric theories of gravity. The best known is the Lense-Thirring precession of the line of nodes due to the presence of a rotating mass [71].

6.7 Conclusions

The addition of a Chern-Simons term to the action for gravity is of interest as it may arise as a low-energy limit of string theory. The theory and formalism of this modification of gravity have been worked out in a number of previous papers, and some of the early-Universe consequences of such a term have been investigated. However, there has been little work on tests of such modifications in the present Universe.

In this chapter, we have calculated the linear-theory spacetime around a spinning massive body, finding new corrections that were overlooked in previous work. The gravitomagnetic field in Chern-Simons gravity differs from that in general relativity in two ways: (1) there is an oscillating component, and (2) there is a toroidal component to the gravitomagnetic field that arises as a consequence of the parity-breaking nature of the theory and that has no counterpart in ordinary general relativity.

We then determined the precession of orbits of test particles in this spacetime and also of gyroscopes moving in this spacetime. We showed that current constraints from the LAGEOS satellites restrict the inverse Chern-Simons mass parameter m_{cs}^{-1} to be less than roughly 1000 km, corresponding to a mass constraint $m_{\text{cs}} \gtrsim 2 \times 10^{-22}$ GeV. This bound may be improved by a factor of 5–10 by future observations.

The mass parameter m_{cs} is related to the more fundamental parameters ℓ and $\dot{\theta}$ of the theory through $m_{cs} = -3/(8\pi G\ell\dot{\theta})$, where ℓ is a length parameter that enters into the Chern-Simons Lagrangian, and $\dot{\theta}$ is presumably related to the time variation of the quintessence field. In principle, a precise constraint to ℓ can be derived once the precise nature of the field (a quintessence field?) θ and its time evolution are specified. We leave such model building for future work.

In this chapter we have also presented a method to compute the perturbations on the orbit of a test body due to a general gravitomagnetic field. The original calculation by Lense and Thirring uses similar methods but only considers gravitomagnetic fields produced by a homogeneous rotating sphere in GR. The derivation we have presented here generalizes their results to include *any* gravitomagnetic field. This includes gravitomagnetic fields due to various mass currents as well as fields produced by alternative theories of gravity.

An ability to calculate these effects for any gravity theory is important given that gravitomagnetism is already constrained by current measurements [271]. Furthermore, there are several ongoing projects to measure gravitomagnetic effects to higher accuracy. In particular, the LARES satellite is expected to measure the Lense-Thirring drag to within 1% of its GR value [274] and LLR has moved from centimeter to millimeter accuracy with the APOLLO system at the Apache Point Observatory [279]. With these measurements it is clear that gravitomagnetic effects are now part of the battery of tests any gravity theory must pass in order to remain viable.

Acknowledgements

TLS thanks Ben Collins, Adrienne L. Erickcek and Marc Kamionkowski, Hilke E. Schlichting, and Ketan Vyas, for useful conversations. MK thanks the Aspen Center for Physics for hospitality during the completion of this work. This work was supported at Caltech by DoE DE-FG03-92-ER40701, NASA NNG05GF69G, and the Gordon and Betty Moore Foundation, and by NSF AST-0349213 at Dartmouth. ALE acknowledges the support of an NSF graduate fellowship.

Appendix A

An expression for the high-frequency gravitational-wave transfer function¹

The derivation of the gravitational-wave transfer function has been presented in many previous studies. For our purposes here we are interested in those wavenumbers which re-entered the Hubble horizon at very high temperatures ($T \sim 10^7$ GeV) during which we suppose that the Universe was radiation dominated. We will therefore restrict our attention to this epoch.

Gravitational radiation represents the true tensor degrees of freedom when perturbing about some background metric. In the case of a spatially-flat Friedmann-Robertson-Walker (FRW) metric we have

$$ds^2 = a^2[-d\tau^2 + (\delta_{ij} + h_{ij})dx^i dx^j]. \quad (\text{A.1})$$

Gravitational radiation is expressed as the gauge invariant quantity h_{ij} which is symmetric ($h_{ij} = h_{ji}$), traceless ($h_i^i = 0$), and transverse ($\nabla^i h_{ij} = 0$). These restrictions remove 4 of the 6 degrees of freedom contained in h_{ij} leading to the two standard polarization states, “+” and “ \times ”, of gravitational radiation.

In general, we may Fourier transform h_{ij} to obtain [1]

$$h_{ij}(\tau, \vec{x}) = \sum_{A=+, \times} \int \frac{d^3k}{(2\pi)^3} \epsilon_{ij}^A(\hat{k}) \sqrt{16\pi G} h_k^A(\tau) e^{i\vec{k}\cdot\vec{x}}, \quad (\text{A.2})$$

where ϵ_{ij}^A are the polarization tensors given by

$$\epsilon_{ij}^+(\hat{k}) = \hat{m}_i \hat{m}_j - \hat{n}_i \hat{n}_j, \quad (\text{A.3})$$

$$\epsilon_{ij}^\times(\hat{k}) = \hat{m}_i \hat{n}_j + \hat{n}_i \hat{m}_j, \quad (\text{A.4})$$

¹This appendix consists of previously unpublished work by the author.

where \hat{m} and \hat{n} are unit vectors orthogonal to the direction of propagation of the wave, \hat{k} . We have also introduced a normalization, $\sqrt{16\pi G}$, which will simplify certain expressions. We also note that $\epsilon_{ij}^A(\hat{k})\epsilon^{A', ij}(\hat{k}) = 2\delta^{AA'}$. The linearized Einstein equations yield an equation of motion for h_{ij} [280]

$$h''_{ij} + 2\frac{a'}{a}h'_{ij} - \nabla^2 h_{ij} = 0, \quad (\text{A.5})$$

where we have neglected the tensor part of the anisotropic stress and the prime denotes a derivative with respect to conformal time, τ . Finally, by Fourier transforming this equation the mode function, $h_{\vec{k}}^A$ can be shown to evolve according to

$$(h_{\vec{k}}^A)'' + 2\frac{a'}{a}(h_{\vec{k}}^A)' + k^2 h_{\vec{k}}^A = 0. \quad (\text{A.6})$$

Changing variables to $g_{\vec{k}}^A \equiv ah_{\vec{k}}^A$ we have

$$(g_{\vec{k}}^A)'' + \left(k^2 - \frac{a''}{a}\right)g_{\vec{k}}^A = 0. \quad (\text{A.7})$$

The second Friedmann equation dictates the evolution of the acceleration of the scale factor,

$$\frac{a''}{a} = -\frac{a^2 H^2}{2}(1 + 3w), \quad (\text{A.8})$$

where $w \equiv P/\rho$ is the equation of state parameter. Therefore, for long wavelength modes (i.e., $k \ll aH$) we have the solution $g_{\vec{k}}^A \propto a$ and once a given mode is well within the horizon (i.e., $k \gg aH$) we have the solution $g_{\vec{k}}^A \propto \sin(k\tau + \phi_k)$. We therefore find

$$h_{\vec{k}}^A \propto \begin{cases} \text{const}, & k \ll aH \\ \sin(k\tau + \phi_k)/a & k \gg aH. \end{cases} \quad (\text{A.9})$$

From this it is clear that the evolution of the gravitational wave spectrum, up to an arbitrary phase and amplitude, is universal for wavenumbers $k \gg aH$. Therefore, the phase and amplitude is established around horizon crossing, when $k \sim aH$. We will now discuss how this amplitude is established assuming that the mode enters the horizon when the energy density is dominated by a fluid with $\rho \propto a^{-p}$ which leads to $a \propto \tau^{1/(p/2-1)} \equiv \tau^\nu$. In this appendix we will consider reheating for both a massive scalar field ($p = 3, \nu = 2$) and expansion due to the domination of the kinetic energy of a scalar field ($p = 6, \nu = 1/2$). With this, the evolution equation for the mode becomes

$$(h_{\vec{k}}^A)'' + \frac{2\nu}{\tau}(h_{\vec{k}}^A)' + k^2 h_{\vec{k}}^A = 0. \quad (\text{A.10})$$

The solution that behaves properly on superhorizon scales is

$$h_{\vec{k}}^A(\tau) = A(k\tau)^{1-\nu} j_{\nu-1}(k\tau), \quad (\text{A.11})$$

where $j_\ell(x)$ is the spherical Bessel function of order ℓ . Taking the limit as $k\tau \rightarrow 0$ we have

$$A = (2\nu + 1)!! h_{\vec{k}}^P, \quad (\text{A.12})$$

where $(2\nu + 1)!! = (2\nu + 1)(2\nu - 1)(2\nu - 3)\dots$ and $h_{\vec{k}}^P$ is the primordial amplitude. Finally, taking the limit that $k\tau \gg 1$ we have

$$h_{\vec{k}}^A(\tau) \approx \frac{(h_{\vec{k}}^P)^P (2\nu + 1)!! \sin(k\tau - (\nu - 1)\pi/2)}{(k\tau_*)^\nu a}, \quad (\text{A.13})$$

where τ_* is the proportionality constant between a and τ^ν . To solve for this constant we need to compute the integral

$$\tau = \int \frac{da}{a^2 H(a)}. \quad (\text{A.14})$$

A given mode can enter the horizon either during reheating or during radiation domination.

A.0.1 Transfer function during reheating

During reheating the Hubble parameter evolves according to

$$H = \sqrt{\frac{8\pi}{3}} \frac{E_{\text{end}}^2}{m_{\text{Pl}}} \left(\frac{a_{\text{end}}}{a}\right)^{p/2}. \quad (\text{A.15})$$

Then, up to a constant we have

$$\tau = \tau_* a^{1/\nu}, \quad (\text{A.16})$$

with

$$\tau_* = \frac{2m_{\text{Pl}}}{\sqrt{8\pi/3} E_{\text{end}}^2 (p-2) a_{\text{end}}^{p/2}}. \quad (\text{A.17})$$

We can then write

$$a_{\text{end}} = T_0 (T_{\text{rh}})^{4/p-1} E_{\text{end}}^{-4/p} \left(\frac{\pi^2}{30}\right)^{1/p} g_*(T_0)^{1/3} g_*(T_{\text{rh}})^{1/p-1/3}. \quad (\text{A.18})$$

With $p = 3$ we get

$$a_{\text{end}} = 2.55 \times 10^{-32} \left(\frac{T_{\text{rh}}}{10^7 \text{ GeV}}\right)^{1/3} \left(\frac{10^{16} \text{ GeV}}{E_{\text{end}}}\right)^{4/3}, \quad (\text{A.19})$$

and with $p = 6$ we get

$$a_{\text{end}} = 1.43 \times 10^{-26} \left(\frac{T_{\text{rh}}}{10^7 \text{ GeV}} \right)^{-1/3} \left(\frac{10^{16} \text{ GeV}}{E_{\text{end}}} \right)^{-2/3} g_{100}^{-1/6}. \quad (\text{A.20})$$

Finally, for $p = 3$, we have

$$\tau_* = 1.3 \times 10^{-4} \left(\frac{T_{\text{rh}}}{10^7 \text{ GeV}} \right)^{-1/2} \text{ Mpc}, \quad (\text{A.21})$$

and for $p = 6$ we have

$$\tau_* = 4.56 \times 10^{25} \left(\frac{T_{\text{rh}}}{10^7 \text{ GeV}} \right) g_{100}^{1/2} \text{ Mpc}. \quad (\text{A.22})$$

A.0.2 Transfer function during radiation domination

In the case of radiation domination the Hubble parameter evolves according to

$$H = \frac{2\pi^{3/2}}{3\sqrt{5}m_{\text{Pl}}} g_*(T_0)^{2/3} g_*(T)^{-1/6} \left(\frac{a_0 T_0}{a} \right)^2. \quad (\text{A.23})$$

We then have

$$\tau_* = \frac{3\sqrt{5}}{2\pi^{3/2}} \frac{m_{\text{Pl}}}{(a_0 T_0)^2 g_*(T_0)^{2/3}} g_*(T_k)^{1/6}, \quad (\text{A.24})$$

where we have evaluated the number of relativistic degrees of freedom on horizon crossing, $k = a(T_k)H(T_k)$. We then have

$$\tau_* \approx 1.42 \times 10^6 \text{ Mpc}. \quad (\text{A.25})$$

As discussed in Ref. [186] we can associate a stress-energy tensor with gravitational radiation which takes the form

$$T_{\mu\nu} = \frac{1}{32\pi G} \langle h_{\alpha\beta,\mu} h^{\alpha\beta}{}_{,\nu} \rangle, \quad (\text{A.26})$$

where the average occurs over length/time scales greater than the wavelength/frequency of the gravitational waves but smaller than the curvature of the background spacetime (for an FRW metric this is approximately equal to H^2). We can identify

$$\rho_{gw} = -T_0^0 = \frac{1}{32\pi G a^2} \langle (h_{ij})' (h^{ij})' \rangle. \quad (\text{A.27})$$

First we note that we are assuming that the stochastic background is isotropic, unpolarized, and stationary so that [1]

$$\langle h_{\vec{k}}^*{}^P h_{\vec{k}'}^P \rangle = (2\pi)^3 \delta^3(\vec{k} - \vec{k}') \frac{1}{2} S_h, \quad (\text{A.28})$$

where we have introduced the spectral density, S_h . We then obtain

$$\rho_{gw} = \frac{1}{a^2} \int \frac{4\pi k^2 dk}{(2\pi)^3} \frac{[(2\nu - 1)!!]^2}{(k\tau_*)^{2\nu}} \left\langle \left[\frac{d}{d\tau} \frac{\sin(k\tau + \phi_\nu)}{a} \right]^2 \right\rangle S_h. \quad (\text{A.29})$$

In the limit where $k \gg aH$ we have

$$\left\langle \left[\frac{d}{d\tau} \frac{\sin(k\tau + \phi_\nu)}{a} \right]^2 \right\rangle \approx \frac{1}{2} \frac{k^2}{a^2}, \quad (\text{A.30})$$

so that

$$\rho_{gw} = \frac{[(2\nu - 1)!!]^2}{a^4 \tau_*^{2\nu}} \int \frac{d \ln k}{(2\pi)^2} \frac{1}{k^{2\nu-5}} S_h. \quad (\text{A.31})$$

Therefore we find that

$$\Omega_{\text{gw}} \equiv \frac{1}{\rho_c} \frac{d\rho_{gw}}{d \ln k} = \frac{[(2\nu - 1)!!]^2}{a^4 \tau_*^{2\nu}} \frac{k^{5-2\nu}}{(2\pi)^2} \frac{S_h(k)}{\rho_c}, \quad (\text{A.32})$$

where $\rho_c = 3m_{\text{pl}}^2 H/(8\pi)$ is the critical energy density. A given source for a stochastic background of gravitational waves will then specify the spectral density S_h . We will consider gravitational waves produced during an epoch of accelerated expansion.

As we saw in Eq. (A.7), the mode function evolves as a scalar field. Following the treatment in Ref. [10, 11] we quantize the field $g(\vec{k}, \tau)$,

$$\hat{g}(\vec{k}, \tau) = v(k, \tau) \hat{a}_{\vec{k}} + v^*(k, \tau) \hat{a}_{\vec{k}}^\dagger, \quad (\text{A.33})$$

and $v(k, \tau)$ satisfies Eq. (A.7). We make the transition from a quantum to a classical analysis by identifying the propagator for \hat{g} with the spectral density of classical gravitational waves,

$$\langle 0 | \hat{g}(\vec{k}, \tau) \hat{g}^\dagger(\vec{k}', \tau) | 0 \rangle = |v(k, \tau)|^2 (2\pi)^3 \delta^3(\vec{k} - \vec{k}') \quad (\text{A.34})$$

$$= \frac{a^2}{2} S_h(k) (2\pi)^3 \delta^3(\vec{k} - \vec{k}'), \quad (\text{A.35})$$

therefore in terms of the mode function we can write

$$S_h(k) = \frac{2}{a^2} |v(k, \tau)|^2. \quad (\text{A.36})$$

A given mode starts well within the horizon, where the mode function satisfies a massless Klein-Gordon equation. Therefore, the properly normalized vacuum state is given by

$$v^{\text{in}}(k, \tau) = \frac{\exp(-ik\tau)}{\sqrt{2k}}. \quad (\text{A.37})$$

Using this as an initial condition, the value of the field after the mode has exited the horizon

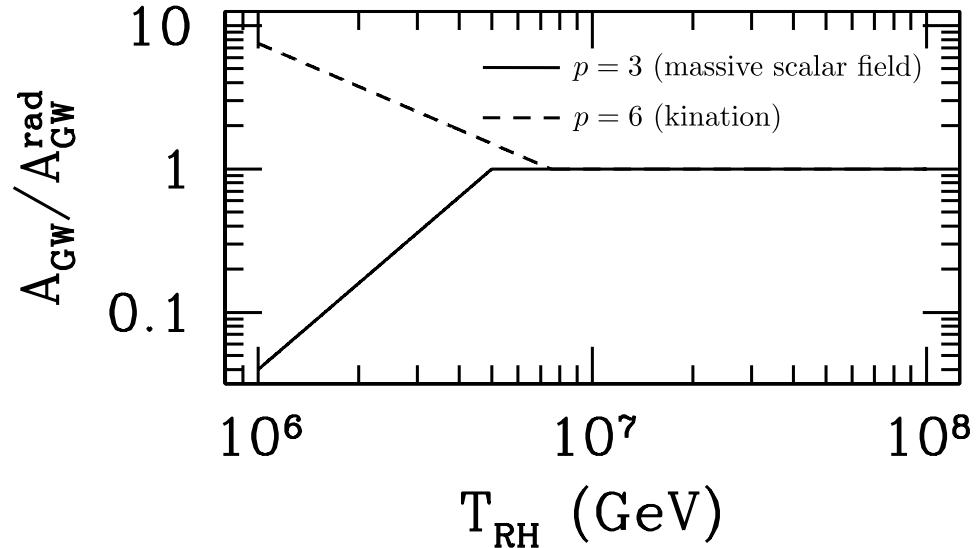


Figure A.1: Here we show the transfer function A_{gw} at a frequency of 0.1 Hz (corresponding to the frequency of BBO) as a function of the reheating temperature. As we discuss in the main body of the text, for reheat temperatures below around 10^7 GeV the gravitational wave enters the horizon during reheating and hence the value of the transfer function is different. Here we show the behavior of two different reheating scenarios: the solid line corresponds to a reheating epoch dominated by the coherent oscillations of a massive scalar field; the dashed line corresponds to a reheating epoch dominated by the kinetic energy of a scalar field. In the first case the transfer function has a negative slope, whereas in the second case the transfer function rises at shorter scales. This leads to a smaller transfer function for a massive scalar field and a large transfer function for the kinetic energy dominated expansion.

($k \ll aH$) is given by

$$v^{\text{out}}(k, \tau) = \frac{\exp(-ik\tau) - i}{\sqrt{2k} k\tau}. \quad (\text{A.38})$$

From this we find

$$S_h = \frac{H_*^2}{k^3} = \frac{8\pi}{3m_{\text{pl}}^2} \frac{V}{k^3}, \quad (\text{A.39})$$

where H_* is the Hubble parameter during inflation when $k = a_*H_*$. We then find

$$\Omega_{\text{gw}} = \frac{16[(2\nu - 1)!!]^2}{9a^4} (k\tau_*)^{-2\nu} \left(\frac{k}{H_0}\right)^2 \frac{V}{m_{\text{pl}}^4}. \quad (\text{A.40})$$

The transition from reheating to the radiation dominated transfer function occurs at the wavenumber

$$k_0 = \left(\frac{[(2\nu - 1)!!] \frac{\tau_* \text{ rad}}{(\tau_* \text{ rh})^\nu}}{1} \right)^{1/(\nu-1)}. \quad (\text{A.41})$$

For a wave that enters during radiation domination we can rewrite the transfer function in a more compact form. Noting that

$$\rho_r^0 = \frac{\pi^2}{30} T_0^4 g_*(T_0), \quad (\text{A.42})$$

and

$$\rho_c^0 = \frac{3H_0^2 m_{pl}^2}{8\pi}, \quad (\text{A.43})$$

we finally obtain

$$\Omega_{\text{gw}} h^2 = \frac{16}{9} \Omega_r h^2 \left(\frac{g_*(T_0)}{g_*(T_k)} \right)^{1/3} \frac{V}{m_{pl}^4}, \quad (\text{A.44})$$

where $\Omega_r \equiv \rho_r^0 / \rho_c^0$.

Appendix B

Setting the homogeneous initial condition for the CGWB¹

In this appendix we show that the evolution equations in conformal Newtonian gauge allow for a solution in which $\delta_{gw} = 0$. We start by considering the equations governing the evolution of perturbations in the conformal Newtonian gauge well outside the horizon and within the radiation-dominated epoch. Corrections due to the fact that the universe is not strictly radiation-dominated come in at the order $(k\tau)^2\tau/\tau_{eq}$, which can be ignored at the time we establish the initial conditions since we are well into the radiation-dominated epoch. Furthermore, during the setting of the initial conditions we suppose that the photons and baryons are tightly coupled so that the photons behave as a perfect fluid; i.e., the anisotropic stress in the photon fluid is negligible. Finally, for the case where the Newtonian potentials, ϕ and ψ , are strictly time independent it is found that on super-horizon scales (the scales on which we set the initial conditions) the higher Boltzmann moments for fully decoupled fluids (in our case, the CGWB fluid and neutrinos) behave as spherical Bessel functions, i.e., the l^{th} moment evolves as $J_l(k\tau)$. Therefore, for $k\tau \ll 1$, the l^{th} moment evolves as $\approx (k\tau)^l$. This allows us to ignore all $l > 3$. Our notation in this appendix follows that of Ref. [185].

In conformal Newtonian gauge the equations which govern the evolution of the perturbations are given by,

Photons:

$$\dot{\delta}_\gamma + \frac{4}{3}\theta_\gamma - 4\dot{\phi} = 0, \quad (\text{B.1})$$

$$\dot{\theta}_\gamma - k^2 \left(\frac{1}{4}\delta_\gamma + \psi \right) = 0. \quad (\text{B.2})$$

Massless Neutrinos:

¹This appendix consists of previously unpublished work by the author.

$$\dot{\delta}_\nu + \frac{4}{3}\theta_\nu - 4\dot{\phi} = 0, \quad (\text{B.3})$$

$$\dot{\theta}_\nu - k^2 \left(\frac{1}{4}\delta_\nu - \sigma_\nu + \psi \right) = 0, \quad (\text{B.4})$$

$$\dot{\sigma}_\nu - \frac{4}{15}\theta_\nu = 0. \quad (\text{B.5})$$

Cosmological gravitational-wave background (CGWB):

$$\dot{\delta}_{gw} + \frac{4}{3}\theta_{gw} - 4\dot{\phi} = 0, \quad (\text{B.6})$$

$$\dot{\theta}_{gw} - k^2 \left(\frac{1}{4}\delta_{gw} - \sigma_{gw} + \psi \right) = 0, \quad (\text{B.7})$$

$$\dot{\sigma}_{gw} - \frac{4}{15}\theta_{gw} = 0. \quad (\text{B.8})$$

Baryons:

$$\dot{\delta}_b + \theta_b - 3\dot{\phi} = 0, \quad (\text{B.9})$$

$$\theta_b = \theta_\gamma. \quad (\text{B.10})$$

CDM:

$$\dot{\delta}_c + \theta_c - 3\dot{\phi} = 0, \quad (\text{B.11})$$

$$\dot{\theta}_c + \frac{1}{\tau}\theta_c - k^2\psi = 0. \quad (\text{B.12})$$

$$(\text{B.13})$$

The linearized Einstein equations are given by,

$$k^2\tau^2\phi + 3\tau \left(\dot{\phi} + \frac{1}{\tau}\psi \right) = -\frac{3}{2} \left(\frac{\rho_\gamma\delta_\gamma + \rho_\nu\delta_\nu + \rho_{gw}\delta_{gw}}{\bar{\rho}} \right), \quad (\text{B.14})$$

$$\tau\dot{\phi} + \psi = \frac{2}{k^2\tau} \left(\frac{\rho_\gamma\theta_\gamma + \rho_\nu\theta_\nu + \rho_{gw}\theta_{gw}}{\bar{\rho}} \right), \quad (\text{B.15})$$

$$\tau^2\ddot{\phi} + \tau \left(\dot{\psi} + 2\dot{\phi} \right) - \psi + \frac{k^2\tau^2}{3}(\phi - \psi) = \frac{1}{2} \left(\frac{\rho_\gamma\delta_\gamma + \rho_\nu\delta_\nu + \rho_{gw}\delta_{gw}}{\bar{\rho}} \right), \quad (\text{B.16})$$

$$\phi - \psi = \frac{6}{k^2\tau^2} \left(\frac{\rho_\nu\sigma_\nu + \rho_{gw}\sigma_{gw}}{\bar{\rho}} \right), \quad (\text{B.17})$$

where $\bar{\rho} = \rho_\gamma + \rho_\nu + \rho_{gw}$. We then take Eq. (B.14) and solve for ψ . When we do this we get,

$$\psi = - \left(\frac{1}{2} \left[\frac{\rho_\gamma\delta_\gamma + \rho_\nu\delta_\nu + \rho_{gw}\delta_{gw}}{\bar{\rho}} \right] + \tau\dot{\phi} + \frac{(\tau k)^2}{3}\phi \right). \quad (\text{B.18})$$

Our starting point will be the assumption that the density contrast in the CGWB is subdominant

to the density contrasts in the photons and neutrinos. We also want to investigate a solution that reverts back to the usual adiabatic mode when $\rho_{gw} \rightarrow 0$. In order to do this we first review the basic results for the adiabatic case,

$$\delta_c = \delta_b = \frac{3}{4}\delta_\nu = \frac{3}{4}\delta_\gamma = \delta_{r0}, \quad (\text{B.19})$$

$$\phi \propto \psi \sim \psi_0, \quad (\text{B.20})$$

where δ_{r0} and ψ_0 are constant. We then suppose that δ_{gw} is at least linear in $k\tau$. In particular, we suppose the following expansion,

$$\psi = \psi_0 + \psi_1(k\tau) + \psi_2(k\tau)^2, \quad (\text{B.21})$$

$$\phi = \phi_0 + \phi_1(k\tau) + \phi_2(k\tau)^2, \quad (\text{B.22})$$

$$\delta_\gamma = \delta_{r0} + A_1(k\tau) + A_2(k\tau)^2, \quad (\text{B.23})$$

$$\delta_\nu = \delta_{r0} + B_1(k\tau) + B_2(k\tau)^2, \quad (\text{B.24})$$

$$\delta_{gw} = C_1(k\tau) + C_2(k\tau)^2, \quad (\text{B.25})$$

$$\delta_b = \frac{3}{4}\delta_{r0} + D_1(k\tau) + D_2(k\tau)^2, \quad (\text{B.26})$$

$$\delta_c = \frac{3}{4}\delta_{r0} + E_1(k\tau) + E_2(k\tau)^2. \quad (\text{B.27})$$

In the usual, adiabatic, case all of the constant pieces can be written in terms of ψ_0 ,

$$\psi_0 = \frac{20C}{15 + 4R_\nu}, \quad (\text{B.28})$$

$$\phi_0 = \left(1 + \frac{2}{5}R_\nu\right) \psi_0, \quad (\text{B.29})$$

$$\delta_{r0} = -2\psi_0, \quad (\text{B.30})$$

where $R_\nu \equiv \rho_\nu/(\rho_\gamma + \rho_\nu)$ and C is the constant that appears in the adiabatic solution in the synchronous gauge as $h = C(k\tau)^2$. We will find that all of the unknowns in the more general case can also be written in terms of ψ_0 .

We now consider the hydrodynamical equations for θ and σ . From the above expressions for the

perturbation potentials and the perturbations we are able to conclude that,

$$\theta_\gamma = \left(\frac{1}{4} \delta_{r0} + \psi_0 \right) k^2 \tau, \quad (\text{B.31})$$

$$\theta_\nu = \left(\frac{1}{4} \delta_{r0} + \psi_0 \right) k^2 \tau, \quad (\text{B.32})$$

$$\theta_{gw} = \psi_0 k^2 \tau, \quad (\text{B.33})$$

$$\theta_c = \frac{1}{2} \psi_0 k^2 \tau, \quad (\text{B.34})$$

$$\sigma_\nu = \frac{2}{15} \left(\frac{1}{4} \delta_{r0} + \psi_0 \right) k^2 \tau^2, \quad (\text{B.35})$$

$$\sigma_{gw} = \frac{2}{15} \psi_0 k^2 \tau^2. \quad (\text{B.36})$$

We are now able to use the linearized Einstein equations to solve for ψ_0 . We can either use the $(0, 0)$ or the $(0, i)$ equation. In both cases we are able conclude that,

$$\psi_0 = -\frac{\delta_{r0}(\rho_\gamma + \rho_\nu)}{2\bar{\rho}}. \quad (\text{B.37})$$

We are now able to use the (i, j) linearized Einstein equation to find ϕ_0 and we find,

$$\phi_0 = \frac{\psi_0}{5\bar{\rho}} [(5 + 9R_{gw})\rho_\gamma + 7(1 + R_{gw})\rho_\nu], \quad (\text{B.38})$$

where we have defined $R_{gw} \equiv \rho_{gw}/(\rho_\gamma + \rho_\nu)$. It is a simple matter to check to see that when $\rho_{gw} = 0$ we regain the adiabatic relationship between ϕ_0 and ψ_0 . To find the higher-order behavior we use the expansions written down above, the three equations that dictate the evolution of the density contrasts, the expression for ψ [Eq. (18)] and the (i, i) linearized Einstein equation [Eq. (16)]. We then get two sets of 4 equations involving 4 unknowns. However, we find that the (i, i) linearized Einstein equation is automatically satisfied for both the linear and second-order terms. We are therefore free to choose one of the coefficients, and we choose to set C_1 and C_2 equal to zero (corresponding to a homogeneous initial condition). We then find for the linear order,

$$A_1 = B_1 = C_1 = D_1 = E_1 = \phi_1 = \psi_1 = 0. \quad (\text{B.39})$$

To quadratic order we find that,

$$A_2 = \frac{\bar{\rho}\psi_0}{3(\rho_\gamma + \rho_\nu)}, \quad (\text{B.40})$$

$$B_2 = A_2, \quad (\text{B.41})$$

$$C_2 = 0, \quad (\text{B.42})$$

$$D_2 = \frac{3}{4}A_2, \quad (\text{B.43})$$

$$E_2 = \frac{\psi_0}{4}, \quad (\text{B.44})$$

$$\phi_2 = \frac{\psi_0}{6}, \quad (\text{B.45})$$

$$\psi_2 = -\frac{1}{6}(3\psi_0 - 2\phi_0). \quad (\text{B.46})$$

Collecting all of these results, we find that in the conformal Newtonian gauge,

$$\delta_\gamma = -\frac{2\bar{\rho}}{\rho_\gamma + \rho_\nu}\psi_0 + \frac{\bar{\rho}}{3(\rho_\gamma + \rho_\nu)}\psi_0 k^2 \tau^2, \quad (\text{B.47})$$

$$\delta_\nu = \delta_\gamma = \frac{4}{3}\delta_b, \quad (\text{B.48})$$

$$\delta_c = -\frac{3}{2}\frac{\bar{\rho}}{\rho_\gamma + \rho_\nu}\psi_0 + \frac{\psi_0}{4}k^2 \tau^2, \quad (\text{B.49})$$

$$\delta_{gw} = 0 + \mathcal{O}(k^3 \tau^3), \quad (\text{B.50})$$

$$\theta_\gamma = \psi_0 \left(1 - \frac{\bar{\rho}}{2(\rho_\gamma + \rho_\nu)}\right) k^2 \tau, \quad (\text{B.51})$$

$$\theta_\nu = \theta_b = \theta_\gamma, \quad (\text{B.52})$$

$$\theta_c = \frac{1}{2}\psi_0 k^2 \tau, \quad (\text{B.53})$$

$$\sigma_\nu = \frac{2}{15}\psi_0 \left(1 - \frac{\bar{\rho}}{2(\rho_\gamma + \rho_\nu)}\right) k^2 \tau^2, \quad (\text{B.54})$$

$$\sigma_{gw} = \frac{2}{15}\psi_0 k^2 \tau^2. \quad (\text{B.55})$$

We now need to transform these results from conformal Newtonian gauge to synchronous gauge. The expressions for this transformation can be found in Ref. [185]. We write them down here for completeness,

$$\psi(\tau) = \ddot{\beta}(\tau) + \frac{\dot{a}}{a}\dot{\beta}(\tau), \quad (\text{B.56})$$

$$\eta(\tau) = \phi(\tau) + \frac{\dot{a}}{a}\dot{\beta}(\tau), \quad (\text{B.57})$$

$$h(\tau) = 2k^2\beta(\tau) - 6\eta(\tau), \quad (\text{B.58})$$

where β describes the shift in the time coordinate between the two gauges, $\tau_{\text{syn}} = \tau_{\text{con}} + \beta(\tau_{\text{con}})$. We note we solve Eq. (B.56) as a power series in $k\tau$ and we are able to conclude that,

$$\beta(\tau) = \frac{\psi_0}{4}\tau^2 + \frac{\psi_2}{16}k^2\tau^4. \quad (\text{B.59})$$

With this, we are able to deduce the functional form for η up to order $k^2\tau^2$ using Eq. (B.57) and using Eq. (B.58) we find a functional form for h up to order $k^2\tau^2$. We note that we ignore the constant term in h since such a term can be eliminated by an appropriate gauge transformation within the

synchronous gauge. Finally we need to transform the perturbed elements of the stress-energy tensor to synchronous gauge. Such a transformation is presented in Ref. [185]. However, here we correct a typo in their Eq. (27a) with our Eq. (B.60):

$$\delta(\text{syn}) = \delta(\text{con}) - \dot{\beta} \frac{\dot{\rho}}{\rho}, \quad (\text{B.60})$$

$$\theta(\text{syn}) = \theta(\text{con}) - \dot{\beta} k^2, \quad (\text{B.61})$$

$$\sigma(\text{syn}) = \sigma(\text{con}). \quad (\text{B.62})$$

We note that these transformations apply to each species individually. Finally, we use the hydrodynamic equations in synchronous gauge in order to derive higher-order corrections to the θ perturbations (we need these corrections, since in the limit of $\rho_{gw} \rightarrow 0$ to our accuracy in conformal Newtonian gauge these perturbations vanish). Finally, we find that in synchronous gauge,

$$h(\tau) = \frac{1}{4}(2\phi_0 + \psi_0)k^2\tau^2, \quad (\text{B.63})$$

$$\eta(\tau) = \frac{1}{2}(2\phi_0 + \psi_0) + \frac{1}{24}(\psi_0 - 2\phi_0)k^2\tau^2, \quad (\text{B.64})$$

$$\begin{aligned} \delta_\gamma &= -2R_{gw}\psi_0 \\ &\quad - \frac{1}{6}[(2\phi_0 + \psi_0) - 2R_{gw}\psi_0]k^2\tau^2, \end{aligned} \quad (\text{B.65})$$

$$\delta_\nu = \frac{4}{3}\delta_b = \delta_\gamma, \quad (\text{B.66})$$

$$\delta_{gw} = 2\psi_0 - \frac{1}{6}(2\phi_0 + 3\psi_0)k^2\tau^2, \quad (\text{B.67})$$

$$\delta_c = -\frac{3}{2}R_{gw}\psi_0 - \frac{1}{8}(2\phi_0 + \psi_0)k^2\tau^2, \quad (\text{B.68})$$

$$\begin{aligned} \theta_\gamma &= -\frac{1}{2}R_{gw}\psi_0k^2\tau - \frac{1}{72}[2\phi_0 \\ &\quad + (1 - 2R_{gw})\psi_0]k^4\tau^3, \end{aligned} \quad (\text{B.69})$$

$$\begin{aligned} \theta_\nu &= -\frac{1}{2}R_{gw}\psi_0k^2\tau \\ &\quad - \frac{1}{360}[10\phi_0 + (13 - 18R_{gw})\psi_0]k^4\tau^3, \end{aligned} \quad (\text{B.70})$$

$$\theta_{gw} = \frac{1}{2}\psi_0k^2\tau - \frac{1}{360}(10\phi_0 + 31\psi_0)k^4\tau^3, \quad (\text{B.71})$$

$$\theta_c = 0, \quad (\text{B.72})$$

$$\theta_b = \theta_\gamma, \quad (\text{B.73})$$

$$\sigma_\nu = \frac{1}{15}\psi_0(1 - R_{gw})k^2\tau^2, \quad (\text{B.74})$$

$$\sigma_{gw} = \frac{2}{15}\psi_0k^2\tau^2. \quad (\text{B.75})$$

In order to use this in the CAMB program² we need to do one more transformation. The CAMB program uses the covariant gauge invariant formalism in order to evolve the perturbations and calculate anisotropies pioneered by Hawking [282] and Ellis and Bruni [283] and expanded upon by many subsequent authors [284, 285]. In this formalism, instead of dealing directly with perturbations to a background metric, one considers a 4-velocity field, u_i , and expands the Reimann tensor in coordinates where the directions orthogonal to u_i define the 3-space hypersurfaces. This approach is manifestly gauge invariant. A particular choice of 4-velocity field is related to a choice of gauge in that it specifies a set of observers in whose frame the perturbations are written. The zero-acceleration (ZA) frame corresponds to the choice that the 4-velocity coincides with the 4-velocity of the cold dark matter fluid, and hence follows geodesics. This frame is related to the synchronous gauge and in order to find this relationship we compare the evolution equations in both formalisms.

We first consider the evolution equation for the perturbation potential (h in the synchronous gauge), and the gradient of the local expansion ($\delta\theta$ in the zero-acceleration frame). In the two formalisms we have,

$$\text{ZA :} \tag{B.76}$$

$$x^2\delta\theta' + x\delta\theta + 3[(1 - R_\nu)\delta_\gamma + R_\nu\delta_\nu] = 0$$

$$\text{Syn :} \tag{B.77}$$

$$x^2h'' + xh' + 6[(1 - R_\nu)\delta_\gamma + R_\nu\delta_\nu] = 0.$$

From this we are able to conclude,

$$\delta\theta = \frac{1}{2}h'. \tag{B.78}$$

Next we consider the evolution of the density contrasts for relativistic species,

$$\text{ZA :} \tag{B.79}$$

$$\delta'_\alpha + q_\alpha + \frac{4}{3}\delta\theta = 0$$

$$\text{Syn :} \tag{B.80}$$

$$\delta'_\alpha + \frac{4}{3k}\theta_\alpha + \frac{2}{3}h' = 0.$$

Using the above result, we are able to conclude from this equation that,

$$q_\alpha = \frac{4}{3k}\theta_\alpha. \tag{B.81}$$

²<http://camb.info/>

Now we look at the equations that determine the evolution of the heat flux of a relativistic species,

$$\text{ZA :} \tag{B.82}$$

$$q'_\alpha - \frac{1}{3}(\delta_\alpha - 2\pi_\alpha) = 0$$

$$\text{Syn :} \tag{B.83}$$

$$\theta'_\alpha - \frac{1}{4}k(\delta_\alpha - 4\sigma_\alpha) = 0.$$

From this we are able to conclude that,

$$\pi_\alpha = 2\sigma_\alpha. \tag{B.84}$$

Finally we look at the equations that dictate the evolution of the anisotropic stress,

$$\text{ZA :} \tag{B.85}$$

$$\pi'_\alpha - \frac{2}{5} \left(q_\alpha + \frac{4}{3}\sigma \right) = 0$$

$$\text{Syn :} \tag{B.86}$$

$$\sigma'_\alpha - \frac{2}{15} \left(\frac{2}{k}\theta_\alpha + h' + 6\eta' \right) = 0.$$

From this we conclude that,

$$2\sigma = h' + 6\eta'. \tag{B.87}$$

One final note is that the CAMB program evolves all of the usual perturbation variables, however the only perturbation potential that it evolves is the 3-curvature perturbation, $\eta_\mu \equiv (1/2)a^{(3)}\nabla_\mu^{(3)}R$ [285, 286] where $^{(3)}\nabla$ is the spatial covariant derivative. Then, in the case where the vorticity of the 4-velocity field vanishes (the assumption needed to investigate scalar-type perturbations, see, e.g., Ref. [285]),

$$^{(3)}R = 2\kappa\rho - \frac{2}{3}\theta^2 + \sigma_{\mu\nu}\sigma^{\mu\nu}, \tag{B.88}$$

where $\kappa \equiv 8\pi G$ and $\sigma_{\mu\nu}$ is the shear of the 4-velocity field, $\sigma_{\mu\nu} \equiv ^{(3)}\nabla_{(\mu}u_{\nu)} - \theta h_{\mu\nu}/3$, and $h_{\mu\nu}$ is the projection operator given by $h_{\mu\nu} \equiv g_{\mu\nu} - u_\mu u_\nu$. From this expression, we are able to write the linear comoving 3-curvature perturbation,

$$\eta_\mu = \kappa\rho\delta_\mu - 2H\delta\theta_\mu. \tag{B.89}$$

When we expand these variables in terms of a generalized harmonic basis discussed in Ref. [285], we note that the powers of k and a are chosen so that the coefficient is dimensionless and so that all harmonic coefficients are comoving. Hence, $\delta\theta_a = \sum_k (k^2/a)\theta_k Q_a^k$. From the expression for the 3-curvature above, we can see that $^{(3)}R \sim a^{-2}$. Furthermore, since $R \sim 1/\lambda^2$ we have

$\eta_a = \sum_k (k^3/a^2)\eta_k Q_a^k$. Finally, equating these expansion coefficients, we find that,

$$\frac{k^3}{a^2}\eta = \kappa\rho k\delta - 2H\frac{k^2}{a}\delta\theta. \quad (\text{B.90})$$

Cleaning things up a bit, we finally obtain,

$$\eta = \kappa\rho\delta\frac{a^2}{k^2} - 2H\frac{a}{k}\delta\theta. \quad (\text{B.91})$$

Now we use the definition, $x \equiv k/(aH)$, to rewrite this as,

$$\eta = \frac{3}{x^2} \left(\frac{\rho_\gamma\delta_\gamma + \rho_\nu\delta_\nu + \rho_{gw}\delta_{gw}}{\bar{\rho}} \right) - 2\frac{\delta\theta}{x}. \quad (\text{B.92})$$

We will now be able to write the zero-acceleration frame variables from what we have already worked out in synchronous gauge. In the following we only present the leading order terms,

$$\eta = -(2\phi_0 + \psi_0), \quad (\text{B.93})$$

$$\delta_\gamma = -2R_{gw}\psi_0, \quad (\text{B.94})$$

$$\delta_\nu = \frac{4}{3}\delta_b = \frac{4}{3}\delta_c = \delta_\gamma, \quad (\text{B.95})$$

$$\delta_{gw} = 2\psi_0, \quad (\text{B.96})$$

$$q_\gamma = -\frac{2}{3}R_{gw}\psi_0x, \quad (\text{B.97})$$

$$q_\nu = q_\gamma, \quad (\text{B.98})$$

$$q_{gw} = \frac{2}{3}\psi_0x, \quad (\text{B.99})$$

$$q_c = 0, \quad (\text{B.100})$$

$$v_b = \frac{3}{4}q_\gamma, \quad (\text{B.101})$$

$$\pi_\nu = \frac{2}{15}\psi_0(1 - R_{gw})x^2, \quad (\text{B.102})$$

$$\pi_{gw} = \frac{4}{15}\psi_0x^2. \quad (\text{B.103})$$

Finally we need to relate our normalization, ϕ_0 , to the normalization used in CAMB. In order to do this we note that $\delta_\gamma = -(1/3)\chi x^2$ in CAMB, which yields,

$$\psi_0 = \frac{10}{15 + 4R_\nu}\chi. \quad (\text{B.104})$$

In Fig. (B.1) we show the numerically determined evolution of the perturbations as a function of $k\tau$. We also show that our analytical expression for the evolution of δ_γ [Eq. (B.65)] follows the numerical solution.

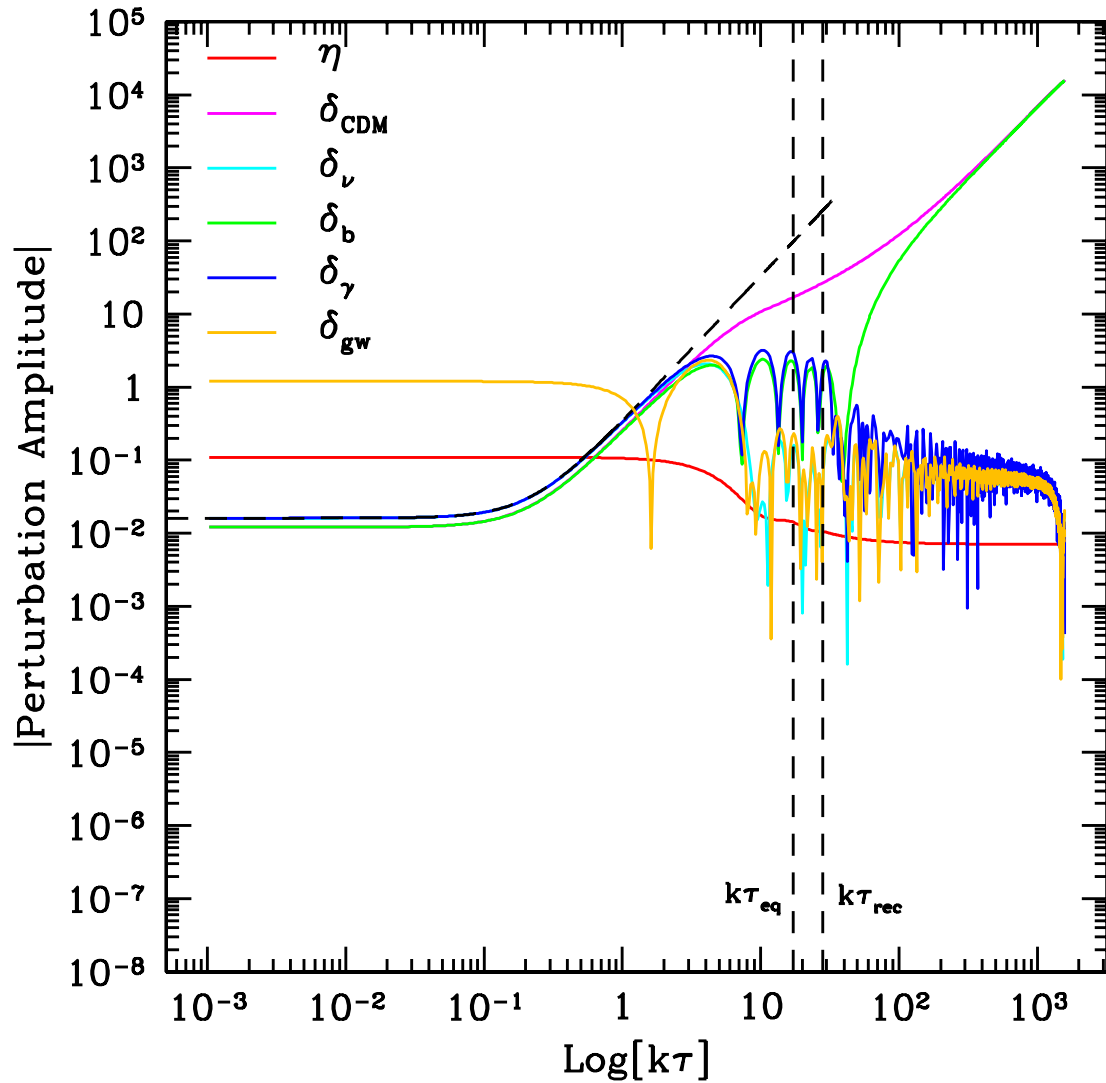


Figure B.1: Evolution of the various perturbation variables as well as the perturbation potential, η . For this figure we took the WMAP concordance model [81], $N_{\text{gw}} = 0.1$ and $k = 0.112 \text{ Mpc}^{-1}$. The dashed line that follows the evolution of δ_γ is the analytic expression given in Eq. (B.65). We can see that this analytic solution follows the numerically determined evolution up to and beyond horizon crossing.

Appendix C

Review of scalar tensor equivalence¹

The action for the scalar-tensor theory that is equivalent to $f(R)$ gravity is

$$S = \frac{1}{2\kappa} \int d^4x \sqrt{-g} [f(\phi) + f_\phi(\phi)(R - \phi)] + S_m, \quad (\text{C.1})$$

where $f_\phi(\phi) \equiv df/d\phi$ and S_m is the matter action. The field equation for ϕ is $\phi = R$ if $d^2f/d\phi^2 \neq 0$. Since the relation between ϕ and R is purely algebraic, it can be resubstituted into the action to reproduce the action for $f(R)$ gravity given by Eq. (5.23). After the conformal transformation $g_{\mu\nu}^E \equiv f_\phi(\phi)g_{\mu\nu}$, the action becomes that of general relativity with a minimally coupled scalar field:

$$S = \frac{1}{2\kappa} \int d^4x \sqrt{-g_E} \left(R_E - \frac{3}{2f_\phi(\phi)^2} g_E^{\mu\nu} [\nabla_{E\mu} f_\phi(\phi)] [\nabla_{E\nu} f_\phi(\phi)] - \frac{1}{f_\phi(\phi)^2} [\phi f_\phi(\phi) - f(\phi)] \right) + S_m \quad (\text{C.2})$$

Introducing a canonical scalar field φ such that $f_\phi(\phi) = \exp(\sqrt{2\kappa/3}\varphi)$, Eq. (C.2) can be rewritten as

$$S = \int d^4x \sqrt{-g_E} \left(\frac{1}{2\kappa} R_E - \frac{1}{2} (\nabla_E \varphi)^2 - V(\varphi) \right) + S_m,$$

where the potential is defined by

$$V(\varphi) \equiv \frac{\phi(\varphi) f_\phi[\phi(\varphi)] - f[\phi(\varphi)]}{2\kappa f_\phi[\phi(\varphi)]^2}. \quad (\text{C.3})$$

The absence of the kinetic term in Eq. (C.1) implies the Brans-Dicke parameter of $f(R)$ gravity theories is $\omega = 0$ [226]. From an analysis of Brans-Dicke gravity, if the scalar degree of freedom can propagate on scales much larger than the solar system, we can conclude that $\gamma = (1+\omega)/(2+\omega) = 1/2$ [226].

¹The material presented this appendix was first published in, *Solar system constraints to general $f(R)$ gravity*, Takeshi Chiba, Tristan L. Smith, and Adrienne L. Erickcek, Phys. Rev. **D75**, 124014 (2007). Reproduced here with permission, copyright (2007) by the American Physical Society.

In the frame where φ is canonical (the Einstein frame) φ has the equation of motion

$$\square_E \varphi = \frac{dV}{d\varphi} + \sqrt{\frac{\kappa}{6}} f'(\phi)^{-2} T^M, \quad (\text{C.4})$$

where the prime denotes differentiation with respect to ϕ . When we re-express Eq. (C.4) in terms of $f'(\phi)$ and the usual metric $g_{\mu\nu}$, we recover Eq. (5.29). Therefore, we stress that this reformulation contains *no new dynamics* compared to the expressions used in this chapter. The two formulations are entirely equivalent.

In order to derive the mass m_φ , we let $\varphi = \varphi_0(t) + \varphi_1(r)$ and $T^M = T^{\text{cos}} + T^{\text{s}}$ so that $\varphi_0(t)$ satisfies Eq. (C.4) with T^{cos} . We then expand to linear order in the perturbation φ_1 , writing Eq. (C.4) in terms of the physical metric $g_{\mu\nu}$. We find

$$\square \varphi_1 = f'(\phi_0) \left(\left. \frac{d^2 V}{d\varphi^2} \right|_{\varphi_0} - \frac{2}{3} \kappa \frac{T^{\text{cos}}}{[f'(\phi_0)]^2} \right) \varphi_1 + \sqrt{\frac{\kappa}{6}} \frac{T^{\text{s}}}{f'(\phi_0)}, \quad (\text{C.5})$$

where ϕ_0 denotes the background field value for the ϕ field. Using Eq. (C.3) to evaluate $d^2 V/d\varphi^2$, we have

$$m_\varphi^2 = \frac{f'(\phi_0)}{3} \left[\frac{1}{f''(\phi_0)} + \frac{\phi_0}{f'(\phi_0)} - \frac{4f(\phi_0)}{[f'(\phi_0)]^2} - 2\kappa \frac{T^{\text{cos}}}{[f'(\phi_0)]^2} \right]. \quad (\text{C.6})$$

Finally, we may rewrite m_φ^2 as Eq. (5.36) since $\phi_0 = R_0$. We conclude that if $m_\varphi^2 r^2 \ll 1$ then $\gamma = 1/2$ as discussed in Ref. [216].

Appendix D

A string-inspired derivation of the Chern-Simons field equations¹

The effective 4-D string action for heterotic and type II string theory can be written as [69, 287]

$$S = \int d^4x \sqrt{-g} \left[-\frac{1}{2\kappa^2} R - \alpha H_{\mu\nu\lambda} H^{\mu\nu\lambda} + \dots \right], \quad (\text{D.1})$$

where R is the Ricci scalar, $H_{\mu\nu\lambda}$ is the Kalb-Ramond (KR) three-form field strength, and α is a constant with units of length squared. We are neglecting numerous terms, including Gauss-Bonnet terms, dilaton terms, and matter terms, some of which depend on compactification. The Kalb-Ramond field is written in differential-form notation as

$$\mathbf{H} = \frac{1}{3} d\mathbf{B} + \boldsymbol{\omega}_L, \quad (\text{D.2})$$

where \mathbf{B} is a two-form field (known as the KR field) and $\boldsymbol{\omega}_L$ is the Lorentz-Chern-Simons term. The Lorentz-Chern-Simons three-form can be written in terms of the spin connection $\boldsymbol{\omega}$ as [288]

$$(\boldsymbol{\omega}_L)_{\mu\nu\lambda} = \frac{1}{2} \text{Tr} \left[\omega_{[\lambda} (d\omega)_{\mu\nu]} + \frac{4}{3} \omega_{[\mu} \omega_{\nu} \omega_{\lambda]} \right], \quad (\text{D.3})$$

where the trace is over the suppressed vector indices of the spin connections. We then have the identity,

$$d\mathbf{H} = \frac{1}{6} \text{Tr}(\mathbf{R} \wedge \mathbf{R}), \quad (\text{D.4})$$

associated with the KR field strength, where \mathbf{R} is the Riemann tensor and the trace is over the tensor indices; the right-hand side is also known as the Hirzebruch density. Taking the Hodge dual

¹The material presented in this appendix was first published in, *The effects of Chern-Simons gravity on bodies orbiting the Earth*, Tristan L. Smith, Adrienne L. Erickcek, Robert R. Caldwell, and Marc Kamionkowski, Phys. Rev. **D77**, 024015 (2008). Reproduced here with permission, copyright (2008) by the American Physical Society.

of the Hirzebruch density, we obtain

$$\frac{1}{6} {}^* \text{Tr}(\mathbf{R} \wedge \mathbf{R}) = \frac{1}{4!} \epsilon^{\mu\nu\rho\lambda} R_{\alpha\beta\mu\nu} R^{\alpha\beta}{}_{\rho\lambda} = -\frac{1}{12} \mathbf{R} \tilde{\mathbf{R}}. \quad (\text{D.5})$$

Let us now consider the equation of motion for the two-form KR field. We can rewrite the action involving \mathbf{B} as

$$\begin{aligned} S_B &\propto \int \mathbf{H} \wedge {}^* \mathbf{H} - \omega_L \wedge {}^* \omega_L \\ &\propto \int \frac{1}{9} d\mathbf{B} \wedge {}^* d\mathbf{B} + \frac{1}{3} d\mathbf{B} \wedge {}^* \omega_L + \frac{1}{3} \omega_L \wedge {}^* d\mathbf{B}. \end{aligned} \quad (\text{D.6})$$

On variation of this action with respect to \mathbf{B} , we have the equation of motion,

$$d {}^* \mathbf{H} = 0. \quad (\text{D.7})$$

Therefore the equation of motion for the KR two-form field shows that ${}^* \mathbf{H}$ is closed. In other words, at least locally, there exists a pseudo-scalar b (the KR axion, or sometimes called the universal axion) such that

$$\mathbf{H} = {}^* db. \quad (\text{D.8})$$

Noting that $-{}^* d {}^* d\phi = \square\phi$, we have the equation of motion for b ,

$$\square b = -{}^* d\mathbf{H} = -\frac{1}{6} {}^* \text{Tr}(\mathbf{R} \wedge \mathbf{R}) = \frac{1}{12} \mathbf{R} \tilde{\mathbf{R}}. \quad (\text{D.9})$$

Varying the action given by Eq. (D.1) with respect to the metric we obtain² [70]

$$-G^{\mu\nu} = \kappa^2 \alpha \{ 6H^\mu{}_{\lambda\rho} H^{\nu\lambda\rho} - g^{\mu\nu} H^{\lambda\rho\sigma} H_{\lambda\rho\sigma} + 4\nabla_\sigma (H^{\lambda\alpha(\mu} R^{\nu)\sigma}{}_{\alpha\lambda}) \}, \quad (\text{D.10})$$

where $G^{\mu\nu}$ is the usual Einstein tensor. Given that the equation of motion for the two-form field \mathbf{B} allows us to write $\mathbf{H} = {}^* db$, we have

$$H_{\mu\nu\rho} = \epsilon^\sigma{}_{\mu\nu\rho} \nabla_\sigma b. \quad (\text{D.11})$$

We can rewrite the field equation as

$$-G^{\mu\nu} = \kappa^2 \alpha 12 \left[T_b^{\mu\nu} + \frac{1}{3} \nabla_\sigma (H^{\lambda\alpha(\mu} R^{\nu)\sigma}{}_{\alpha\lambda}) \right], \quad (\text{D.12})$$

where $T_b^{\mu\nu}$ is the canonical stress-energy tensor for the pseudo-scalar field b . We will now show that

²The sign of the last term in this equation is different in Ref. [70]. The sign given here makes the divergence of the right-hand side vanish as required by the Bianchi identity.

the last term is actually the Cotton-York tensor.

Using the Bianchi identities for the Riemann tensor, we first note that we have the identity,

$$\nabla_\sigma \tilde{R}^{\sigma(\mu|\tau|\nu)} = \epsilon^{(\mu|\tau\sigma\rho} \nabla_\rho R^{\nu)}_\sigma. \quad (\text{D.13})$$

With this, it is straightforward to show that

$$\nabla_\sigma([\nabla_\tau b] \epsilon^{\tau\lambda\alpha(\mu} R^{\nu)\sigma}_{\alpha\lambda}) = 2\nabla_\sigma([\nabla_\tau b] \tilde{R}^{\sigma(\nu|\tau|\mu)}) = 2C^{\mu\nu}, \quad (\text{D.14})$$

where $C^{\mu\nu}$ is the Cotton-York tensor defined in Eq. (6.6). Choosing $\alpha = \ell^2/12$ and taking $b \rightarrow -\theta/\ell$ so that in the absence of the Cotton-York tensor we regain general relativity sourced by a canonical scalar field θ , the equations of motion are

$$G^{\mu\nu} - \frac{2\ell\kappa^2}{3} C^{\mu\nu} = -\kappa^2 T_\theta^{\mu\nu}, \quad (\text{D.15})$$

$$\square\theta = -\frac{1}{12} \ell \mathbf{R}\tilde{\mathbf{R}}. \quad (\text{D.16})$$

We can see that these field equations are identical to Eqs. (6.4) and (6.5) with vanishing scalar potential.

Appendix E

Calculation of the vector potential¹

In Lorenz gauge ($\partial_\mu A^\mu = 0$) the Chern-Simons Ampère's law, Eq. (6.23), can be written,

$$\square \left[\vec{A} + \frac{1}{m_{\text{cs}}} \vec{B} \right] = -4\pi G \vec{J}, \quad (\text{E.1})$$

where we have neglected the time variation in $\dot{\theta}$ in order to place m_{cs} inside the d'Alembertian operator. We are dealing with a stationary source, and so $\square = \nabla^2$. We may invert Eq. (E.1) to obtain

$$\vec{A} + \frac{1}{m_{\text{cs}}} \vec{\nabla} \times \vec{A} = G \int \frac{\vec{J}}{|\vec{r} - \vec{r}'|} d^3 r'. \quad (\text{E.2})$$

We can write this as

$$\left(\mathcal{I} + \frac{1}{m_{\text{cs}}} \vec{\nabla} \times \right) \vec{A} = G \int \frac{\vec{J}}{|\vec{r} - \vec{r}'|} d^3 r', \quad (\text{E.3})$$

where \mathcal{I} is the identity matrix. Multiplying both sides of the equation by $\left[\mathcal{I} - (1/m_{\text{cs}}) \vec{\nabla} \times \right]$, we obtain

$$\vec{A} - \frac{1}{m_{\text{cs}}^2} \vec{\nabla} \times \vec{\nabla} \times \vec{A} = G \left(\mathcal{I} - \frac{1}{m_{\text{cs}}} \vec{\nabla} \times \right) \int \frac{\vec{J}}{|\vec{r} - \vec{r}'|} d^3 r'. \quad (\text{E.4})$$

Noting that $\vec{\nabla} \times \vec{\nabla} \times \vec{A} = -\nabla^2 \vec{A}$ in Lorenz gauge, we have

$$\nabla^2 \vec{A} + m_{\text{cs}}^2 \vec{A} = \vec{S}, \quad (\text{E.5})$$

where

$$\vec{S} \equiv m_{\text{cs}}^2 G \left(\mathcal{I} - \frac{1}{m_{\text{cs}}} \vec{\nabla} \times \right) \int \frac{\vec{J}}{|\vec{r} - \vec{r}'|} d^3 r'. \quad (\text{E.6})$$

We recognize this as the inhomogeneous Helmholtz equation. For a rotating homogeneous sphere, the mass current is given by

$$\vec{J} = \rho [\vec{\omega} \times \vec{r}] \Theta(R - r), \quad (\text{E.7})$$

¹The material presented in this appendix was first published in, *The effects of Chern-Simons gravity on bodies orbiting the Earth*, Tristan L. Smith, Adrienne L. Erickcek, Robert R. Caldwell, and Marc Kamionkowski, Phys. Rev. **D77**, 024015 (2008). Reproduced here with permission, copyright (2008) by the American Physical Society.

where ρ is the density, ω is the angular velocity, R is the radius, and Θ is the Heaviside step function.

The most general Green's function for the inhomogeneous Helmholtz equation is

$$G(\vec{r}, \vec{r}') = -\frac{\cos(m_{\text{cs}}|\vec{r} - \vec{r}'|) + \tilde{\gamma} \sin(m_{\text{cs}}|\vec{r} - \vec{r}'|)}{4\pi|\vec{r} - \vec{r}'|}, \quad (\text{E.8})$$

where $\tilde{\gamma}$ is a constant. However, the second term (that is proportional to $\tilde{\gamma}$) remains constant for $|\vec{r}' - \vec{r}| \ll m_{\text{cs}}^{-1}$, implying that the influence of the source does not decrease with distance (for distances $r \ll m_{\text{cs}}^{-1}$), which we interpret as unphysical. We therefore set $\tilde{\gamma} = 0$. We then use multipole expansions for the Green's function,

$$-\frac{\cos(m_{\text{cs}}|\vec{r} - \vec{r}'|)}{4\pi|\vec{r} - \vec{r}'|} = m_{\text{cs}} \sum_{\ell, m} j_{\ell}(m_{\text{cs}}r_{<}) y_{\ell}(m_{\text{cs}}r_{>}) Y_{\ell m}^*(\hat{r}') Y_{\ell m}(\hat{r}), \quad (\text{E.9})$$

where $j_{\ell}(x)$ and $y_{\ell}(x)$ are, respectively, spherical Bessel function of the first and second kind, $Y_{\ell m}(\hat{r})$ is a spherical harmonic, and the subscript $<$ ($>$) means the argument is the lesser (greater) of r or r' . The solution for \vec{A} is then obtained by integrating,

$$\vec{A} = \int d^3r' G(\vec{r}, \vec{r}') \vec{S}(\vec{r}'), \quad (\text{E.10})$$

where all vectors are expanded in a Cartesian basis.

The resulting expression for \vec{A} may be split into a general-relativistic and a Chern-Simons term, $\vec{A} = \vec{A}_{\text{GR}} + \vec{A}_{\text{CS}}$, where

$$\vec{A}_{\text{GR}} = -\frac{4\pi G\rho R^3}{3} (\hat{r} \times \vec{\omega}) \times \begin{cases} \frac{r}{R} \left[\frac{1}{2} - \frac{3}{10} \left(\frac{r}{R} \right)^2 \right], & r \leq R, \\ \frac{R^2}{5r^2}, & r \geq R, \end{cases} \quad (\text{E.11})$$

is the gravitomagnetic vector potential in general relativity, and

$$\vec{A}_{\text{CS}} = -\frac{4\pi G\rho R^3}{m_{\text{cs}} R} \left[C_1(r) \vec{\omega} + C_2(r) \hat{r} \times \vec{\omega} + C_3(r) \hat{r} \times (\hat{r} \times \vec{\omega}) \right], \quad (\text{E.12})$$

with

$$\begin{aligned} C_1(r) &= -\frac{r^2}{5R^2} + \frac{1}{3} + \frac{2}{m_{\text{cs}}^2 R^2} + \frac{2R}{r} y_2(m_{\text{cs}}R) j_1(m_{\text{cs}}r), \\ C_2(r) &= \frac{m_{\text{cs}}r}{m_{\text{cs}}^2 R^2} + m_{\text{cs}}R y_2(m_{\text{cs}}R) j_1(m_{\text{cs}}r), \\ C_3(r) &= \frac{r^2}{5R^2} + m_{\text{cs}}R y_2(m_{\text{cs}}R) j_2(m_{\text{cs}}r), \end{aligned} \quad (\text{E.13})$$

inside the sphere, and

$$\begin{aligned}
C_1(r) &= \frac{2R^3}{15r^3} + \frac{2R}{r} j_2(m_{\text{cs}}R)y_1(m_{\text{cs}}r), \\
C_2(r) &= m_{\text{cs}}R j_2(m_{\text{cs}}R)y_1(m_{\text{cs}}r), \\
C_3(r) &= \frac{R^3}{5r^3} + m_{\text{cs}}R j_2(m_{\text{cs}}R)y_2(m_{\text{cs}}r),
\end{aligned}
\tag{E.14}$$

outside the sphere. We note that this solution for \vec{A} is finite at the origin and continuous across the boundary of the sphere, so it produces a finite \vec{B} at the origin and a continuous metric. Taking the curl of this solution for \vec{A} yields the expressions for \vec{B} given in Section 6.4.

Thus far, we have not discussed any boundary conditions on the gravitomagnetic field \vec{B} at the surface of the sphere. The field equations for \vec{B} imply two such boundary conditions, and we will now prove that the continuity of \vec{A} guarantees that these two boundary conditions are satisfied. The first boundary condition follows from $\vec{\nabla} \cdot \vec{B} = 0$; as in electromagnetism, this condition implies that the component of \vec{B} that is perpendicular to the surface must be continuous. The second boundary condition follows from the Chern-Simons version of Ampère's law:

$$\vec{\nabla} \times \vec{B} - \frac{1}{m_{\text{cs}}} \nabla^2 \vec{B} = 4\pi G \vec{J}.
\tag{E.15}$$

Integrating this equation over a surface with vanishing area that is perpendicular to the surface of the sphere and contains the boundary implies that the components of $[\vec{B} + (1/m_{\text{cs}})\vec{\nabla} \times \vec{B}]$ that are parallel to the sphere's surface must be continuous across the boundary.

Generally, the continuity of \vec{A} would not imply continuity of its curl. However, our \vec{A} is a solution to Eq. (E.2), which may be rewritten as

$$\vec{A} + \frac{1}{m_{\text{cs}}} \vec{B} = \vec{A}_{\text{GR}}.
\tag{E.16}$$

Since \vec{A} and \vec{A}_{GR} are both continuous across the surface of the sphere, this equation implies that \vec{B} is also continuous across the surface of the sphere. Furthermore, taking the curl of this equation shows that $\vec{\nabla} \times \vec{B}$ is continuous provided that \vec{B} and $\vec{\nabla} \times \vec{A}_{\text{GR}}$ are continuous. Taking the curl of Eq. (E.11) confirms that $\vec{\nabla} \times \vec{A}_{\text{GR}}$ is continuous across the surface of the sphere. Therefore, we have shown that the continuity of \vec{A} implies that both \vec{B} and $\vec{\nabla} \times \vec{B}$ are also continuous, which guarantees that both boundary conditions on \vec{B} are satisfied by our solution.

Appendix F

An alternative method to solve the Chern-Simons gravitomagnetic field equations¹

Here we present an alternative method to solve the Chern-Simons altered Amperè's law. This method allows us to explicitly derive the complete set of homogeneous solutions to the Chern-Simons Amperè's law.

We begin with a quick review of the relevant field equation. For a homogeneous scalar field, $\theta(t)$, we find that in Chern-Simons gravity the new Amperè's law is given by

$$\vec{\nabla} \times \vec{B} - \dot{\vec{E}} - \frac{1}{2}\ell^3\dot{\theta}\square\vec{B} = 4\pi G\vec{J}. \quad (\text{F.1})$$

We can rewrite this equation as

$$\square \left[\vec{A} + \frac{1}{m_{cs}}\vec{B} \right] = -4\pi G\vec{J}, \quad (\text{F.2})$$

where we have defined a mass, $m_{cs} \equiv 2/(\ell^3\dot{\theta})$. For a general mass current, \vec{J} , we can invert the above equation and we are now left to solve the system of equations

$$\vec{\nabla} \times \vec{A} + m_{cs}\vec{A} = m_{cs}\vec{S}, \quad (\text{F.3})$$

where $\vec{S} \equiv -4\pi G\square^{-1}\vec{J}$. Now we wish to rewrite this expression so that the unknown vector field has vanishing divergence. Clearly, in general, the above expression implies

$$m_{cs}\vec{\nabla} \cdot \vec{A} = \vec{\nabla} \cdot \vec{S}. \quad (\text{F.4})$$

¹This appendix consists of previously unpublished work by the author.

We then define a new vector field, $\vec{\chi} \equiv \vec{A} - \vec{S}$. Rewriting Eq. (F.3) in terms of $\vec{\chi}$ we have

$$\vec{\nabla} \times \vec{\chi} + m_{cs} \vec{\chi} = -\vec{\nabla} \times \vec{S}. \quad (\text{F.5})$$

With this, we can see that $\vec{\nabla} \cdot \vec{\chi} = 0$. It is therefore said that $\vec{\chi}$ is a solenoidal vector field. This is what we wanted because with this there is a very nice decomposition theorem that will allow us to solve Eq. (F.3) directly.

F.0.3 Decomposition of a solenoidal vector field

The general theory of the decomposition of a solenoidal vector field is presented in Refs. [289–291]. We now review the necessary details of this decomposition.

It can be shown that any solenoidal vector field $\vec{\chi}$ can be generally written in terms of two scalar functions,

$$\vec{\chi} = \vec{\nabla} \times \left(\frac{\Psi}{r} \vec{r} \right) + \vec{\nabla} \times \vec{\nabla} \times \left(\frac{\Phi}{r} \vec{r} \right). \quad (\text{F.6})$$

The first term on the right-hand side is said to be toroidal with defining scalar Ψ and the second term is said to be poloidal with defining scalar Φ . It can then be shown that, if we expand these defining scalars in terms of spherical harmonics,

$$\Psi = \sum_{\ell, m} T_{\ell m}(r) Y_{\ell m}(\theta, \phi), \quad (\text{F.7})$$

$$\Phi = \sum_{\ell, m} P_{\ell m}(r) Y_{\ell m}(\theta, \phi), \quad (\text{F.8})$$

then in spherical coordinates we have

$$T_r = 0, \quad (\text{F.9})$$

$$T_\theta = \frac{T_{\ell m}(r)}{r \sin(\theta)} \frac{\partial Y_{\ell m}}{\partial \phi}, \quad (\text{F.10})$$

$$T_\phi = -\frac{T_{\ell m}(r)}{r} \frac{\partial Y_{\ell m}}{\partial \theta}, \quad (\text{F.11})$$

$$P_r = \frac{\ell(\ell+1)}{r^2} P_{\ell m} Y_{\ell m}, \quad (\text{F.12})$$

$$P_\theta = \frac{1}{r} \frac{dP_{\ell m}}{dr} \frac{\partial Y_{\ell m}}{\partial \theta}, \quad (\text{F.13})$$

$$P_\phi = \frac{1}{r \sin(\theta)} \frac{dP_{\ell m}}{dr} \frac{\partial Y_{\ell m}}{\partial \phi}, \quad (\text{F.14})$$

where for the rest of the chapter the sum over ℓ and m is implied, T_i is the component of the toroidal vector field, and P_i is the component of the poloidal vector field.

We want to solve the equation

$$\vec{\nabla} \times \vec{\chi} + m_{cs} \vec{\chi} = \vec{\mathcal{S}}, \quad (\text{F.15})$$

for some known source $\vec{\mathcal{S}}$. We write $\vec{\chi}$ as in Eq. (F.6) and expand the scalar functions as in Eqs. (F.7) & (F.8). We now wish to express $\vec{\nabla} \times \vec{\chi}$ in terms of $T_{\ell m}$ and $P_{\ell m}$.

We have that

$$\vec{\chi} = \vec{\nabla} \times \vec{\nabla} \times \left(\frac{\Psi}{r} \vec{r} \right) + \vec{\nabla} \times \vec{\nabla} \times \vec{\nabla} \times \left(\frac{\Phi}{r} \vec{r} \right). \quad (\text{F.16})$$

We can see that the first term is just a poloidal vector field with defining scalar Ψ and it turns out that we can rewrite the second term as a toroidal vector field with defining scalar given by

$$\tilde{\Phi} = -r \nabla^2 \frac{\Phi}{r}. \quad (\text{F.17})$$

Rewriting the last term in terms of $P_{\ell m}$ we have

$$\tilde{\Phi} = \sum_{\ell, m} \left[\frac{\ell(\ell+1)}{r^2} P_{\ell m} - \frac{d^2 P_{\ell m}}{dr^2} \right] Y_{\ell m}(\theta, \phi). \quad (\text{F.18})$$

We can now write out Eq. (F.15) for each component:

$$\mathcal{S}_r = m_{cs} \frac{\ell(\ell+1)}{r^2} P_{\ell m} Y_{\ell m} + \frac{\ell(\ell+1)}{r^2} T_{\ell m} Y_{\ell m}, \quad (\text{F.19})$$

$$\begin{aligned} \mathcal{S}_\theta &= m_{cs} \left[\frac{T_{\ell m}}{r \sin(\theta)} \frac{\partial Y_{\ell m}}{\partial \phi} + \frac{1}{r} \frac{dP_{\ell m}}{dr} \frac{\partial Y_{\ell m}}{\partial \theta} \right] + \frac{1}{r} \frac{dT_{\ell m}}{dr} \frac{\partial Y_{\ell m}}{\partial \theta} \\ &\quad + \frac{1}{r \sin(\theta)} \frac{\partial Y_{\ell m}}{\partial \phi} \left[\frac{\ell(\ell+1)}{r^2} P_{\ell m} - \frac{d^2 P_{\ell m}}{dr^2} \right], \end{aligned} \quad (\text{F.20})$$

$$\begin{aligned} \mathcal{S}_\phi &= m_{cs} \left[-\frac{T_{\ell m}}{r} \frac{\partial Y_{\ell m}}{\partial \theta} + \frac{1}{r \sin(\theta)} \frac{dP_{\ell m}}{dr} \frac{\partial Y_{\ell m}}{\partial \phi} \right] + \frac{1}{r \sin(\theta)} \frac{dT_{\ell m}}{dr} \frac{\partial Y_{\ell m}}{\partial \phi} \\ &\quad - \frac{1}{r} \frac{\partial Y_{\ell m}}{\partial \theta} \left[\frac{\ell(\ell+1)}{r^2} P_{\ell m} - \frac{d^2 P_{\ell m}}{dr^2} \right]. \end{aligned} \quad (\text{F.21})$$

We now write

$$\mathcal{S}_r = \sum_{\ell, m} \mathcal{S}_{\ell m}^r Y_{\ell m} \quad (\text{F.22})$$

and with this we see that Eq. (F.19) implies

$$T_{\ell m} = \tilde{\mathcal{S}}_{\ell m}^r - m_{cs} P_{\ell m}, \quad (\text{F.23})$$

where we have defined

$$\tilde{\mathcal{S}}_{\ell m}^r \equiv \frac{r^2}{\ell(\ell+1)} \mathcal{S}_{\ell m}^r. \quad (\text{F.24})$$

It is clear that this equation isn't defined for $\ell = 0$. However, we can see that since $\vec{\nabla} \cdot \vec{\mathcal{S}} = 0$ we

have that $\mathcal{S}_{00}^r = 0$. We can now rewrite Eqs. (F.20) and (F.21) to find

$$\tilde{\mathcal{S}}_\theta = \frac{1}{\sin(\theta)} \frac{\partial Y_{\ell m}}{\partial \phi} \left[\frac{\ell(\ell+1)}{r^2} (P_{\ell m} - m_{cs}^2) - \frac{d^2 P_{\ell m}}{dr^2} \right], \quad (\text{F.25})$$

$$\tilde{\mathcal{S}}_\phi = -\frac{\partial Y_{\ell m}}{\partial \theta} \left[\frac{\ell(\ell+1)}{r^2} (P_{\ell m} - m_{cs}^2) - \frac{d^2 P_{\ell m}}{dr^2} \right], \quad (\text{F.26})$$

where we have defined

$$\tilde{\mathcal{S}}_\theta \equiv r\mathcal{S}_\theta - m_{cs} \frac{\tilde{\mathcal{S}}_{\ell m}^r}{\sin(\theta)} \frac{\partial Y_{\ell m}}{\partial \phi} - \frac{d\tilde{\mathcal{S}}_{\ell m}^r}{dr} \frac{\partial Y_{\ell m}}{\partial \theta}, \quad (\text{F.27})$$

$$\tilde{\mathcal{S}}_\phi \equiv r\mathcal{S}_\phi + m_{cs} \tilde{\mathcal{S}}_{\ell m}^r \frac{\partial Y_{\ell m}}{\partial \theta} - \frac{1}{\sin(\theta)} \frac{d\tilde{\mathcal{S}}_{\ell m}^r}{dr} \frac{\partial Y_{\ell m}}{\partial \phi}. \quad (\text{F.28})$$

We now note that the raising/lowering operator for spherical harmonics is given by

$$L_\pm = e^{\pm i\phi} \left[i \cot(\theta) \frac{\partial}{\partial \phi} \pm \frac{\partial}{\partial \theta} \right]. \quad (\text{F.29})$$

With this we can see that we have

$$e^{-i\phi} [i \cos(\theta) \tilde{\mathcal{S}}_\theta + \tilde{\mathcal{S}}_\phi] = \sqrt{(\ell+m)(\ell-m+1)} Y_{\ell m-1} \times \left[\left(\frac{\ell(\ell+1)}{r^2} - m_{cs}^2 \right) P_{\ell m} - \frac{d^2 P_{\ell m}}{dr^2} \right]. \quad (\text{F.30})$$

At first glance this is an odd equation since it seems to place a restriction on the source function. In particular it seems to imply that in its spherical harmonic expansion this source function cannot have nonzero terms with $\ell+m=0$. However, this is a consequence of the fact that we have supposed that the source function is solenoidal itself. Assuming that we knew the two defining scalars for the source, we can show that the source function in Eq. (F.31) can be written as

$$\sqrt{(\ell+m)(\ell-m+1)} Y_{\ell m-1} [\mathcal{S}_{\ell m}^T - m_{cs} \mathcal{S}_{\ell m}^P], \quad (\text{F.31})$$

where $\mathcal{S}_{\ell m}^{T,P}$ are the spherical harmonic coefficients for the toroidal and poloidal defining scalars for the source. Therefore, Eq. (F.31) allows us to find $P_{\ell m}$ for $\ell+m \neq 0$. We must use either Eq. (F.27) or Eq. (F.28) in order to solve for cases where $\ell+m=0$.

Let us now consider how we are to solve this equation for the two cases we are interested in: the field due to a moving point mass and the field due to a rotating homogeneous sphere. It will turn out that for both of these sources we have the condition that $\mathcal{S}_r = 0$. With this we also have $\tilde{\mathcal{S}}_\theta = r\mathcal{S}_\theta$ and $\tilde{\mathcal{S}}_\phi = r\mathcal{S}_\phi$. Then solving the CS gravitomagnetic field equations entails two steps. First, we expand

$$e^{-i\theta} r [i \cos(\theta) \mathcal{S}_\theta + \mathcal{S}_\phi] \quad (\text{F.32})$$

in spherical harmonics and solve Eq. (F.31). We then have to check that we haven't missed any terms with $\ell + m = 0$. We do so by looking at either Eq. (F.27) or Eq. (F.28) and expanding \mathcal{S}_θ or \mathcal{S}_ϕ in spherical harmonics, respectively, for values of ℓ and m such that $\ell + m = 0$. We then solve each equation that respects this condition. With this, we have found the particular solution for Φ . Since $\mathcal{S}_r = 0$ we have that $T_{\ell m} = -m_{cs}P_{\ell m}$ therefore we have $\Psi = -m_{cs}\Phi$. With this, we can reconstruct $\vec{\chi}$ through Eq. (F.6).

Bibliography

- [1] M. Maggiore, Phys. Rept. **331**, 283 (2000), [gr-qc/9909001](#).
- [2] A. H. Guth, Phys. Rev. **D23**, 347 (1981).
- [3] A. Albrecht and P. J. Steinhardt, Phys. Rev. Lett. **48**, 1220 (1982).
- [4] A. D. Linde, Phys. Lett. **B108**, 389 (1982).
- [5] A. H. Guth and S. Y. Pi, Phys. Rev. Lett. **49**, 1110 (1982).
- [6] J. M. Bardeen, P. J. Steinhardt, and M. S. Turner, Phys. Rev. **D28**, 679 (1983).
- [7] S. W. Hawking, Phys. Lett. **B115**, 295 (1982).
- [8] A. D. Linde, Phys. Lett. **B116**, 335 (1982).
- [9] A. A. Starobinsky, JETP Lett. **30**, 682 (1979).
- [10] L. F. Abbott and M. B. Wise, Nucl. Phys. **B244**, 541 (1984).
- [11] A. Starobinskii, Sov. Astron. Lett. **11**, 133 (1985).
- [12] V. A. Rubakov, M. V. Sazhin, and A. V. Veryaskin, Phys. Lett. **B115**, 189 (1982).
- [13] R. Fabbri and M. D. Pollock, Phys. Lett. **B125**, 445 (1983).
- [14] B. Allen, Phys. Rev. **D37**, 2078 (1988).
- [15] V. Sahni, Phys. Rev. **D42**, 453 (1990).
- [16] A. Kosowsky and M. S. Turner, Phys. Rev. **D47**, 4372 (1993), [astro-ph/9211004](#).
- [17] M. Kamionkowski, A. Kosowsky, and M. S. Turner, Phys. Rev. **D49**, 2837 (1994), [astro-ph/9310044](#).
- [18] A. D. Dolgov, D. Grasso, and A. Nicolis, Phys. Rev. **D66**, 103505 (2002), [astro-ph/0206461](#).
- [19] L. A. Boyle, P. J. Steinhardt, and N. Turok, Phys. Rev. **D69**, 127302 (2004), [hep-th/0307170](#).

- [20] S. Perlmutter et al. (Supernova Cosmology Project), *Astrophys. J.* **517**, 565 (1999), [astro-ph/9812133](#).
- [21] A. G. Riess et al. (Supernova Search Team), *Astron. J.* **116**, 1009 (1998), [astro-ph/9805201](#).
- [22] C. Wetterich, *Nucl. Phys.* **B302**, 668 (1988).
- [23] B. Ratra and P. J. E. Peebles, *Phys. Rev.* **D37**, 3406 (1988).
- [24] R. R. Caldwell, R. Dave, and P. J. Steinhardt, *Phys. Rev. Lett.* **80**, 1582 (1998), [astro-ph/9708069](#).
- [25] P. J. Steinhardt, L.-M. Wang, and I. Zlatev, *Phys. Rev.* **D59**, 123504 (1999), [astro-ph/9812313](#).
- [26] C. Armendariz-Picon, T. Damour, and V. F. Mukhanov, *Phys. Lett.* **B458**, 209 (1999), [hep-th/9904075](#).
- [27] E. J. Copeland, M. Sami, and S. Tsujikawa, *Int. J. Mod. Phys.* **D15**, 1753 (2006), [hep-th/0603057](#).
- [28] G. R. Dvali, G. Gabadadze, and M. Porrati, *Phys. Lett.* **B485**, 208 (2000), [hep-th/0005016](#).
- [29] C. Deffayet, G. R. Dvali, and G. Gabadadze, *Phys. Rev.* **D65**, 044023 (2002), [astro-ph/0105068](#).
- [30] N. Arkani-Hamed, S. Dimopoulos, G. Dvali, and G. Gabadadze (2002), [hep-th/0209227](#).
- [31] G. Dvali and M. S. Turner (2003), [astro-ph/0301510](#).
- [32] S. M. Carroll, V. Duvvuri, M. Trodden, and M. S. Turner, *Phys. Rev.* **D70**, 043528 (2004), [astro-ph/0306438](#).
- [33] S. Nojiri and S. D. Odintsov, *ECONF* **C0602061**, 06 (2006), [hep-th/0601213](#).
- [34] R. Wald, *General Relativity* (University of Chicago Press, 1999).
- [35] A. S. Eddington, *The Mathematical Theory of Relativity* (Cambridge University Press, 1924).
- [36] R. A. Hulse and J. H. Taylor, *Astrophys. J.* **195**, L51 (1975).
- [37] J. H. Taylor and J. M. Weisberg, *Astrophys. J.* **345**, 434 (1989).
- [38] I. H. Stairs, S. E. Thorsett, and Z. Arzoumanian, *Phys. Rev. Lett.* **93**, 141101 (2004), [astro-ph/0408457](#).
- [39] M. Kramer et al., *Science* **314**, 97 (2006), [astro-ph/0609417](#).

- [40] B. C. Barish and R. Weiss, *Physics Today* **52**, 44 (1999), <http://www.ligo.caltech.edu/>.
- [41] E. C. G. Stueckelberg, *Phys. Rev.* **106**, 388 (1957).
- [42] K. S. Thorne, *300 Years of Gravitation* (Cambridge University Press, 1987), eds. S. W. Hawking and W. Israel, pp. 300-458.
- [43] M. Kamionkowski, A. Kosowsky, and A. Stebbins, *Phys. Rev.* **D55**, 7368 (1997), [astro-ph/9611125](#).
- [44] M. Kamionkowski, A. Kosowsky, and A. Stebbins, *Phys. Rev. Lett.* **78**, 2058 (1997), [astro-ph/9609132](#).
- [45] M. Zaldarriaga and U. Seljak, *Phys. Rev.* **D55**, 1830 (1997), [astro-ph/9609170](#).
- [46] U. Seljak and M. Zaldarriaga, *Phys. Rev. Lett.* **78**, 2054 (1997), [astro-ph/9609169](#).
- [47] P. Cabella and M. Kamionkowski (2004), [astro-ph/0403392](#).
- [48] URL http://www.astro.caltech.edu/~lgg/spider_front.htm.
- [49] E. Komatsu et al. (WMAP) (2008), 0803.0547.
- [50] L. A. Boyle, P. J. Steinhardt, and N. Turok, *Phys. Rev. Lett.* **96**, 111301 (2006), [astro-ph/0507455](#).
- [51] L. Pagano, A. Cooray, A. Melchiorri, and M. Kamionkowski (2007), [arXiv:0707.2560\[astro-ph\]](#).
- [52] S. L. Larson (2003), online Sensitivity Curve Generator [<http://www.srl.caltech.edu/~shane/sensitivity/>] based on Shane L. Larson and William A. Hiscock, *Phys. Rev.* **D62**: 062001, 2000.
- [53] A. Buonanno, G. Sigl, G. G. Raffelt, H.-T. Janka, and E. Muller, *Phys. Rev.* **D72**, 084001 (2005), [astro-ph/0412277](#).
- [54] B. Allen (1996), [gr-qc/9604033](#).
- [55] T. L. Smith, E. Pierpaoli, and M. Kamionkowski, *Phys. Rev. Lett.* **97**, 021301 (2006), [astro-ph/0603144](#).
- [56] N. Seto and A. Cooray, *Phys. Rev.* **D73**, 023005 (2006), [astro-ph/0502054](#).
- [57] T. Pyne, C. R. Gwinn, M. Birkinshaw, T. M. Eubanks, and D. N. Matsakis, *Astrophys. J.* **465**, 566 (1996), [astro-ph/9507030](#).

- [58] C. R. Gwinn, T. M. Eubanks, T. Pyne, M. Birkinshaw, and D. N. Matsakis, *Astrophys. J.* **485**, 87 (1997), [astro-ph/9610086](#).
- [59] *LIGO Science Collaboration White Paper*, URL <http://www.ligo.caltech.edu/docs/T/T990080-00.pdf>.
- [60] B. Abbott et al. (LIGO Scientific), *Phys. Rev.* **D69**, 122004 (2004), [gr-qc/0312088](#).
- [61] B. Abbott et al. (LIGO Scientific) (2005), [astro-ph/0507254](#).
- [62] V. M. Kaspi, J. H. Taylor, and M. F. Ryba, *Astrophys. J.* **428**, 713 (1994).
- [63] A. N. Lommen (2002), [astro-ph/0208572](#).
- [64] M. Kramer (2004), [astro-ph/0409020](#).
- [65] S. Capozziello, S. Carloni, and A. Troisi, *Recent Res. Dev. Astron. Astrophys.* **1**, 625 (2003), [astro-ph/0303041](#).
- [66] A. S. Bolton, S. Burles, L. V. E. Koopmans, T. Treu, and L. A. Moustakas, *Astrophys. J.* **638**, 703 (2006), [arXiv:astro-ph/0511453](#).
- [67] A. Lue, L.-M. Wang, and M. Kamionkowski, *Phys. Rev. Lett.* **83**, 1506 (1999), [astro-ph/9812088](#).
- [68] R. Jackiw and S. Y. Pi, *Phys. Rev.* **D68**, 104012 (2003), [gr-qc/0308071](#).
- [69] B. A. Campbell, M. J. Duncan, N. Kaloper, and K. A. Olive, *Nucl. Phys.* **B351**, 778 (1991).
- [70] B. A. Campbell, M. J. Duncan, N. Kaloper, and K. A. Olive, *Phys. Lett.* **B251**, 34 (1990).
- [71] J. Lense and H. Thirring, *Phys. Z.* **19**, 711 (1918), translated by B. Mashhoon, F. W. Hehl, and D. S. Theiss, *Gen. Rel. Grav.* **16**, 711 (1984).
- [72] C. M. Will, *Phys. Rev.* **D67**, 062003 (2003), <http://einstein.stanford.edu>, [gr-qc/0212069](#).
- [73] M. Kamionkowski and A. Kosowsky, *Ann. Rev. Nucl. Part. Sci.* **49**, 77 (1999), [astro-ph/9904108](#).
- [74] P. de Bernardis et al. (Boomerang Collaboration), *Nature* **404**, 955 (2000), [astro-ph/0004404](#).
- [75] A. D. Miller et al., *Astrophys. J.* **524**, L1 (1999), [astro-ph/9906421](#).
- [76] S. Hanany et al., *Astrophys. J.* **545**, L5 (2000), [astro-ph/0005123](#).
- [77] N. W. Halverson et al., *Astrophys. J.* **568**, 38 (2002), [astro-ph/0104489](#).
- [78] B. S. Mason et al., *Astrophys. J.* **591**, 540 (2003), [astro-ph/0205384](#).

- [79] A. Benoit et al. (Archeops Collaboration), *Astron. Astrophys.* **399**, L25 (2003), [astro-ph/0210306](#).
- [80] J. H. Goldstein et al., *Astrophys. J.* **599**, 773 (2003), [astro-ph/0212517](#).
- [81] D. N. Spergel et al. (WMAP), *Astrophys. J. Suppl.* **148**, 175 (2003), [astro-ph/0302209](#).
- [82] URL universe.nasa.gov/program/bbo.html.
- [83] N. Seto, S. Kawamura, and T. Nakamura, *Phys. Rev. Lett.* **87**, 221103 (2001), [astro-ph/0108011](#).
- [84] M. Kamionkowski and A. Kosowsky, *Phys. Rev.* **D57**, 685 (1998), [astro-ph/9705219](#).
- [85] A. H. Jaffe, M. Kamionkowski, and L.-M. Wang, *Phys. Rev.* **D61**, 083501 (2000), [astro-ph/9909281](#).
- [86] R. Bar-Kana, *Phys. Rev.* **D50**, 1157 (1994), [astro-ph/9401050](#).
- [87] M. S. Turner, *Phys. Rev.* **D55**, 435 (1997), [astro-ph/9607066](#).
- [88] C. Ungarelli, P. Corasaniti, R. A. Mercer, and A. Vecchio, *Class. Quant. Grav.* **22**, S955 (2005), [astro-ph/0504294](#).
- [89] A. R. Liddle, *Phys. Rev.* **D49**, 3805 (1994), [gr-qc/9307036](#).
- [90] R. A. Battye and E. P. S. Shellard, *Class. Quant. Grav.* **13**, A239 (1996), [astro-ph/9610196](#).
- [91] D. Polarski, *Phys. Lett.* **B458**, 13 (1999), [gr-qc/9906075](#).
- [92] S. Dodelson, W. H. Kinney, and E. W. Kolb, *Phys. Rev.* **D56**, 3207 (1997), [astro-ph/9702166](#).
- [93] W. H. Kinney, *Phys. Rev.* **D58**, 123506 (1998), [astro-ph/9806259](#).
- [94] D. N. Spergel et al. (WMAP), *Astrophys. J. Suppl.* **170**, 377 (2007), [astro-ph/0603449](#).
- [95] H. K. Eriksen et al., *Astrophys. J.* **656**, 641 (2007), [astro-ph/0606088](#).
- [96] J. R. Kristiansen, H. K. Eriksen, and O. Elgaroy (2006), [astro-ph/0608017](#).
- [97] URL http://www.esa.int/esaSC/120398_index_0_m.html.
- [98] A. R. Liddle, P. Parsons, and J. D. Barrow, *Phys. Rev.* **D50**, 7222 (1994), [astro-ph/9408015](#).
- [99] E. D. Stewart and D. H. Lyth, *Phys. Lett.* **B302**, 171 (1993), [gr-qc/9302019](#).
- [100] J. E. Lidsey et al., *Rev. Mod. Phys.* **69**, 373 (1997), [astro-ph/9508078](#).

- [101] A. R. Liddle and D. H. Lyth, *Cosmological inflation and large-scale structure* (Cambridge, UK: Univ. Pr. 400 p, 2000).
- [102] A. Kosowsky and M. S. Turner, Phys. Rev. **D52**, 1739 (1995), [astro-ph/9504071](#).
- [103] M. S. Turner, Phys. Rev. **D28**, 1243 (1983).
- [104] A. R. Liddle and D. H. Lyth, Phys. Rept. **231**, 1 (1993), [astro-ph/9303019](#).
- [105] R. A. C. Croft, D. H. Weinberg, N. Katz, and L. Hernquist, Astrophys J **495**, 44 (1998).
- [106] R. Mandelbaum, P. McDonald, U. Seljak, and R. Cen, Mon. Not. Roy. Astron. Soc. **344**, 776 (2003), [astro-ph/0302112](#).
- [107] U. Seljak et al. (2004), [astro-ph/0407372](#).
- [108] J. Dunkley et al. (WMAP) (2008), [arXiv:0803.0586\[astro-ph\]](#).
- [109] U. Seljak, A. Slosar, and P. McDonald, JCAP **0610**, 014 (2006), [astro-ph/0604335](#).
- [110] M. Cortes, A. R. Liddle, and P. Mukherjee, Phys. Rev. **D75**, 083520 (2007), [astro-ph/0702170](#).
- [111] M. S. Turner, M. J. White, and J. E. Lidsey, Phys. Rev. **D48**, 4613 (1993), [astro-ph/9306029](#).
- [112] J. R. Pritchard and M. Kamionkowski (2004), [astro-ph/0412581](#).
- [113] J. C. Mather et al., Astrophys. J. **420**, 439 (1994).
- [114] N. Christensen, Phys. Rev. **D46**, 5250 (1992).
- [115] E. E. Flanagan, Phys. Rev. **D48**, 2389 (1993), [astro-ph/9305029](#).
- [116] N. J. Cornish and S. L. Larson, Class. Quant. Grav. **18**, 3473 (2001), [gr-qc/0103075](#).
- [117] A. J. Farmer and E. S. Phinney, Mon. Not. Roy. Astron. Soc. **346**, 1197 (2003), [astro-ph/0304393](#).
- [118] R. Schneider, V. Ferrari, S. Matarrese, and S. F. Portegies Zwart, Mon. Not. Roy. Astron. Soc. **324**, 797 (2001), [astro-ph/0002055](#).
- [119] A. R. Cooray, Mon. Not. Roy. Astron. Soc. **354**, 25 (2004), [astro-ph/0406467](#).
- [120] M. Kesden, A. Cooray, and M. Kamionkowski, Phys. Rev. Lett. **89**, 011304 (2002), [astro-ph/0202434](#).
- [121] L. Knox and Y.-S. Song, Phys. Rev. Lett. **89**, 011303 (2002), [astro-ph/0202286](#).

- [122] U. Seljak and C. M. Hirata, Phys. Rev. **D69**, 043005 (2004), [astro-ph/0310163](#).
- [123] K. Sigurdson and A. Cooray (2005), [astro-ph/0502549](#).
- [124] C. Cutler and J. Harms, Phys. Rev. **D73**, 042001 (2006), [gr-qc/0511092](#).
- [125] H. Peiris and R. Easther, JCAP **0607**, 002 (2006), [astro-ph/0603587](#).
- [126] F. S. Accetta, D. J. Zoller, and M. S. Turner, Phys. Rev. **D31**, 3046 (1985).
- [127] D. La and P. J. Steinhardt, Phys. Rev. Lett. **62**, 376 (1989).
- [128] J. Bock et al. (2006), [astro-ph/0604101](#).
- [129] E. S. Phinney, private communication.
- [130] N. Seto, Phys. Rev. **D73**, 063001 (2006), [gr-qc/0510067](#).
- [131] H. Kudoh, A. Taruya, T. Hiramatsu, and Y. Himemoto, Phys. Rev. **D73**, 064006 (2006), [gr-qc/0511145](#).
- [132] A. D. Linde, Phys. Lett. **B129**, 177 (1983).
- [133] T. L. Smith, M. Kamionkowski, and A. Cooray (2005), [astro-ph/0506422](#).
- [134] A. D. Linde, Phys. Rev. **D49**, 748 (1994), [astro-ph/9307002](#).
- [135] G. R. Dvali, Q. Shafi, and R. K. Schaefer, Phys. Rev. Lett. **73**, 1886 (1994), [hep-ph/9406319](#).
- [136] A. D. Linde and A. Riotto, Phys. Rev. **D56**, 1841 (1997), [hep-ph/9703209](#).
- [137] D. H. Lyth and E. D. Stewart, Phys. Rev. **D54**, 7186 (1996), [hep-ph/9606412](#).
- [138] E. J. Copeland, A. R. Liddle, D. H. Lyth, E. D. Stewart, and D. Wands, Phys. Rev. **D49**, 6410 (1994), [astro-ph/9401011](#).
- [139] W. H. Kinney and K. T. Mahanthappa, Phys. Rev. **D53**, 5455 (1996), [hep-ph/9512241](#).
- [140] K. Freese, J. A. Frieman, and A. V. Olinto, Phys. Rev. Lett. **65**, 3233 (1990).
- [141] K. Freese and W. H. Kinney, Phys. Rev. **D70**, 083512 (2004), [hep-ph/0404012](#).
- [142] C. Savage, K. Freese, and W. H. Kinney, Phys. Rev. **D74**, 123511 (2006), [hep-ph/0609144](#).
- [143] W. H. Kinney, AIP Conf. Proc. **928**, 3 (2007), [arXiv:0706.3699\[astro-ph\]](#).
- [144] Q. Shafi and A. Vilenkin, Phys. Rev. **D29**, 1870 (1984).
- [145] Q. Shafi and V. N. Senoguz, Phys. Rev. **D73**, 127301 (2006), [astro-ph/0603830](#).

- [146] W. H. Kinney and K. T. Mahanthappa, Phys. Lett. **B383**, 24 (1996), [hep-ph/9511460](#).
- [147] S. R. Coleman and E. Weinberg, Phys. Rev. **D7**, 1888 (1973).
- [148] S.-Y. Pi, Phys. Rev. Lett. **52**, 1725 (1984).
- [149] H. V. Peiris et al., Astrophys. J. Suppl. **148**, 213 (2003), [astro-ph/0302225](#).
- [150] E. D. Stewart and D. H. Lyth, Phys. Lett. **B302**, 171 (1993), [gr-qc/9302019](#).
- [151] A. A. Starobinsky, JETP Lett. **55**, 489 (1992).
- [152] J. Lesgourgues, D. Polarski, and A. A. Starobinsky, Mon. Not. Roy. Astron. Soc. **297**, 769 (1998), [astro-ph/9711139](#).
- [153] M. Kamionkowski and A. R. Liddle, Phys. Rev. Lett. **84**, 4525 (2000), [astro-ph/9911103](#).
- [154] A. R. Zentner and J. S. Bullock, Phys. Rev. **D66**, 043003 (2002), [astro-ph/0205216](#).
- [155] A. R. Zentner and J. S. Bullock, Astrophys. J. **598**, 49 (2003), [astro-ph/0304292](#).
- [156] P. J. Steinhardt and N. Turok, Science **296**, 1436 (2002).
- [157] G. Veneziano, Phys. Lett. **B265**, 287 (1991).
- [158] M. Gasperini and G. Veneziano, Phys. Rev. **D50**, 2519 (1994), [gr-qc/9403031](#).
- [159] F. Vernizzi, A. Melchiorri, and R. Durrer, Phys. Rev. **D63**, 063501 (2001), [astro-ph/0008232](#).
- [160] G. Veneziano (2000), [hep-th/0002094](#).
- [161] R. Brustein, M. Gasperini, M. Giovannini, and G. Veneziano, Phys. Lett. **B361**, 45 (1995), [hep-th/9507017](#).
- [162] A. Buonanno, M. Maggiore, and C. Ungarelli, Phys. Rev. **D55**, 3330 (1997), [gr-qc/9605072](#).
- [163] W. H. Kinney, A. Melchiorri, and A. Riotto, Phys. Rev. **D63**, 023505 (2001), [astro-ph/0007375](#).
- [164] N. Seto and J. Yokoyama, J. Phys. Soc. Jap. **72**, 3082 (2003), [gr-qc/0305096](#).
- [165] A. Cooray, Mod. Phys. Lett. **A20** (2005), [astro-ph/0503118](#).
- [166] L. Verde, H. Peiris, and R. Jimenez, JCAP **0601**, 019 (2006), [astro-ph/0506036](#).
- [167] Y.-S. Song and L. Knox, Phys. Rev. **D68**, 043518 (2003), [astro-ph/0305411](#).
- [168] D. J. Schwarz, C. A. Terrero-Escalante, and A. A. Garcia, Phys. Lett. **B517**, 243 (2001), [astro-ph/0106020](#).

- [169] M. B. Hoffman and M. S. Turner, Phys. Rev. **D64**, 023506 (2001), [astro-ph/0006321](#).
- [170] W. H. Kinney, Phys. Rev. **D66**, 083508 (2002), [astro-ph/0206032](#).
- [171] R. Easther and W. H. Kinney, Phys. Rev. **D67**, 043511 (2003), [astro-ph/0210345](#).
- [172] A. R. Liddle, Phys. Rev. **D68**, 103504 (2003), [astro-ph/0307286](#).
- [173] N. Kaloper, M. Kleban, A. E. Lawrence, and S. Shenker, Phys. Rev. **D66**, 123510 (2002), [hep-th/0201158](#).
- [174] S. Chongchitnan and G. Efstathiou, Phys. Rev. **D73**, 083511 (2006), [astro-ph/0602594](#).
- [175] L. A. Boyle and P. J. Steinhardt (2005), [astro-ph/0512014](#).
- [176] M. S. Turner and F. Wilczek, Phys. Rev. Lett. **65**, 3080 (1990).
- [177] T. Biswas and A. Notari, Phys. Rev. **D74**, 043508 (2006), [hep-ph/0511207](#).
- [178] M. Gasperini and G. Veneziano, Phys. Rept. **373**, 1 (2003), [hep-th/0207130](#).
- [179] R. H. Cyburt, B. D. Fields, K. A. Olive, and E. Skillman, Astropart. Phys. **23**, 313 (2005), [astro-ph/0408033](#).
- [180] E. Pierpaoli, Mon. Not. Roy. Astron. Soc. **342**, L63 (2003), [astro-ph/0302465](#).
- [181] A. Kosowsky, A. Mack, and T. Kahniashvili, Phys. Rev. **D66**, 024030 (2002), [astro-ph/0111483](#).
- [182] D. R. Brill and J. B. Hartle, Phys. Rev. **135**, B271 (1964).
- [183] R. A. Isaacson, Phys. Rev. **166**, 1263 (1968).
- [184] R. A. Isaacson, Phys. Rev. **166**, 1272 (1968).
- [185] C.-P. Ma and E. Bertschinger, Astrophys. J. **455**, 7 (1995), [astro-ph/9506072](#).
- [186] K. S. Thorne, C. W. Misner, and J. A. Wheeler, *Gravitation* (W. H. Freeman 1215 p, 1973).
- [187] M. S. Turner, M. J. White, and J. E. Lidsey, Phys. Rev. **D48**, 4613 (1993), [astro-ph/9306029](#).
- [188] A. F. Heckler, Phys. Rev. **D49**, 611 (1994).
- [189] R. E. Lopez and M. S. Turner, Phys. Rev. **D59**, 103502 (1999), [astro-ph/9807279](#).
- [190] D. A. Dicus et al., Phys. Rev. **D26**, 2694 (1982).
- [191] A. D. Dolgov, S. H. Hansen, and D. V. Semikoz, Nucl. Phys. **B503**, 426 (1997), [hep-ph/9703315](#).

- [192] A. D. Dolgov, S. H. Hansen, and D. V. Semikoz, Nucl. Phys. **B543**, 269 (1999), hep-ph/9805467.
- [193] W. Hu and N. Sugiyama, Astrophys. J. **444**, 489 (1995), astro-ph/9407093.
- [194] R. Bowen, S. H. Hansen, A. Melchiorri, J. Silk, and R. Trotta, Mon. Not. Roy. Astron. Soc. **334**, 760 (2002), astro-ph/0110636.
- [195] S. Dodelson, *Modern cosmology* (Amsterdam, Netherlands: Academic Pr. (2003) 440 p, 2003).
- [196] D. J. Eisenstein et al. (SDSS), Astrophys. J. **633**, 560 (2005), astro-ph/0501171.
- [197] W. J. Percival et al., Mon. Not. Roy. Astron. Soc. **381**, 1053 (2007), arXiv:0705.3323[astro-ph].
- [198] W. Hu and N. Sugiyama, Astrophys. J. **471**, 542 (1996), astro-ph/9510117.
- [199] S. Bashinsky and U. Seljak, Phys. Rev. **D69**, 083002 (2004), astro-ph/0310198.
- [200] J. M. Bardeen, Phys. Rev. **D22**, 1882 (1980).
- [201] U. Seljak and M. Zaldarriaga, Astrophys. J. **469**, 437 (1996), astro-ph/9603033.
- [202] C. L. Bennett et al., Astrophys. J. Suppl. **148**, 1 (2003), astro-ph/0302207.
- [203] C.-l. Kuo et al. (ACBAR), Astrophys. J. **600**, 32 (2004), astro-ph/0212289.
- [204] A. C. S. Readhead et al., Astrophys. J. **609**, 498 (2004), astro-ph/0402359.
- [205] C. Dickinson et al., Mon. Not. Roy. Astron. Soc. **353**, 732 (2004), astro-ph/0402498.
- [206] W. C. Jones et al., Astrophys. J. **647**, 823 (2006), astro-ph/0507494.
- [207] F. Piacentini et al., Astrophys. J. **647**, 833 (2006), astro-ph/0507507.
- [208] T. E. Montroy et al., Astrophys. J. **647**, 813 (2006), astro-ph/0507514.
- [209] M. Colless et al. (The 2DFGRS), Mon. Not. Roy. Astron. Soc. **328**, 1039 (2001), astro-ph/0106498.
- [210] W. J. Percival et al. (The 2dFGRS), Mon. Not. Roy. Astron. Soc. **327**, 1297 (2001), astro-ph/0105252.
- [211] M. Tegmark et al. (SDSS), Astrophys. J. **606**, 702 (2004), astro-ph/0310725.
- [212] M. Viel, M. G. Haehnelt, and V. Springel, Mon. Not. Roy. Astron. Soc. **354**, 684 (2004), astro-ph/0404600.

- [213] M. Viel, J. Weller, and M. Haehnelt, *Mon. Not. Roy. Astron. Soc.* **355**, L23 (2004), [astro-ph/0407294](#).
- [214] P. Crotty, J. Lesgourgues, and S. Pastor, *Phys. Rev.* **D69**, 123007 (2004), [hep-ph/0402049](#).
- [215] S. Burles, K. M. Nollett, J. N. Truran, and M. S. Turner, *Phys. Rev. Lett.* **82**, 4176 (1999), [astro-ph/9901157](#).
- [216] T. Chiba, *Phys. Lett.* **B575**, 1 (2003), [astro-ph/0307338](#).
- [217] A. Rajaraman (2003), [astro-ph/0311160](#).
- [218] T. Multamaki and I. Vilja, *Phys. Rev.* **D74**, 064022 (2006), [astro-ph/0606373](#).
- [219] V. Faraoni, *Phys. Rev.* **D74**, 023529 (2006), [gr-qc/0607016](#).
- [220] M. L. Ruggiero and L. Iorio, *JCAP* **0701**, 010 (2007), [gr-qc/0607093](#).
- [221] G. Allemandi, M. Francaviglia, M. L. Ruggiero, and A. Tartaglia, *Gen. Rel. Grav.* **37**, 1891 (2005), [gr-qc/0506123](#).
- [222] C.-G. Shao, R.-G. Cai, B. Wang, and R.-K. Su, *Phys. Lett.* **B633**, 164 (2006), [gr-qc/0511034](#).
- [223] J. A. R. Cembranos, *Phys. Rev.* **D73**, 064029 (2006), [gr-qc/0507039](#).
- [224] A. D. Dolgov and M. Kawasaki, *Phys. Lett.* **B573**, 1 (2003), [astro-ph/0307285](#).
- [225] G. J. Olmo, *Phys. Rev.* **D72**, 083505 (2005).
- [226] C. Brans and R. H. Dicke, *Phys. Rev.* **124**, 925 (1961).
- [227] C. M. Will, *Theory and experiment in gravitational physics* (Cambridge, UK: Univ. Pr. (1993) 380 p, 1993).
- [228] B. Bertotti, L. Iess, and P. Tortora, *Nature* **425**, 374 (2003).
- [229] S. S. Shapiro, J. L. Davis, D. E. Lebach, and J. S. Gregory, *Phys. Rev. Lett.* **92**, 121101 (2004).
- [230] T. Clifton and J. D. Barrow, *Phys. Rev.* **D72**, 103005 (2005), [gr-qc/0509059](#).
- [231] A. L. Erickcek, T. L. Smith, and M. Kamionkowski, *Phys. Rev.* **D74**, 121501 (2006), [astro-ph/0610483](#).
- [232] D. N. Vollick, *Class. Quant. Grav.* **21**, 3813 (2004), [gr-qc/0312041](#).
- [233] E. E. Flanagan, *Phys. Rev. Lett.* **92**, 071101 (2004), [astro-ph/0308111](#).
- [234] S. M. Carroll et al., *Phys. Rev.* **D71**, 063513 (2005), [astro-ph/0410031](#).

- [235] S. M. Carroll, I. Sawicki, A. Silvestri, and M. Trodden, *New J. Phys.* **8**, 323 (2006), [astro-ph/0607458](#).
- [236] K. Kainulainen, V. Reijonen, and D. Sunhede, *Phys. Rev.* **D76**, 043503 (2007), [gr-qc/0611132](#).
- [237] X.-H. Jin, D.-J. Liu, and X.-Z. Li (2006), [astro-ph/0610854](#).
- [238] A. A. Starobinsky, *Phys. Lett.* **B91**, 99 (1980).
- [239] G. V. Bicknell, *J. Phys. A: Math. Nucl. Gen.* **7**, 1061 (1974).
- [240] W. Hu and I. Sawicki, *Phys. Rev.* **D76**, 064004 (2007), [0705.1158](#).
- [241] I. Sawicki and W. Hu, *Phys. Rev.* **D75**, 127502 (2007), [astro-ph/0702278](#).
- [242] W. L. Freedman et al. (HST), *Astrophys. J.* **553**, 47 (2001), [astro-ph/0012376](#).
- [243] H. Sirousse-Zia, *Gen. Rel. Grav.* **30**, 1273 (1998).
- [244] A. S. Bolton, S. Rappaport, and S. Burles, *Phys. Rev.* **D74**, 061501 (2006), [astro-ph/0607657](#).
- [245] H.-W. Rix and S. D. M. White, *Mon. Not. Roy. Astron. Soc.* **254**, 389 (1992).
- [246] L. V. E. Koopmans (2005), [astro-ph/0511121](#).
- [247] J. Binney and S. Tremaine, *Galactic dynamics* (Princeton University Press, 1987, 747 p., 1987).
- [248] R. Kormann, P. Schneider, and M. Bartelmann, *A. & A.* **284**, 285 (1994).
- [249] C. S. Kochanek, *Astrophys. J.* **373**, 354 (1991).
- [250] J. D. Bekenstein and R. H. Sanders, *Astrophys. J.* **429**, 480 (1994), [astro-ph/9311062](#).
- [251] H. W. Lilliefors, *J. Am. Stat. Assoc.* **62**, 399 (1967).
- [252] H. W. Lilliefors, *J. Am. Stat. Assoc.* **64**, 387 (1969).
- [253] M. W. Auger, *Mon. Not. Roy. Astron. Soc.* **383**, L40 (2008).
- [254] T. Treu (2007), private communication.
- [255] L. V. E. Koopmans, T. Treu, A. S. Bolton, S. Burles, and L. A. Moustakas, *Astrophys. J.* **649**, 599 (2006), [astro-ph/0601628](#).
- [256] I. Navarro and K. Van Acoleyen, *JCAP* **0702**, 022 (2007), [gr-qc/0611127](#).

- [257] S. Deser, R. Jackiw, and S. Templeton, *Ann. Phys.* **140**, 372 (1982).
- [258] S. H. S. Alexander and J. Gates, S. James, *JCAP* **0606**, 018 (2006), [hep-th/0409014](#).
- [259] S. H.-S. Alexander, M. E. Peskin, and M. M. Sheikh-Jabbari, *Phys. Rev. Lett.* **96**, 081301 (2006), [hep-th/0403069](#).
- [260] S. Alexander and N. Yunes, *Phys. Rev.* **D75**, 124022 (2007), [0704.0299](#).
- [261] S. Alexander and N. Yunes, *Phys. Rev. Lett.* **99**, 241101 (2007), [hep-th/0703265](#).
- [262] S. M. Carroll, *Phys. Rev. Lett.* **81**, 3067 (1998), [astro-ph/9806099](#).
- [263] S. M. Carroll, G. B. Field, and R. Jackiw, *Phys. Rev.* **D41**, 1231 (1990).
- [264] K. Konno, T. Matsuyama, and S. Tanda, *Phys. Rev.* **D76**, 024009 (2007), [0706.3080](#).
- [265] I. Newton, *The Principia* (University of California Press, 1999).
- [266] D. Brouwer and G. M. Clemence, *Methods of Celestial Mechanics* (Academic Press, New York, 1961, 1961).
- [267] L. Iorio, *Nuovo Cim.* **B116**, 777 (2001), [gr-qc/9908080](#).
- [268] G. Beutler, *Methods of celestial mechanics* (Springer-Verlag, Berlin, 2005).
- [269] T. L. Smith, A. L. Erickcek, R. R. Caldwell, and M. Kamionkowski, *Phys. Rev.* **D77**, 024015 (2008), [0708.0001](#).
- [270] C. D. Murray and S. F. Dermott, *Solar System Dynamics* (Cambridge U. Press, 1999).
- [271] I. Ciufolini and E. C. Pavlis, *Nature* **431**, 958 (2004).
- [272] E. C. Pavlis (2007), private communication.
- [273] V. A. Brumberg, *Essential Relativistic Celestial Mechanics* (Adam Hilger, 1991).
- [274] I. Ciufolini, A. Paolozzi, D. G. Currie, and E. C. Pavlis (2004), prepared for International Workshop on Frontier Science: Physics and Astrophysics in Space, Frascati and Rome, Italy, 14-19 Jun 2004.
- [275] G. E. Pugh, Weapons System Evaluation Group, Research Memorandum No. 111, Department of Defense (USA) (1959).
- [276] L. I. Schiff, *Phys. Rev. Lett.* **4**, 215 (1960).
- [277] L. I. Schiff, *Proc. Nat. Acad. Sci.* **46**, 871 (1960).

- [278] G. Brunfiel, *Nature* **444**, 978 (2006).
- [279] J. G. Williams, S. G. Turyshev, and J. Murphy, Thomas W., *Int. J. Mod. Phys.* **D13**, 567 (2004), [gr-qc/0311021](#).
- [280] E. Bertschinger (1993), [astro-ph/9503125](#).
- [281] C. W. Misner, K. S. Thorne, and J. A. Wheeler (1973), san Francisco 1973, 1279p.
- [282] S. W. Hawking, *Astrophys. J.* **145**, 544 (1966).
- [283] G. F. R. Ellis and M. Bruni, *Phys. Rev.* **D40**, 1804 (1989).
- [284] P. K. S. Dunsby, *Class. Quant. Grav.* **14**, 3391 (1997), [gr-qc/9707022](#).
- [285] A. Challinor and A. Lasenby (1998), [astro-ph/9804301](#).
- [286] A. Lewis, PhD Thesis, University of Cambridge (2000).
- [287] M. B. Green and J. H. Schwarz, *Phys. Lett.* **B149**, 117 (1984).
- [288] B. A. Campbell, N. Kaloper, R. Madden, and K. A. Olive, *Nucl. Phys.* **B399**, 137 (1993), [hep-th/9301129](#).
- [289] S. Chandrasekhar, *Hydrodynamic and Hydromagnetic Stability* (Clarendon Press, 1961).
- [290] W. H. Warner, *ZAMP* **23**, 221 (1972).
- [291] D. D. Joseph, *Stability of Fluid Motions I*, vol. 27 (Springer Tracts in Natural Philosophy, 1970).